eman ta zabal zazu

Universidad del País Vasco
Euskal Herriko Unibertsitatea

PhD Thesis

Lipid-lipid interactions in bilayers containing polar sphingolipids, ceramide and cholesterol

Biofisika Institute (UPV/EHU, CSIC)

Department of Biochemistry and Molecular Biology

Faculty of Science and Technology

University of the Basque Country (UPV/EHU)

Emilio José González Ramírez

Supervisor: Prof. F. M. Goñi

Leioa 2019

CONTENTS

ABBREVIATIONS

ΔH	Enthalpy change (in calorimetry)	D_B	Bilayer thickness
$\Delta T_{1/2}$	Width at half-height (in calorimetry)	DiI	1,1'-dioctadecyl-3,3,3',3'-tetramethylindocarbocyanine perchlorate
γ	Ripple offset angle		
λ_r	Ripple wavelength	DLS	Dynamic light scattering
A_C	Area/chain perpendicular to the chains	DMPC	1,2-dimyristoyl-*sn*-glycero-3-phosphocholine
A_L	Area per lipid	DPH	1,6-diphenyl-1,3,5-hexatriene
A_o	Lipid-water interface		
A_H	Area of hydrophobic tail	DPPC	1,2-dipalmitoyl-*sn*-glycero-3-phosphocholine
AFM	Atomic force microscopy		
ANTS	8-aminonaphthalene-1,3,6-trisulfonic acid	DPX	p-xylene-bis-pyridinium bromide
ATP	Adenosine triphosphate	DSC	Differential scanning calorimetry
bCer	Brain ceramide		
bCrb	Brain cerebroside(s)	DOPC	1,2-dioleoyl-L-α-phosphatidylcholine
bSM	Brain sphingomyelin		
C	Crystalline phase	eCer	Egg ceramide
C_P	Heat capacity	EDTA	Ethylenediaminetetra-acetic acid
Cer	Ceramide(s)		
CL	Cardiolipin	ER	Endoplasmatic reticulum
C1P	Ceramide-1-phosphate		
Chol	Cholesterol	Egg PC	L-α-phosphatidylcholine
Crb	Cerebroside		
D	Diffusion coefficient	ERG	Ergosterol

eSM	Egg sphingomyelin
F_b	Breakthrough force
GalCer	Galactosylceramide
GlcCer	Glucosylceramide
GP	General polarization
GSL	Glycosphingolipid(s)
GUV	Giant unilamellar vesicle(s)
H	Hexagonal phase
HOPG	Hydrophobic highly oriented pyrolytic graphite
k_B	Boltzmann constant
k_C	Bending modulus
L	Lamellar phase
L_α	Disordered or fluid phase
L_β	Gel phase
$L_{\beta'}$	Ripple phase
L_c	Liquid crystalline phase
L_o	Liquid ordered phase
Laurdan	6-lauroyl,1-2-dimethylaminonaphthalene
LAXS	Low angle X-ray scattering
LUV	Large unilamellar vesicle(s)
M	Micellar phase
MLV	Multilamellar vesicle(s)
NAP	Naphtho[2,3-a]pyrene
NBD-PE	N-(7-nitrobenz-2-oxa-1,3-diazol-4-yl)-1,2-dihexadecanoyl-*sn*-glycero-3-phosphoethanolamine
nCer	N-nervonoyl-D-erythro-sphingosine
nSM	N-nervonoyl-D-erythro-sphingosylphosphoryl-choline
NSOM	Near-field scanning optical microscopy
P	Oblique phase
PALM	Photoactivated localization microscopy
PC	Phosphatidylcholine
pCer	N-palmitoyl-D-erythro-sphingosine
PDI	Polydispersity index
PE	Phosphatidylethanol-amine
PI	Phosphatidylinositol
PIPES	1,4-Piperazinediethane-sulfonic acid
PL	Total phospholipid
POPC	1-palmitoyl-2-oleoyl-*sn*-glycero-3-phosphocholine
PS	Phosphatidylserine
pSM	N-palmitoyl-D-erythro-sphingosylphosphoryl-choline
PTFE	Polytetrafluoroethylene
P	Tridimensional cubic phase

R_h	Hydrodynamic radius	S1P	Sphingosine-1-phosphate
RH	Relative humidity	SUV	Small unilamellar vesicle(s)
(Rho-PE)	18:1 phosphatidylethanol-amine-N-(lissamine rhodamine B sulfonyl)	T_m	Mid-point transition temperature
SM	Sphingomyelin(s)	T_p	Pretransition temperature
SPB	Supported lipid bilayer(s)	tPA	trans-parinaric acid
Sph	Sphingosine	TFE	2,2,2-Trifluoroethanol
STED	Stimulated emission depletion	Triton-X-100	Octylphenoxypoly-ethoxyethanol
STM	Scanning tunneling microscope	WAXS	Wide angle X-ray scattering

CHAPTER 1:

INTRODUCTION AND AIMS

CHAPTER 1: INTRODUCTION AND AIMS

1.1 Cell membranes

Cell membranes are currently understood in terms of boundaries consisting of a hydrophobic matrix, formed by an oriented double layer of polar lipids, intercalated with proteins. Membrane carbohydrates exist bound to either lipids or proteins (Goñi, 2014). Moreover, eukaryotic sub-cellular organelles and both endocytic and exocytic vesicles are also delimited by a membrane. Cell membranes act not only as boundaries between two aqueous compartments but also perform a number of essential functions: i) they are a semipermeable barrier with the ability of exchanging essential materials between them, ii) help provide a shape to the cell, iii) interact with the extracellular matrix to maintain tissue organisation, and iv) are involved in many molecular processes such as cell signaling, cell adhesion, cell differentiation or cell death (Stillwell, 2016).

The cell membrane model accepted nowadays has been defined as a result of a series of studies performed during the last century. The existence of cell membranes was not clearly suggested until the 1890s when Overton confirmed the presence of a semipermeable membrane in cells, after observing how non-polar molecules diffuse across the cell membrane with less difficulty than polar ones (Overton, 1895; Kleinzeller, 1997). Gorter and Grendel confirmed Overton proposition of phospholipids and cholesterol being the main components of cell membranes when they compared the surface occupied by the lipids of a cell against its total surface and concluded that the cell was surrounded by a lipid double layer, or bilayer (Gorter & Grendel, 1926). Even though the lipid bilayer hypothesis is widely accepted these days, the Gorter and Grendel experiment presented theoretical and technical issues (Dervichian & Macheboeuf, 1938). In 1935 Danielli and Davson proposed the paucimolecular model in which the lipid bilayer was sandwiched between proteins in β-conformation (Danielli & Davson, 1935). Although this model remained unchanged for almost 30 years, the development of electron microscopy led Robertson to rename it as “unit membrane”, when he replaced with globular proteins the proteins in β-sheet conformation. Additionally, Robertson confirmed that this structure could be

found in all biological membranes (Robertson, 1960). Moreover, the possibility to study membrane protein conformation showed how proteins were in a globular or alpha-conformation rather than a beta-structure (Maddy & Malcolm, 1965; Lenard & Singer, 1966; Zahler *et al.*., 1966). All these pieces of evidence were combined by Singer and Nicolson in 1972 when they postulated the basics of the current "fluid mosaic model" (Singer & Nicolson, 1972).

Singer and Nicolson´s model was defined as a mosaic because they proposed lipids and proteins as its main components, organized in a structure reminiscent of the Roman mosaics. Lipids were forming a double layer because of their amphipathic nature, and proteins were scattered along the bilayer. Proteins could interact with the lipids, either being embedded in the lipid matrix (integral proteins), or being associated with them through polar interactions (peripheral proteins). In addition, the model was named fluid because they suggested that lipids and proteins were in constant motion in each of the lipid monolayers, making both sides of the bilayer different in composition and structure.

Although the fluid mosaic is the current model describing the cell membranes, it has required several adjustments during the last decades (Jacobson *et al.*, 1995; Engelman, 2005; Goñi, 2014). Nowadays, it is widely known that membranes are highly crowded with proteins. The idea of proteins not being always in contact with the membrane and existing part-time in the cytosol and part-time docked to a membrane is currently accepted. This dynamic view of the bilayer affects also the lipids, accepting the presence of a high number of lipid phases and non-lamellar structures. The Singer and Nicolson model pointed to liquid-crystalline phases as the only relevant ones in the well-organized lamellar structure, however a number of phases as the liquid-ordered, the inverted hexagonal or the cubic ones must also be considered, because the membrane can transiently adopt non-lamellar structures in small regions. Moreover, the presence of non-lamellar structures confirms that the lipid bilayer is curved and that the previous flat drawing

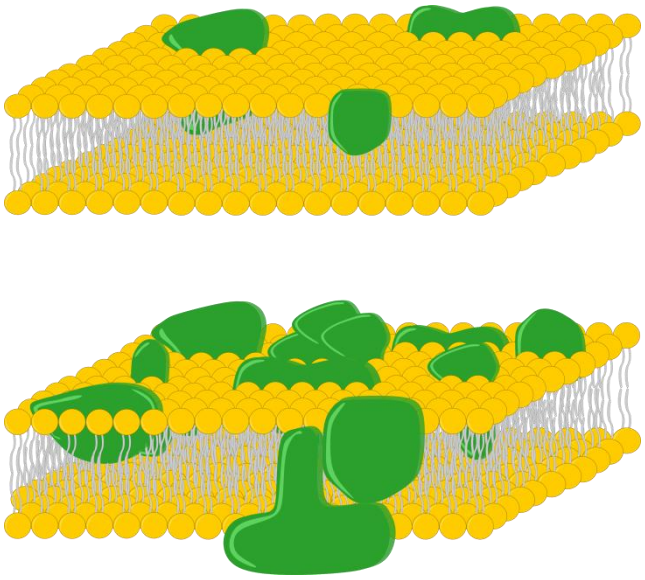

Figure 1.1. The Singer and Nicolson model originally proposed (upper) and an amended and updated version (down). [Redrawn from (Engelman, 2005)].

requires some modifications. The current data point to the lateral heterogeneity of membranes in which small patches enriched in lipids and proteins (also called domains) can be found. These domains are associated with many molecular processes such as cell signaling, cell adhesion, cell differentiation or cell death. A further adjustment is related to the (limited) movement of the lipids across the bilayer since transbilayer lipid motion has been confirmed in several studies (Contreras *et al.*, 2010).

1.2 Membrane Lipids

One of the main components of cell membranes are the lipids. Lipids are organic molecules of an amphipathic nature, containing both hydrophobic (tail) and hydrophilic (headgroup) moieties. Lipids tend to be insoluble in water, so when they are exposed to a polar solvent they form the most thermodynamically stable structure, maximizing both hydrophobic and hydrophilic interactions. This tendency is due to the hydrophobic effect and can be affected by several parameters such as the chemical nature of the molecules, their size, the salinity, or pH of the solution. The most common structure is a double layer in which the polar headgroups are in contact with the solvent and the hydrophobic tails are facing each other, this is commonly known as the lipid bilayer, fundamental architecture of the membranes (Lombard, 2014; Stillwell, 2016).

Lipids have several functions apart from maintaining the membrane structure, those include acting as energy and heat sources, because of their chemically reduced state, signaling molecules, protein recruitment platforms and substrates for translational protein-lipid modifications (Harayama & Riezman, 2018).

Most membrane lipids have fatty acids as their hydrophobic moieties. A fatty acid is a monocarboxylic acid that may be either saturated or unsaturated. Fatty acids usually have a chain of 4 to 24 carbons, being classified as short-chain (4-6 carbons), medium-chain (8-10 carbons) and long-chain (12-24 carbons). Long-chain fatty acids are the most common in membranes, in which they are relevant for the maintenance of membrane structure. Furthermore, fatty acid melting points and insolubility increase with chain length. The most common fatty acids found in membrane lipids are summarized in Table 1.1.

Table 1.1. The most common fatty acids in membranes.

Name	Structure	Melting Point (°C)
Lauric	12:0	44.2
Myristic	14:0	53.9
Palmitic	16:0	63.1
Stearic	18:0	69.6
Linoleic ($\Delta^{9,12}$)	18:2	-5
Linolenic ($\Delta^{9,12,15}$)	18:3	-11
Arachidic	20:0	75.3
Lignoceric	24:0	84.2
Palmitoleic (Δ^{9})	16:1	0.5
Oleic (Δ^{9})	18:1	16.2
Arachidonic ($\Delta^{5,8,11,14}$)	20:4	-50
Nervonic (Δ^{9})	24:1	39

1.2.1 Membrane lipid classification

The chemical structures of lipids are related to their physicochemical properties, so it is crucial to focus on their chemical diversity to understand how lipids behave in cell membranes. The predominant lipids in cell membranes are glycerolipids, sphingolipids, and sterols.

Glycerolipids

Glycerolipids can be further classified into glycerophospholipids and glyceroglycolipids. Glycerophospholipids are typically composed of one glycerol, two fatty acids, a phosphate group, and an alcohol. The fatty acids are bonded to the glycerol by an ester linkage at carbon positions *sn*-1 and *sn*-2, usually *sn*-1 is saturated and *sn*-2 is unsaturated. In mammalian cells, there are seven major classes of glycerolipids depending on the polar group bonded to the phosphate and on the length of the acyl chains (Box 1.1). Phosphatidylcholine (PC), phosphatidylethanolamine (PE), phosphatidylserine (PS) and phosphatidylinositol (PI) are the most common lipids in mammalian cells, making up to 65 mol% of the lipid composition (van Meer & de Kroon, 2011).

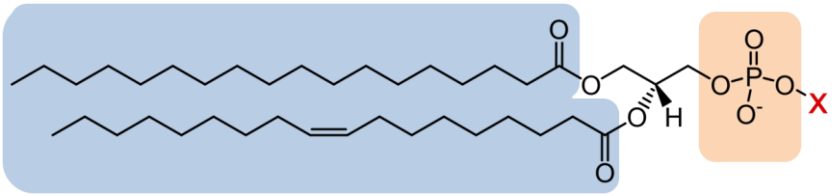

Figure 1.2. General structure of glycerophospholipids. A glycerol group (black), a saturated fatty acid in *sn*-1 and an unsaturated one in *sn*-2 (blue box), a phosphate group (orange box) and the polar headgroup substituent (red).

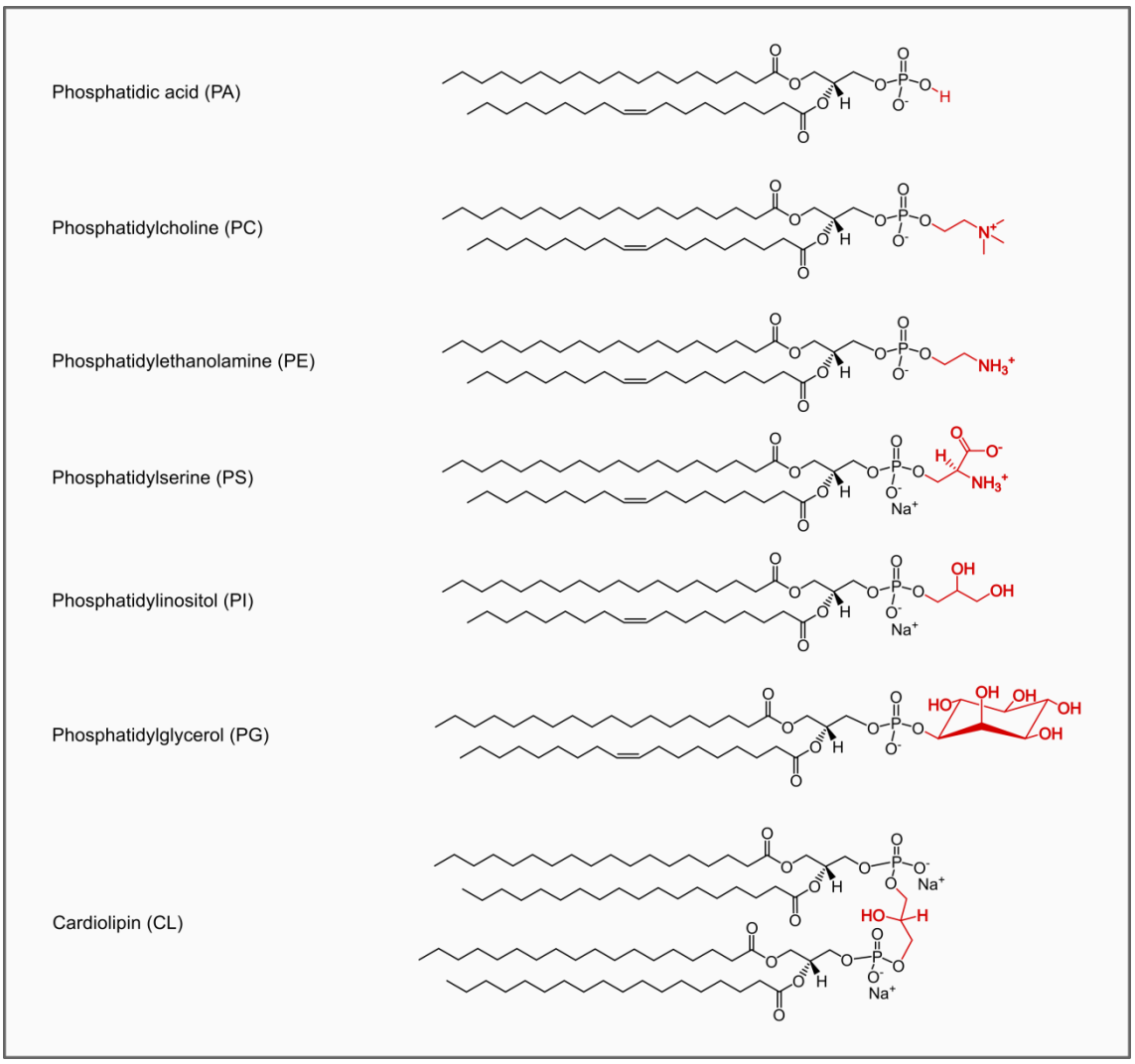

Box 1.1. Structures of common glycerophospholipids. All saturated and unsaturated fatty acids in this box contain 18 carbon atoms.

Glyceroglycolipids have a mono- or oligosaccharide group bound to carbon *sn*-3 of glycerol through an *O*-glycosyl linkage, instead of a phosphate group. Glyceroglycolipids are the predominant lipids in chloroplasts of plants and eukaryotic algae and in cyanobacteria (Hölzl & Dörmann, 2007; Rahim *et al.*, 2018).

Sphingolipids

The basic building block of all sphingolipids is sphingosine, a long hydrophobic unsaturated amino octadecyl alcohol ((2S,3R,4E)-2-amino-octadec-4-ene-1,3-diol). There are many sphingolipid species in cell membranes, which can be distinguished by the headgroup or the fatty acid attached to the sphingosine by an amide linkage. The headgroup can be a simple hydroxyl group (ceramide), a phosphorylcholine polar residue (sphingomyelin), a sugar (cerebroside) or several sugars (ganglioside), while the fatty acid is usually long and saturated.

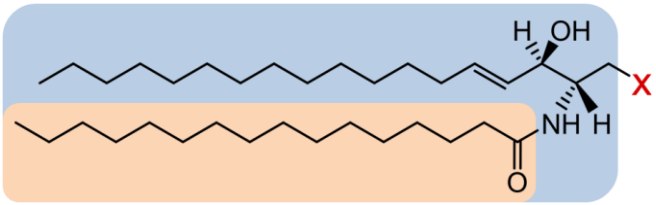

Figure 1.3. General structure of sphingolipids. A sphingosine backbone (blue box), a saturated fatty acid (orange box) and the polar headgroup substituent (red).

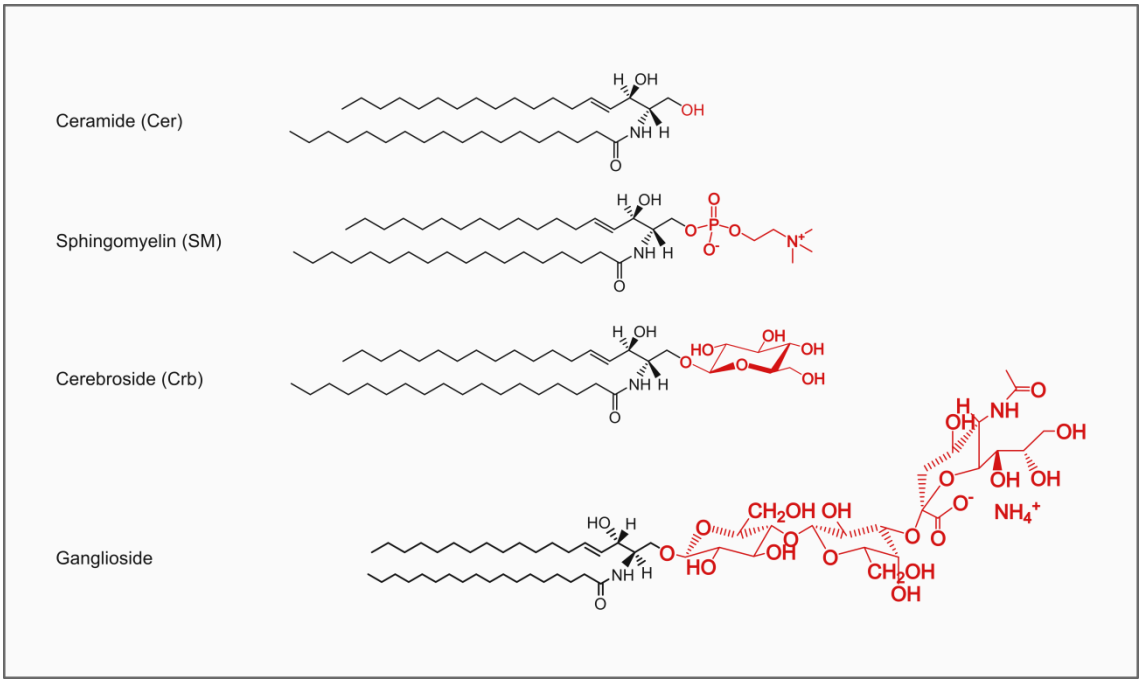

Box 1.2. Structures of common sphingolipids. All saturated and unsaturated fatty acids in this box contain 18 carbon atoms.

Sterols

Sterols are the major non-polar lipids in cell membranes, cholesterol being the most common one in mammalian cells. Its structure is composed of four hydrophobic fused rings attached to a hydrocarbon tail at one side and containing a hydrophilic alcohol at the opposite side. There are other sterols as ergosterol (fungi) and β-sitosterol (plants), whose structure is quite similar to cholesterol.

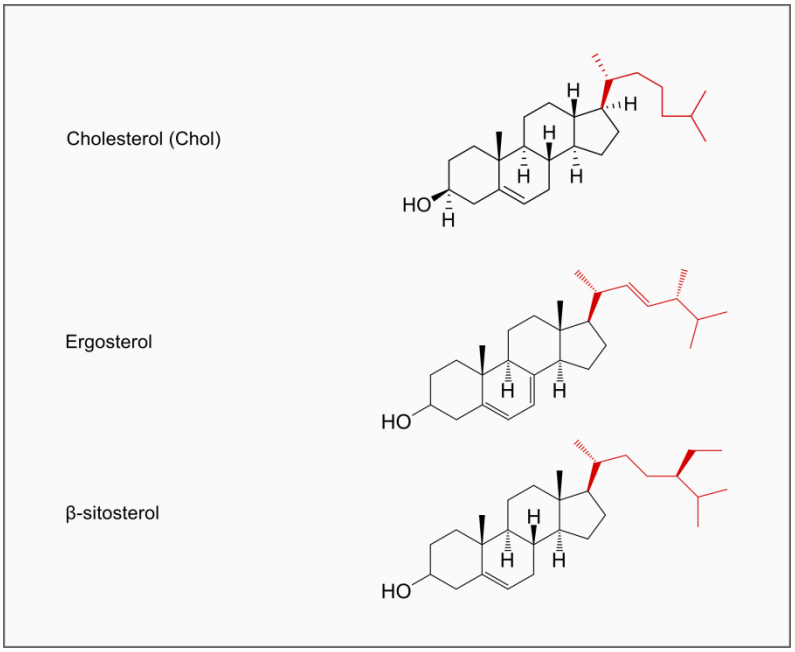

Box 1.3. Structures of common sterols.

1.2.2 Lipid distribution

The most common lipids in cell membranes are glycerophospholipids, sphingolipids, and sterols. Additionally, the variety of headgroups or acyl chains that can be attached to their backbones it is the main reason why the existence of more than 1000 different lipid species is estimated. Their distribution inside the cell is not homogeneous and is related to the local lipid metabolism of the organelles. Some lipids are transported away from where they are synthesized to their final destination where they perform their function.

Organelles such as the endoplasmatic reticulum (ER), the Golgi apparatus, and the mitochondria have an autonomous lipid synthesis system, in which at least some of their structural lipids are synthesized, while other organelles like the plasma membrane are composed of lipids transported from other regions. These systems are a good example of the heterogeneity in cells since the Golgi apparatus

is specialized in sphingolipid synthesis, almost all of which are destined to the plasma membrane, and the mitochondria is the only organelle that synthesizes cardiolipin. The ER produces structural and non-structural triacylglycerol and cholesteryl esters as much as ceramide (Van Meer *et al.*, 2008).

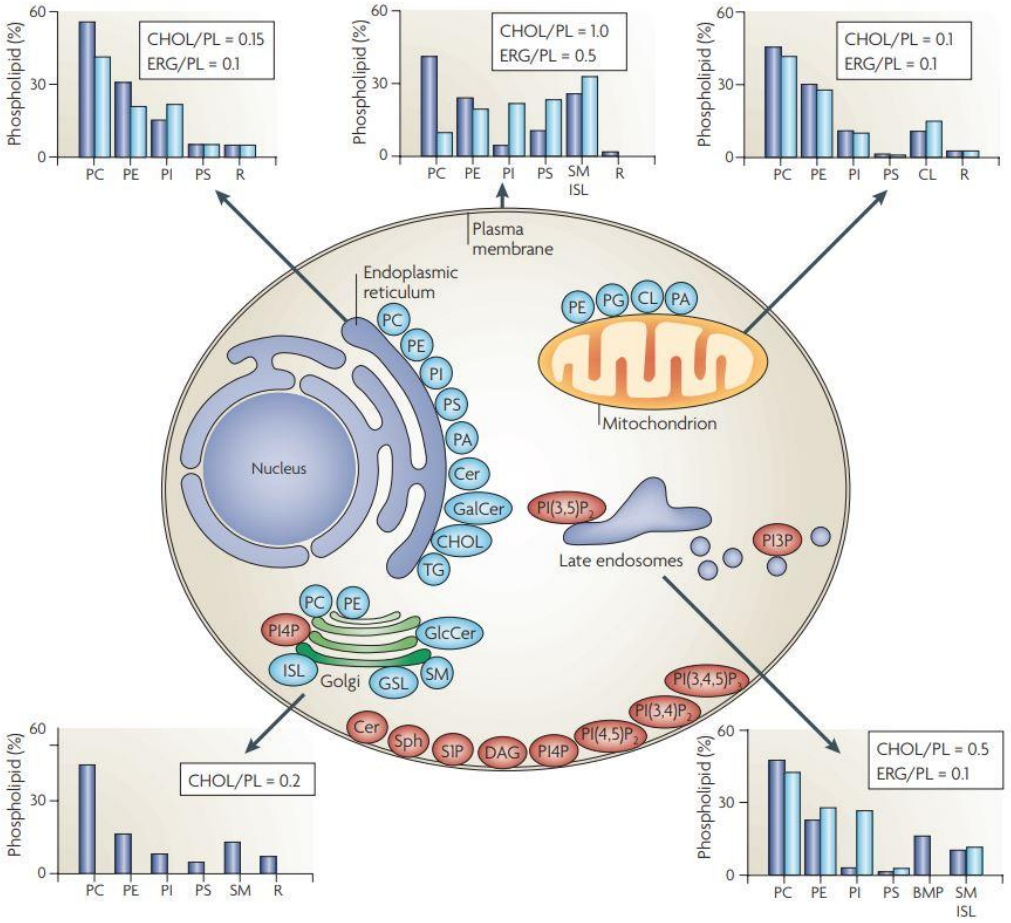

Figure 1.5. Lipid compositions of different organelles and plasma membranes inside the cell. [Taken from (Van Meer *et al.*, 2008)]. Abbreviations: ERG, Ergosterol; PL, Total lipid in mammals (blue) in yeast (light blue); CHOL, Cholesterol.

The basis of lipid heterogeneity in cell membranes is found in the lipid synthesis but how lipids distribute in membranes has also a strong impact. For example, the Golgi apparatus and the plasma membrane present an asymmetric distribution of their lipids. Most of PC and SM from the plasma membrane are found in the outer leaflet while PS and PE are found in the cytoplasmatic leaflet. In the ER, in order to maintain the symmetry, almost one-half of its newly-synthesized lipids have to be transferred to the outer leaflet. Nevertheless, transbilayer movement is limited by the high energy barrier that must be overcome to move a polar headgroup through a hydrophobic core and by the increase in lateral tension in the membrane upon insertion. The presence of

proteins (flippases) assists lipid transport from one side of the membrane to another, decreasing the energy needed (Contreras *et al.*, 2010).

1.2.3 Lipid geometry and polymorphism

The lipid bilayer is the main structure in cell membranes. Lipids become arranged in a lamellar structure in water, so that their hydrophilic and hydrophobic moieties are compensated by the hydrophobic effect. Several parameters such as chemical nature of the molecules, temperature, pressure, salinity, and pH of the solution affect this arrangement. However, it has been observed that the formation of transient non-lamellar structures in lipid bilayers is related to important biological processes such as membrane fusion and fission, reproduction, vesicular transport, and viral infection (Epand, 1998; Burger, 2000; Basañez, 2002).

In 1980 Israelachvili proposed that the formation of lamellar and non-lamellar structures is influenced by the lipid molecular geometry, suggesting that the structures of lipid aggregates are determined by the cross-sectional area of the lipid (Israelachvili *et al.*, 1980). Thus, lipid shapes can be classified into three groups: conical, cylindrical or inverted-cone shapes. This classification depends on the relationship between the volume of the lipid molecule (V), the area of the molecule at the lipid-water interface (A_0), and the length of the extended acyl chain (L_C).

$$S = \frac{V}{L_C \cdot A_0}$$

The parameter S is related to the area of the molecule at the lipid-water interface (A_0) and the lipid cross-sectional area in the hydrophobic tail (A_H), which would reflect a volume of $V = A_H \cdot L_c$ for a lipid displaying cylindrical shape. We can review the different morphological geometries as:

- $A_0 = A_H$ ($S = 1$): The molecule presents a cylinder shape
- $A_0 < A_H$ ($S > 1$): The molecule presents a cone shape
- $A_0 > A_H$ ($S < 1$): The molecule presents an inverted cone shape

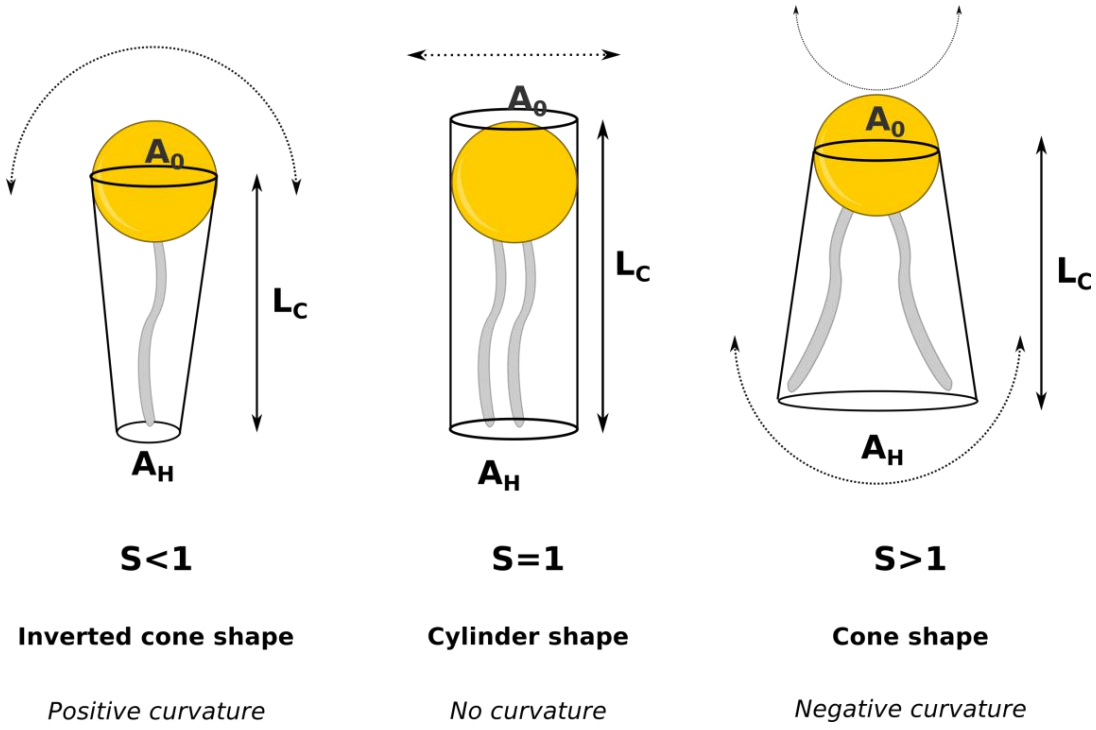

Figure 1.6. Molecular shape and curvature of physiological lipids.

Depending on their molecular geometry lipids self-aggregate into different phases, in which all their properties are uniform. Their formation in a polar environment has been widely studied through X-ray scattering and ^{31}P-NMR (Quinn & Wolf, 2010; Cullis & Kruijff, 1979; Luzzati & Tardieu, 1974). These phases can be lamellar (with cylindrical shape lipids) and non-lamellar (with cone- or inverted cone-shaped lipids) and are named using a capital letter, which describes their kind of lattice: unidimensional micellar (M) or lamellar (L), bidimensional hexagonal (H) or oblique (P) and tridimensional cubic (Q) or crystalline (C). Referring to non-lamellar phases, the curvature of their shape is classified into type I (positive) and type II (negative).

As previously described, biological membranes adopt essentially a lamellar structure. Moreover, the presence of certain lipids gives rise to different coexisting phases in the membrane, which contribute to its overall heterogeneity. Among these phases the most common ones are a disordered or fluid phase (L_α), a solid ordered phase with fatty acyl chains perpendicular to the plane of the membrane (also called gel) (L_β), a fluid-ordered phase with intermediate properties between fluid disordered and gel (L_o), a solid ordered phase with fatty acyl chains tilted with respect to the plane of the membrane ($L_{\beta'}$), and a crystalline phase (L_c).

Unsaturated lipids are normally arranged in a L_α phase, in which they can diffuse laterally or rotationally. However, saturated lipids are arranged in a L_β phase, in which the movement is not allowed. Temperature, pressure, and solvent proportion changes can cause phase transitions between phases. For example, temperature affects the transition between the gel and the fluid phase, commonly known as the main phase transition.

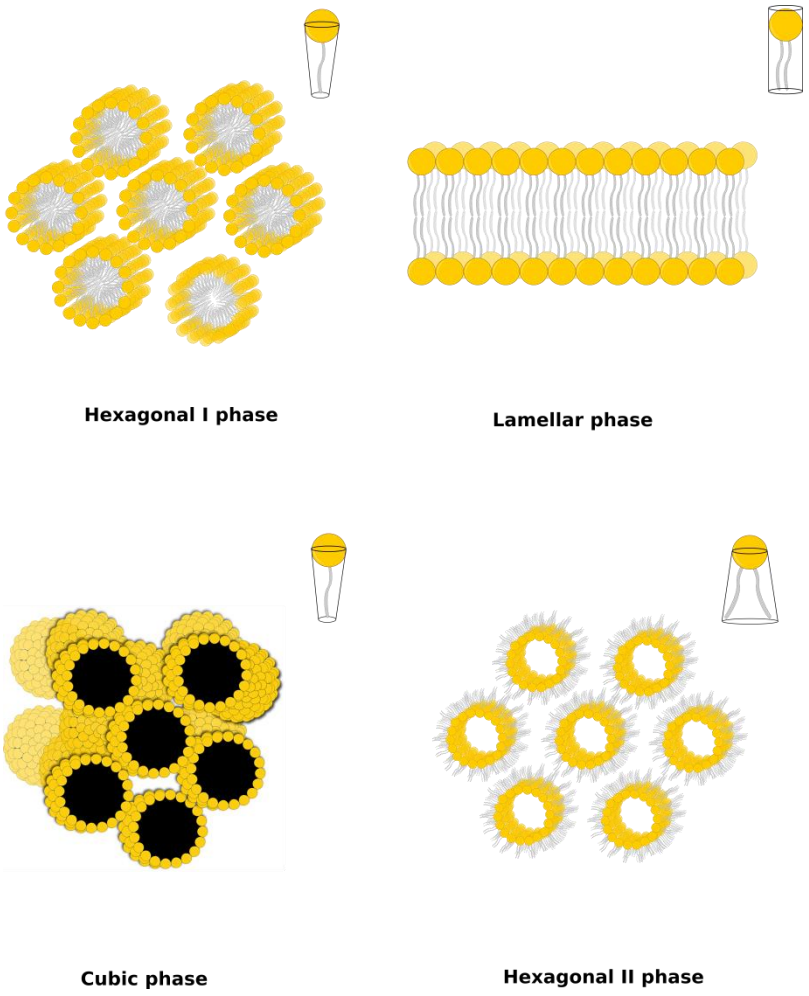

Figure 1.7. Lipid phases of physiological lipids.

In this thesis most studies will be performed on membrane models based on PC or SM, organized in lamellar phases due to their cylindrical shape. Others, like ceramide, cerebrosides, and sterols, with a cone shape and a spontaneous tendency to form inverted hexagonal phases will also be used.

1.3 Sphingolipids

Sphingolipids were named by J.L.W. Thudichum in 1884 when a brain compound with unusual properties was isolated. Thudichum´s interest in Greek mythology and the riddle of the new lipid function were the reasons why their name was related to the Sphinx (Thudichum, 1884). The field of sphingolipids was not relevant in biology for decades because they were considered as inert structural components of plasma membranes. Nowadays, they are considered as bioactive molecules of great interest due to their role as second messengers in many signaling pathways (Hannun *et al.*, 1986; Merrill *et al.*, 1986; Kolesnick, 1987). Additionally, sphingolipids have attracted the attention of scientists due to recent findings of sphingolipid metabolism pathways, their biophysical properties, and their role in the formation of lateral structures or membrane domains (Hannun & Obeid, 2008; Goñi *et al.*, 2014; Simons & Ikonen, 1997).

Sphingosine is the basic building block of sphingolipids. Other bioactive sphingolipids are ceramide and their related phosphate analogs, sphingosine-1-phosphate (S1P) and ceramide-1-phosphate (C1P). However, as previously described, lipids can suffer a great number of modifications that increase their complexity. At least five different sphingoid bases are known in mammalian cells, more than 20 species of fatty acid (varying in chain length, degree of saturation, and degree of hydroxylation) can be attached to the sphingoid base, and around 500 different carbohydrate structures have been described in GSL (Futerman & Hannun, 2004).

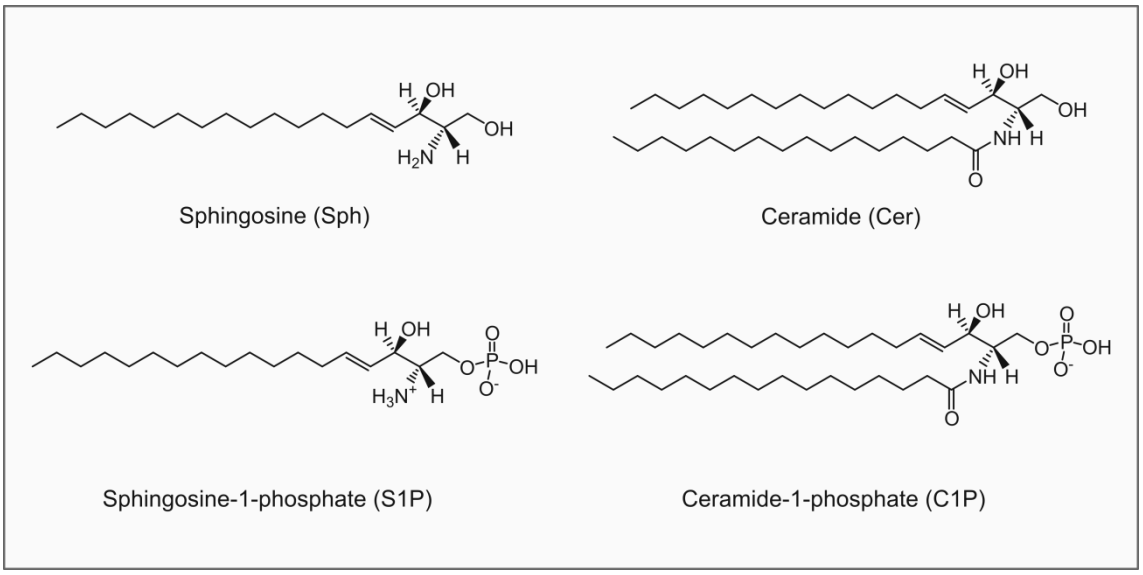

Box 1.4. Molecular structures of simple sphingolipids.

These sphingolipids play an important role in cell processes. Sphingosine is involved in the regulation of the actin cytoskeleton, endocytosis, the cell cycle and apoptosis (Smith *et al.*, 2000), and it has been recently related to atherosclerosis (Smith, 1960). Ceramide and S1P have opposite roles: the first is involved in apoptosis and cell senescence (Obeid *et al.*, 1993; Venable *et al.*, 1995), while the second has a crucial role in cell survival, cell migration, and inflammation (Hla, 2004). C1P has also a role in the inflammatory response and vesicular trafficking (Chalfant & Spiegel, 2005; Hinkovska-Galcheva *et al.*, 2005). It has been suggested that the biophysical properties of the sphingolipids can have an influence on the physical properties of cell membranes, and be the basis for some of their physiological functions (Goñi *et al.*, 2014).

Table 1.2. The main biophysical properties of simple sphingolipids.

Sphingolipid	Property
Sphingosine	Net positive charge at physiological pH Increases membrane permeability Rigidifies bilayer acyl chains Facilitates cubic phase formation (with negatively charged lipids)
Sphingosine-1-phosphate	Somewhat water-soluble (critical micellar concentration 12 μM) Stabilizes lipid micellar structure
Ceramide	Increases lipid chain order Segregates laterally into rigid domains Increases membrane permeability Induces flip-flop motion of lipids Facilitates H_{II} phase formation
Ceramide-1-phosphate	Spontaneously forms bilayers pKa very sensitive to phospholipid composition

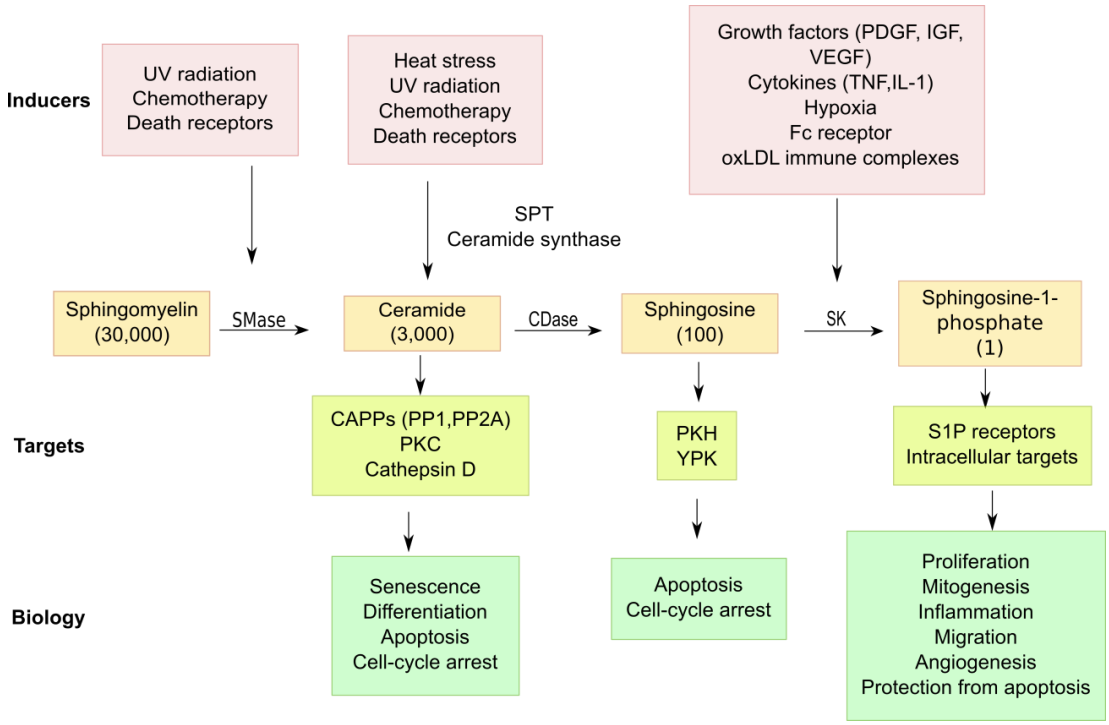

Figure 1.8. An overview of the roles of sphingolipids in biology. The numbers in parentheses indicate the relative concentrations of these sphingolipids. Abbreviations: SMase, sphingomyelinases; SPT, Serin palmitoyl transferase; CDases, ceramidases; SK, sphingosine kinases; CAPP, ceramide-activated Ser-Thr phosphatase; IGF, insulin-like growth factor; IL-1, interleukin-1; oxLDL, oxidized low-density lipoprotein; PDGF, platelet-derived growth factor; PKC, protein kinase C; PKH, PKB homologue; TNFα, tumour necrosis factor-α; VEGF, vascular endothelial growth factor; YPK, yeast protein kinase. [Redrawn from (Hannun & Obeid, 2008)].

The formation of lateral nanostructures or "rafts" (Simons & Ikonen, 1997) has been widely studied since their proposal, generating a huge amount of experimental work. However, the difficulty associated to their visualization, their complicated molecular composition, and the fact that they have been observed only in model membranes are the main drawbacks of this hypothesis (Munro, 2003; Pike, 2006; Goñi, 2019). Lateral segregation of sphingolipids will be discussed in more detail in section 1.4.

1.3.1 Sphingolipid metabolism

The metabolic pathway of sphingolipids (Figures 1.9, 1.10) in eukaryotes has only one entry point. Serine and palmitate are condensed to 3-keto-dihydrosphingosine, the first sphingolipid in the *de novo* pathway, by the action of serine palmitoyltransferase (SPT). Then, 3-keto-dihydrosphingosine is reduced to dihydrosphingosine, which is acylated to form dihydroceramide by ceramide synthase (CerS). Its desaturation gives rise to ceramide. Ceramide occupies the central position in sphingolipid biosynthesis and catabolism. All these processes happen in the endoplasmic reticulum (ER) and its associated membranes.

After that, ceramide is transported to the Golgi through the action of a transfer protein (CERT) or through vesicular transport. The transport of Cer by a transfer protein is the way for sphingomyelin (SM) synthesis in mitochondria, while vesicular transport delivers Cer for Glucosylceramide (GluCer). To transform GluCer in complex glycosphingolipids (GSLs) inside the mitochondria another transfer protein is needed, FAPP2. Ceramide can be phosphorylated by ceramide kinase (CK), glycosylated by glucosyl or galactosyl ceramide synthases (GCS), or can receive phosphatidylcholine (PC) in the biosynthesis of sphingomyelin through the action of SM synthases (SMS).

Sphingomyelin and complex GSLs are transferred to the plasma membrane through vesicular transport. In the plasma membrane, SM is metabolized to Cer and other bioactive lipids by the action of acid sphingomyelinase (in the outer leaflet) or neutral sphingomyelinase (in the inner leaflet). Then Cer can be transformed into sphingosine through the action of many ceramidases (CDase). Finally, sphingosine can be phosphorylated by a sphingosine kinase (SK), and S1P be treated with SAP lyase to generate ethanolamine phosphate and hexadecenal.

The endosomal pathway is responsible for the introduction of sphingolipids to the metabolic pathway. When SM and GSLs reach the lysosome, they are degraded through the action of sphingomyelinases and glucosidases to form sphingosine. After some processes, sphingosine is recycled in the ER to form ceramide (Hannun & Obeid, 2008).

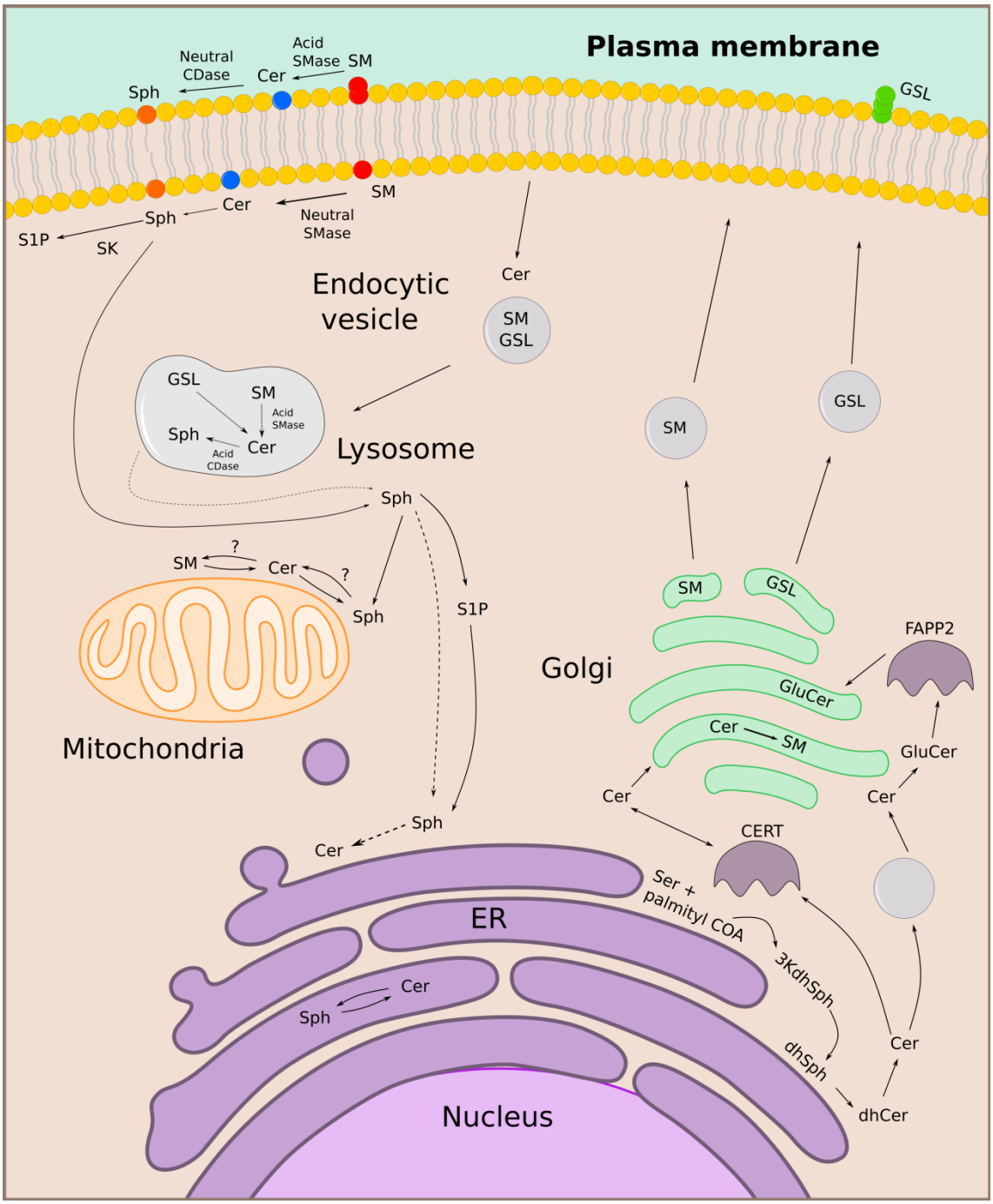

Figure 1.9. Compartmentalization of sphingolipid metabolism. Abbreviations: CDase, ceramidase; CERT, ceramide transfer protein; CK, ceramide kinase; CoA, Coenzyme A; FAPP2, four-phosphate-adaptor protein 2; GALC, galactosylceramidase; GCase, glucosylceramidase; SMase, sphingomyelinase. [Redrawn from (Hannun & Obeid, 2008)].

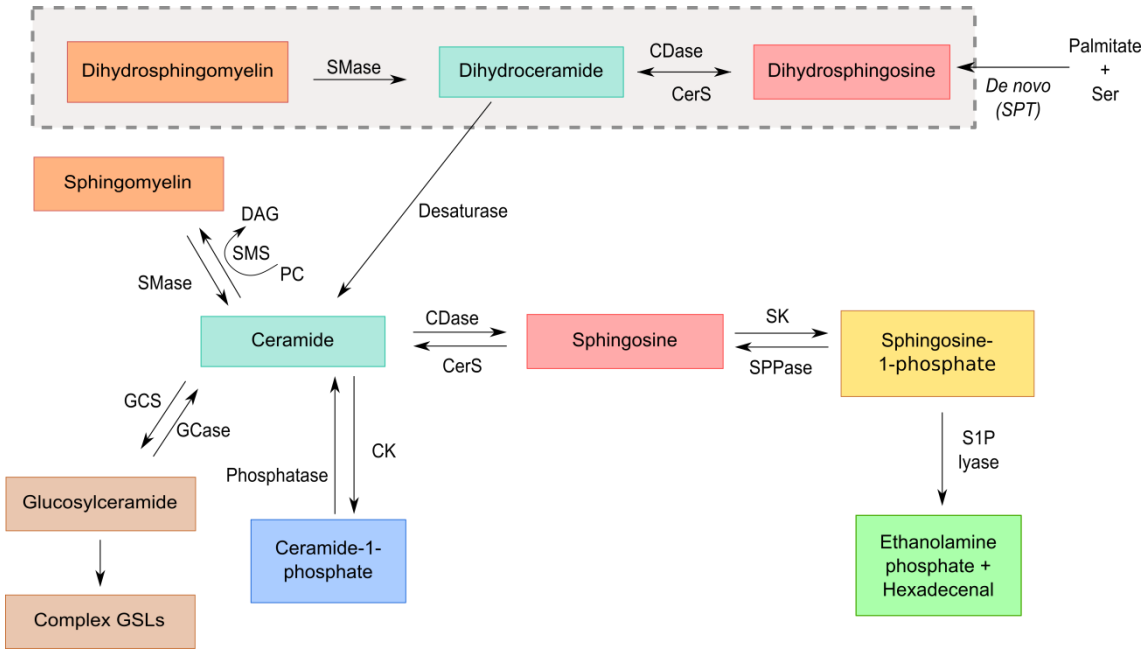

Figure 1.10. Diagram of sphingolipid metabolism showing enzymatic pathways. Abbreviations: CDase = ceramidase, CerS = (dihydro)ceramide synthase, CK = ceramide kinase, , GCase = glucosylceramidase, GCS = glucosylceramide synthase, SK= sphingosine kinase, SMase = sphingomyelinase, SMS = sphingomyelin synthase, SPPase = sphingosine phosphate phosphatase, SPT = serine palmitoyl transferase. [Redrawn from (Hannun & Obeid, 2008)].

1.3.2 Structure and functions

The work performed in this thesis is focused on lipid-lipid interaction studies of sphingolipids such as sphingomyelin, ceramide, and cerebroside in model membranes. Here, a general overview of sphingolipids and specifically on their biophysical properties and their structure is given.

Sphingomyelin:

Sphingomyelin is the most abundant sphingolipid in mammalian cell membranes, constituting 2-15% in most tissues like brain, peripheral nervous, and also in ocular lenses, representing approximately 80% of total sphingolipids. As it was previously described, its cylindrical shape tends to form lamellar structures when it is dispersed in water. It is mostly located in the external leaflet of the plasma membrane.

Its structure was reported in 1927, it is composed of a sphingosine molecule with a fatty acid linked through an amide linkage, and phosphorylcholine as the polar headgroup (Ramstedt & Slotte, 2002). Sphingomyelin can be classified based

on the fatty acid attached to the sphingosine moiety, being the saturated C16, C18 and C24 and the unsaturated C24:1 the most common in plasma membrane (Manni *et al.*, 2018).

Sphingomyelin presents a gel-fluid phase transition at around 40 °C, much higher than most natural phospholipids, so that in the pure state it would exist in the gel phase at room temperature, unlike most natural phospholipids. These physical properties can be associated with its tendency to form highly ordered membrane domains. In this regard, cholesterol and ceramide display a preference for sphingomyelin instead of phosphatidylcholine (PC), its phospholipid analog (Ramstedt & Slotte, 2006; García-Arribas *et al.*, 2016b) (see section 1.4 for more details).

Sphingomyelin exerts a wide range of functions in the plasma membranes: from its structural role together with other phospholipids, sterols, and integral proteins to its specific role in cell signaling, and in some cell functions like apoptosis, cell ageing, and cell development, due to its role as a precursor of other bioactive lipids such as ceramides (Merrill *et al.*, 1997; Hannun *et al.*, 2001).

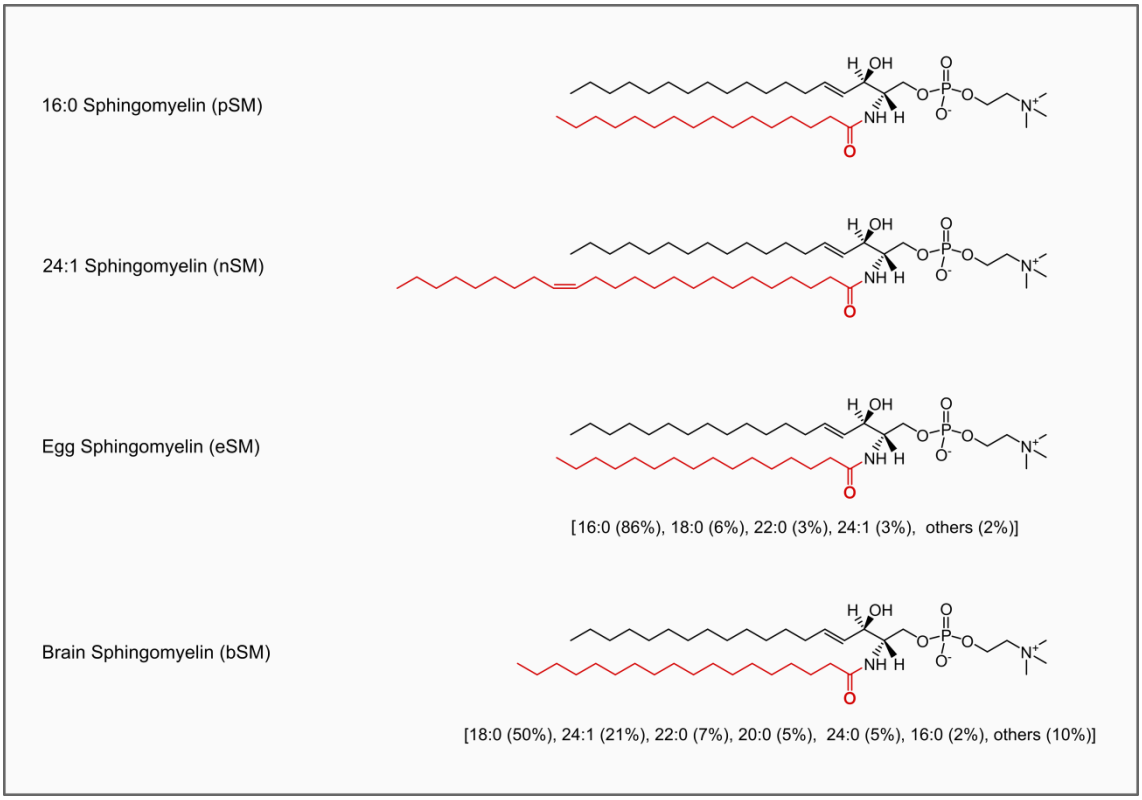

Box 1.5. Sphingomyelin molecular structures used in this study.

Ceramides

In the last decades, ceramides have attracted the attention of the scientific community for their important role in biological processes. It is now well known that ceramides are involved in cell proliferation, apoptosis, cell senescence and disease (Hannun & Obeid, 2002; Goñi & Alonso, 2006a; Castro *et al.*, 2014). Moreover, the increase of ceramide levels in resting cells when they are exposed to several stimuli or under stress conditions (cytokines, death receptors, anti-cancer drugs), explains their important role even when the basal amount of ceramides in cells is very low (Plesofsky *et al.*, 2008; Yabu *et al.*, 2015).

Ceramide structurally differs from sphingosine in having a fatty acyl chain attached through an amide linkage. Both the length and the presence of unsaturations in the acyl chain are responsible for the high variety of ceramides in cells. They can be classified according to their acyl chain in short- and long-chain ceramides. The low polarity and highly hydrophobic structure of long-chain ceramides justify their high concentration in the stratum corneum, to avoid water evaporation through the skin (Wertz & Downing, 1983). However, short-chain ceramides can be dissolved in water forming micelles. See Sot *et al.*, (2005a, 2005b) for a comparative study of how differently short- and long-chain ceramides affect the membrane properties.

As mentioned for the simple sphingolipids, ceramides can modify the membrane biophysical properties, which are associated with the cell functions. The cone-shape geometry of ceramide induces the formation of non-lamellar structures in small regions of the bilayers promoting processes such as membrane permeabilization (Ruiz-Argüello *et al.*, 1996; Montes *et al.*, 2002), transmembrane (flip-flop) lipid motion (Contreras *et al.*, 2003, 2005) or membrane fusion (Basañez *et al.*, 1997).

The hydroxyl groups and the amide linkage confer ceramides the ability to form hydrogen bonds, which contribute to their high melting point and segregation into highly ordered gel-like domains, due to their low miscibility with other membrane lipids (Sot *et al.*, 2006; Castro *et al.*, 2007; Busto *et al.*, 2009). Ceramide main transition temperature (92-93 °C) is significantly affected by the presence of unsaturations, while an increase in their acyl chain from 16 to 24 carbons barely changes that value (Jiménez-Rojo *et al.*, 2014). Furthermore, an increase in length affects the morphology and size of the domains while the degree of unsaturation causes a decrease in order (Pinto *et al.*, 2011). Moreover, it has been proposed that ceramide domains can act as recruiting sites for different proteins that play a role in signal transduction processes (Cremesti *et al.*, 2001; Zhang *et al.*, 2009).

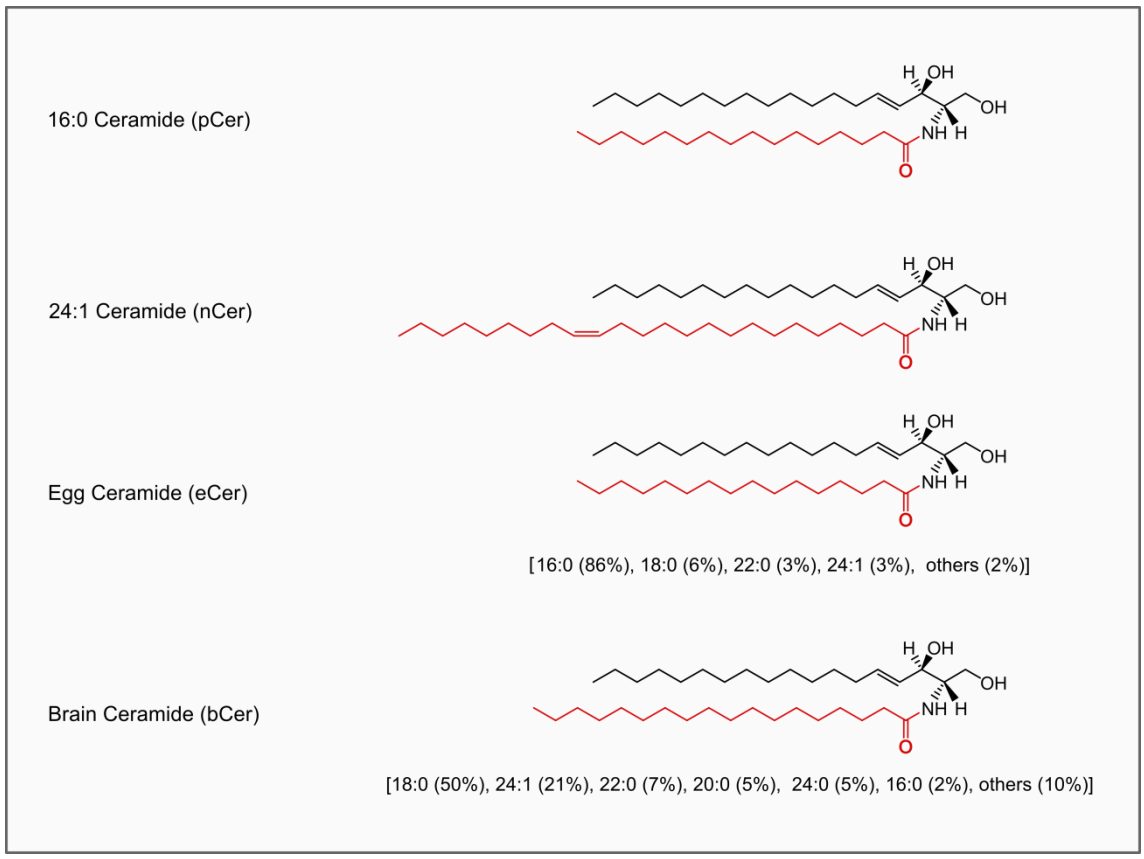

Box 1.6. Ceramide molecular structures used in this study.

Glycosphingolipids

Glycosphingolipids (GSL) are, as sphingomyelin, components of most eukaryotic cell plasma membranes, but the amount of GSL is usually much lower (Hoetzl *et al.*, 2007). Nevertheless, a high level of glycosphingolipids has been reported for apical membranes of epithelial cells, myelin, and neurons (Simons & Meers, 1988; Vanier, 1999). Cerebrosides (Crb) are among the simplest GSL and make up to 20 mol% of the lipids in myelin, as well as occurring in sizable amounts in epithelial cells from the small intestine and colon, and in the skin epidermis (Van Meer *et al.*, 2003).

Glycosphingolipids as glucosylceramides are synthesized in the luminal surface of the Golgi and then transported by vesicular transfer to the plasma membrane. There, GSL are mostly located at the outer leaflet of the membrane, where they interact with toxins, hormones, viruses and other external ligands (Ledeen *et al.*, 1998). However, they are also located in the inner leaflet where they can be bound to cytoskeletal elements, cytoplasmic proteins, and enzymes (Maggio *et al.*, 2006).

They differ structurally from SM in the polar headgroup, GSL containing one or more carbohydrates linked through an *O*-glycosidic linkage to the C1-hydroxyl of their backbone. Their polar head group consists in the simplest case of a hexose, commonly galactose (galactosylceramide, GalCer) or glucose (glucosylceramide, GlcCer) (Maggio *et al.*, 2006).

Their headgroup confers the glycosphingolipids a complex thermotropic behavior and a temperature transition higher than SM. Furthermore, these headgroups contribute to the creation of a hydrogen bonding network, which is associated to their ability to segregate laterally. GSL, and Crb in particular are known to segregate laterally into membrane domains, at least in model and probably also in cell membranes. Presumed GSL-enriched domains in cells have been related to signaling by immune receptors and other signal transduction events (Varela *et al.*, 2017; Holowka *et al.*, 2005; Hakomori, 2002; Mayor *et al.*, 2006).

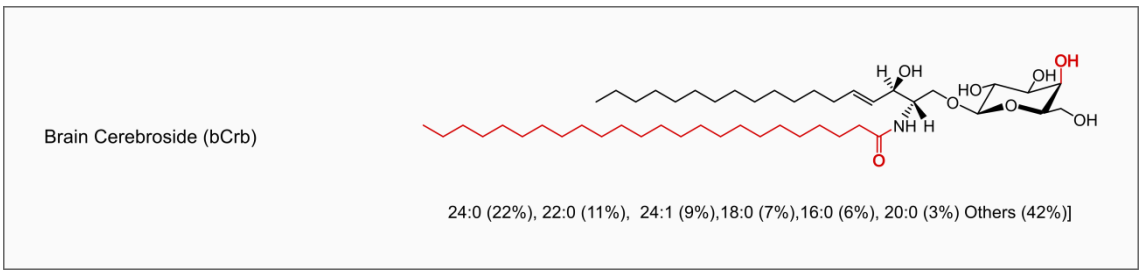

Box 1.7. Glycosphingolipid molecular structure used in this study.

1.4 Lateral segregation of membrane lipids

As mentioned above, sphingolipids and other membrane lipids have the ability to segregate laterally, giving rise to regions, also referred to as membrane domains. This segregation contributes not only to the existence of heterogeneity among membranes but also within the same membrane. In this section, membrane lipid segregation as well as the lipid-lipid interactions will be reviewed.

1.4.1 Phase segregation: membrane rafts

The concept of membrane rafts was proposed by Simons and Ikonen (Simons & Ikonen, 1997). Rafts are defined as small (10-200 nm), transient, heterogeneous and highly dynamic microdomains enriched in sphingolipids and cholesterol, which associated with proteins can compartmentalize relevant signaling processes.

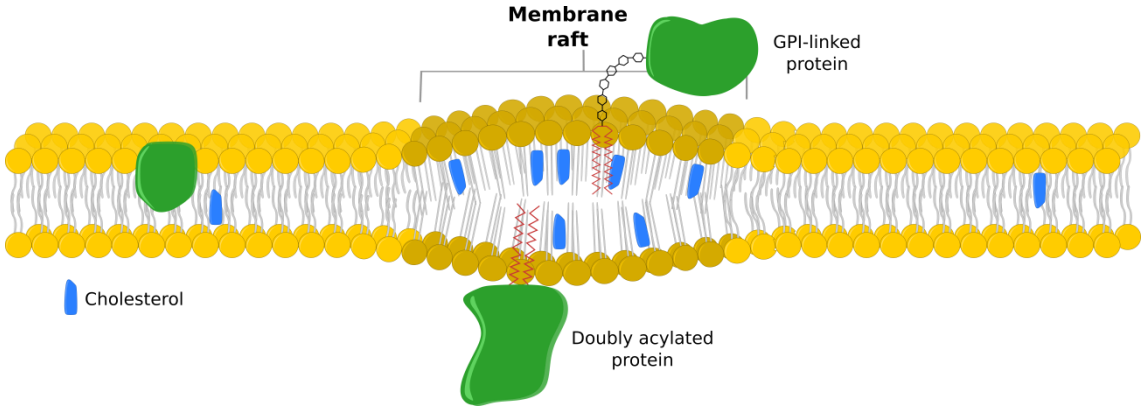

Figure 1.11. Representation of membrane rafts. [Redrawn from (Luckey, 2008)].

Although the membrane raft hypothesis was widely accepted and generated a huge amount of work since its proposal, it has not been possible to demonstrate the existence of rafts due to the difficulty associated to their visualization and their complex molecular composition (Pike, 2006; Goñi, 2019). Nowadays, the development of super-resolution optical microscopy such as photoactivated localization microscopy (PALM), stimulated emission depletion (STED) microscopy and near-field scanning optical microscopy (NSOM) has overcome the resolution limit of conventional optical microscopy and these techniques can play a key role in the resolution of a debate that has been alive for two decades (Sezgin *et al.*, 2017).

1.4.2 Lipid-lipid interactions: lipid domains.

In order to study the lateral segregation of lipids in the plasma membrane and due to its highly complex and heterogeneous environment, membrane model systems are used. In our studies these systems are usually composed of three or four components, among them: one with a high phase transition temperature (T_m), one with a low T_m, and cholesterol. Lipids are chosen to try to replicate the putative phase segregation present in a plasma membrane and not because they are necessarily a good mimic of cell membrane components (Feigenson, 2007).

Lipid lateral segregation ability is particularly related to their structure. Thus, lipids with long and saturated acyl chains tend to segregate into densely packed or highly ordered phases. However, the presence of double bonds in the acyl chain favors the packing defects and the formation of disordered or fluid phases. Additionally, their C-C bonds are preferentially found in a *trans* conformation maintaining a linear structure, which also favors the formation of packed and ordered phases. On the contrary, as long as temperature increases, the number of gauche isomers also increases, promoting the formation of disordered phases (Luckey, 2008). In addition to the presence of unsaturations in the acyl chain, other factors such as the polar headgroup or the hydrogen bonding ability play a key role in the lipid-lipid interactions associated to lateral segregation (García-Arribas *et al.*, 2016b; Slotte, 2016).

Sphingomyelin is one of the most widely studied lipids in phase segregation due to its biophysical properties. Its saturated acyl chain and its high phase transition temperature favor its interaction with other lipids such as cholesterol to form liquid-ordered phases enriched in sphingomyelin and cholesterol. These lipids together with glycerophospholipids such as 1,2-dipalmitoyl-*sn*-glycero-3-phosphocholine (DPPC) or 1-palmitoyl-2-oleoyl-*sn*-glycero-3-phosphocholine (POPC) constitute a widely studied membrane model system (Veiga *et al.*, 2001; De Almeida *et al.*, 2003; Halling *et al.*, 2008; Ramstedt & Slotte, 2006). All these studies confirm the preferential partition of cholesterol into sphingomyelin to form L_o phases.

When cholesterol interacts with sphingomyelin or its glycerophospholipid analog dipalmitoylphosphatidylcholine (DPPC), it tends to occupy the space in the boundary between the acyl chains and the phosphocholine (PC), which is large enough to avoid its interaction with the polar solvent (Björkbom *et al.*, 2010; Huang & Feigenson, 1999). Additionally, it was recently shown that sterols have a higher affinity for SM than for a saturated PC at equal acyl chain order (Lönnfors *et al.*, 2011). Thus, the structural similarities between these lipids pointed to their hydrogen bonding ability as the determining factor involved. The interfacial region of SM has an amide group, a free hydroxyl, and an amide carbonyl, which confer SM the ability to act as hydrogen bond donor and acceptor, while PC has two ester carbonyls which act only as hydrogen bond acceptors. Consequently, the interaction between cholesterol and sphingomyelin could be a stronger one.

A lipid that somehow mimics the behavior of cholesterol in membrane model systems is ceramide. Its hydroxyl polar headgroup and the possibility to act as an electron donor or acceptor for hydrogen bonds, result in a strong interaction with lipids such as sphingomyelin. Ceramide is able to segregate into highly-ordered phases with different packing properties than the gel phases formed by

glycerophospholipids and sphingolipids, perhaps due to the high phase transition temperature of pure ceramides (around 90 ºC) (Jiménez-Rojo *et al.*, 2014). An example of the different packing properties of SM and Cer is observed when giant unilamellar vesicles of SM:Cer are observed using confocal microscopy, SM is shown stained by the fluorescent probe used, while Cer domains appear in black because their highly packed domains exclude the probe (Sot *et al.*, 2006).

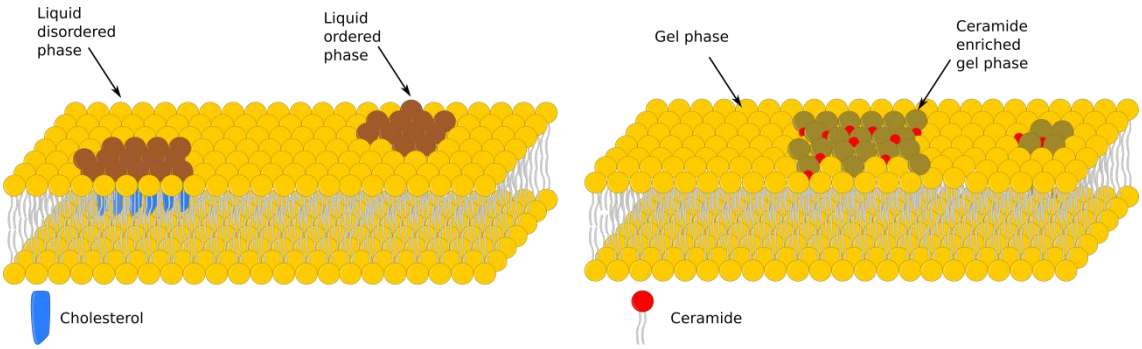

Figure 1.12. Representation of liquid-ordered and liquid-disordered phase coexistence, and of gel and liquid-disordered phases. A lipid bilayer (yellow), segregated phases (brown), cholesterol (blue) and ceramide (red).

This kind of phase segregation has been extensively studied (Sot *et al.*, 2006; Busto *et al.*, 2009; Pinto *et al.*, 2011; Castro *et al.*, 2007) and it was proposed that the shape and size of ceramide domains arise as a result of a balance between the domain line tension and the dipole-dipole repulsion. If the domain line tension is the predominant force, round-shaped domains are formed; however, if dipole-dipole repulsion is the strongest force, flower-shape domains are obtained as a result (Perkovic & Mcconnell, 1997). A mixture of DPPC, SM and Chol (liquid ordered and disordered phases) (De Almeida *et al.*, 2003) shows round-shape domains, while ceramide domains in samples with a gel and fluid phase coexistence appear with a flower-shape (Fidorra *et al.*, 2006; Garcia-Arribas *et al.*, 2015). Several studies have shown how different ceramide domains are if they have been premixed with other lipids upon preparation or generated *in situ* by sphingomyelinase. The generation of ceramides upon activation of sphingomyelinases gives rise to heterogeneous ceramides located at the boundaries of a liquid-ordered phase (Ira & Johnston, 2008; Ira *et al.*, 2009).

The high amount of cholesterol and sphingomyelin in the plasma membrane, and the fact that sphingomyelin is considered as the main source of ceramide stimulated the study of the interaction between these lipids. A relevant work in this regard was developed by Megha and London, who observed how ceramide displaced cholesterol from the raft-like structure (Megha & London, 2004). Further studies confirmed the higher affinity of SM for ceramide due to its higher hydrogen bonding ability (Chiantia *et al.*, 2006a; Sot *et al.*, 2008; Alanko *et*

al., 2005). More recent studies suggested that other factors could play a key role in this interaction when ceramide domain solubilization was observed at higher cholesterol concentrations (Silva *et al.*, 2007, 2009). All these results pointed to a competition for SM between ceramide and cholesterol, in which cholesterol concentration would modulate the formation of ceramide-enriched domains. However, Castro *et al*. (2009) observed how cholesterol and ceramide maintain their behavior even in the absence of sphingomyelin, suggesting an interaction rather than a competition. Recent studies in our laboratory have explored the interaction between these lipids in the absence of a disordered phase (Busto *et al.*, 2010) and the incorporation of ceramide and cholesterol into bilayers of either palmitoylsphingomyelin (pSM) or DPPC (Busto *et al.*, 2014; Garcia-Arribas *et al.*, 2015).

1.5 Aims

The present thesis is intended to explore lipid-lipid interactions associated with the lateral segregation of sphingolipids and cholesterol in membrane model systems of three and four components.

The specific aims of this thesis are the following:

- To define the structure of pure sphingolipids (egg SM and pSM) through their phase transitions in a broad temperature interval using X-ray scattering.

- To characterize the interaction between ceramide, cholesterol and a saturated phospholipid (pSM or DPPC) in ternary mixtures and analyze how the system evolves at different lipid ratios.

- To study the behavior of a three-component system (DOPC, SM, and Chol) upon ceramide incorporation and how the presence of unsaturation in the acyl chains affects its biophysical properties.

- To describe the mixing behavior of brain glycosphingolipids (cerebrosides) in binary mixtures with ceramide, cholesterol, ePC or bSM, using mainly differential scanning calorimetry.

CHAPTER 2:

EXPERIMENTAL TECHNIQUES

CHAPTER 2: EXPERIMENTAL TECHNIQUES

2.1 Membrane lipid model systems

Lipid vesicles or liposomes have been the main membrane model systems used in this work. These are small lipid bilayers of spherical shape which form closed structures when they are hydrated in aqueous solution (Bangham & Horne, 1964). The main reason why many membrane studies rely on model membranes is the complexity of cell membranes and the problem caused by the presence of molecules like proteins, phospholipids, and sterols when a study of the properties and behavior of each component has to be independently observed. Even when the liposome results cannot be directly related to a cell membrane, these can be used to evaluate the interactions of its membrane components. Liposomes are usually prepared of pure lipids, lipid mixtures or lipid-protein mixtures (proteoliposomes) and their properties differ considerably with lipid composition, surface charge, size, and the method of preparation.

These systems can be classified according to their size and number of lamellae (either unilamellar or multilamellar). Unilamellar vesicles can also be classified into three categories: giant unilamellar vesicles (GUV), large unilamellar vesicles (LUV), and small unilamellar vesicles (SUV) (Figure 2.1). The main difference between unilamellar and multilamellar vesicles is the number of lipid bilayers that form the vesicles. A unilamellar vesicle is formed by a single phospholipid bilayer sphere that encloses the aqueous solution, while a multilamellar vesicle is formed by several unilamellar vesicles inside others separated by layers of water, giving rise to an onion-like structure. Additionally, these models can be adapted to several other techniques and can be used to prepare multilayers, or supported planar bilayers (Gennis, 1989).

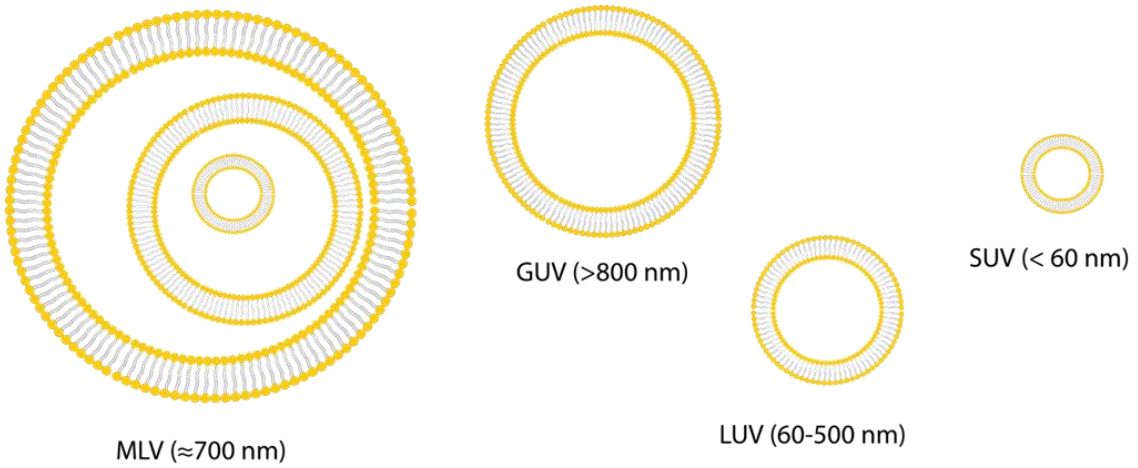

Figure 2.1. Representation of different sized liposomes and their phospholipid organization. (Figure not drawn to scale).

Biophysical phenomena such as fusion, fission, solubilization, leakage, lipid flip-flop, or lipid-protein interactions can be measured using liposomes. Additionally, liposomes have diagnostic and therapeutic applications in medicine and pharmacology containing markers or drugs, reducing the side effects and releasing the drug gradually within the target area (Gregoriadis, 1978; Gregoriadis, 2008). Liposomes have been extensively tested as drug carriers in anticancer therapies (Yingchoncharoen *et al.*, 2016).

2.1.1. Multilamellar vesicles (MLV)

Multilamellar vesicles are lipid vesicles usually containing 7 - 10 concentric bilayers, displaying an average diameter of around 700 nm, but ranging from 100 to 5000 nm. Their generation is the simplest and fastest of all liposome formation methods. These vesicles can be further treated to form unilamellar vesicles of different sizes. A detailed protocol for multilamellar vesicle preparation used in the present work is described below (Protocol 1. Figure 2.2).

In this work, MLV is used to study lipid-lipid interactions in lipid mixtures through differential scanning calorimetry (DSC).

Protocol 1: Multilamellar vesicles (MLV)

1) Pure lipid stocks are prepared by diluting lipids in powder in chloroform:methanol (2:1 v/v) to the desired concentration. If the stock is previously prepared, it is recommended to check the concentration by phosphorus determination assay.

2) The desired amount of lipids is pipetted from the stock in organic solution into a glass test tube. Then, it is evaporated under a stream of nitrogen gas until a lipid film is formed.

3) The sample is introduced into a high-vacuum desiccator for 2 h to completely remove any residual solvent that might remain.

4) The dried lipid film obtained is hydrated by addition of the desired buffer solution and mixed for lipid detachment from the bottom of the test tube. Both sample and buffer are maintained at a temperature above the lipid main phase transition temperature in order to obtain a homogeneous MLV solution when the sample is mixed by vigorous vortexing.

5) The sample is then sonicated in a bath sonicator at the same temperature as hydration for 10 min, in order to obtain a more homogeneous sample.

6) If the lipid mixture is formed by lipids with a high-temperature phase transition the hydration step is slightly different. Increasing amounts of the buffer solution are added while the sample is stirred with a glass rod. Finally, in order to obtain a homogeneous solution, the vesicles are passed through a narrow tube (0.5 mm internal diameter, 10 cm long) 50-100 times between two syringes.

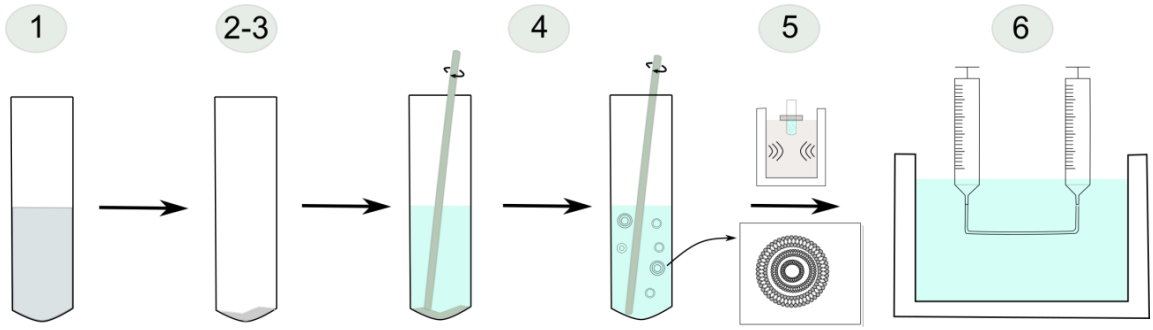

Figure 2.2. Outline of MLV formation protocol as explained above. (Figure not drawn to scale).

2.1.2. Large unilamellar vesicles (LUV)

MLV is easy and fast to prepare but its onion-like structure is an important drawback. Some biophysical phenomena like leakage or flip-flop motion require a single bilayer and the presence of multiple bilayers makes difficult data analysis and interpretation. To overcome this issue, unilamellar vesicles are generally used. These are classified according to their size: giant unilamellar vesicles (GUV) with a micrometer-range diameter, large unilamellar vesicles (LUV) with an average diameter between 60 and 500 nm, and small unilamellar vesicles (SUV) with an average diameter of less than 60 nm. Each of them differs not only in size but also in the method of preparation.

Large unilamellar vesicles have been used for the leakage and flip-flop motion experiments due to their size, which makes curvature stress considerably lower than in SUV. When preparing LUV containing a mixture of lipid species, a homogeneous lipid distribution through both monolayers in stable lipid vesicles is generally obtained. LUV are prepared by mechanical extrusion of MLV suspensions through polycarbonate porous filters of the desired size (Mayer, 1986). A protocol is detailed below (Protocol 2. Figure 2.3):

Protocol 2: Large unilamellar vesicles (LUV)

1) Pure lipid stocks are prepared by diluting lipids in powder in chloroform:methanol (2:1 v/v) to the desired concentration. If the stock is previously prepared, it is recommended to check the concentration by phosphorus determination assay.

2) The desired amount of lipids is pipetted from the stock in organic solution into a glass test tube. Then, it is evaporated under a stream of nitrogen gas until a lipid film is formed.

3) The sample is introduced into a high-vacuum desiccator for 2 h to completely remove any residual solvent that might remain.

4) The dried lipid film obtained is hydrated by addition of the desired buffer solution and mixed for lipid detachment from the bottom of the test tube. Both sample and buffer are maintained at a temperature above the lipid main phase transition temperature in order to obtain a homogeneous MLV solution when the sample is mixed by vigorous vortexing.

5) MLV are subjected to 10 freeze/thaw cycles. In each cycle, the sample is immersed in liquid nitrogen for 1 minute. Once frozen, the sample is transferred into a water bath at a temperature above that of the lipid in the mixture with the highest main phase transition temperature until it is defrosted. Then, it is vortexed.

6) The vesicles are finally extruded by passing the sample 10 times through polycarbonate filters with the desired pore diameter (usually between 0.1 and 0.4 μm) in an extruder with the help of nitrogen gas pressure (18-20 bar). The extruder is maintained at a constant temperature above that of the lipid with the highest main phase transition temperature using a water bath.

7) Large unilamellar vesicles of the desired size are generated and their size checked using dynamic light scattering (DLS). It is recommended to check the concentration by phosphorus determination assay due to the loss of some lipid within the polycarbonate filters while extruding.

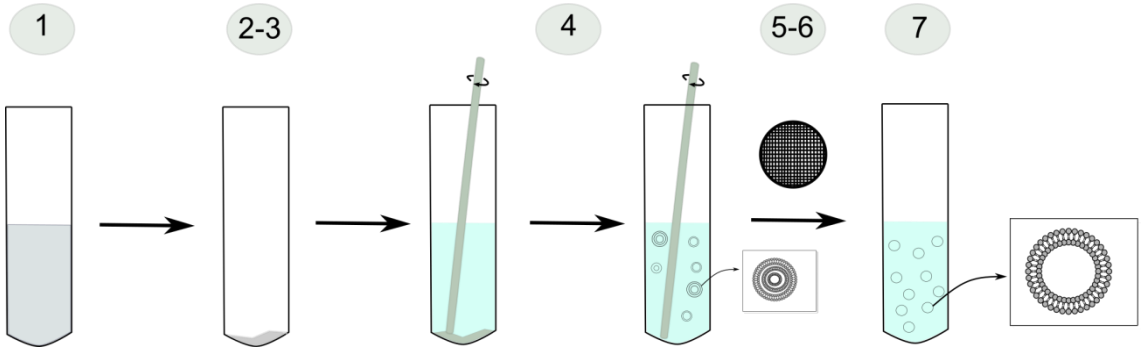

Figure 2.3. Outline of LUV formation protocol as explained above. (Figure not drawn to scale).

2.1.3. Small unilamellar vesicles (SUV)

SUV are characterized by the high-stress curvature of their structure due to their small diameter (smaller than 60 nm), which induces an asymmetry. The lipid concentration is higher in the external monolayer compared to the inner one (F. Szoka & Papahadjopoulos, 1980). Their curvature stress makes these vesicles good model membranes for the study of membrane fusion- and/or fission-related processes (Nieva *et al.*, 1989), in which such stress conditions occur *in vivo*.

Small unilamellar vesicles are prepared sonicating MLV suspensions. This is basically done either with bath sonication or by the use of probe tip sonication, with Ti probes that are immersed within the MLV suspension for sonication. Bath sonicators are often used for the preparation of SUV instead of probe sonicators because the latter deliver high energy to the lipid suspension causing overheating and degradation. Sonication tips also tend to release titanium particles into the lipid suspension which must be removed by centrifugation prior to use.

In this work, SUV is used to prepare supported planar bilayers (SPB), to be measured under atomic force microscopy (AFM).

Protocol 3: Small unilamellar vesicles (SUV)

1) Pure lipid stocks are prepared by diluting lipids in powder in chloroform:methanol (2:1 v/v) to the desired concentration. If the stock is previously prepared, it is recommended to check the concentration by phosphorus determination assay.

2) The desired amount of lipids is pipetted from the stock in organic solution into a glass test tube. Then, it is evaporated under a stream of nitrogen gas until a lipid film is formed.

3) The sample is introduced into a high vacuum desiccator for 2 h to completely remove any residual solvent that might remain.

4) The dried lipid film obtained is hydrated by addition of the desired buffer solution and mixed for lipid detachment from the bottom of the test tube. Both sample and buffer are maintained at a temperature above the lipid main phase transition temperature in order to obtain a homogeneous MLV solution when the sample is mixed by vigorous vortexing.

5) The sample is then sonicated in a FB-15049 bath sonicator (Fisher Scientific Inc., Waltham, MA) at the same temperature as hydration for 1 hour, in order to obtain SUV. Sonication effects which can be directly observed as the vesicle solution becomes transparent.

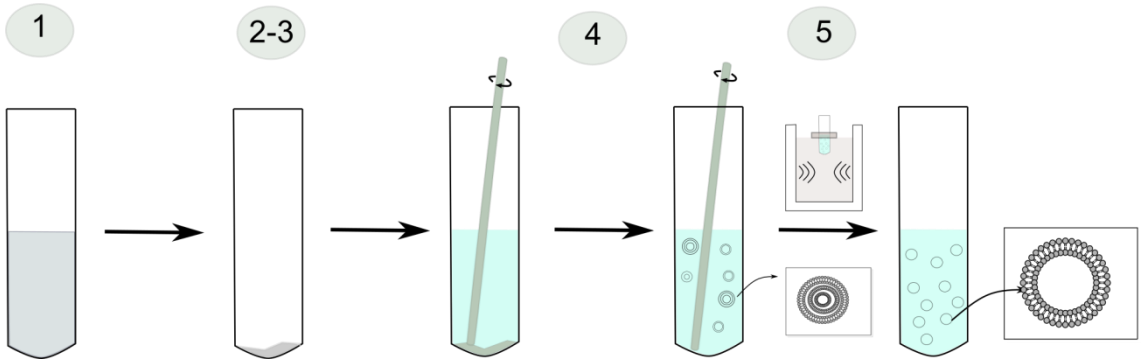

Figure 2.4. Outline of SUV formation protocol as explained above. (Figure not drawn to scale).

2.1.4 Giant unilamellar vesicles (GUV)

Giant unilamellar vesicles are used in this work because their size makes them suitable for imaging. GUV was first described in 1969 by John P. Reeves and Robert M. Dowben (Reeves & Dowben, 1969), who exposed dry lipid films to aqueous solutions at temperatures above the lipid main transition temperature for 24 h. This method has been modified along the years, and nowadays an electric field is used following the method developed by Angelova et al.. (Angelova & Dimitrov, 1986; Angelova *et al.*, 1992) (Figure 2.5). Vesicle generation under electric fields is strongly dependent on the lipid composition, aqueous solution ionic strength and pH, and on the electric voltage and frequency conditions (Bagatolli, 2003). In particular, only very low ionic strengths can be used in the buffers to prepare GUV under this procedure. However, improvements to this method have allowed using physiological salt solutions and even generating giant vesicles from erythrocyte membranes (Montes *et al.*, 2007).

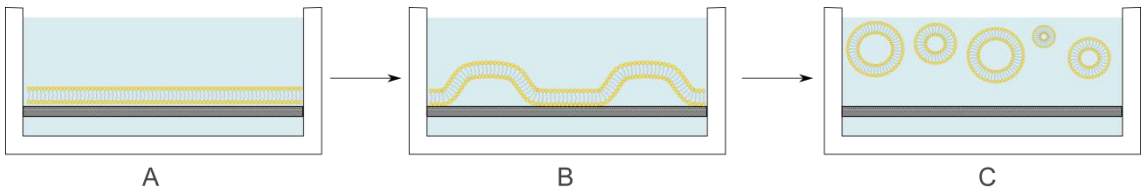

Figure 2.5. Liposome electroformation (not drawn to scale). A lipid film is deposited onto platinum wires (A) then an electric field is applied to make the lipid bilayers grow (B) and detach (C). [Adapted from Angelova and Dimitrov (1986)].

Regarding the present work, an important application for the use of giant vesicles is the study of lipid lateral segregation by direct confocal microscopy of individual vesicles. With this aim, a vesicle generation procedure has been applied to obtain giant vesicles attached to a platinum wire for direct microscopy measurements. A special chamber designed for direct microscopy is used, based on

the design by Prof. Luis A. Bagatolli (University of Southern Denmark, Odense, Denmark) (Figure 2.6). A general overview of the procedure is given.

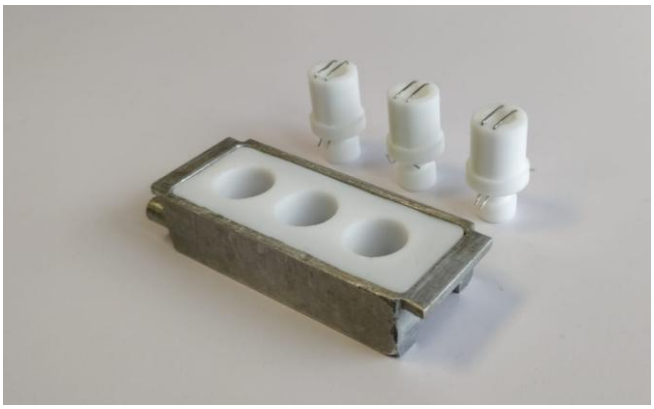

Figure 2.6. Electroformation chamber and polytetrafluoroethylene (PTFE)-made cylindrical cells for obtaining GUV attached to platinum wires.

Protocol 4: GUV attached to a platinum wire

1) Pure lipid stocks are prepared by diluting lipids in powder in chloroform:methanol (2:1 v/v) to the desired concentration. If the stock is previously prepared, it is recommended to check the concentration by phosphorus determination assay.

2) 2-3 µl of the appropriate stock solution are added onto the surface of different platinum electrodes attached to specially designed PTFE-made cylindrical units.

3) The chamber is covered with aluminum foil to protect fluorescent molecules from bleaching, and it is introduced into a high vacuum desiccator for 2 hours to remove any remaining solvent traces.

4) Then, the units are fitted into specific holes within a specially designed chamber to which a glass cover slide has been previously attached using epoxy glue. Once fitted, the platinum wires stay in direct contact with the glass cover slide.

5) The chamber is then equilibrated to the desired temperature by an incorporated water bath for 15 min.

6) Later, the platinum wires are covered with the desired aqueous solution (previously equilibrated at the desired temperature) through a small hole within the cylindrical polytetrafluoroethylene (PTFE) units, which are then covered with tightly fitting caps to avoid evaporation during electroformation.

7) The platinum electrodes are connected to a generator and the desired electric field applied for 2 hours. Vesicles are then generated attached to the platinum wires. Temperature during the assay is always higher than that of the lipid with the highest main phase transition temperature.

8) The electric field and water bath are disconnected and vesicles left to equilibrate for 30 min.

9) The chamber is finally mounted on top of the microscope and direct confocal fluorescence microscopy performed on vesicles attached to the platinum wire.

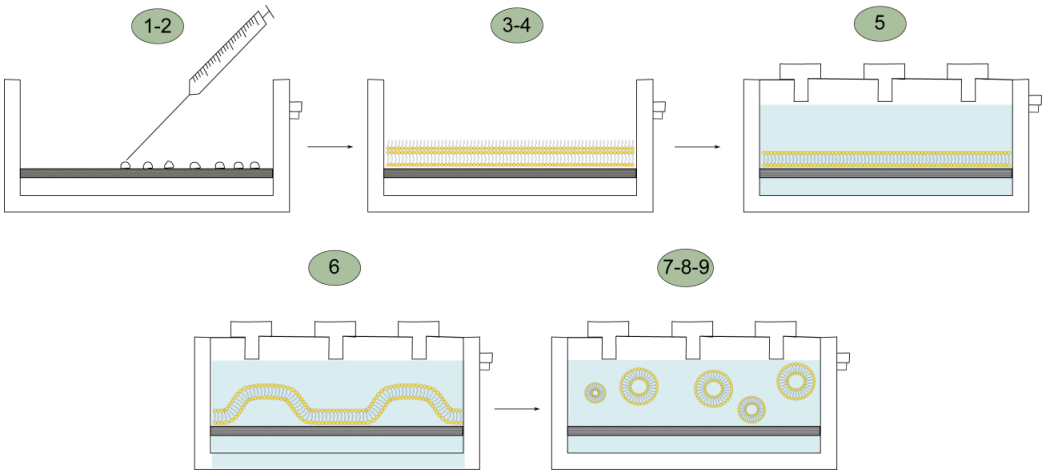

Figure 2.7. Representative image showing GUV formation protocol explained above.

2.1.5 Supported planar bilayers (SPB)

The generation of supported lipid bilayers on top of solid supports is a powerful and largely used model system for the study of lipid domains or lateral phase segregation by means of scanning atomic force microscopy (AFM). In this work, SPB have been achieved following two protocols: vesicle adsorption method and spin-coated film method.

The vesicle adsorption method is based on the spontaneous liposome adsorption upon incubation with specific solid support such as glass or mica. It

was adapted for the AFM in 2000 by Jass and collaborators (Jass *et al.*, 2000). It is known that upon incubation liposomes adsorb to the solid support, get deformed and break down leading to the generation of a single planar bilayer. The exact mechanism by which such an energetically unfavorable process occurs remains unclear. A possible explanation has been depicted in Figure 2.8. In this way, vesicles will adsorb onto the surface, suffer a strong deformation leading to a superposition of bilayer areas from opposing poles on the vesicle and would then break down at the edges due to the high curvature stress. A superposition of two bilayers would be generated. Finally, the upper bilayer would slide through the bilayer on the bottom towards the solid support leading to a homogeneous single bilayer patch on top of the solid support.

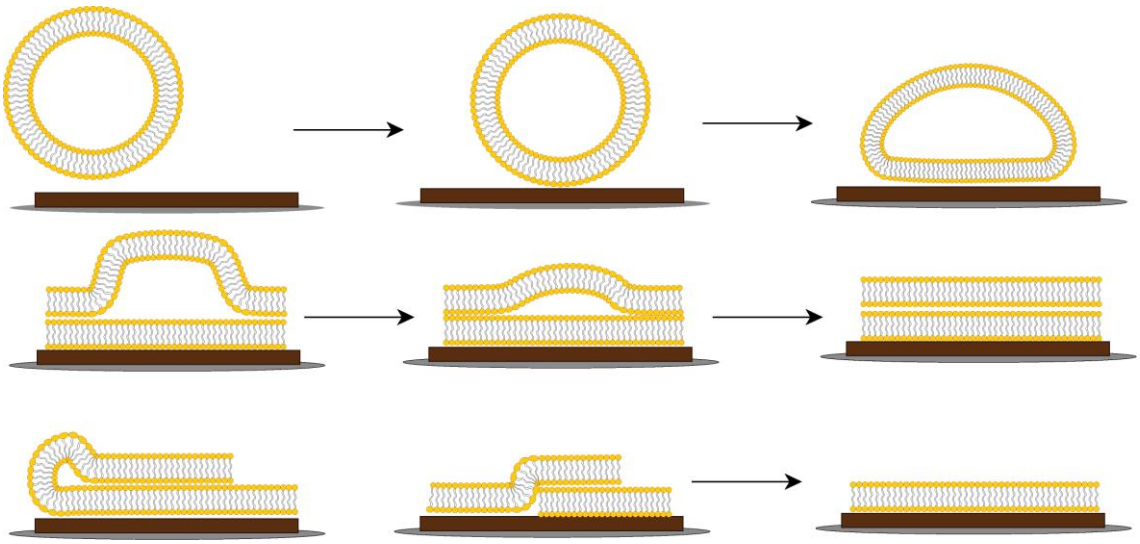

Figure 2.8. Representative image showing the proposed vesicle adsorption and single surface planar bilayer generation. [Adapted from Jass et al.. (2000)].

In order to enhance the absorption method a series of guidelines are followed: i) small vesicles are preferably used due to their high curvature stress because upon contact with the solid support their high instability leads to a good adsorption and nice bilayer extensions, ii) the presence of divalent cations such as Mg^{2+} or Ca^{2+} appears to facilitate as well as increase the rate of planar membrane formation from liposomes (Attwood *et al.*, 2013), iii) if the sample is heated at a temperature higher than that of the lipid with the highest main phase transition temperature a better lipid motion and leaflet coupling would be achieved (Alessandrini *et al.*, 2012), iv) after heating, lipids are left to equilibrate at room temperature for at least 40 minutes in order to avoid artifacts due to rapid cooling (Attwood *et al.*, 2013) and rinsed in calcium-free buffer, as divalent ions are not desirable and can affect nanomechanical resistance of SPB (Garcia-Manyes & Sanz, 2010). Proper rinsing is needed to clean the SPB from extra bilayers, lipid aggregates or non-fused vesicles (Oncins et al.., 2005).

Protocol 5: Supported planar bilayer formation: Adsorption method

1) Small or large unilamellar vesicles are prepared as previously described.

2) A sheet of muscovite mica (1.5 x 1.5 cm) is adhered with epoxy glue into a glass slide fitting the liquid cell for AFM measurements.

3) The mica surface is cleaved with common scotch tape and mounted on the BioCell temperature controller (JPK Instruments, Berlin, Germany).

4) A small amount of assay buffer with divalent ions such as calcium or magnesium is added over the mica.

5) A 100 µL 400 µM liposome suspension with 200 µL of assay buffer at a temperature above that of the lipid with the highest main phase transition temperature is added on top of the mica and left adsorb for 30 min at a constant temperature. The sample must be kept hydrated at every moment with calcium-free buffer and MilliQ.

6) SPB are left to slowly cool down to room temperature (30-45 min). Then, the temperature controller is set to the desired temperature (23 ºC) and the SPB are rinsed with assay buffer. Later, the sample is left to equilibrate at room temperature for at least 40 minutes. Note: never allow the mica surface to dehydrate as the SPB will break down.

7) SPB are generated and ready for scanning under AFM.

The vesicle absorption method is used with lamellar fluid phase lipids whose temperature phase transition is below 60 °C, the maximum temperature reached with our set-up (BioCell, from JPK Instruments). For samples with higher temperature phase transitions, another method like spin coating is required.

Adam Simonsen and Luis Bagatolli were pioneers in the formation of supported lipid bilayers using a spin-coater (Simonsen & Bagatolli, 2004). It was developed to solve the problem of working with high transition temperature lipids, whose adsorption capacity is quite low. Usually these lipids are made of gel phases that also exhibit ceramide-enriched domains, for example, SUV formed by pSM:pCer (from 9:1 to 7:3 mol ratios) are unable to extend onto mica surfaces due to high transition temperatures (Sot *et al.*, 2006; Busto *et al.*, 2010). Its main disadvantage is the formation of stacked extra bilayers that need thorough rinsing

to be removed. Nevertheless, spin-coating formation method has been successfully used since its development (Fidorra *et al.*, 2006; Nielsen & Simonsen, 2013; Garcia-Arribas *et al.*, 2015).

Protocol 6: Supported planar bilayer formation: Spin-coating

1) Pure lipid stocks are prepared by diluting lipids in powder in chloroform:methanol (2:1 v/v) to the desired concentration. If the stock is previously prepared, it is recommended to check the concentration by phosphorus determination assay.

2) The desired amount of lipids is pipetted from the stock in organic solution into a glass test tube. Then, it is evaporated under a stream of nitrogen gas until a lipid film is formed.

3) The sample is introduced into a high vacuum desiccator for 2 h to completely remove any residual solvent that might remain.

4) The dried lipid film obtained is hydrated by addition of isopropanol:hexane:water (3:1:1).

5) A droplet (5 – 10 μL) of the spin-coating stock is added onto a freshly cleaved mica sheet and spin-coated at 3000 rpm for 40 seconds in a KW-4A spin-coater (Chemat Technology, Northridge, CA, USA).

6) Spin-coated film is left under high-vacuum overnight.

7) The sample is transferred to in the BioCell (JPK Instruments, Berlin, Germany) and hydrated with 400 μL assay buffer. Then, it is heated at a temperature above that of the lipid with the highest main phase transition temperature for 30 min.

8) The sample is rinsed thoroughly with hot MilliQ and assay buffer.

9) SPB are left to slowly cool down to room temperature (30-45 min). Then the temperature controller is set to the desired temperature (23 ºC). Later, the sample is left to equilibrate at room temperature for at least 40 minutes. Note: never allow the mica surface to dehydrate as the SPB will break down.

10) SPB are generated and ready for scanning under AFM.

2.2 Lipid phosphorous concentration assay

The method to accurately quantify the phospholipid concentration is based on the initial procedure for the quantification of inorganic phosphorus developed in 1925 by Fiske and Subbarow (Fiske and Subbarow, 1925), later modified by Bartlett (Bartlett *et al.*, 1958) and Böttcher (Böttcher *et al.*, 1961). This approach consists of hydrolyzing the phospholipids until the phosphate group is free to interact with other reagents, which will color the solution in a concentration-dependent manner.

All of the phospholipid stock solutions or liposomes prepared in this thesis were assayed following the procedure shown below. Note that some key lipids under study such as cholesterol, cerebroside or ceramide cannot be quantified by this method. Nevertheless, other methodologies are commercially available for cholesterol detection and quantification.

Protocol 7: Lipid phosphorous concentration assay

1) A calibration curve is prepared pippeting 0, 25, 50, 75, 100 nmol phosphorous into duplicate test tubes from Na_2HPO_4 standard solution.

2) The sample is then pipetted into separate tubes to contain approximately 50 nmol lipid phosphorous, which will be in the center of the calibration curve (at least a triplicate).

3) 500 µL of a 60% perchloric acid (HCl_4) are added to each tube. After that, all tubes are vortexed and placed into a heating block over 200 ^oC for 45-60 minutes. Phospholipid hydrolysis is achieved yielding free inorganic phosphate.

4) Tubes are cooled down at room temperature. 4 mL of an ammonium heptamolybdate solution (22 g $[(NH_4)_6Mo_7O_{24}.4H_2O]$, 143 ml H_2SO_4, 857 ml H_2O) and 500 µl of 10% ascorbic acid solution are added to each tube, followed by vigorous vortexing. The inorganic phosphate reacts with molybdate, which in turns reacts with ascorbic acid generating a yellow-colored solution.

5) The tubes are placed into a boiling water bath for 7 minutes. The solution color is blueshifted depending on the amount of phosphorous.

6) Finally, the tubes are cooled down and their absorbance is measured at 812 nm in a Ultrospec 500 pro spectrophotometer from Amersham Biosciences (Piscataway, NJ, USA).

7) To obtain the concentration of our sample, the standard values are plotted against the phosphorous concentration and adjusted to a straight line. The slope of the curve and the sample absorbance values are used to calculate the concentration of interest.

2.3 Dynamic light scattering (DLS)

Dynamic light scattering (DLS, also known as photon correlation spectroscopy or quasi-elastic light scattering) measures the particle size in emulsions, micelles, polymers, proteins, nanoparticles, or colloids in suspension, which undergo Brownian motion. Particle velocity can be used to measure the hydrodynamic radius (R_h) using the Stokes-Einstein equation.

$$D = \frac{k_B \cdot T}{6 \cdot \pi \cdot \rho \cdot R_h}$$

where:

- D = diffusion coefficient.
- k_B = Boltzmann constant.
- T = temperature.
- ρ = viscosity of the medium.
- R_h = hydrodynamic radius of spherical particles.

DLS extracts information from time-dependent fluctuations of the light scattered from a small volume within the sample. When a suspension of particles is hit by a beam of light, generated scattered light intensities are measured. These intensities provide a correlation function from which, by the use of several algorithms, a vesicle size distribution in solution can be obtained (Figure 2.9). Information about the homogeneous or heterogeneous vesicle size distribution is obtained from a polydispersity index (PDI). The PDI varies between 0 and 1, where values close to zero indicate clean homogeneous monodisperse solutions.

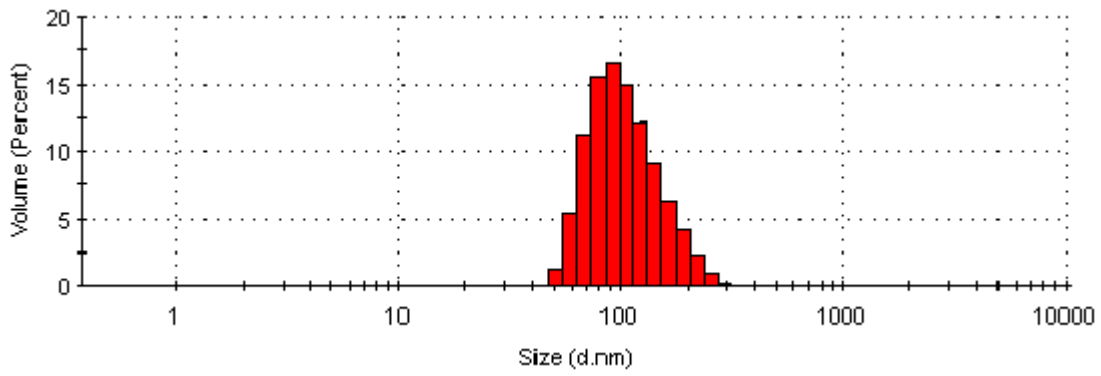

Figure 2.9. Size distribution plot for an eSM:ePE:Chol (2:1:1) vesicle population extruded using 100 nm polycarbonate filters.

Measurements have been performed in a Malvern Zeta-Sizer Nano ZS (Malvern Instruments, Malvern, UK) with a detection range for sizes between 0.6 nm to 6 μm and a He-Ne laser beam of 5 mW (λ = 633 nm). 50 μl of the samples (0.1-0.2 mM in lipid) were measured in standard acryl-cuvettes at room temperature and the scattered light was detected with a photomultiplier placed at 173º to the beam. The results were analyzed by the commercial software of the instrument.

2.4 Differential scanning calorimetry (DSC)

Differential scanning calorimetry (DSC) is a useful technique for measuring how the thermodynamic properties of biomolecules, such as proteins, polymers, and lipid membranes, change with temperature (Goñi & Alonso, 2006b). Protein denaturation, DNA unfolding or lipid phase transition are some of its most common applications.

A differential scanning calorimeter is composed of two cells: the reference (a buffer solution) and the sample (lipid in suspension, usually MLV). To avoid signal noise coming from gasses, bubble generation, or liquid boiling, both solutions have to be degassed before adding to the cells. These are been closed, and then the pressure is increased up to a pre-fixed constant value. The difference in temperature between the cells is controlled by a Peltier system, which heats or cools the cells at a controlled temperature rate. In an ordinary DSC experiment, temperature is varied in the cells until the sample undergoes a physical transition, either absorbing (endothermic process) or releasing (exothermic process) energy. The system, trying to keep the same temperature in both cells, will absorb or give energy to the sample cell. This parameter is given by the calorimeter as heat capacity (C_p) in units of energy/temperature. In our case, the results are

normalized with the lipid concentration and the C_p units are kcal/mol/ºC. The amount of energy provided is associated to the phase transition of the lipid and represented as C_p against temperature in a thermogram. Three main thermodynamic parameters can be obtained from such data: phase transition temperature (T_m), phase transition width ($\Delta T_{1/2}$) and phase transition enthalpy (ΔH).

- T_m is usually given at the maximum of the transition, the center in the case of symmetric transitions.
- $\Delta T_{1/2}$ is the transition width in the middle of the transition height. $\Delta T_{1/2}$ provides information about the molecular cooperativity between lipids molecules, a higher cooperativity causing a lower $\Delta T_{1/2}$ value.
- ΔH measures the amount of heat necessary to complete the phase transition, determined by integration of C_p over the whole phase transition.

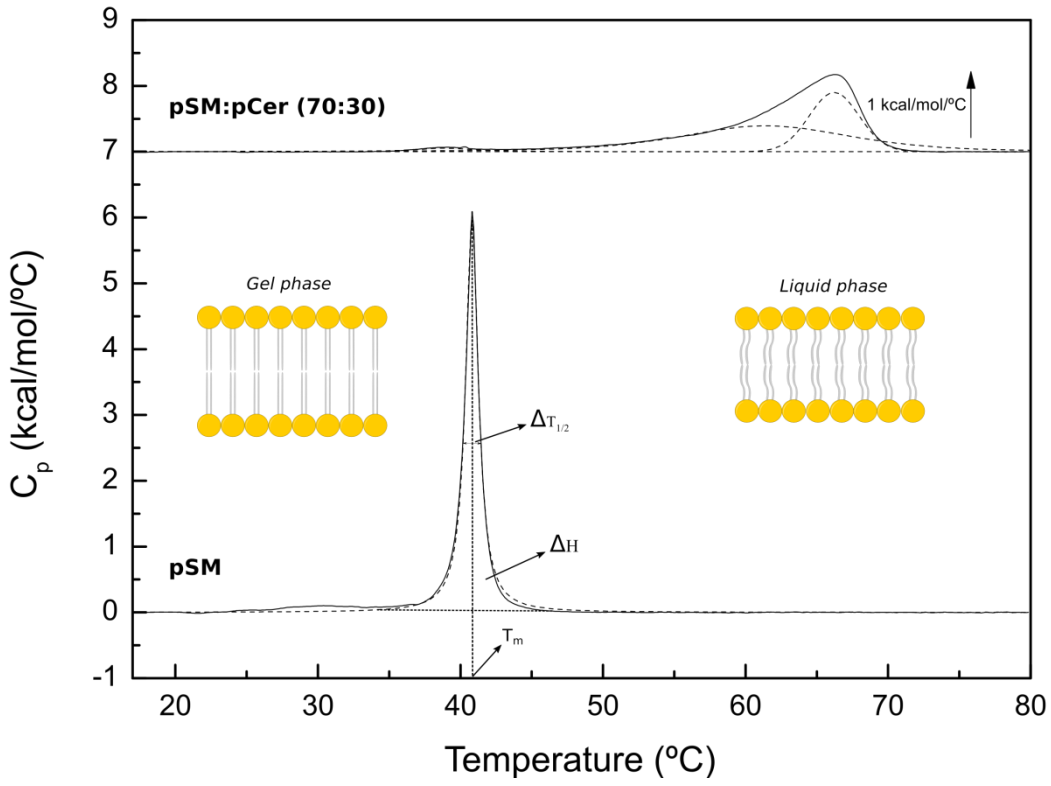

Figure 2.10. A DSC thermogram of pure palmitoylsphingomyelin (pSM) and its endothermic main phase transition with its associated thermodynamic parameters are shown. A DSC thermogram of pSM:pCer (70:30) and its sub-transitions are also shown.

In this work, differential scanning calorimetry is used to study lipid-lipid interactions. The effects of the lipid addition are studied in binary, ternary and quaternary mixtures. The presence of another lipid in the sample changes its phase transition: increasing, decreasing, displacing or creating a new one. These samples usually give rise to an asymmetric transition, which has to be fitted to different symmetric peaks to obtain their thermodynamic parameters. The number of different symmetric transition components is related to the lipid regions present in the sample. In this way, each transition component will have its own thermodynamic parameters.

Protocol 8: Differential scanning calorimetry (DSC)

1) Multilamellar vesicles (MLV) are prepared as previously described in assay buffer (20 mM PIPES, 150 mM NaCl, 1 mM EDTA, pH 7.4).

2) 5 mL buffer solution are degassed for 30 minutes before adding it into the VP-DSC high-sensitivity microcalorimeter (MicroCal, Northampton, MA, USA).

3) A buffer scan is performed, under the same conditions to be used with the sample, to obtain the reference thermogram.

4) After the first scan, when the microcalorimeter is cooling and equilibrating the cells for the next scan, it is possible to exchange the buffer solution for the previously degassed sample.

5) Once the sample is inside the sample cell, 7 scans are performed trying to reach a constant thermogram.

6) When the scans are finished, the original MLV sample concentration is calculated in terms of lipid phosphorous.

7) Knowing the concentration, ORIGIN 7.0 (Microcal) software provided with the microcalorimeter is used to subtract the reference thermogram to the last sample thermogram. The resulting thermogram baseline is adjusted and normalized using the sample concentration to obtain its thermodynamic parameters.

2.5 Fluorescence confocal microscopy

Confocal microscopy was pioneered by Marvin Minsky in 1955 and its development resulted in one of the major advances in optical microscopy, making possible to generate high-resolution images with less haze and better contrast. Epifluorescence microscopy and confocal microscopy differ in the fluorescence that reaches the detector. Modern microscopy avoids out-of-focus plane fluorescence by the use of a pinhole next to the detector that only allows emission from the focal plane to reach the detector, however, when viewed with a conventional microscope these images would be blurred.

Figure 2.11 shows the main components of a fluorescence confocal microscope. The sample is excited by a laser beam focused into a dichroic mirror, which selects the light that will be directed through an objective into a small spot in the sample. Then, emitted fluorescence will be directed across the same dichroic mirror into a pinhole that will let in-focus plane fluorescence pass to the detector while it blocks out-of-focus fluorescence.

Thus, a confocal microscope has the ability to build three-dimensional (3D) images using data from the x-y plane. In this way, by precisely controlling the z sample movement, 3D images can be constructed. For this purpose, special mirrors are introduced.

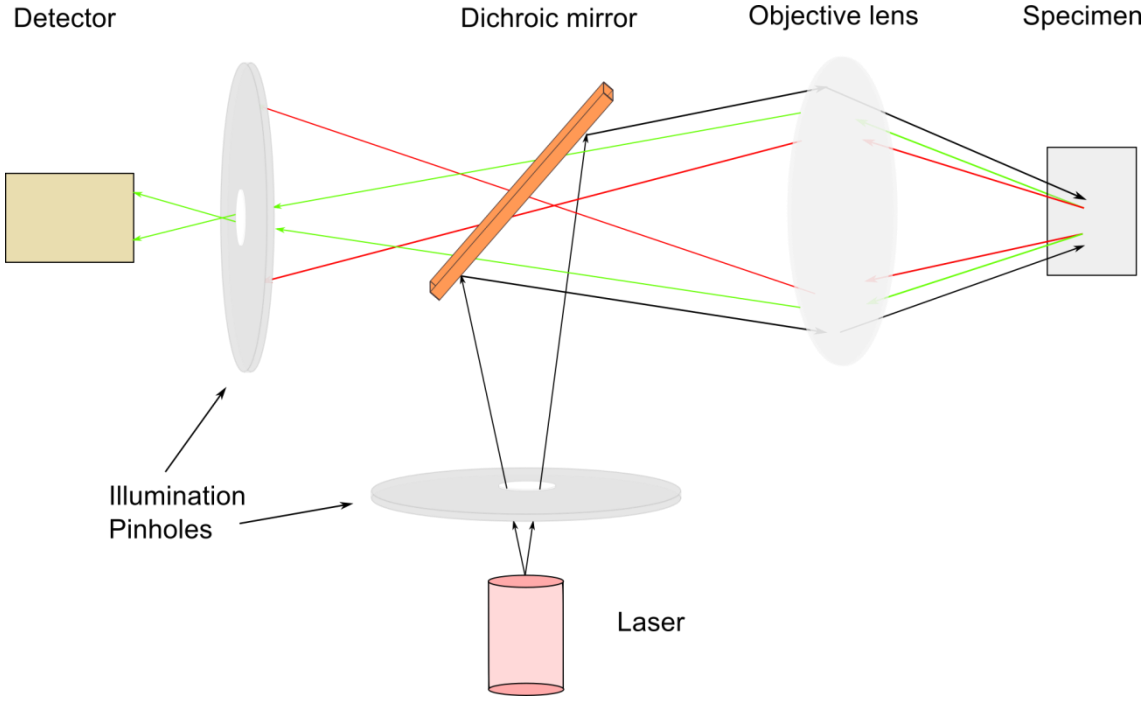

Figure 2.11. Central components of a fluorescence confocal microscope.

Confocal microscopy is commonly used in the characterization of membrane lateral heterogeneity in GUV (Bagatolli, 2006). Domain segregation can be visualized in giant liposomes using fluorescent probes with differential partitioning between domains with different properties. Most fluorescent dyes, such as the fluorescently labeled lipid Rhodamine PE or the hydrophobic probe DiI, partition favourably into the most disordered domains present in the bilayer, while some probes such as napthopyrene show a preference for cholesterol-enriched domains (Juhasz *et al.*, 2010; Baumgart *et al.*, 2007; Klymchenko & Kreder, 2014). There are also probes, for example NBD-ceramide, which distribute homogeneously between fluid and gel domains (Sot *et al.*, 2008). However, all such fluorescent probes are completely unable to enter the highly rigid ceramide-enriched domains.

2.6 Atomic force microscopy

Atomic force microscopy (AFM) is a member of the family of scanning probe microscopes. AFM was a development of the scanning tunneling microscope (STM) invented by Binning and Rohrer in 1982, who received the Nobel Prize in 1986. STM scanned the surface at atomic resolution; however, it was limited to conducting surfaces because both, the tip and the sample, should be conductive. In 1986, Binning *et al.*. invented the atomic force microscope making possible to study any kind of surface, including biological samples (Binnig *et al.*, 1986). Nowadays, AFM is one of the most powerful techniques to obtain topographical information of biological membranes at a lateral resolution of less than 1 nm and a vertical resolution between 0.1 and 0.2 nm. The set of biological samples ranges from the smallest biomolecules (phospholipids, proteins, DNA, RNA) to subcellular structures (membranes), all the way down to living cells and tissues. Furthermore, AFM allows the analysis of mechanical, chemical or functional properties.

The basic principle of AFM is that a probe, which is mounted at the end of a cantilever, is maintained in contact with the sample surface across the x-y axis and the sample topography is obtained by the movement of the probe over the surface. The movement of the probe is controlled by a scanner (piezoelectric material). The interaction between the sample and the tip is measured with a laser beam, which is focused on the top-end of the cantilever. The beam is reflected towards a position-sensitive four quadrant photodetector by the use of a mirror. The signal from the photodetector passes through a feedback circuit, which relates the movement in z-axis needed by the scanner to maintain the cantilever deflection constant with the sample topography.

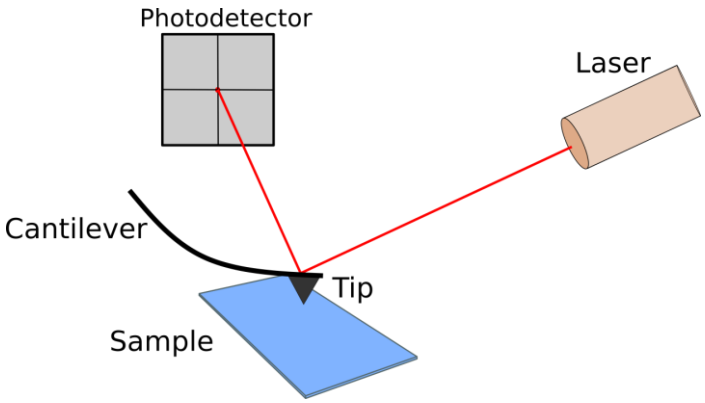

Figure 2.12. Basic principle of atomic force microscopy measurements.

The tip and the cantilever play a crucial role in AFM. The quality of the data and the resolution of the AFM depend to a large extent on them. The material being machined of, its shape, the coating, the spring constant and its resonance frequency among other characteristics have to be specifically selected for a tip to work with during each assay. Silicon nitride cantilever chips are normally used to work in liquid, with typical spring constants ranging from 0.01 N/m to 100 N/m. However biological sample softness limits the force applied during the imaging process so the recommended spring constant is below 1 N/m (usually between 0.01-0.5 N/m). Tips can be rectangular or triangular, and usually have a metal coating for increased reflectivity. Nowadays, the technique has evolved in such a way that tips can be functionalized with specific molecules or even cells for the measurement of protein-protein or cell-cell interaction studies.

The correct selection and preparation of the support is also an important element in AFM measurements. In 1994, Schabert and Engel described a method to prepare support for AFM in which the support is glued to a teflon disc. The teflon repels the fluid droplet and contains it on the mica support. In our case, muscovite mica (Mica) glued to a coverslip is used in our experiments. Mica has to be atomically flat prior to sample incubation, upon cleavage of the upper sheets, and clean to avoid a poor image resolution. Hydrophobic, highly oriented pyrolytic graphite (HOPG) and glass are also commonly used as supports.

When imaging samples in aqueous media, the absorption of the sample depends on the buffer conditions, which needs optimal pH and ionic strength. Furthermore, the scan speed, scanning angle and/or the force applied by the tip on the sample must be properly controlled. Please refer to reviews: Alessandrini and Facci (2005); Goldsbury, Scheuring, and Kreplak (2009) for a more extended overview.

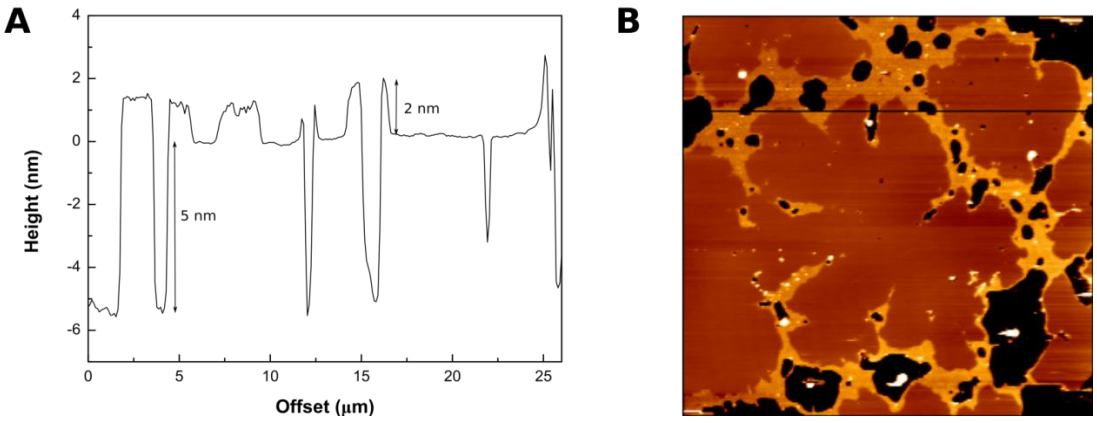

Figure 2.13. AFM height profile along the thick black line in B. Ceramide-enriched domains in a gel-like phase state (approximately 2 nm) can be observed (A). AFM image of pSM:pCer (70:30)(B).

The force applied between the sample and the tip during imaging is related to the operation modes in AFM. Measurements can be performed under two different modes: contact or intermittent, also denoted as tapping mode. The principal characteristics of both modes are described:

Contact mode: In this mode, the force between the sample and the tip is always repulsive and the tip is physically in contact with the sample. The force applied is maintained constant during scanning and the topography is obtained by recording the piezo-vertical movement required to keep the force constant. The highest resolution is obtained; however, the high force applied can damage soft samples. Lateral deflection is also measured, to give information about the friction between tip and sample, which greatly depends on the physical properties of the sample. Thus, areas with different chemical compositions can be distinguished even when displaying no height differences. The error signal is also measured during the scan; this reflects the vertical deflection of the cantilever and shows contrast at the edges of areas with different heights.

Intermittent mode: In this mode, the tip is not always in contact with the sample, therefore both attractive and repulsive forces are present, and it is less aggressive with the sample. The oscillation of the cantilever at its resonance frequency plays an important role in this mode. When the tip is in contact with the sample, a change in its signal amplitude is observed and the feedback signal required to maintain the signal amplitude constant will be used to obtain the topography. Its development made possible the analysis of soft samples and the use of stiffer cantilevers.

The measurement of molecular interaction forces or even the surrounding solvent environment using force spectroscopy mode is also possible. The force curve is a single molecule experiment and is the AFM tool used to characterize our samples. In this experiment, the tip is approached to the sample with an increasing force and then retracted, resulting in a force curve as shown in Figure 2.14. How the van der Waals interactions and the electrostatic and steric-hydration forces influence the approaching process and how an increasing force, applied over the sample, affects its elastic and plastic regime can be observed using this tool. Garcia-Manyes and Sanz (2010) is recommended for a review about the approaching and retracting process and to study the effect of additional parameters like temperature or ionic strength (Garcia-Manyes & Sanz, 2010).

The indentation process is summarized in Figure 2.14 (A). The tip is approached and exerts pressure atop the SPB until the bilayer is pierced by the tip. Finally, the tip is retracted using the same way that was already opened by the approaching process. Panel B shows a force curve generated by the software after the indentation process. When the tip and the sample are in contact the electrostatic and steric-hydration forces have been overcome, and the sample is deformed elastically until a force is reached and the tip pierces the bilayer. The force that the membrane is able to withstand before breaking is called breakthrough force (F_b) and it is shown as a step in the force curve. It can be related to the mechanical stability of the bilayer. After that, the tip presses the mica in a linear plastic regime until the maximum (defined) force is reached. The retracted curve can show hysteresis when the tip adheres to the sample, which depends on the bilayer and tip chemistries.

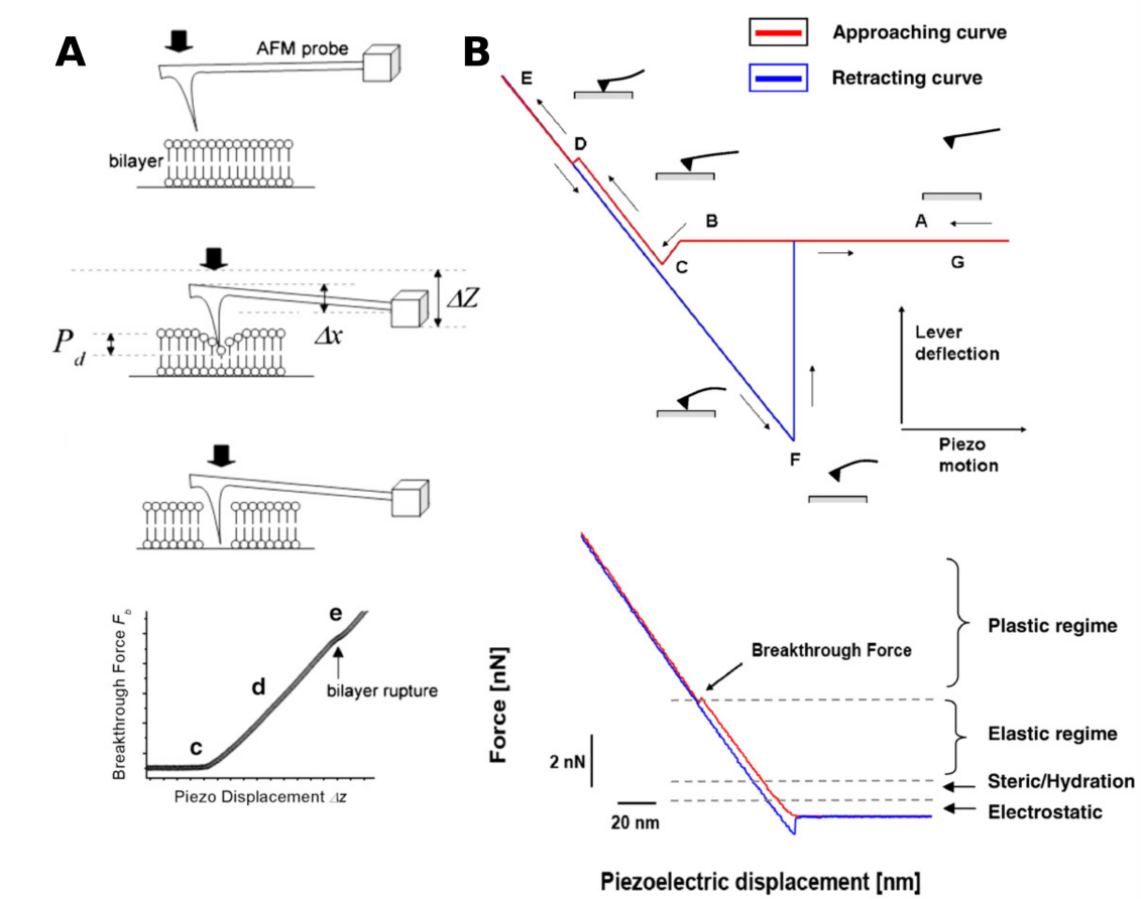

Figure 2.14. Outline of the indentation process of a supported planar lipid bilayer (A) and information about the different areas that can be found in the generated force curve (B). [Adapted from Garcia-Manyes and Sanz (2010)].

In our case, AFM is used to measure the topography of supported lipid bilayers of different compositions and compare the formation of lipid domains within them (Chiantia *et al.*, 2006a; Connell & Smith, 2006). After imaging, force spectroscopy is applied to obtain the breakthrough force, which is the force that the membrane is able to withstand before being indented. It is a measurement of the nanomechanical stability and it is used to characterize supported planar bilayers and evaluate the differences under the same conditions of ionic strength and temperature. As mechanical stability can act as a 'fingerprint' of a lipid mixture, a change in the lipid mixing ratios will supply information about the evolution of our system.

2.7 Fluorescence anisotropy

Photoselective oxidation of fluorophores by polarized light is the basis of fluorescence anisotropy. This technique shows how the rotational diffusion of a fluorophore changes in an excited state. Consider a homogeneous solution in which all fluorophores in a ground-state are oriented randomly. When these fluorophores are exposed to polarized light, those fluorophores whose absorption transition dipole is parallel to the electric vector of the excitation will be excited. At this moment, the excited-state population is partially oriented and its emission will be polarized too. Nevertheless, there are several phenomena that decrease the value of anisotropy, e.g. energy transfer or rotational diffusion. Rotational diffusion changes the direction of these transition moments during the lifetime of the excited state.

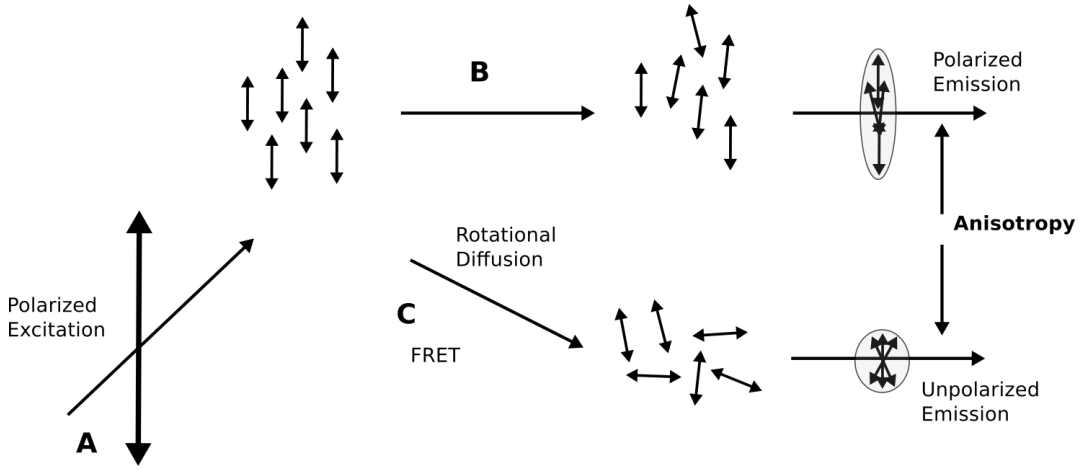

Figure 2.15. Fluorescence anisotropy. Fluorophores are exposed to polarized light and are excited (A). Fluorophores with a slow rotation will have a highly polarized emission with a high anisotropy value (B). Rotation diffusion decreases the polarization and the polarized emission and anisotropy value are lower (C).

Fluorescence anisotropy measurements are carried out with vertically polarized light. In the beginning, the sample is exposed to this light and the emission intensity is measured through a polarizer. If the sample emission intensity and the polarized excitation intensity are oriented, parallel $I_{\parallel}$ is obtained, but if the orientation is perpendicular the intensity obtained is $I_{\perp}$. Fluorescence anisotropy value is calculated using the equation (Lakowicz, 2006):

$$r = \frac{(I_{\parallel} - I_{\perp})}{(I_{\parallel} + 2I_{\perp})}$$

When the emission intensity is completely parallel to the polarized light $I_{\perp}$= 0, and r =1. This situation can be observed with scattered light and oriented samples. However, if the emission is completely depolarized $I_{\perp} = I_{\parallel}$ and r = 0.

The method used to measure anisotropy when the fluorometer has a single emission channel is the L-Format or Single-Channel method. In this case, the emission is observed using a monochromator. The monochromator usually has different transmission efficiency for vertically and horizontally polarized light. The intensities measured are not exact but are proportional to the transmission efficiencies of the monochromator. In fact, the intensities measured and the true values differ by a factor G, which is the relation between the sensitivities of the detection system by vertically (S_V) and horizontally (S_H) polarized light. Factor G is calculated using horizontally polarized excitation doing both the horizontally and vertically polarized components equal and proportional to $I_{\perp}$.

$$G = \frac{(S_V \cdot I_{\perp})}{(S_H \cdot I_{\perp})} = \frac{S_V}{S_H}$$

The measurement of fluorescence anisotropy is widely used in biochemical research. For example, anisotropy measurements can be used to measure the association of proteins with other macromolecules. As these measurements are rapid and simple they can be used to study reaction kinetics occurring in fractions of a second, like the unwinding of DNA by helicase. Furthermore, fluorescence measurements can also be used to study biological membranes. The steady-state polarization of 1,6-diphenyl-1,3,5-hexatriene (DPH) is commonly used to study phase transition temperatures, which allow us to determine the order of lipid bilayers. When DPH is present in an ordered bilayer, its movements will be restricted and a high anisotropy will be observed, however, if DPH is in a disordered bilayer a low anisotropy will be observed.

In this work, DPH has been used to study the anisotropy changes during different phase transition temperatures and how the presence of cholesterol affects these samples. These experiments have been measured with MLV at 0.2 mM plus 1 mol% DPH using a 1-cm path length quartz cuvette in a QuantaMaster 40 spectrofluorometer (Photon Technology International, Lawrenceville, NJ) under continuous stirring. DPH was excited at 360 nm and its emission recovered at 430 nm. The anisotropy was calculated by the software (PTI FelixGX), automatically corrected for factor G.

2.8 Membrane polarization (Laurdan assay)

Laurdan (6-lauroyl,1-2-dimethylaminonaphthalene) is one of the most used sensitive dyes based on a naphthalene structure, designed and synthesized by Weber in 1979 (Weber & Farris, 1979). Laurdan has an electron donor (alkyl amino group) and an acceptor (acyl substituted carbonyl group) in position 2 and 6, which confer a dipole moment due to its partial charge separation in polar solvents (Sanchez *et al.*, 2007).

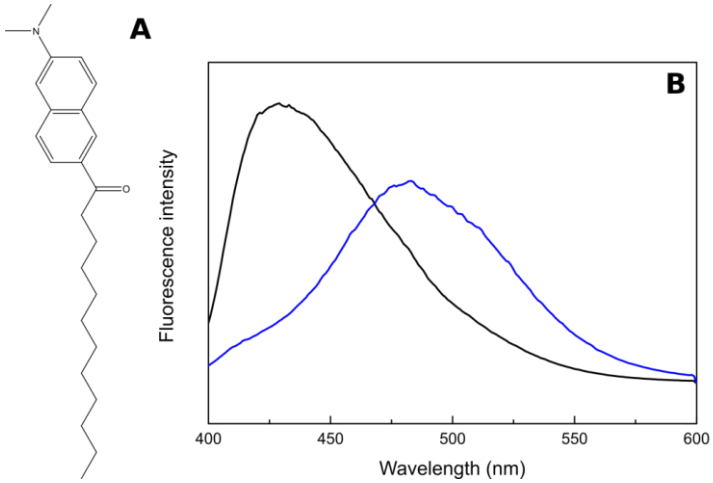

Figure 2.16. Laurdan molecule structure (A). Laurdan emission spectra (B). More ordered (black); less ordered (blue).

When Laurdan is excited, its dipole moment increases and may cause reorientation of the surrounding solvent dipoles. This reorientation decreases the energy of its excited state and a shift in its emission spectrum is observed. The General Polarization (GP) function was proposed by Parasassi in 1990 and it is used to study this displacement (Parasassi *et al.*, 1990).

$$GP = \frac{I_{440} - I_{490}}{I_{440} + I_{490}}$$

where:

I_{440} = emission intensity at 440 nm.

I_{490} = emission intensity at 490 nm.

Theoretically the values for the GP function vary from +1.0 and -1.0; however, experimentally they range from +0.6 to -0.3. For membranes in a gel

phase, the emission maximum is centered at 440 nm with a GP value that ranges from 0.5 to 0.6, while for membranes in liquid phase GP goes from +0.3 to -0.3, with an emission maximum around 490 nm.

The spectral shift of Laurdan can be used to study the lipid order in cellular membranes or to detect the lipid main phase transition, among other applications.

Protocol 9: Membrane polarisation (Laurdan assay)

1) Prepare multilamellar vesicles (MLV) as previously described with 1 mol% Laurdan in assay buffer (20 mM PIPES, 150 mM NaCl, 1 mM EDTA, pH 7.4).

2) Acquire fluorescence spectra using a Quanta Master 40 spectrofluorometer (Photon Technology International) under the following conditions:
   * λ_{ex} = 360 nm
   * λ_{em} = 400- 600 nm

2.9 Vesicle content efflux measurements (Leakage assay)

One of the main functions of lipid bilayers is to act as natural barriers creating a non-selective permeability barrier. This technique measures the ability of particular molecules such as detergents, pore-forming proteins, and lipids to permeabilize the vesicle lipid bilayer using a fluorescence probe as an indicator. Detergent addition to the sample causes the solubilization of vesicle regions through which entrapped fluorescent molecules are externalized. This approach is of great interest for instance in the characterization of the pore and/or channel forming molecules. Nevertheless, in the present study, the solubilizing effects of different lipids were tested by following the externalization of the low molecular weight 8-aminonaphthalene-1,3,6-trisulfonic acid (ANTS) fluorescent molecules and its quencher p-xylene-bis-pyridinium bromide (DPX) (Ellens *et al.*, 1985).

When ANTS and DPX are encapsulated inside the vesicles, their proximity allows DPX to interact with ANTS, quenching its fluorescence. The addition of a permeabilization agent causes the slow externalization of the fluorophores. Now, ANTS fluorescence can be measured because of the dilution of the fluorophores into the external medium, decreasing their interaction. Finally, Triton addition gives us information about the percentage of leakage observed (Goñi *et al.*, 2003; Nieva *et al.*, 1989). An outline of the ANTS-DPX assay is shown in Figure 2.17.

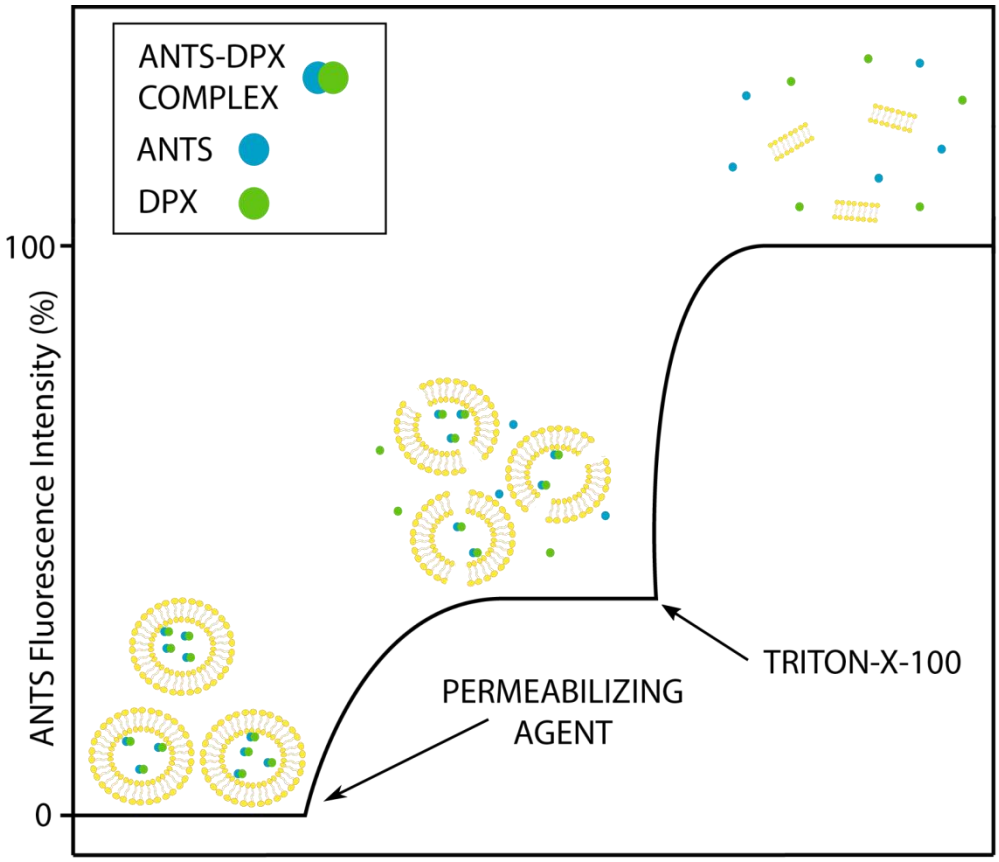

Figure 2.17. Outline of the vesicle content efflux measurement (leakage assay).

Protocol 10: Vesicle content efflux measurements (Leakage assay)

1) Large unilamellar vesicles (LUV) are prepared as previously described in the following buffer containing both ANTS and DPX (20 mM ANTS, 70 mM DPX, 10 mM Hepes, 40 mM NaCl, pH 7.4). A high DPX/ANTS ratio is used to ensure complete quenching inside the vesicles. Samples are covered with aluminum foil to protect fluorescent molecules from bleaching.

2) The vesicle suspension is passed through a Sephadex G-25 column to remove non-entrapped ANTS and DPX molecules using an isoosmotic buffer solution (10 mM Hepes, 150 mM NaCl, pH 7.4), previously adjusted.

3) Lipid concentration is determined using the lipid phosphorous concentration assay as previously described.

4) 10 mol% permeability agent (e.g. ceramide) is added to 0.1 mM vesicles in a 1-cm path length quartz cuvette and leakage is followed in terms of ANTS fluorescence in FluoroMax-3 spectrofluorometer (Horiba Jobin Yvon, Edison, NY), under continuous stirring with the following conditions:

   - λ_{ex}: 355 nm
   - λ_{em}: 520 nm
   - Interference filter at 515 nm.
   - 0% release: Initial fluorescence of pure vesicles.
   - 100% release: Fluorescence after complete vesicle solubilization with Triton X-100 10% detergent.

   To calculate the amount of leakage the following equation is used:

$$\text{Leakage } (\%) = \left(\frac{(F - F_0)}{(F_{100} - F_0)}\right) * 100$$

   F= Fluorescence at the end of the time course.
   F_0 = Fluorescence of vesicles at time zero.
   F_{100} = Maximum leakage (after Triton-X addition).

2.10 Lipid transbilayer movement (Flip-flop assay)

The rapid movement of lipids across the membrane is needed in order to maintain the symmetric (endoplasmatic reticulum, ER) or asymmetric (plasma membrane) lipid distribution. Their movement is usually very slow due to the unfavorable transit of a polar headgroup through a hydrophobic area (Kornberg & Mcconnell, 1971) and requires the action of lipid transport proteins, flippases, to increase the movement across the membrane using the energy of ATP hydrolysis. However, some lipids as ceramides, cholesterol or diacylglycerol, composed of a simple hydroxyl moiety as a headgroup, have a fast transbilayer movement by themselves.

In order to study the transbilayer movement of different lipids, N-(7-nitrobenz-2-oxa-1,3-diazol-4-yl)-1,2-dihexadecanoyl-*sn*-glycero-3-phosphoethanolamine (NBD-PE) is used. NBD-PE is a phosphatidylethanolamine whose headgroup is labeled with the fluorophore NBD. Once NBD-PE is symmetrically distributed across the vesicle, a sodium dithionite solution is slowly added to reduce the NBD NO_2 groups present in the outer leaflet of the vesicle into amine groups, and abolish its fluorescence transforming the NBD group to a non-

fluorescent derivative termed ABD (McIntyre & Sleight, 1991). After that, the sample must be passed through a Sephadex G-25 (GE Healthcare, UK) to remove the sodium dithionite excess, which tends to permeate after a short time. NBD-PE movement from the inner to the outer leaflet is promoted adding different lipids to the solution. Finally, sodium dithionite is used to confirm the transbilayer movement reducing the NBD groups present in the outer leaflet.

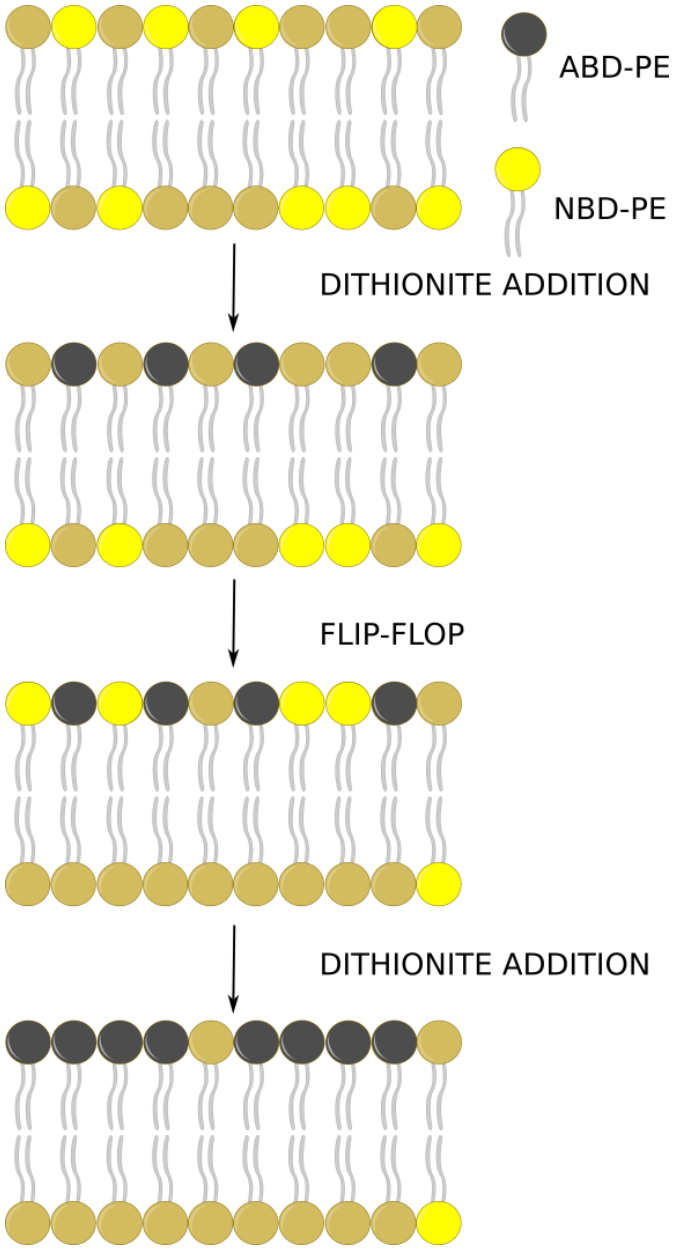

Figure 2.18. NBD-PE flip-flop measurements. The probe is symmetrically added to the vesicles. NBD-PE translocation is confirmed by the loss of fluorescence when sodium dithionite is added. If there is no translocation, the fluorescence value remains constant.

Protocol 11: Lipid transbilayer movement (Flip-flop assay)

1) Large unilamellar vesicles (LUV) are prepared as previously described with 0.6 mol% NBD-PE in buffer (10 mM Hepes, 150 mM NaCl, pH 7.4). Samples are covered with aluminum foil to protect fluorescent molecules from bleaching.

2) 0.6 mM sodium dithionite is added to reduce the NBD groups present in the outer leaflet of the vesicle. Fluorescence reduction is monitored in an Aminco-Bowman (Urbana, IL) AB-2 spectrofluorometer using a 1 mL quartz cuvette with continuous starring.

3) The vesicle suspension is quickly passed through a Sephadex G-25 column to remove the excess sodium dithionite and to avoid the reduction of the inner leaflet NBD groups.

4) Lipid concentration is determined using the lipid phosphorous concentration assay as previously described.

5) 0.1 mM vesicles are incubated with 10 mol% lipid for 30 minutes. After incubation, 50 µL 0.5 mM sodium dithionite are added and flip-flop is followed in terms of NBD fluorescence in Aminco-Bowman (Urbana, IL) AB-2 spectrofluorometer, under continuous stirring under the following conditions:

   - λ_{ex}: 463 nm
   - λ_{em}: 536 nm
   - Interference filter at 515 nm.

   To calculate the amount of flip-flop the following equation is used:

$$\text{Flip} - \text{flop}\ (\%) = \left(1 - \frac{F_R}{F_0}\right) * 100$$

   F_R= Fluorescence after sodium dithionite addition.
   F_0 = Fluorescence before sodium dithionite addition.

2. 11 X-ray scattering

X-ray scattering is a powerful non-invasive technique, which is commonly used to characterize structures of materials (polymers and fibers) and biological systems as lipids. In X-ray-scattering experiments, a laser beam strikes the sample of interest and the scattered radiation intensity is collected by a detector at given scattering angles with respect to the incident radiation direction.

In our case, through a collaboration with S. Tristram-Nagle (Carnegie Mellon University, Pittsburgh, USA), we have used their X-ray scattering setup to obtain diffuse scattering data that yields not only structure but also elastic parameters of N-palmitoyl-D-erythro-sphingosylphosphorylcholine (pSM) and egg sphingomyelin (eSM) vesicles. The X-ray pattern provides information about the sample structure, as the bending modulus (k_c) and the order parameter S_{xray} in the fluid phase and the area per lipid (A_L), the bilayer thickness (D_B) and the tilt angle in the gel phase.

In the present work, samples measured were either oriented or unoriented. Oriented samples were prepared by the "rock and roll" method, which was designed in Tristram-Nagle´s group (Tristram-Nagle 2007). X-ray scattering setup consists of a Rigaku rotating anode and a CCD detector. Low angle X-ray scattering (LAXS) and wide angle X-ray scattering (WAXS) were obtained from a Rigaku RUH3R rotating anode. Wavelength was 1.5418 Å, and sample-to-detector (S)-distance was 280.6mm (LAXS) or 133.7mm (WAXS). Data were collected using a Rigaku (The Woodlands, TX, United States) Mercury CCD array detector (1024×1024, 68 μm pixels) for 5 or 10 min. Temperature was controlled using a Julabo Model F25 circulating water bath. Data analysis for the ripple phase was performed using TiffView software. Brief protocols for sample preparation are given:

Protocol 12: Oriented sample preparation by the "rock and roll" method

1) To prepare the substrate, the Si wafers have to be bathed with a mixture of sulfuric and chromic acid in a Petri dish for 1 hour. Then, the wafers are cleaned with water. Finally, Si wafers are bathed with chloroform in a glass Petri dish inside the glove box and rubbed with a cotton swab. Thus a chloroform-saturated atmosphere is created in the glove box. The Si wafers are sometimes rubbed with a Kimwipe in the final step to remove any remaining residue, and any lint is carefully blown away with a small rubber bulb.

2) Lyophilized lipid is weighed using an analytical balance and placed into a disposable, small glass test tube. Disposable test tubes are used to assure cleanliness. 400 µL Chloroform:2,2,2-Trifluoroethanol (TFE) (1:1) are added to solubilize the lipid.

3) In the glove box, the lipid in solvent is poured onto the substrate with rocking and rolling. As the sample dries, a higher angle of rocking (up to 90°) may be required in order to induce the now-viscous solution to move down the wafer. The rocking continues until the rolling of lipid in solvent over the surface stops; at this point the substrate is removed from the sticky tack and placed onto a flat surface in the glove box, which is why flat substrates work best. The entire process takes about 5 min. The film is left to dry for 2 hours in the hood to ensure complete removal of the solvent.

4) If the film is completely smooth, well oriented, and homogeneous, the sample is prehydrated at close to 100% relative humidity (RH) in a polypropylene hydration chamber at 60 °C for 2 h and allowed to slowly cool to room temperature.

5) Approximately 10 µm thick samples were trimmed to leave 5mm (in the direction of the X-ray beam) by 30 mm (to provide many locations for the ~1 mm wide beam to minimize radiation damage), using a fresh single-edge razor blade, followed by wiping off any remaining lipid with a dry cotton swab.

Protocol 13: Unoriented sample preparation

1) 2–10 mg of lyophilized lipid is mixed with 100 µL of MilliQ water.

2) Then, the sample is hydrated by vortexing and temperature cycling 3 times between 60 °C and 0 °C to form multilamellar vesicles (MLV).

3) Hydrated lipids are mildly centrifuged using a desk-top centrifuge in a glass test tube at 1000 rpm for 10 min and the concentrated lipid is loaded into 1 mm diameter thin-walled X-ray capillaries (Charles Supper Company, Natick, MA) and flame-sealed.

4) Finally, the X-ray capillaries are centrifuged in a capillary holder at 1000 rpm for an additional 2 min to further concentrate the lipid in the beam. The final ratio of water to lipid was at least 2:1 so the MLV was fully hydrated as evidenced by their contact with excess water in the capillary.

Protocol 14: Volumetric sample preparation

1) 10-50 mg of lyophilized lipid is added to 1.204 g MilliQ water.

2) Then, the sample is hydrated by vortexing and cycling three times between 60 ºC and 0 ºC.

CHAPTER 3:

PHASE BEHAVIOR OF PALMITOYL AND EGG SPHINGOMYELIN

CHAPTER 3: PHASE BEHAVIOR OF PALMITOYL AND EGG SPHINGOMYELIN

3.1 Introduction

The major lipids in biological membranes are glycerophospholipids, sphingolipids and sterols. While sphingolipids include glycosphingolipids and sphingomyelins (SMs), the latter are the most abundant sphingolipids in mammalian cells (Van Meer *et al.*, 2008) reaching concentrations of 15% of the total phospholipid content in the outer leaflet of the plasma membranes (Shaw *et al.*, 2012). Structurally, SMs are similar to phosphatidylcholines (PCs) in that both lipids have phosphatidylcholine as the polar headgroup and both have long hydrocarbon tails, but there are considerable differences in the linkages to these parts of the lipids (Ramstedt & Slotte, 2002).

Recent interest in SMs arises from their interaction with cholesterol in generating cholesterol-rich lateral membrane domains, their specific binding to and regulation of particular membrane proteins, and their involvement as precursors to simpler sphingolipids in cell signaling events (Goñi & Alonso, 2006c; Slotte, 2013). The preferential mixing of sterols with SMs over PCs is mainly attributed to two properties: Firstly, SMs usually have saturated or *trans*-unsaturated tails and they apparently pack more tightly (Van Meer *et al.*, 2008); secondly, the amide and hydroxyl groups in SMs can act as hydrogen bond donors and acceptors, so they can form both intra- and intermolecular hydrogen bonding (Slotte, 2016; Venable *et al.*, 2014).

Since pure SMs are more expensive than pure PCs, many experimental studies of systems involving them are performed using natural SM extracts e.g., egg, brain and milk SMs, which have mixtures of hydrocarbon chains. On the other hand, simulation studies use pure SM lipids with homogeneous chains. ESM stands out as the most homogeneous of the natural SMs; it has predominantly 86% N-palmitoyl (16:0) acyl chain (Filippov & Ora, 2006) with 93% of the sphingosine (18:1) long-chain base (Ramstedt & Slotte, 1999). Therefore from the viewpoint of

composition, eSM is the closest natural extract to the pure palmitoyl sphingomyelin (pSM), so experimental properties using eSM are frequently compared to simulation studies using pSM (Niemela *et al.*, 2004); such comparisons should be made carefully, especially as the main transition temperature of pSM (T_m=41°C) (Barenholz *et al.*, 1979) is somewhat higher than for eSM (T_m = 38 °C) (Jiménez-Rojo *et al.*, 2014). This chapter will further address differences between eSM and pSM.

Even the nature of the generic SM main transition has been unclear. By analogy with saturated PC lipids, the transition is often inferred to be from ripple phase to fluid (liquid-crystalline or liquid-disordered) phase if a pretransition is observed and gel-to-fluid phase if it is not. Many thermotropic studies did not observe a pretransition, either in pSM (De Almeida *et al.*, 2003; Maulik & Shipley, 1996), or in eSM (Mannock *et al.*, 2003; Steinbauer *et al.*, 2003; Veiga *et al.*, 2001; Chien & Huang, 1991; Filippov & Ora, 2006; García-Arribas *et al.*, 2016c; Jiménez-Rojo *et al.*, 2014; Mckeone *et al.*, 1986; Epand & Epand, 1980; Rujanavech *et al.*, 1986; Anderle & Mendelsohn, 1986; Arsov & Quaroni, 2008), and have described the transition as a gel-to-fluid (liquid-crystalline or liquid-disordered) phase.

In other pSM studies (Barenholz *et al.*, 1979; Calhoun & Shipley, 1979a) a pretransition was observed using DSC. Turning to structural studies one of the first low- and wide-angle X-ray scattering (LAXS and WAXS) studies on pSM reported a gel phase structure below T_m despite observing a pretransition using DSC (Calhoun & Shipley, 1979a). Maulik & Shipley (1996) also reported no X-ray evidence for a ripple phase in pSM. However, other X-ray studies have reported that eSM is in a ripple phase below T_m (Chemin *et al.*, 2008; Quinn & Wolf, 2009a; Shaw *et al.*, 2012). All of these X-ray studies employed unoriented MLV samples where ripple reflections are either small or weak. By contrast, X-ray diffraction from oriented lipid samples is particularly well suited to differentiate between flat gel or interdigitated phases and the ripple phase (Akabori & Nagle, 2015; Guler *et al.*, 2009; Katsaras *et al.*, 2000; Sun *et al.*, 1996a). To clarify the above mentioned differences in the literature for both eSM and pSM individually, as well as what the actual differences are between eSM and pSM, the aim of this work is to characterize the structure of the phases, particularly for $T < T_m$, using oriented hydrated samples.

Furthermore, the interaction between eSM and eCer has been studied using 15 mol% and 30 mol% egg ceramide in binary mixtures. Their phases are characterized in a broad temperature interval through their main phase transition (Sot *et al.*, 2006) to observe how the presence of ceramide affects to the ripple phase of eSM. Additionally, the suitability of X-ray scattering to study the formation of ceramide domains is tested.

3.2 Materials and methods

3.2.1 Materials

Egg sphingomyelin (Lot Egg-SM 860061-01-115) (eSM) palmitoyl sphingomyelin (pSM) (Lot 860584-01-017), and egg ceramide (eCer) (Lot ECER-18) were purchased from Avanti Polar Lipids (Alabaster, AL) and used as received. Avanti estimates 1–1.5% L-erythro impurity, no D- or L-threo impurity, and greater than 99% purity with respect to total sphingomyelin content in PSM, whereas as much as 10% L-threo may occur when synthesizing by hydrolysis of natural SM. HPLC organic solvents were purchased from Sigma/Aldrich (St. Louis, MO).

3.2.2 Sample preparation

Oriented samples. 4 mg of lyophilized lipid was dissolved in 200 mL chloroform:TFE (1:1) (v/v) and plated onto a silicon wafer (15x30x1 mm) via the rock and roll method (Tristram-Nagle, 2007) to produce stacks of ~1800 aligned bilayers (Tristram-Nagle *et al.*, 2002). Solvents were removed by evaporation in a fume hood, followed by 2 hours under vacuum at room temperature. The oriented samples were prehydrated at close to 100% RH (relative humidity) in a polypropylene hydration chamber at 60 °C for 2 hours and allowed to slowly cool to room temperature. Thin layer chromatography indicated no degradation due to this annealing procedure. Approximately 10 μm thick samples were trimmed to leave 5mm (in the direction of the X-ray beam) by 30 mm (to provide many locations for the 0.5 mm wide beam to minimize radiation damage).

Unoriented samples. 2-10 mg of lyophilized lipid was mixed with 100 μL of MilliQ water. Samples were hydrated by vortexing and temperature cycling 3 times between 60 °C and 0 °C to form multilamellar vesicles (MLV). Hydrated lipids were mildly centrifuged using a desk-top centrifuge in a glass test tube at 1000 rpm for 10 minutes and the concentrated lipid was loaded into X-ray capillaries (Charles Supper Company, Natick, MA) and flame-sealed. The X-ray capillaries were centrifuged in a capillary holder at 1000 rpm for an additional 2 minutes to further concentrate the lipid in the beam. The final ratio of water to lipid was at least 2:1 so the MLVs were fully hydrated as evidenced by their contact with excess water in the capillary.

Volumetric samples. 48.9 mg lyophilized eSM was added to 1.204 g MilliQ water and hydrated by vortexing and cycling three times between 60 and 0 °C. ~10

mg lyophilized pSM was added to ~1.1 g MilliQ water and hydrated by vortexing and cycling three times between 60 ºC and 0 ºC.

3.2.3 X-ray Scattering

Oriented stacks of membrane mimics were hydrated through the vapor phase in a temperature-controlled hydration chamber described in (Kucerka *et al.*, 2008). Low angle X-ray scattering (LAXS) and wide angle X-ray scattering (WAXS) were obtained from a Rigaku RUH3R rotating anode as described in (Tristram-Nagle *et al.*, 2002, 1994). Wavelength was 1.5418 Å, and sample-to-detector (S)-distance was 280.6 mm (LAXS) and 133.7 mm (WAXS). Data were collected using a Rigaku (The Woodlands, TX) Mercury CCD array detector (1024x1024, 68 μm pixels) during 5- or 10-minute dezingered scans. Temperature was controlled using a Julabo Model F25 circulating water bath. Data analysis for the ripple phase was performed as in (Sun *et al.*, 1996a; Akabori & Nagle, 2015) using our proprietary TiffView software.

3.2.4 Volume measurements

The 4.1% aqueous eSM or ~1% aqueous pSM suspension was loaded into the Anton-Paar 5000M DMA scanning density meter and heated at 12 degrees/h.

3.3. Results

3.3.1 Characterization of pure eSM and pSM

Figure 3.1 A shows the typical X-ray pattern obtained for eSM. Oriented samples clearly show off-specular peaks below T_m, indicated by white arrows; such peaks are required for in-plane periodicity that occurs for the ripple phase. The peaks are arranged symmetrically around the meridian because the sample is a powder average, in-plane only. This rippled pattern was present at every temperature investigated in this work from 3 to 35 °C. Additional oriented eSM data are shown in the Supplementary Material (Figures 3.S1 – 3.S8). Following the literature (Akabori & Nagle, 2015; Sun *et al.*, 1996a; Wack & Webb, 1989) these peaks can be indexed as (h,k) where the (h,0) peaks are the usual lamellar peaks that occur on the meridian with q_r=0. The ripple side peaks are labeled with the k index. In Figure 3.1 A, the visible side peaks are, from the top, (4,-2), (3,-1), (3,-2), (2,-1), (1,-1) and a weak (1,1). Figure 3.1 B shows that eSM is also in the ripple phase at 35 °C.

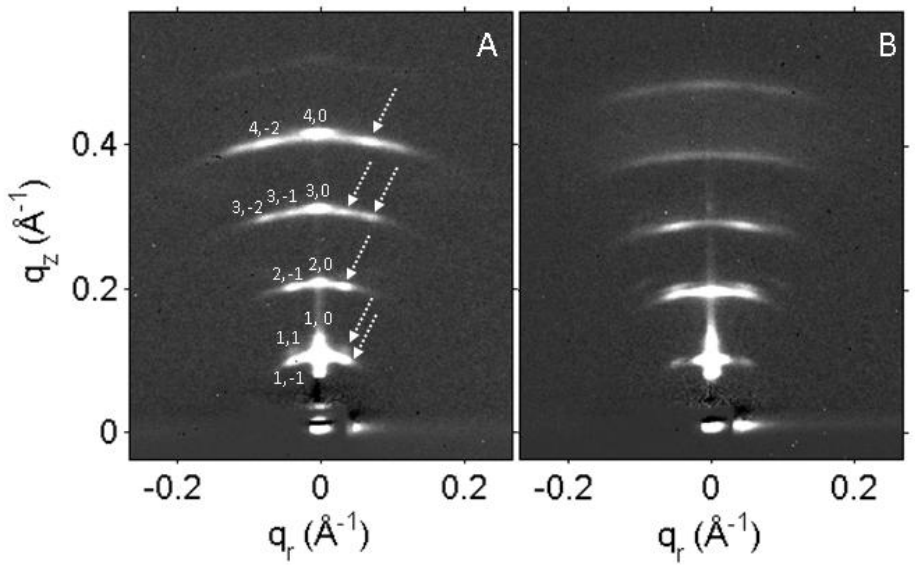

Figure 3.1. LAXS data from oriented eSM. Overnight equilibration at 3 °C (A), followed by equilibration at 35 °C (B). White arrows in A point to the off-specular peaks. D-spacing is 60.3 Å in A and is 65.8 Å in B.

Figure 3.2 shows LAXS data for pSM. At 37 °C (Figure 3.2 B) pSM is clearly in the ripple phase, however, at 3 °C (Figure 3.2 A) the absence of side peaks is consistent with a gel phase. In Figure 3.2 A, arcs with FWHM ~6°, instead of spots, are due to mosaicity (Nagle *et al.*, 2016). Additional oriented pSM data are shown in the Supplementary Material (Figures 3.S9-3.S15).

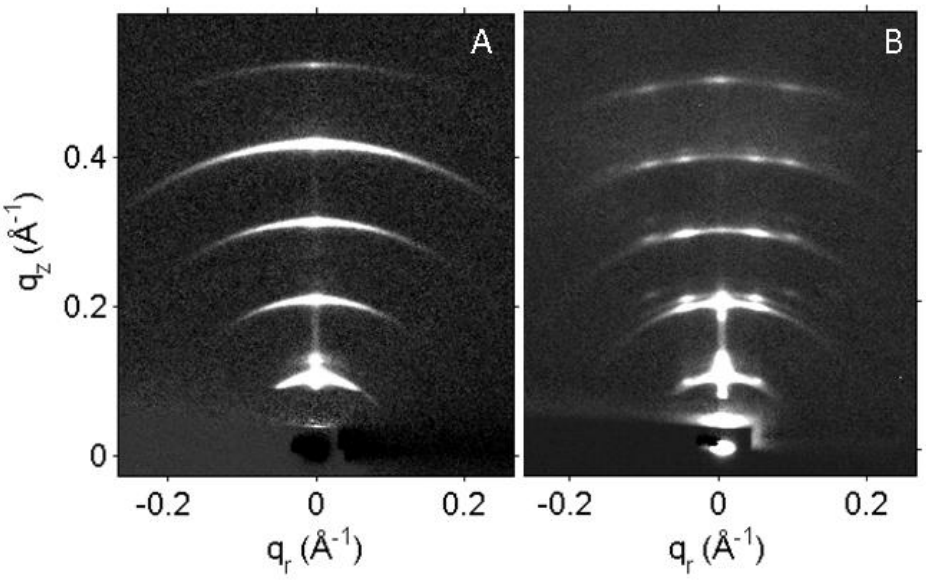

Figure 3.2. LAXS data from oriented pSM. After overnight equilibration at 3 °C (A), and at 37 °C (B). D-spacing in A is 60.0 Å, and in B is 63.6 Å

.

In order to describe our structural results, a diagram of some of the basic structural parameters of ripple phases is shown in Figure 3.3. The usual lamellar D-spacing in the z direction perpendicular to the substrate and the stack of bilayers includes the average bilayer thickness and the water spacing; it was obtained from the q_z positions of the specular (h,0) peaks. Following previous studies (Akabori & Nagle, 2015; Sun *et al.*, 1996a; Wack & Webb, 1989), the in-plane spacing λ_r is the length of the rippled repeat distance; it was obtained from the q_x positions of the off-specular (h,k) peaks. γ is the angle in the two dimensional unit cell; it was obtained from the angle of the lines joining the central (h,0) peaks to the (h,k<0) side peaks (Akabori & Nagle, 2015; Sun *et al.*, 1996a).

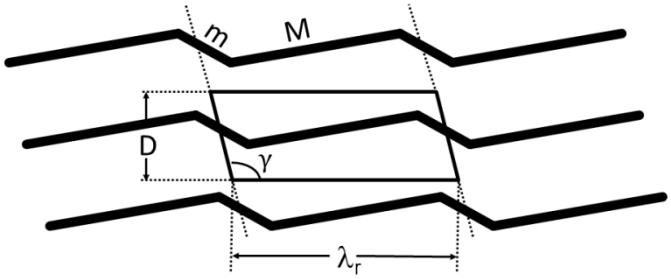

Figure 3.3. Diagram of structural parameters characterizing the ripple phase. The bold solid lines represent the centers of three adjacent bilayers. M represents the major arm and m the minor arm in a typical saw-toothed asymmetric ripple (Akabori and Nagle, 2015; Katsaras et al.., 2000; Sun et al.., 1996b). D is the usual lamellar repeat D-spacing, λ_r is the ripple wavelength and γ the ripple offset angle in the unit cell indicated by the parallelogram containing the middle of the 2nd bilayer.

Figure 3.4 shows results for λ_r and γ. The result that γ values differ from 90° requires that the ripple be asymmetric unlike the symmetric ripple phases that occur metastably in DPPC and which have λ_r greater than 200 Å (Katsaras *et al.*, 2000; Mason & Gaulin, 1999; Rappolt & Rapp, 1996; Yao *et al.*, 1991). Furthermore, the stronger intensity of the negative k peaks compared to the positive k peaks means that the asymmetry is as drawn in Figure 3.3 (Akabori & Nagle, 2015; Sun *et al.*, 1996a).

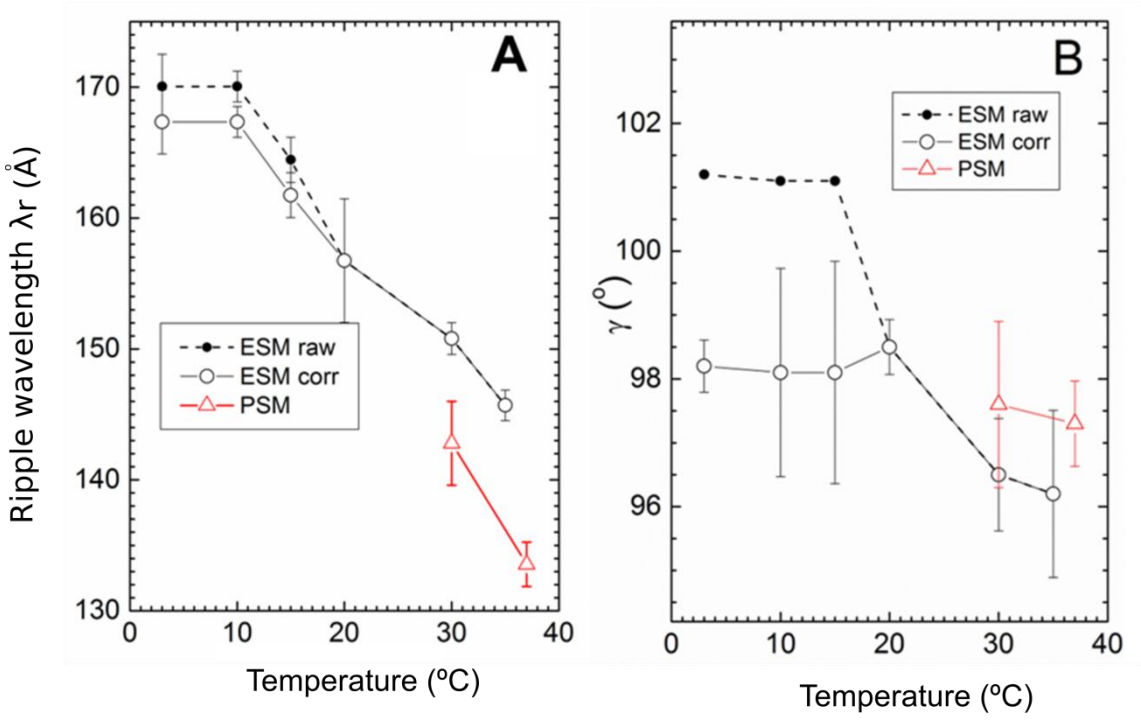

Figure 3.4. Temperature dependence of λ_r of the ripple phase (A), and the γ angle (B) for eSM (open black circles) and pSM (open red triangles). The solid symbols show values before correction for hydration level (see below).

Figure 3.5 shows wide-angle WAXS scattering for the same pSM sample as in Figure 3.2. With the longer exposure time appropriate for the WAXS scattering, Figure 3.5 A shows LAXS orders h=1-4 that are overexposed and weak h=5, 7 and 9 LAXS orders. The WAXS scattering in Figure 3.5 A looks similar to the WAXS pattern from the L_β gel phase in DMPC (Tristram-Nagle *et al.*, 2002), where tilted chains cause the (1,1) peak to be lifted up off the equator near q_r = 1.4 Å^{-1}. Also visible at the same q_r and smaller q_z is a satellite that comes from modulation of the continuous form factor along the (1,1) Bragg rod (Sun *et al.*, 1994). The wide angle scattering in Figure 3.5 B is consistent with the much higher resolution WAXS from DMPC in the ripple phase (Akabori & Nagle, 2015) suggesting that there is a stronger Bragg rod centered near q_r = 1.5 Å^{-1} and $q_z \sim 0.3$ Å^{-1} and a weaker Bragg rod at smaller q_r and q_z, although such a separation is not visible in Figure 3.5 B. Figures S3-S5 for eSM are more suggestive of such a wide angle pattern.

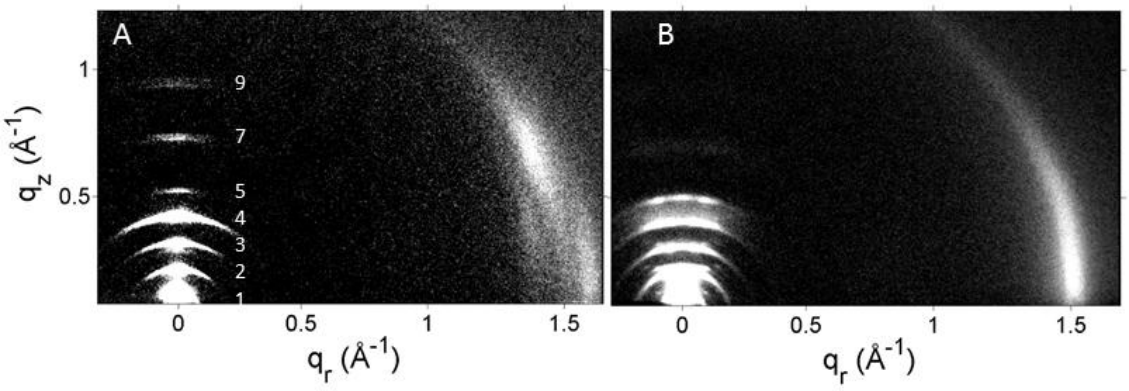

Figure 3.5. Wide angle WAXS intensity together with overexposed LAXS for the same sample and temperatures as in Figure 2. pSM at 3 ^{o}C (A), pSM at 37 ^{o}C (B). D-spacing in A is 59.2 Å, and in B it is 63.0 Å.

WAXS data shown in Figure 3.5 A were used to determine the gel phase chain tilt angle for PSM, θ_{tilt} = 30.4, the area/chain perpendicular to the chains, A_C = 19.2 Å^2, and the area/lipid $A_L = 2A_C/\cos\theta_{tilt}$ following Tristram-Nagle et al.. (2002); Tristram-Nagle et al.. (1994).

Although data from oriented samples are more important, unoriented MLV samples are also informative. Figure 3.6 shows X-ray scattering from eSM MLVs. In the WAXS regime, a single sharper ring is observed below the transition temperature, indicating chain ordering, and this becomes broad at 50 °C, indicating chain melting. PC lipids have a single sharp WAXS ring in their ripple phase, whereas in their gel phase there are two separate WAXS rings, one sharp and one

broader, due to chain tilt. It is important to note that the single WAXS ring below T_m in Figure 3.6 does not prove, contrary to what is commonly assumed, that eSM is in a ripple phase. Separation of the two rings in PC lipids is just due to orthorhombic splitting of the hexagonal packing of the chains. A gel phase does not require such splitting, in which case one would also observe a single ring that would be misidentified with a ripple phase even though it is a gel phase.

Several peaks are observed in the LAXS regime in Figure 3.6, but these can be satisfactorily indexed as lamellar peaks with no obvious off-specular reflections that would indicate that the sample is in the ripple phase. To further illustrate the difficulty of verifying a ripple phase in unoriented samples, we have taken the oriented data in Figure 3.1 A and powder averaged it into isotropic rings (Figure 3.S16); this blurs the relatively weak but clearly separated off-specular peaks in Figure 3.1 A with the lamellar orders and gives intensity plots similar to the isotropic data in Figure 3.6 B.

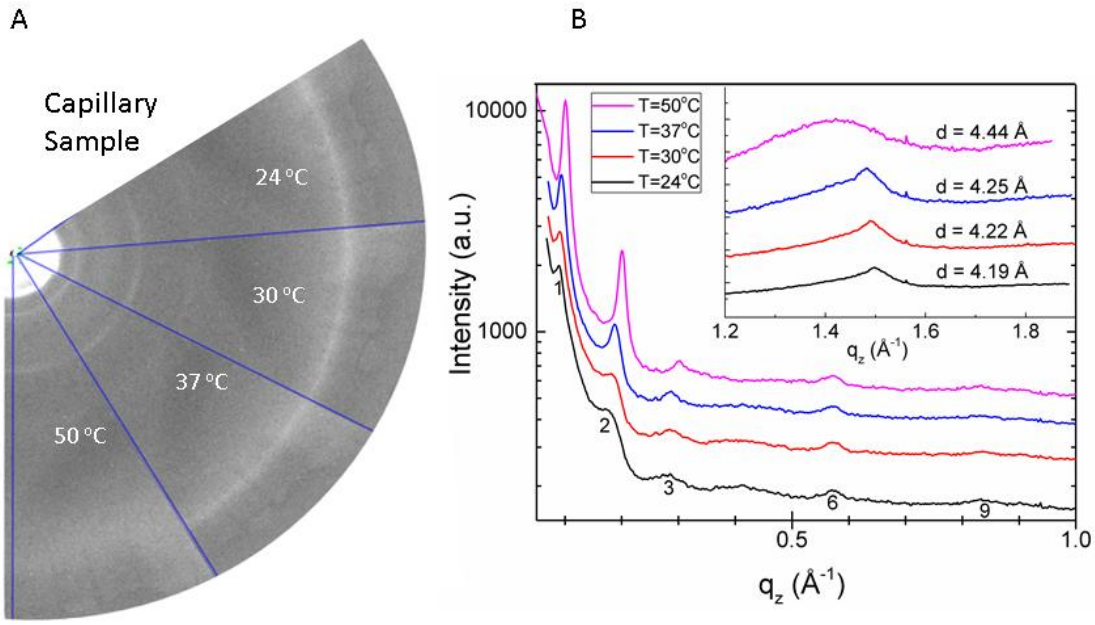

Figure 3.6. X-ray scattering data from eSM MLVs in a glass capillary collected on a 2D CCD detector at the temperatures indicated (A). The rings close to the beam (white center) are in the LAXS regime, while the single ring close to the edge of the pie sectors is in the WAXS regime. **Intensity plots of capillary data shown in A (B).** Small black numbers indicate lamellar orders, h= 1,2,3,6,9. Inset: zoomed WAXS region.

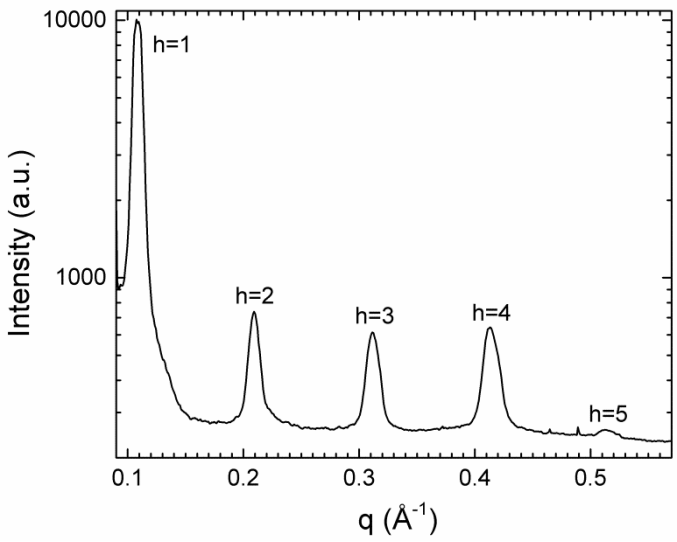

Figure 3.7. Powder average of LAXS data shown in Figure 1A, eSM at 3 °C. As shown, off-specular side peaks are difficult to distinguish from the background scattering between lamellar peaks (numbered). D-spacing is 60 Å.

There is one advantage of unoriented MLV samples, which are immersed in excess water and are therefore fully hydrated, over our oriented samples, which are hydrated from the vapor. While it is an advantage to be able to hydrate oriented samples to different D-spacings, it is time consuming to achieve the preferred full hydration. As shown previously, D-spacing is extremely sensitive to humidity close to 100% relative humidity (Chu *et al.*, 2005). Figure 3.7 compares the actual D-spacings of our oriented samples with those of the fully hydrated MLV samples. Although we did not achieve full hydration for all temperatures in the oriented samples, our experience has been that this amount of dehydration is small enough that the basic properties of fluid and gel phase bilayers are little changed. In Supplementary Material, it is shown how our capillary data compare to capillary D-spacings from the literature (Figures 3.S16).

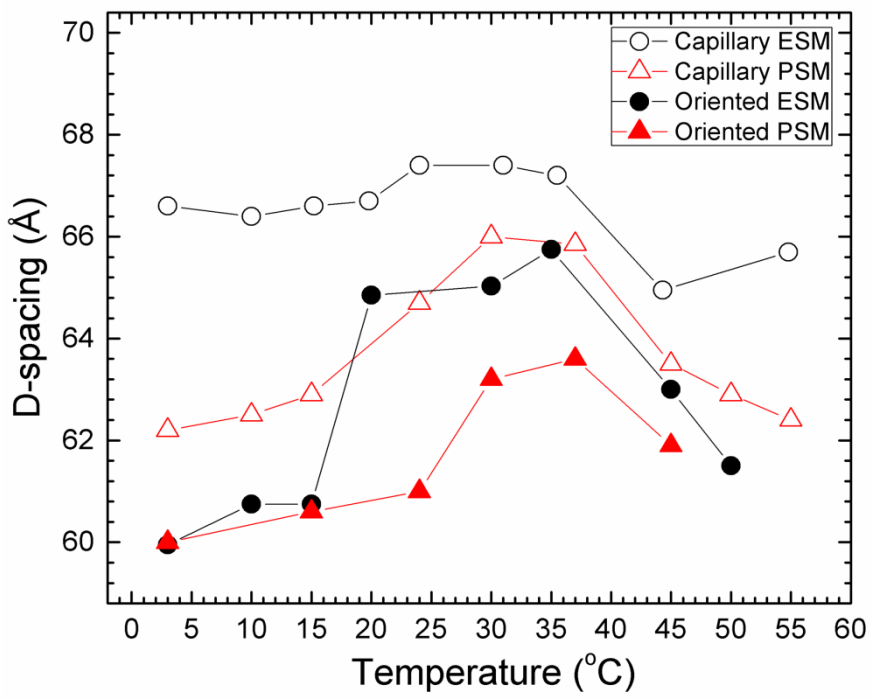

Figure 3.8. D-spacings of capillary and oriented samples as a function of temperature. Capillary eSM (open circles), oriented eSM (black circles), capillary pSM (open triangles), oriented pSM (red triangles).

However, relative humidity affects the values of the ripple phase unit cell parameters as is shown in Figure 3.8 for pSM. This impacts the temperature dependence of the raw data in Figure 3.4 because those values were affected by both temperature and relative humidity. Figure 3.8 shows how much the hydration level differed from full hydration in terms of the D-spacing for our sample at different temperatures. Figure 3.9 shows how much λ_r and γ change as a function of D-spacing at the same temperature. Combining these two sets of data allows us to estimate the effect of temperature alone, as is shown by the corrected values in Figure 3.4.

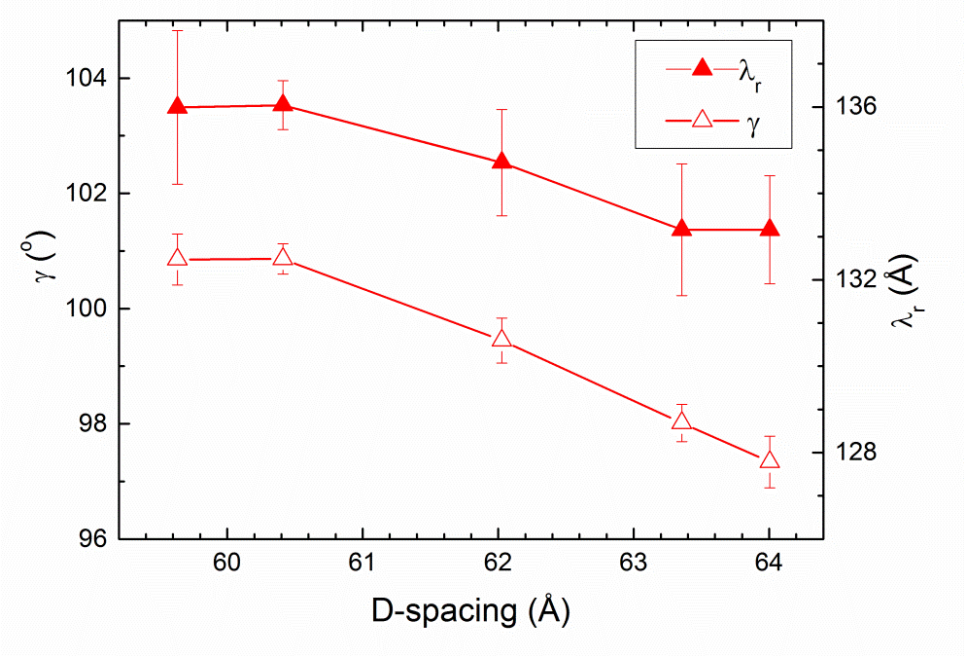

Figure 3.9. Effect of hydration level, as indicated by D-spacing, upon unit cell parameters λ_r (solid red triangles, right axis) and γ (open red triangles, left axis). Sample was pSM at 37 °C.

Density data yielded a molecular volume for eSM as shown in Figure 3.10 A. The main phase transition was centered at T_m=38.3 °C, but it was broad (~4 degrees) as expected for a mixture of chain lengths. No pretransition was observed for eSM. Similar density traces were obtained for pSM, but the absolute molecular volumes are not accurate because the amount of material was much smaller and was not quantitated precisely. The scan in Figure 3.10 B gave T_m = 40.7 °C for pSM with a smaller width of ~2 degrees, but no pretransition was visible. However, when the sample was held at 3 °C for 4.5 days, a pretransition was readily visible at T_p = 24.2 °C in Figure 3.10 C, which is a similar value to the DSC literature results for T_p shown in Table 3.S1.

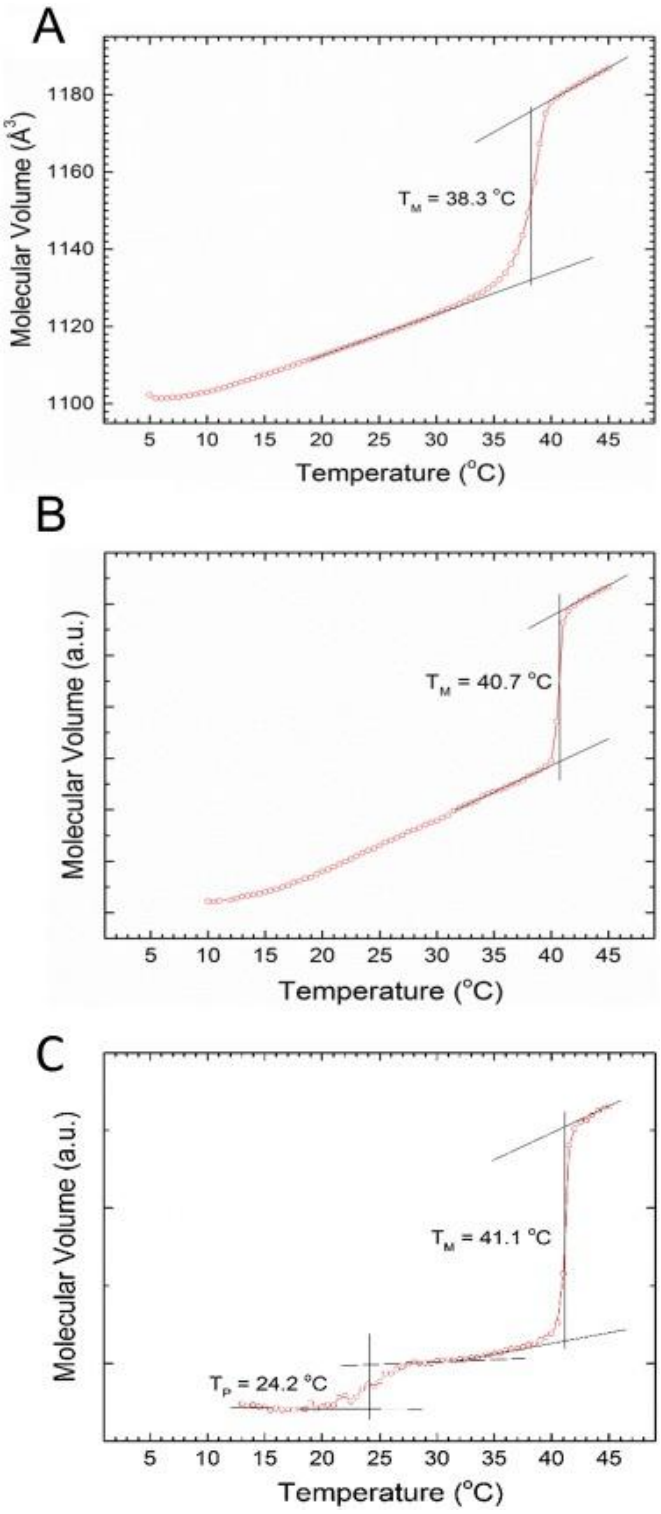

Figure 3.10. Densitometer scan of eSM immediately after cooling to 3 °C (A). Densitometer scan of pSM immediately after cooling to 3 °C (B). Densitometer scan of pSM after incubating the sample at 3 °C for 4-1/2 days (C). The T_m was determined as the midpoint of the straight line connecting the extensions of the upper and lower slopes. The heating rate was 12 °C/h.

For the fluid phase, measured volume data were used to construct electron density profiles (Figure 3.11) which were used to obtain A_L at 45 °C by fitting the

form factors (Figure 3.S17) that result from diffuse LAXS (Figures S8 and S15) to a model of the electron density of a bilayer (Scattering Density Profile program) (Kucerka *et al.*, 2008). One input into the SDP program is the headgroup volume with the volume ratio of the two headgroup components (phosphocholine and sphingosine linkage). To estimate these, we subtracted the hydrocarbon chain volume from the total lipid volume (see 3.4.6); the sphingosine linkage volume was obtained by subtracting the phosphocholine volume from the total headgroup volume (Armen *et al.*, 1998).

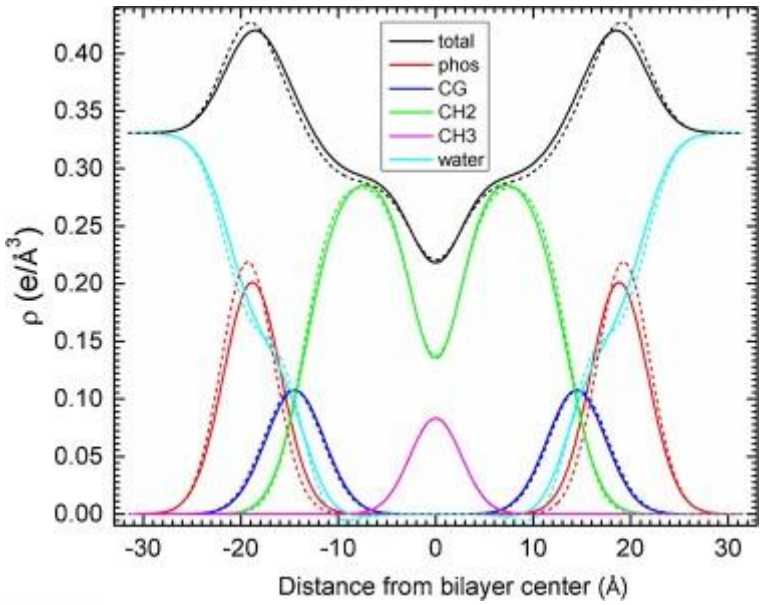

Figure 3.11. Electron density profiles of pSM (solid lines) and eSM (dashed lines) in the fluid phase at 45 °C. Bilayer components are: total (black), phosphocholine headgroup (red), glycerol backbone linkage (blue), CH2 groups (green), terminal CH3 groups (magenta) and water (cyan).

3.3.2 Characterization of eSM:eCer binary mixtures

Figure 3.12 shows the X-ray pattern obtained for the eSM:eCer (85:15) binary mixture. In contrast to the previous results, the sample is clearly in a gel phase bellow the SM main phase transition. This is confirmed by LAXS images, that show the absence of side peaks, and WAXS images, that confirm a tilted gel phase. This is further evidenced by a wide-angle reflection that is lifted up off the equator. Additional oriented eSM:eCer (85:15) data are shown in the supplementary material (Figures 3.S18-3.S24). These images are used to calculate the gel phase chain tilt angle θ_{tilt}=28.4º, the area/chain perpendicular to the chain, A_c=24.7 Å^2 and the area/lipid, A_L=56.1 Å^2 at 3 °C.

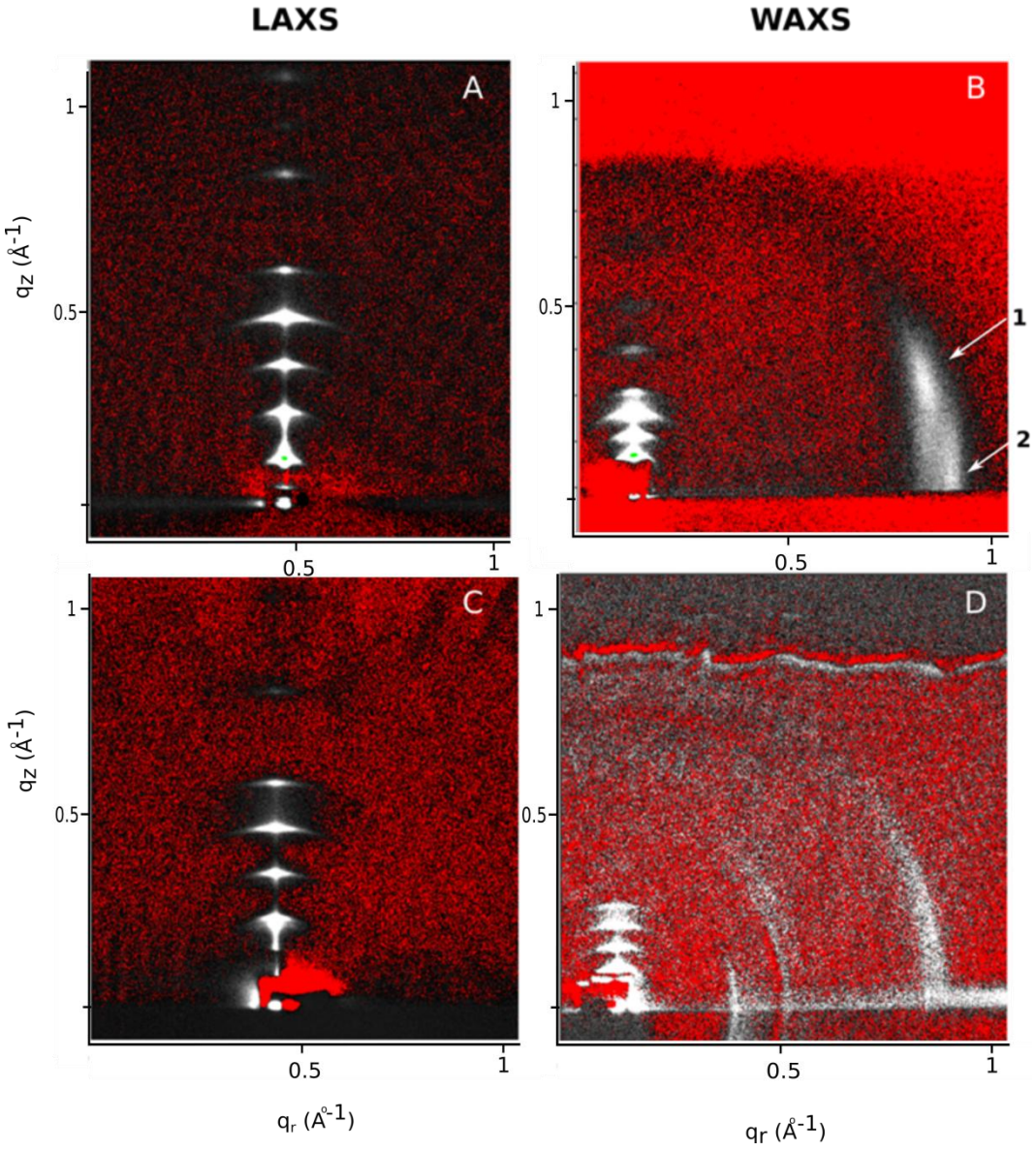

Figure 3.12. LAXS data from oriented eSM:eCer (85:15). LAXS image after equilibrating the sample for two days at 3 °C (A), WAXS image after equilibrating the sample for two days at 3 °C (B). LAXS image at 35 °C (C), WAXS image at 35 °C (D). White arrows point to the tilt of the gel phase, which is evidenced by a wide-angle reflection that is lifted up (1) off the equator (2). D-spacing in A,B. is 63.4 Å and in C,D. is 65.5 Å.

Figure 3.13 shows the X-ray data for eSM:eCer (70:30) binary mixture. An increase in egg ceramide concentration confirms the existence of a tilted gel phase instead of the ripple phase, which is maintained until the end of its main transition when it becomes fluid. However, the tilt angle is notably smaller than the one observed in eSM:eCer (85:15). Additional oriented eSM:eCer (70:30) data are shown in the supplementary material (Figures 3.S25-3.S31). These images are

used to calculate the gel phase chain tilt angle θ_{tilt}=10.1º, the area/chain perpendicular to the chain, A_c=25.5 Å^2 and the area/lipid, A_L=51.8 Å^2 at 3ºC.

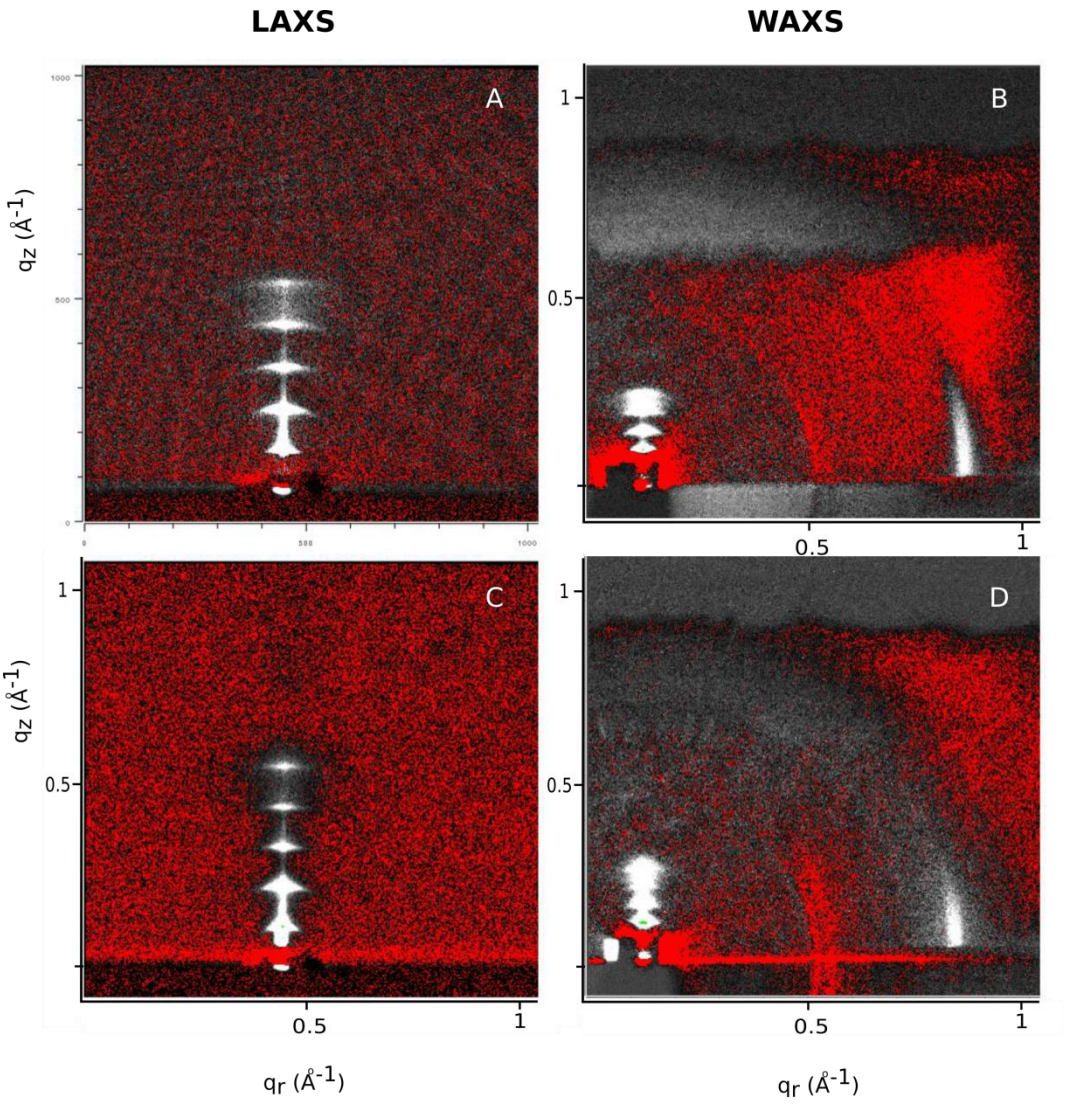

Figure 3.13. LAXS data from oriented eSM:eCer (70:30). LAXS image at 30 °C (A), WAXS image at 30 °C (B). LAXS image at 59 °C (C), WAXS image at 59 °C (D). D-spacing in A,B. is 67.2 Å and in C,D. is 68.9 Å.

Unoriented samples are analyzed to obtain D-spacing values for fully hydrated samples. Figure 3.14 compares the D-spacing of both, oriented and unoriented samples. As in the pSM and eSM experiments, D-spacing values for our oriented samples are lower than for the unoriented ones. The difference in eSM:eCer (85:15) is small enough to obtain valuable data except at 35 °C. However, unoriented eSM:eCer (70:30) shows two different D-spacing values from the

beginning of its main phase transition to its end. The existence of two D-spacing values can be related to the presence of two populations in the sample.

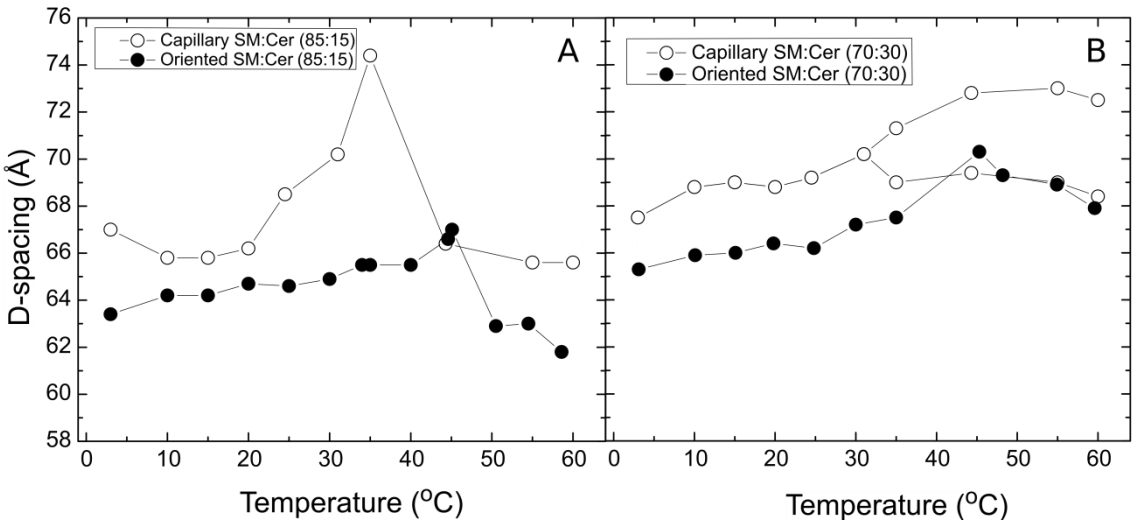

Figure 3.14. D-spacings of capillary and oriented samples as a function of temperature. eSM:eCer (85:15) (A), eSM:eCer (70:30) (B).

3.4 Discussion

3.4.1 Identification of phases

The most important result from this work is the difference in phase behavior between eSM and pSM at $T<T_m$. We clearly find that the ripple phase in eSM is the stable phase below the main transition at least down to 3 °C. Our result that there is no phase transition below the main transition at T_m agrees with many previous investigations that have reported only a single transition in eSM at 36-39.5 °C by differential scanning calorimetry (Calhoun & Shipley, 1979a; Chien & Huang, 1991; Filippov & Ora, 2006; García-Arribas *et al.*, 2016c; Jiménez-Rojo *et al.*, 2014; Mannock *et al.*, 2003; Mckeone *et al.*, 1986), scanning densitometry (Epand & Epand, 1980), fluorescence spectroscopy (Rujanavech *et al.*, 1986), ^{2}H-NMR spectroscopy (Steinbauer *et al.*, 2003) and FTIR spectroscopy (Anderle & Mendelsohn, 1986; Arsov & Quaroni, 2008; Veiga *et al.*, 2001). (Additional DSC literature results are summarized in Table 3.S1). However, in all of these studies, the transition at T_m was interpreted as a gel-to-fluid transition, whereas our results clearly identify the main transition as a ripple-to-fluid transition. Our result agrees with previous X-ray studies that have reported a ripple phase for eSM. The SAXS data of (Chemin *et al.*, 2008) showed weak (0,1) and (1,1) ripple reflections. Using X-ray diffraction, (Shaw *et al.*, 2012) found that the SAXS pattern below T_m in eSM showed a number of broad peaks which could not be resolved from each other.

These peaks fit within the same envelope as the ripple phase peaks of bovine brain sphingomyelin which they were able to resolve, so they concluded that eSM was also likely to be in a ripple phase below T_m. A third X-ray investigation reported that after prolonged equilibration at 20 °C, bilayers of eSM formed a ripple structure with a somewhat smaller periodicity of 125 Å that was obtained from the (0,1) in-plane reflection (Quinn & Wolf, 2009a). Based on this peak and on their WAXS results, the authors suggested that at 20 °C eSM showed a phase coexistence of a ripple phase with an interdigitated phase, but it appears that they misinterpreted the higher order ripple peaks. Unlike these previous X-ray works which studied isotropic MLV samples, our oriented samples much more clearly show a rippled phase that is stable from 35 down to 3 °C. This is because oriented samples have clear separations between lamellar and off-specular peaks (Hentschel & Rustichelli, 1991), that are easily measured using a two-dimensional digital CCD detector.

In contrast to eSM, in pSM the ripple phase is only stable down to about 24 ^{o}C and below that the stable phase is a flat gel phase. Previous structural studies (Calhoun & Shipley, 1979a; Maulik & Shipley, 1996) found no evidence for a ripple phase in pSM. Some calorimetric studies (Maulik & Shipley, 1996) did not observe a pre-transition in pSM and concluded that pSM is in the gel phase below T_m. Other calorimetric studies reported a pre-transition (Barenholz *et al.*, 1979; Calhoun & Shipley, 1979a), and those are consistent with our pSM structural results. It has been suggested that this difference in results may be due to the synthesis of pSM resulting in a fraction being in the L-threo form instead of the D-erythro form (Ramstedt & Slotte, 1999; Venable *et al.*, 2014). In any case, we believe that we have now established the pSM phase behavior and that it differs from eSM.

What could be the origin of the stability of the ripple phase in eSM? Recall that the fatty acid composition of Avanti Polar Lipid eSM is 86% 16:0, 6% 18:0, 3% 22:0, 3% 24:0 and 2% unknown. We suggest that it is the presence of a small percentage of longer chain length lipids (18, 22 and 24 carbons) that stabilize the ripple phase in eSM, perhaps by locating in the major arm (M), since the major arm has been shown to be thicker than the minor arm (m), at least in DMPC (Akabori & Nagle, 2015; Sun *et al.*, 1996a). Adding longer chain lipids to the M arm would then increase the disparity between the M and m arms, which would have the tendency to stabilize the ripple phase in eSM to lower temperature. Future experiments on well-defined mixtures could test this suggestion.

3.4.2 Ripple phase wavelength λ_r

The temperature change is the primary modulator of the ripple structure in our study. As shown in Figure 3.4 A for eSM, the ripple wavelength λ_r decreases from ~170 to 145 Å over a 32 degree increase. This result is in the same direction, but not as dramatic, as that observed using X-ray diffraction for DMPC, where the ripple repeat decreased from 135 to 120 Å when the temperature increased from 15.2 to 20 ^{o}C (Matuoka *et al.*, 1994).

3.4.3 Ripple phase γ angle

Hydration is the primary modulator of the stacking angle γ which is an indicator of the asymmetry of ripples (Lubensky & Mackintosh, 1993). Asymmetric ripples are defined by the length of the M arm being different from the length of the m arm. Then, interbilayer interactions establish different thickness of the water layers between adjacent bilayers and the stacking of adjacent unit cells may be shifted along the x axis as well as along the z axis, thereby resulting in a value of γ not necessarily equal to 90°. In contrast, if the ripples were symmetric, γ would necessarily be 90°. In *l*-DPPC and *dl*-DPPC (Katsaras *et al.*, 2000) and in DMPC by (Wack & Webb, 1989) γ decreases as a function of increasing D-spacing. In *l*-DPPC, γ decreased from ~98^{o} at 64 Å to ~90° at 68 Å, and then decreased further to 85° at 73 Å lamellar D-spacing (Katsaras *et al.*, 2000). In eSM, we find that γ > 90^{o} at our largest D-spacings close to T_m, although these D-spacings are not as large as those for *l*-DPPC. In pSM γ decreases from 101 to 98° at lamellar D from 59.5 to 64 Å (Figure 3.8). For the same level of hydration, Fig. 4B indicates little effect of temperature on γ.

3.4.4 Gel and fluid phase properties

Results for pSM and eSM in the fluid phase are summarized in Table 3.1, including bending modulus K_C and the order parameter S_{xray} (Mills *et al.*, 2008) in the fluid phase, area/lipid A_L, and bilayer thickness ($D_B = V_L/A_L$) and tilt angle in the gel phase. As shown, there was little difference in fluid phase structure between eSM and pSM, although pSM was stiffer than eSM and somewhat more ordered as determined by S_{xray}. Literature results for DPPC are shown for comparison. Except for the considerably smaller value of S_{xray}, which agrees with NMR $<S_{CD}>$ result of Mehnert et al.. (2006), differences are small. Further comparison of these results with X-ray and NMR studies from the literature can be found in Tables 3.S2 and 3.S3.

Results for the gel phase of pSM are also compared in Table 3.1 to results for DPPC extrapolated to 3 °C. Not shown in Table 3.1 are values for the area/chain A_C perpendicular to the chains. That value is 19.2±0.2 Å^2 for pSM and for DPPC it is 19.5±0.2 Å^2 (Sun *et al.*, 1996b). This indicates a slightly tighter packing of pSM than DPPC. The other primary difference is the smaller tilt angle in pSM. Those two differences make a noticeable difference in the area/lipid through the relation $A_L = 2A_C/\cos\theta_{tilt}$.

Table 3.1. Elastic and structural results for gel and fluid phases

Sample	K_C x10^{-20} (J)$^+$	S_{xray}	A_L (Å^2)	Tilt Angle (^{o})	D_B (Å)
pSM (fluid, 45^{o}C)	8.3 ± 0.1	0.54 ± 0.02	64 ± 2	---	36.6 ± 1.2
eSM (fluid, 45^{o}C)	6.7 ± 0.4	0.48 ± 0.02	64 ± 2	---	37.1 ± 1.2
DPPC (fluid, 50^{o}C)*	6.7 ± 0.7	0.41 ± 0.03	64 ± 1* 63 ± 1**	---	38.5 ± 0.5* 39 ± 0.5**
pSM (gel, 3^{o}C)	---	---	44.5 ± 0.5	30.4 ± 0.6	49.4 ± 0.3
DPPC (gel, 3^{o}C)***	---	---	47.0 ± 0.3	34.0 ± 0.4	48.0 ± 0.2

$^+$ Results without including a tilt degree of freedom (Nagle, 2017)
*(Guler et al.., 2009) , **(Kucerka et al.., 2008), ***(Sun et al.., 1996a)

3.4.5 Contact with MD simulations

Simulations are very poor for ripple phases and even problematic for gel phases. One point of contact we can make presently is with our obtained volume of 1187± 1 Å^3 at 45 °C for eSM in the fluid phase. To compare to simulations of pSM at 50^{o}C, using (Nagle & Wilkinson, 1978) we added 6 Å^3 for thermal expansion and subtracted 27 Å^3 per extra methylene in the longer chains in the eSM mixture to obtain 1178 Å^3. Lipid volumes from GROMACS MD simulations of pSM at 50 °C yielded 1168 ± 12 Å^3 (Metcalf & Pandit, 2012) and 1180 ± 10 Å^3 (Niemela *et al.*, 2004). Another point of contact is our A_L of 64 Å^2 for both eSM and pSM. Our area in Table 3.1 is significantly larger than the average 54 ± 3 Å^2 obtained in several MD simulations, (Venable et al.. 2014 and references therein), which suggests that the SM force fields might have to be re-evaluated.

3.4.6 General comment

Our results address the question of whether the less expensive eSM mixture is likely to be a suitable replacement for the more specific pSM lipid in bilayer studies that assume that eSM is a single component or when comparing simulations that use pSM to compare to experimental data obtained from eSM. Our result that the lipid areas are essentially the same is encouraging that such replacements can be used in the fluid phase, which is where simulations are most reliable. However, for phase behavior, our results show different propensities to form ripple versus gel phases. While ripple phases are unlikely to form in ternary mixtures, the different propensity to form them shows that pSM and eSM have different interactions that could affect the stability of liquid ordered phases in lipid raft mixtures, depending on which lipid is used. However, this difference in interactions that could play a role in ternary mixtures for which the interaction of sphingomyelin with cholesterol induces the liquid ordered phase. However, this difference occurs only for temperatures substantially below the main transition temperature, which is itself different by a few degrees between eSM and pSM. Probably, these differences would only be significant for the most careful studies of phase behavior.

3.4.7 Identification of ceramide domains

The interaction of eCer with eSM is investigated using two binary mixtures at different ceramide proportions. In agreement with the calorimetry results of eSM:eCer (Sot *et al.*, 2006), when 15 mol% eCer is added a complex main phase transition is observed, that includes components associated to the melting of pure eSM domains. However, when eCer is saturating the system (30 mol% Cer), pure eSM lamellar phase transition is no longer observed so that a full mixing of both lipids can be inferred. These phase transitions can be followed using X-ray scattering with the same results: a single phase transition is observed.

The addition of ceramide produces a change in the ripple phase of eSM below the transition since both samples present a tilted gel phase, the tilt angle being smaller at higher ceramide concentrations. The effects of ceramide can be studied using gel phase data as the area/chain perpendicular to the chain (A_c) and the area per lipid (A_L). These data indicate a higher packing for the sample with 30 mol% of ceramide due to its higher A_c and its smaller value of A_L, which can be confirmed by previous atomic force microscopy results of pSM:pCer binary mixtures in which the presence of ceramide increases the force needed to pierce the bilayer (Garcia-Arribas *et al.*, 2015).

Despite structural data confirming the presence of ceramide in the sample, a double D-spacing, associated to the formation of ceramide domains could only be observed for eSM:eCer (70:30) mixtures. X-ray scattering seems to require a high concentration of ceramide to detect the formation of highly ordered ceramide domains as compared to other techniques like electron microscopy and atomic force microscopy (Sot *et al.*, 2006; Busto *et al.*, 2009).

3.5 Supplementary data

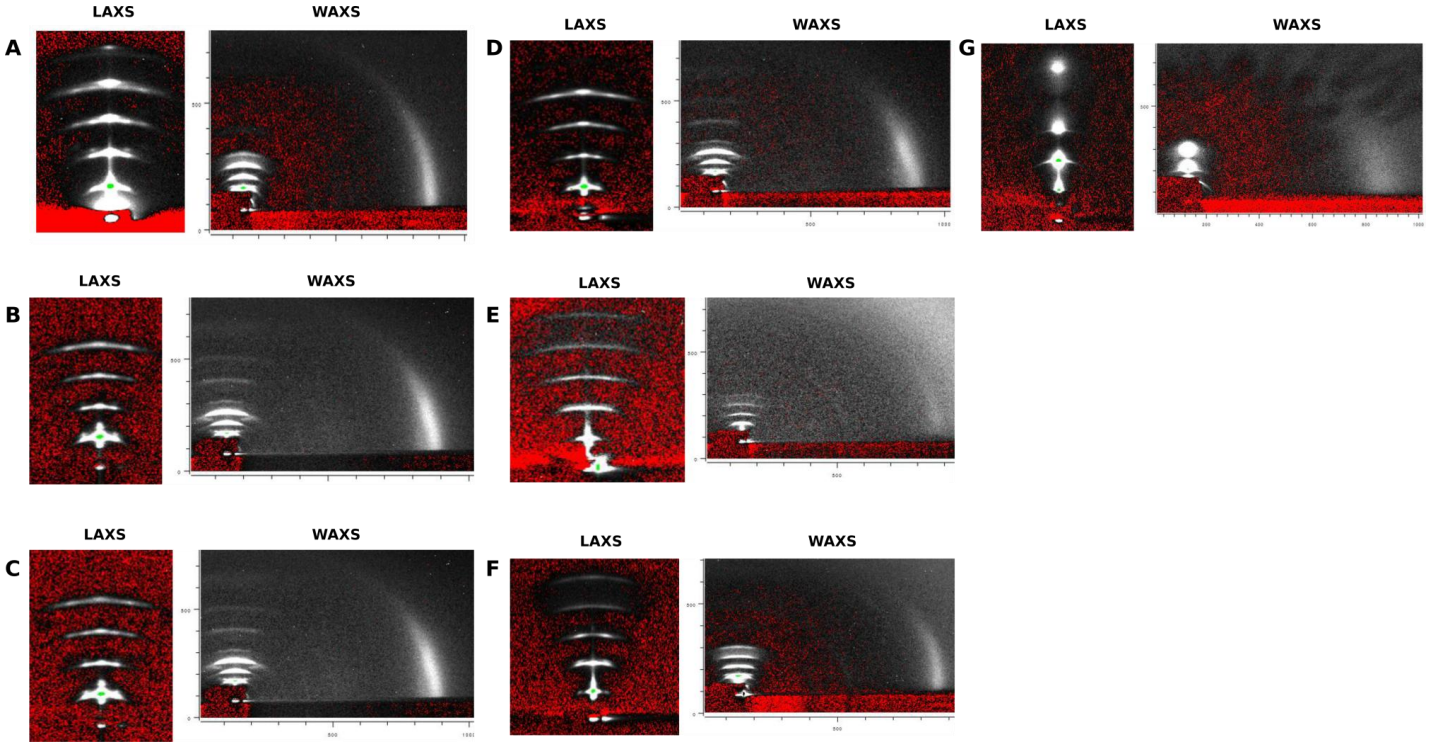

Figure 3.S1. 2D CCD X-ray scattering data from oriented, hydrated eSM collected at the following temperatures: Ripple phase. 20 °C, after annealing at 60 °C for 2 hours (A), 15 °C, upon cooling from 20 °C (B), 10 °C, upon cooling from 15 ^{o}C (C), 3 °C, upon cooling from 10 ^{o}C (D), 30 ^{o}C, upon heating from 3 °C (E), 35 °C, upon heating from 30 °C (F), Fluid phase. 45 °C, after annealing at 60 °C for 2 hours (G). Red pixels indicate negative intensity after background subtraction.

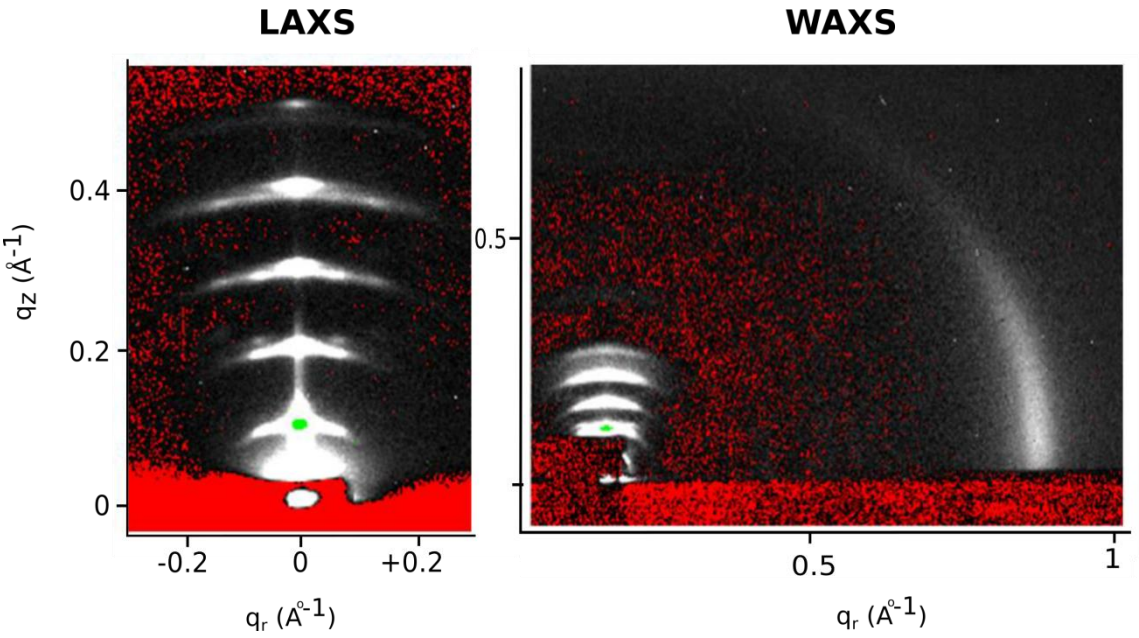

Figure 3.S2. Oriented eSM at 20 °C in the ripple phase, collected after annealing at 60 °C for 2 hours. D-spacing is 64.9 ± 0.9 Å.

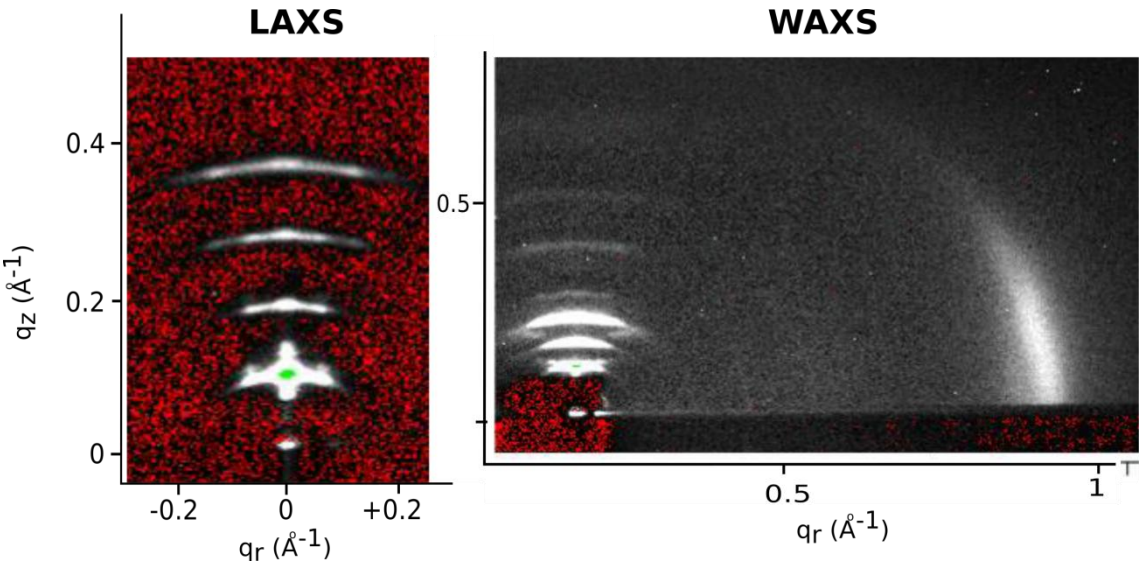

Figure 3.S3. Oriented eSM at 15 °C in the ripple phase, collected after cooling from 20 °C. D-spacing is 60.8 ± 0.8 Å.

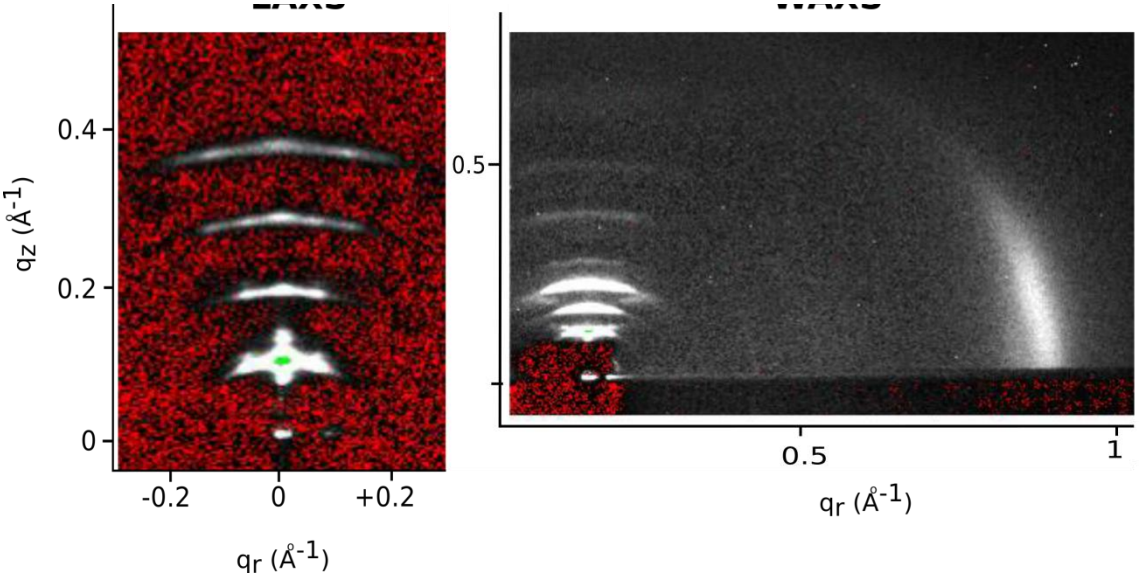

Figure 3.S4. Oriented egg SM at 10 °C in the ripple phase, collected after cooling from 15 °C. D-spacing is 60.8 ± 0.8 Å.

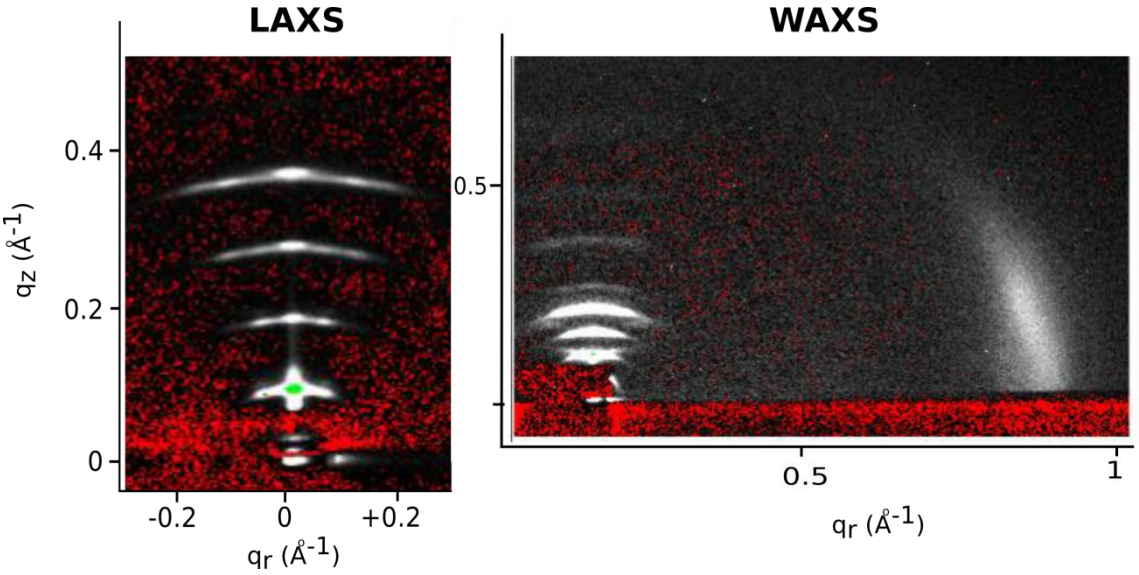

Figure 3.S5. Oriented eSM at 3 °C in the ripple phase, collected after cooling from 10 °C. D-spacing is 60 ± 0.2 Å.

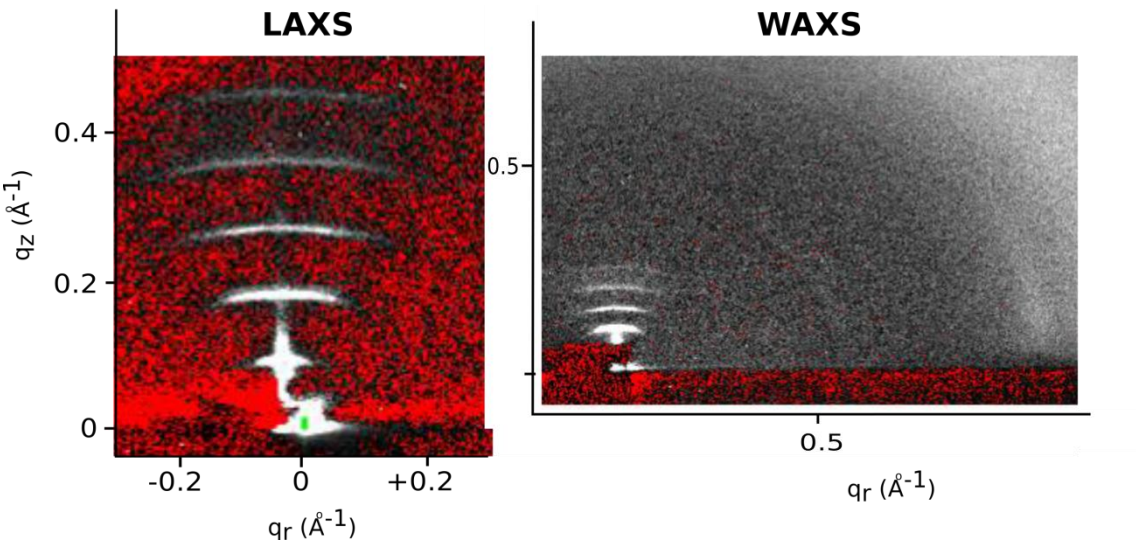

Figure 3.S6. Oriented eSM at 30 °C in the ripple phase, collected after heating from 3 °C. D-spacing is 65 Å. The light, diffuse scattering in the upper right hand corner of the WAXS image is due to excess water on the sample.

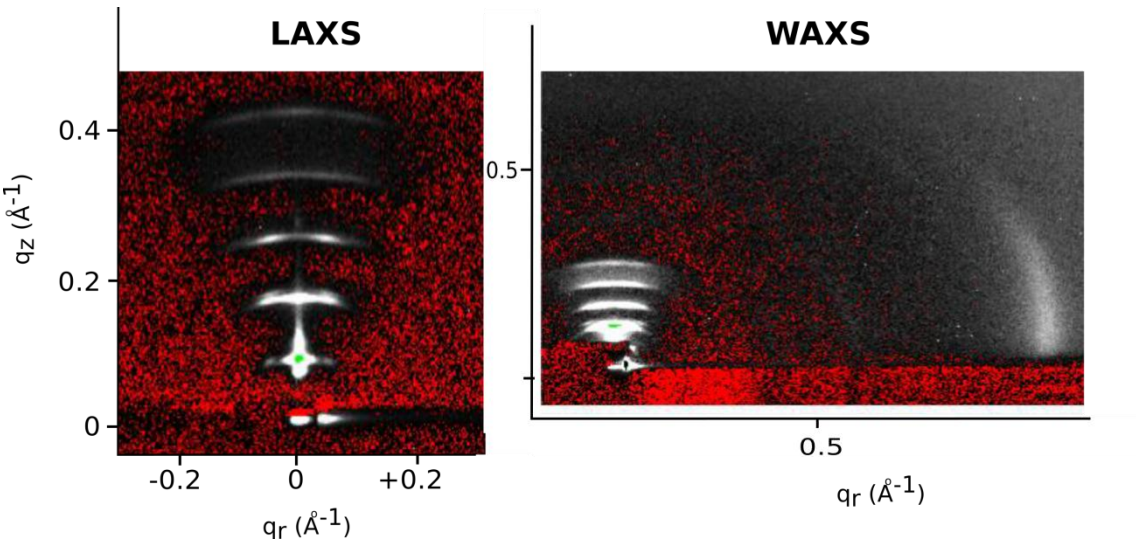

Figure 3.S7. Oriented eSM at 35 °C in the ripple phase, collected after heating from 30 °C. D-spacing is 65.8 ± 1.2 Å.

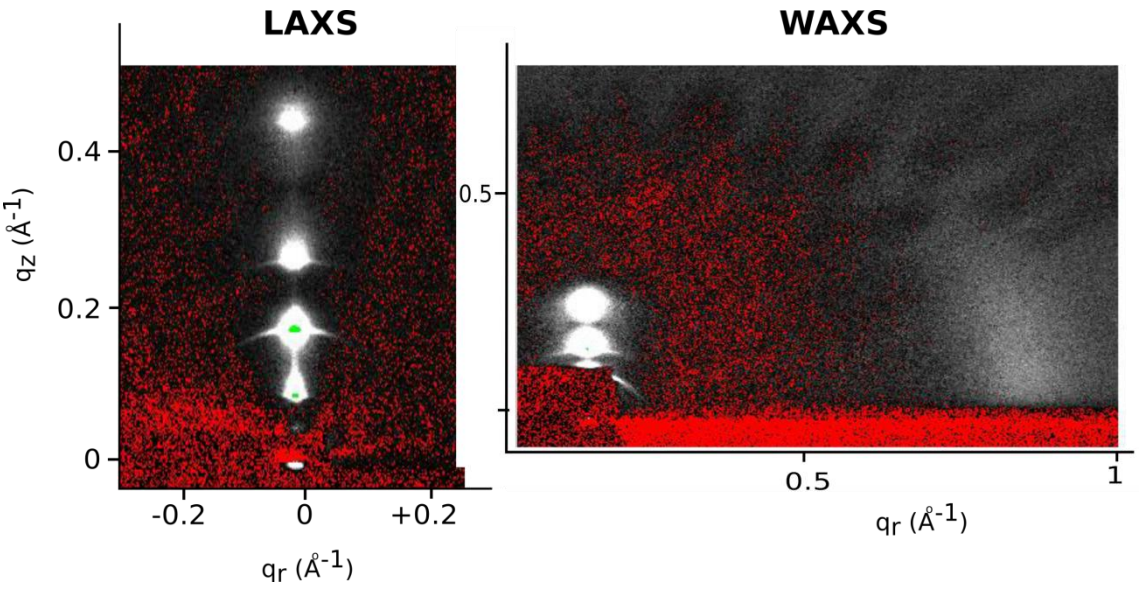

Figure 3.S8. Oriented eSM at 45 °C in the fluid phase, collected after annealing at 60 °C for 2 hours. At 45 °C, SPM is in the fluid phase, as evidenced by the absence of ripple reflections in LAXS and broad, diffuse scattering in WAXS. D-spacing is 62.7 ± 1.1 Å.

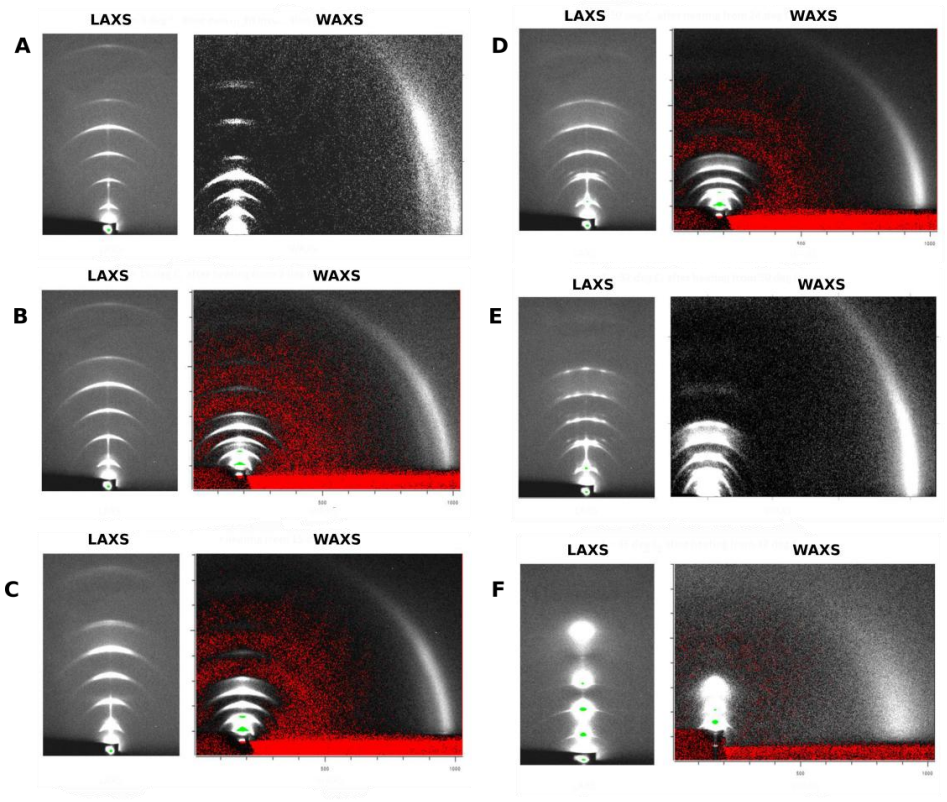

Figure 3.S9. 2D CCD X-ray scattering data from oriented, hydrated pSM collected at the following temperatures: Gel phase: 3 °C, upon cooling from 37 °C and equilibrating overnight at 3 °C (A), 15 °C, upon heating from 3 °C (B), 24 °C, upon heating from 15 °C (C), Ripple phase: 30 °C, upon heating from 24 °C (D), 37 °C, upon heating from 24 °C (E), Fluid phase: 45 °C, upon heating from 37 °C (F).

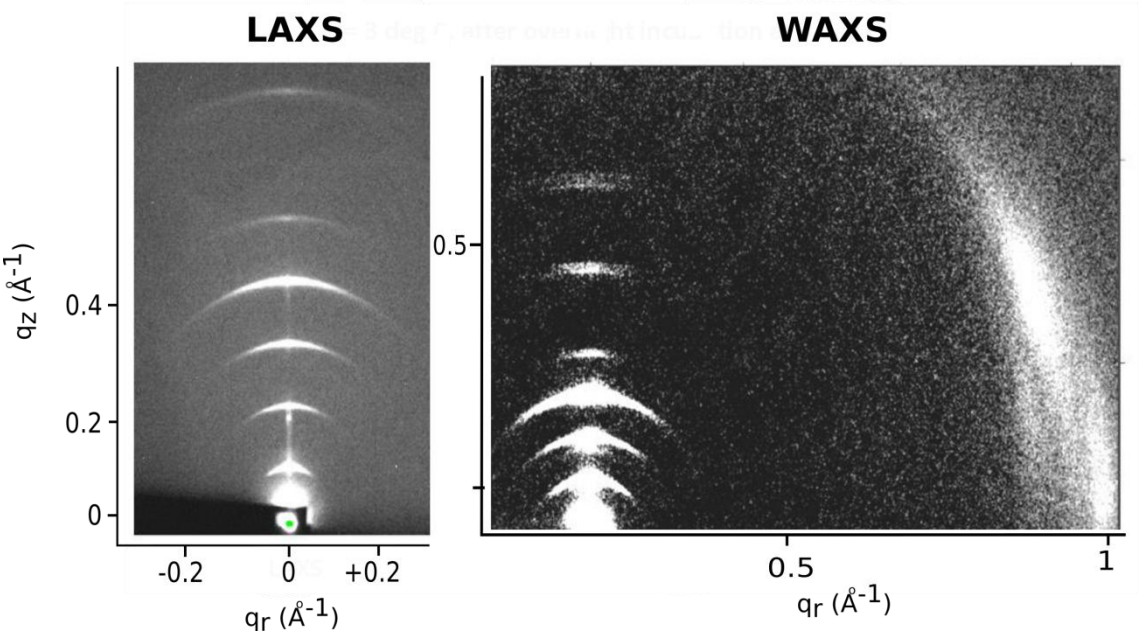

Figure 3.S10. Oriented pSM at 3 °C in the gel phase, collected after cooling from 37 °C and equilibrating overnight at 3 °C. D-spacing is 60 ± 0.2 Å.

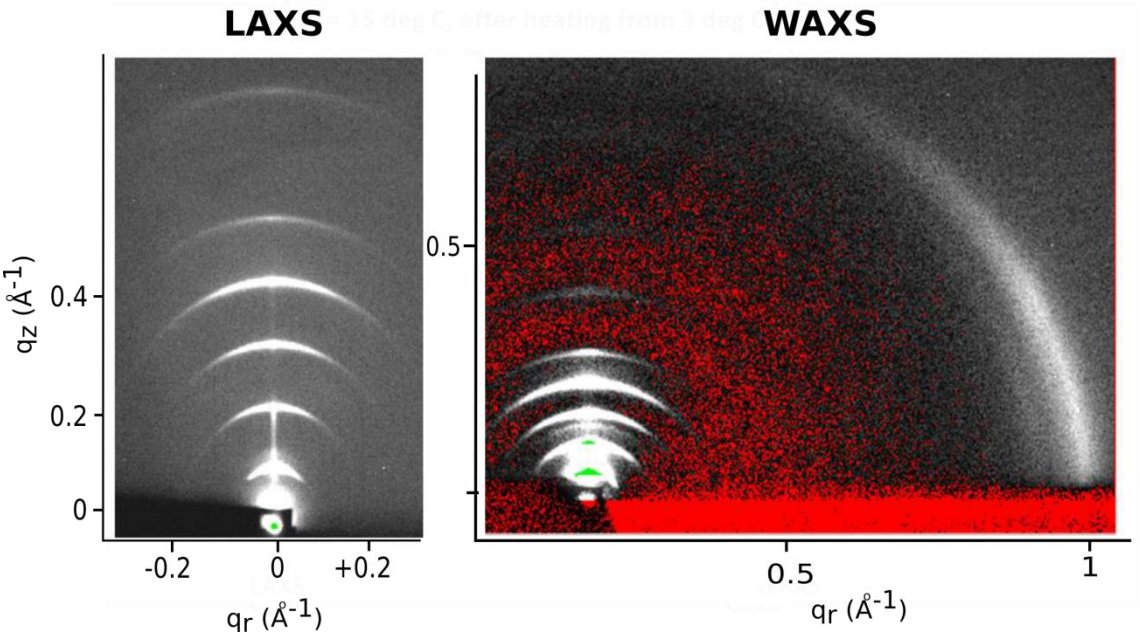

Figure 3.S11. Oriented pSM at 15 °C in the gel phase, collected after heating from 3 °C. D-spacing is 60.6 ± 0.3 Å.

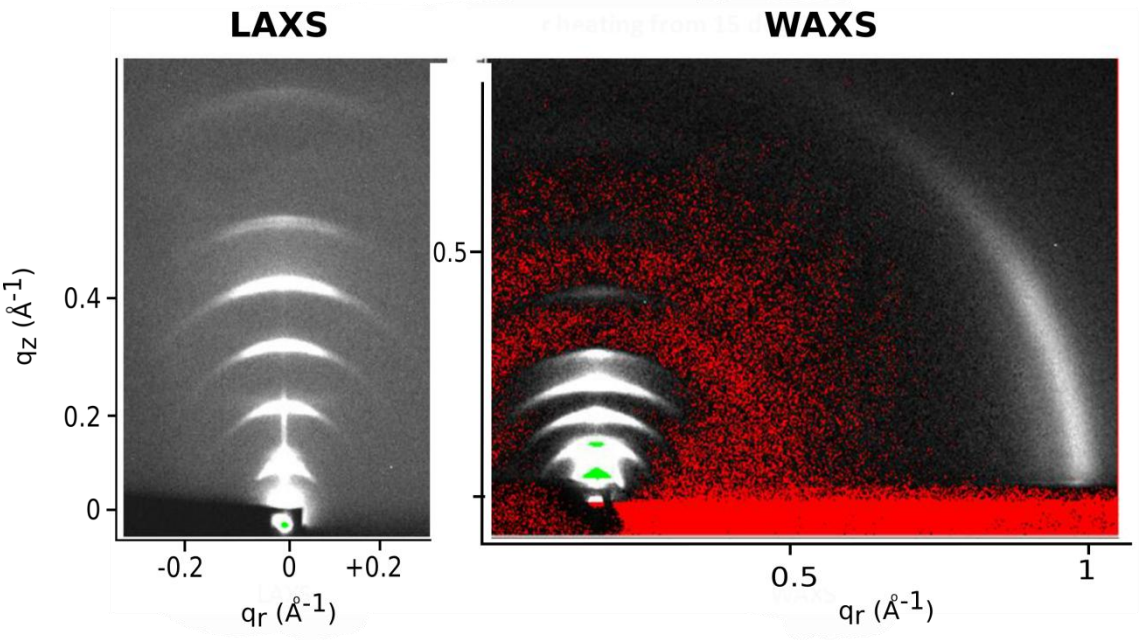

Figure 3.S12. Oriented pSM at 24 °C gel phase with incipient ripple phase, collected after heating from 15 °C. D-spacing is 61 ± 0.3 Å.

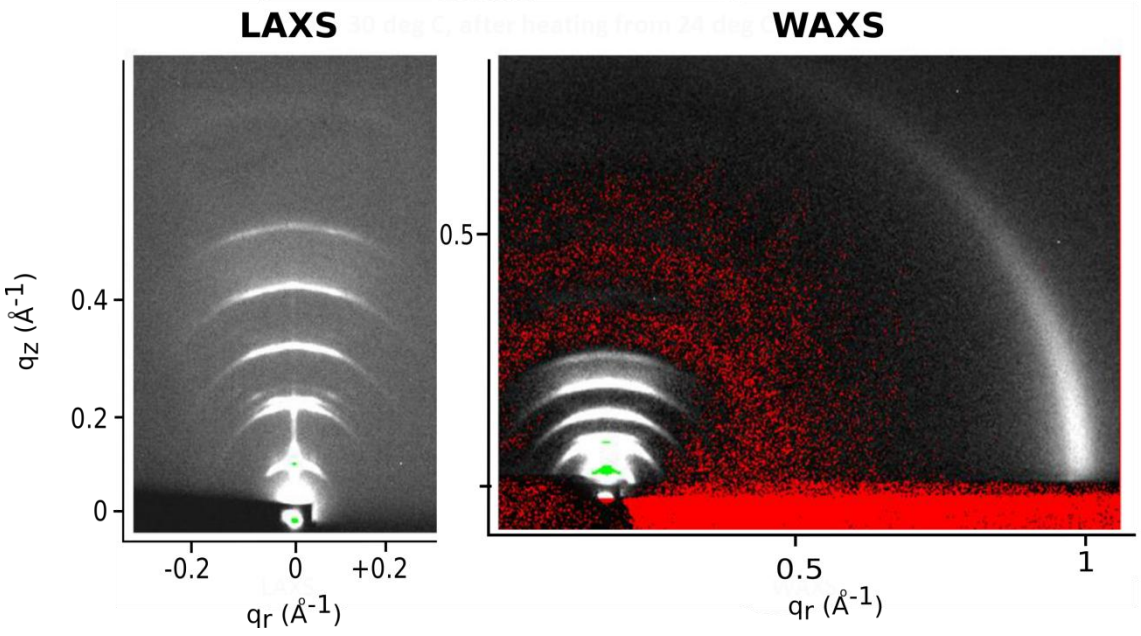

Figure 3.S13. Oriented pSM at 30 °C in the ripple phase, collected after heating from 24 °C. D-spacing is 63.2 ± 0.2 Å.

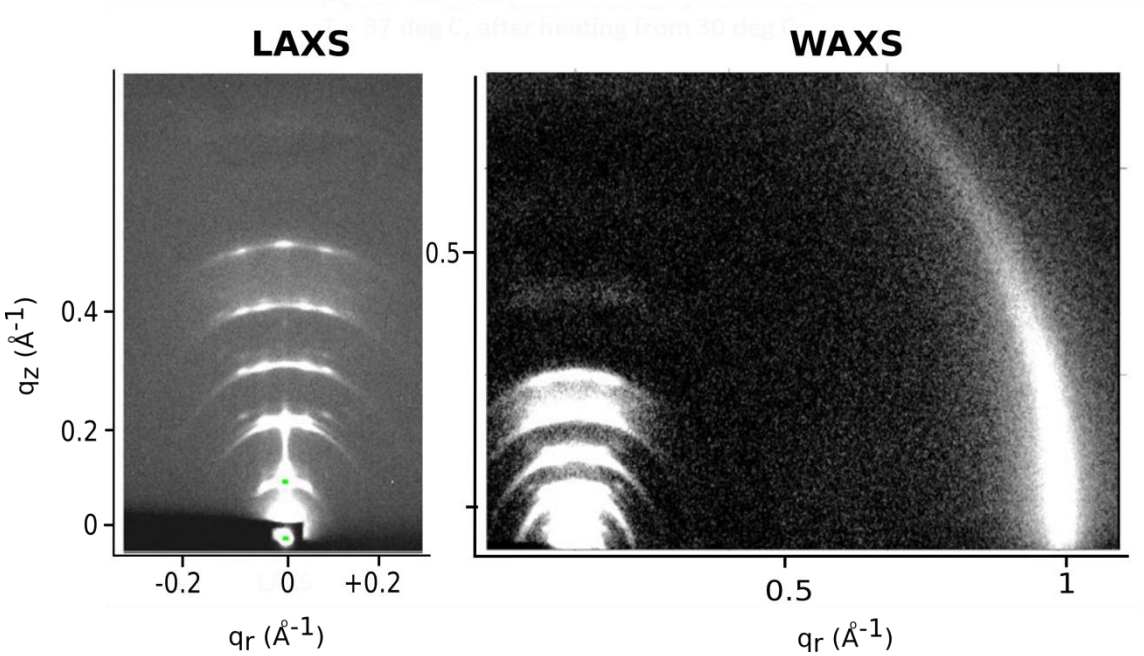

Figure 3.S14. Oriented pSM at 37 °C in the ripple phase, collected after heating from 30 °C. D-spacing is 63.6 ± 0.8 Å.

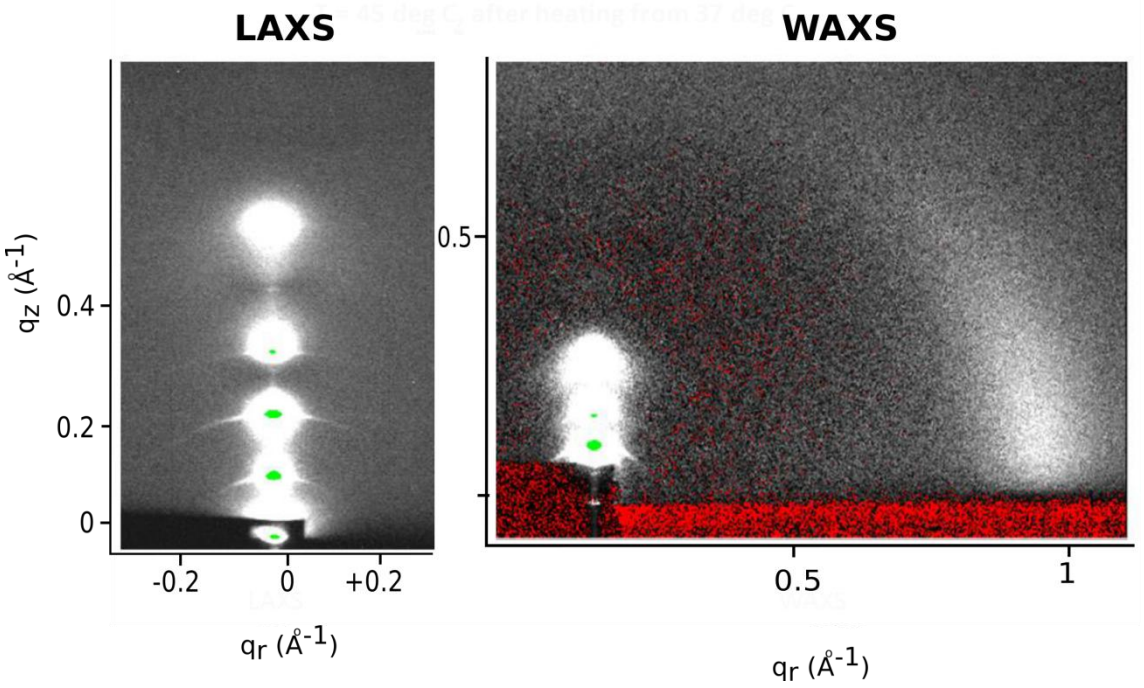

Figure 3.S15. Oriented PSM at 45 °C in the fluid phase, collected after heating from 37 °C. D-spacing is 61.9 ± 0.2 Å.

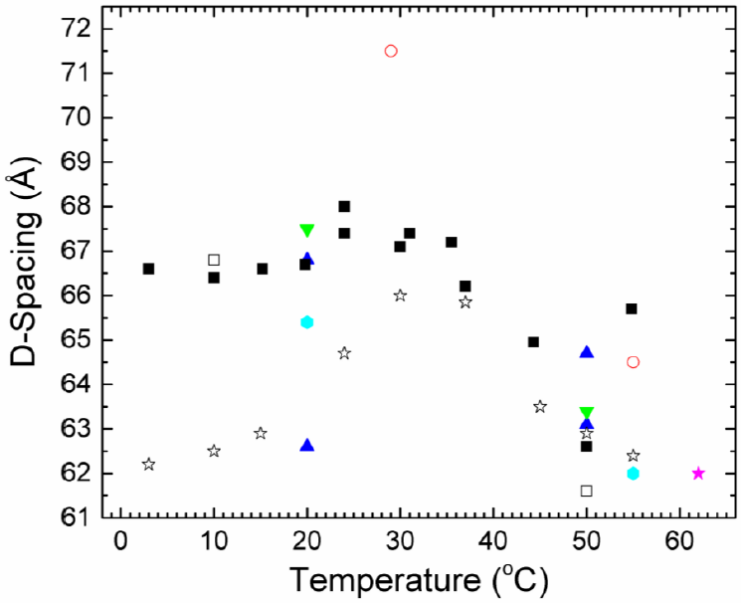

Figure 3.S16. Capillary D-spacings from literature: pSM, open black squares (Calhoun and Shipley, 1979a), open red circles (Maulik and Shipley, 1996), open black stars (ThisWork, 2018); ESM, solid green inverted triangles (Chachaty et al.., 2005), solid blue triangles (Quinn and Wolf, 2009), solid cyan hexagons (Chemin et al.., 2008), solid magenta star (Shaw et al.., 2012), solid black squares (ThisWork, 2018).

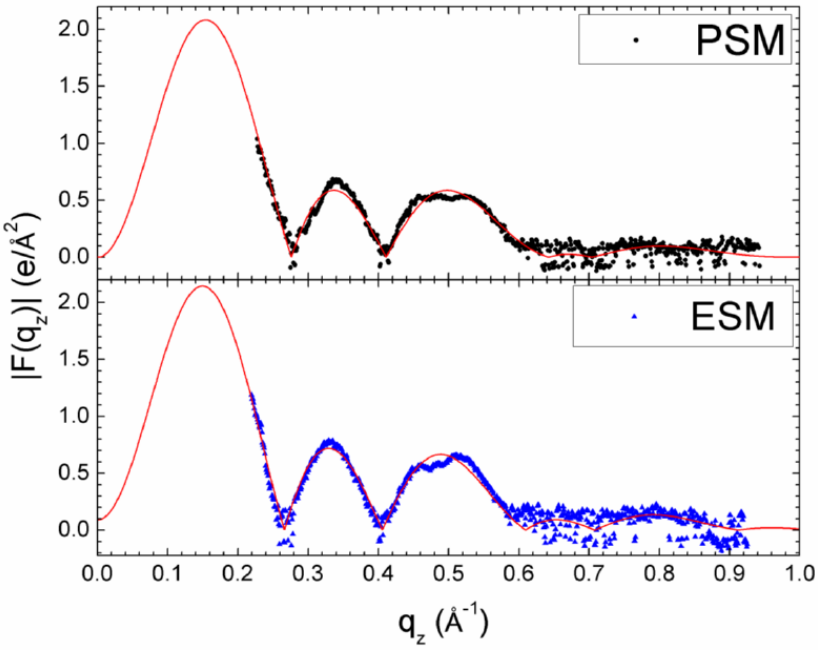

Figure 3.S17. Form factor data obtained from x-ray diffuse scattering used to obtain the EDPs shown in Fig. 11 in the main chapter.

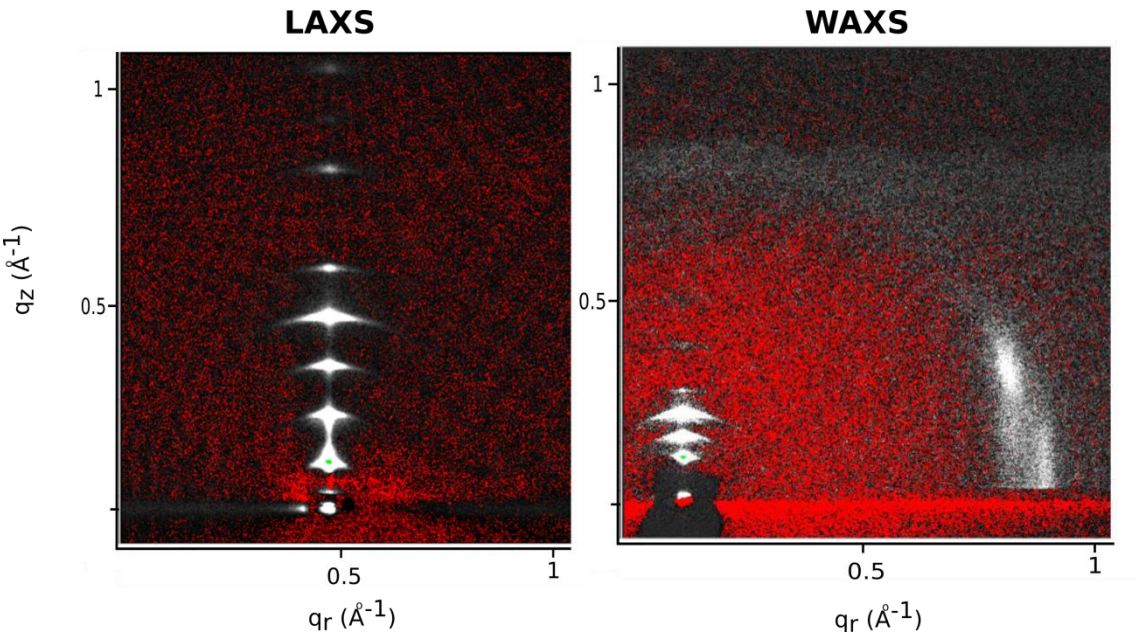

Figure 3.S18. Oriented eSM:eCer (85:15) at 3 °C in a tilted gel phase after holding for 2 days at 3 °C. D-spacing is 63.4 Å.

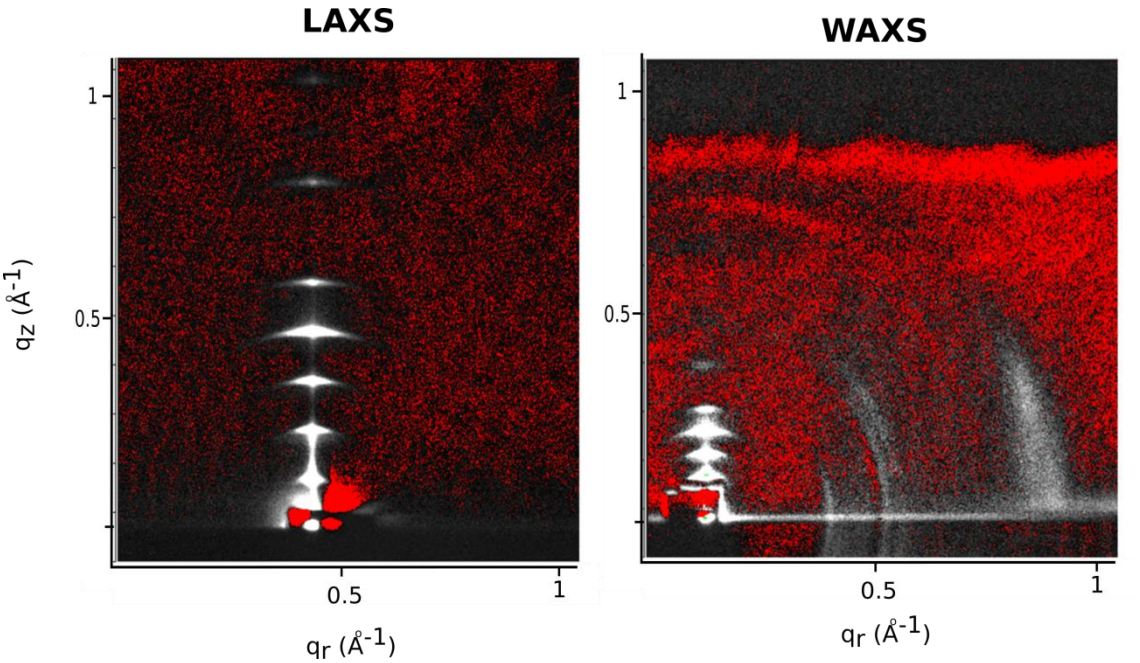

Figure 3.S19. Oriented eSM:eCer (85:15) at 10 °C in a tilted gel phase, collected after heating from 3 °C. D-spacing is 64.2 Å.

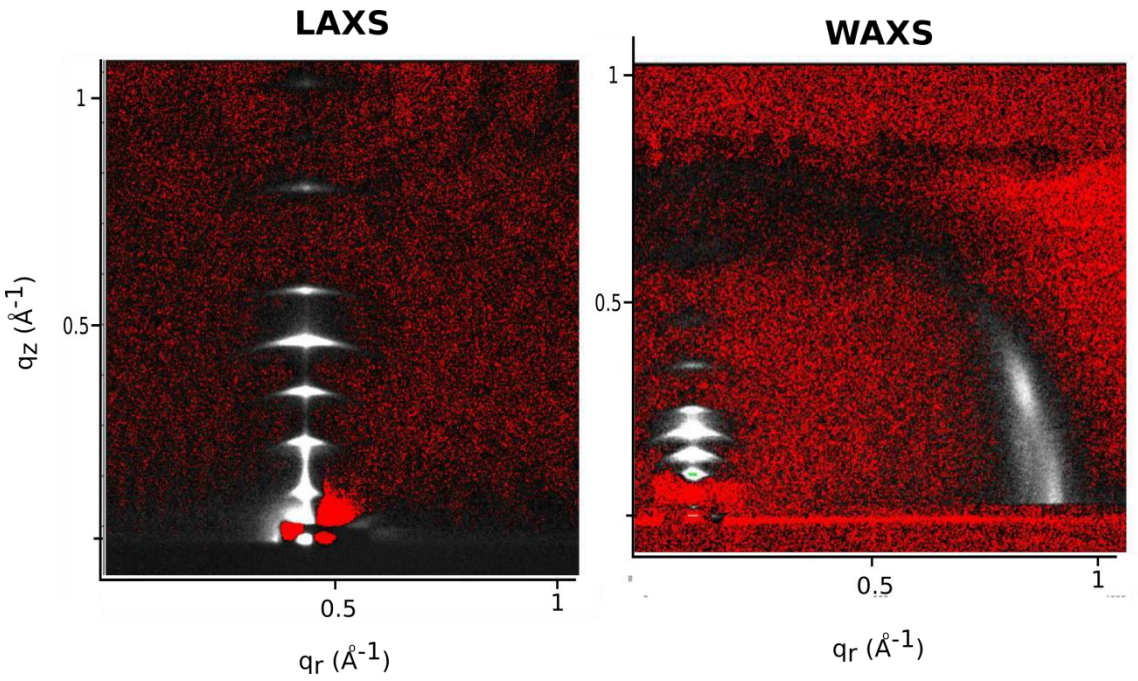

Figure 3.S20. Oriented eSM:eCer (85:15) at 15 °C in a tilted gel phase, collected after heating from 10 °C. D-spacing is 62.2 Å.

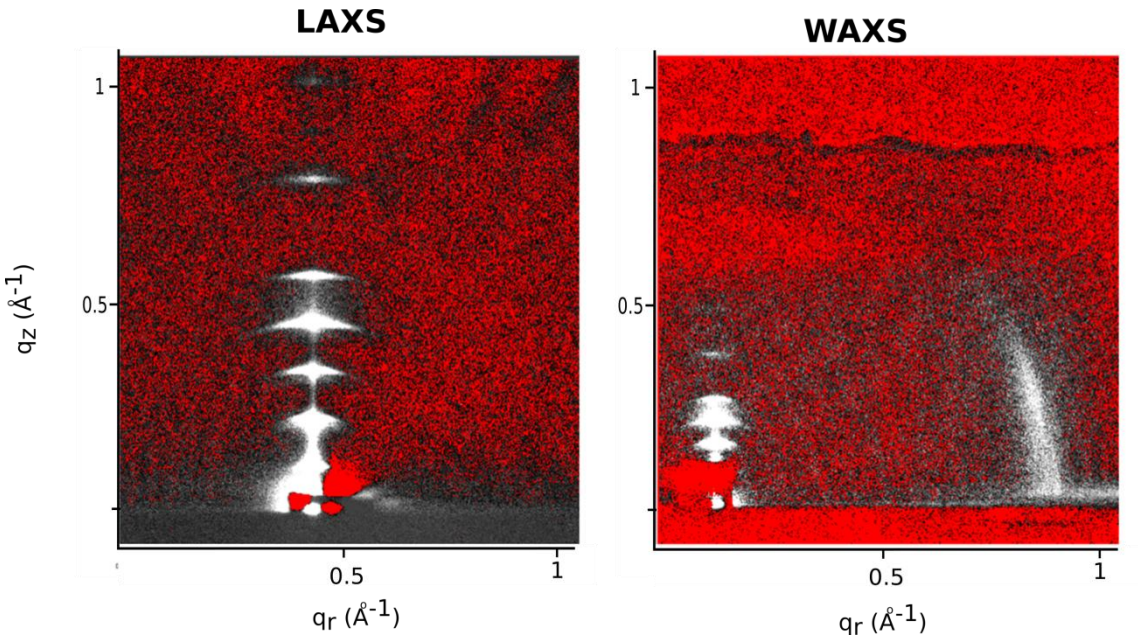

Figure 3.S21. Oriented eSM:eCer (85:15) at 20 °C in a tilted gel phase, collected after heating from 15 °C. D-spacing is 64.7 ± 0.2 Å.

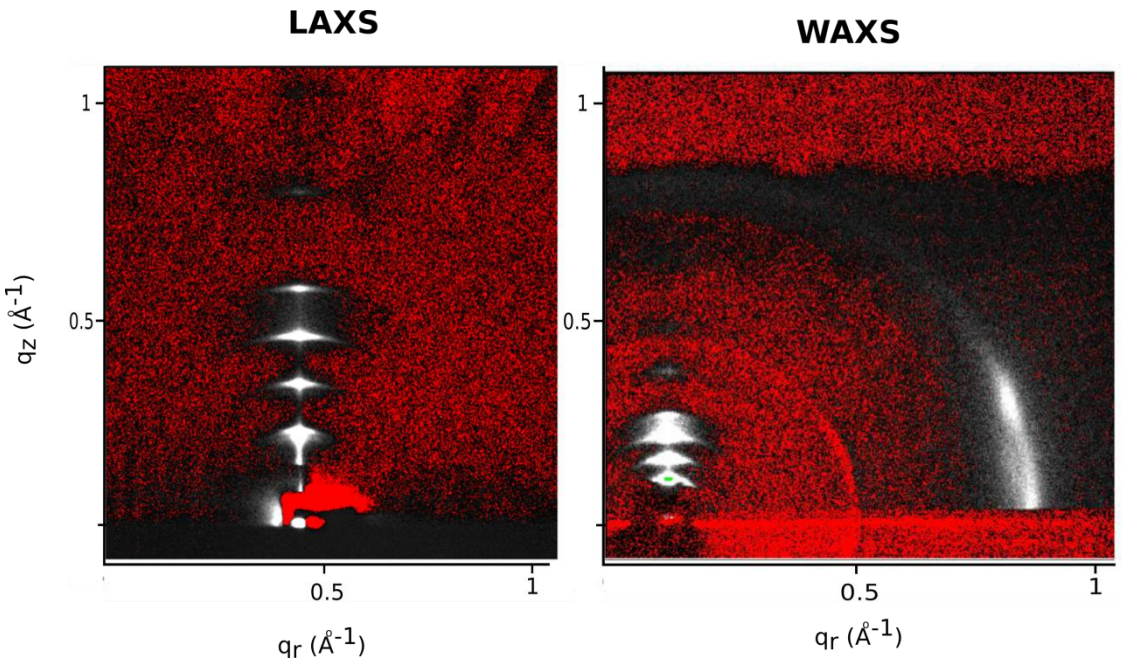

Figure 3.S22. Oriented eSM:eCer (85:15) at 30 °C in a tilted gel phase, collected after heating from 20 °C. D-spacing is 64.9 Å.

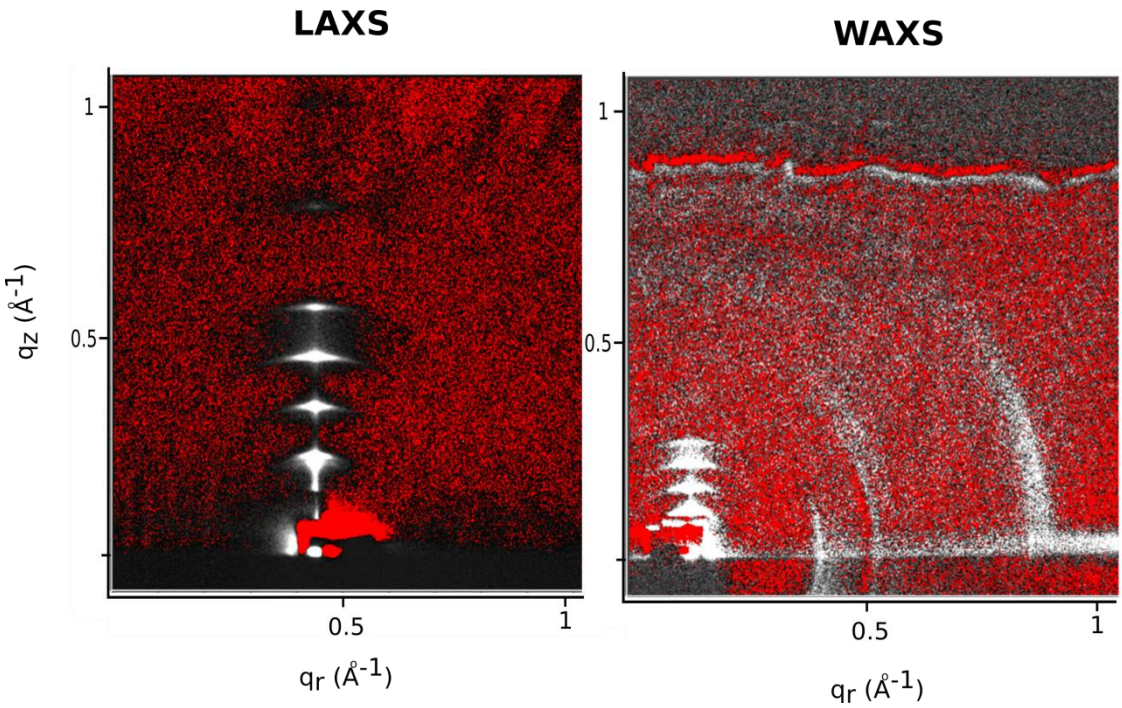

Figure 3.S23. Oriented eSM:eCer (85:15) at 35 °C in a tilted gel phase, collected after heating from 30 °C. D-spacing is 65.5 Å.

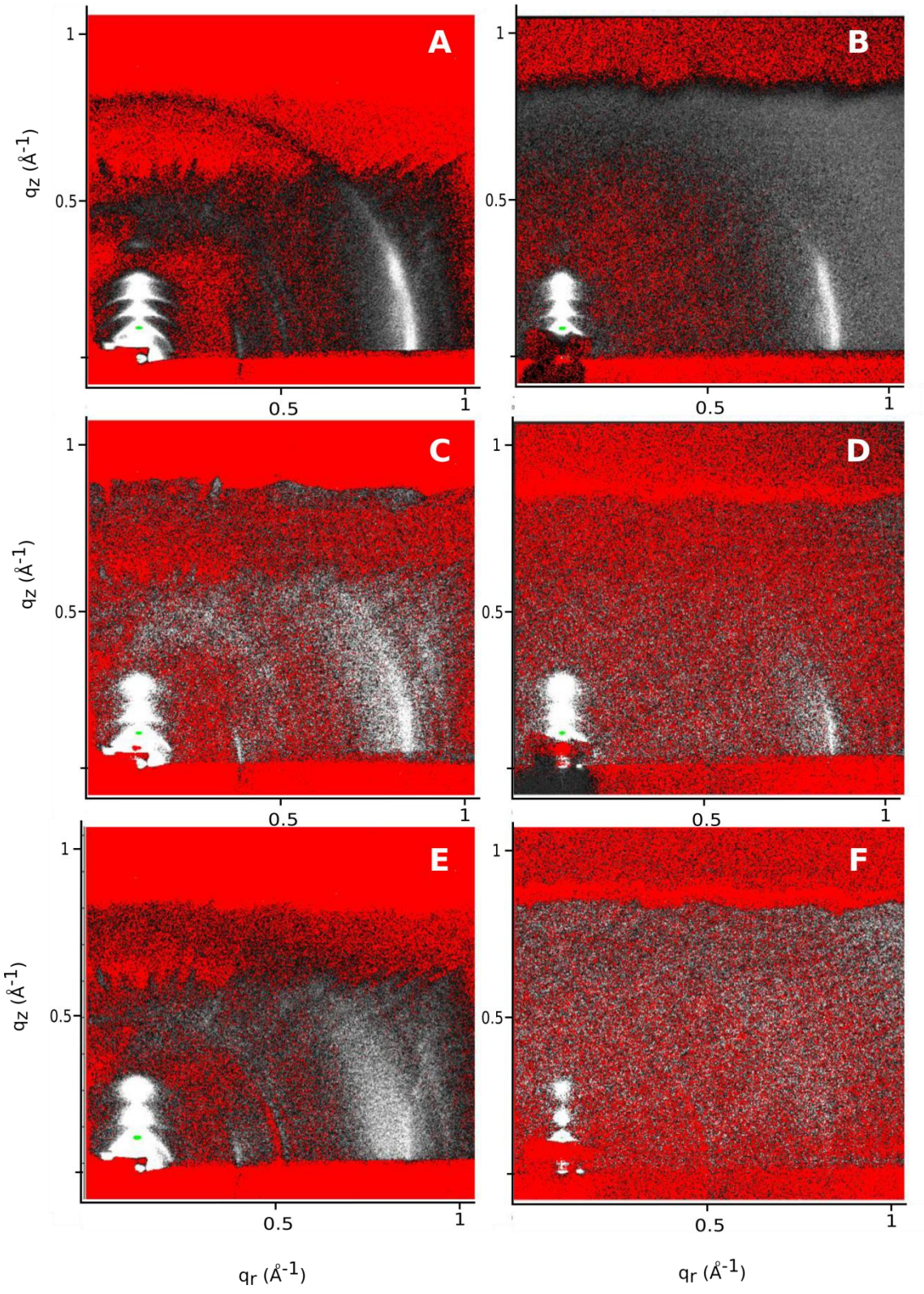

Figure 3.S24. Oriented eSM:eCer (85:15) at 39 °C (A), 44.6 °C (B), 50.5 °C (C), 55 °C (D), 58.6 °C (E), in a tilted gel phase, at 59.5 °C (F) in a fluid phase, collected after heating from the previous sample. D-spacing is 64.3 Å. (A), 66.6 Å. (B), 62.9 ± 0.2 Å. (C), 63.0 Å. (D), 61.8 Å. (E), 62.1 Å. (F).

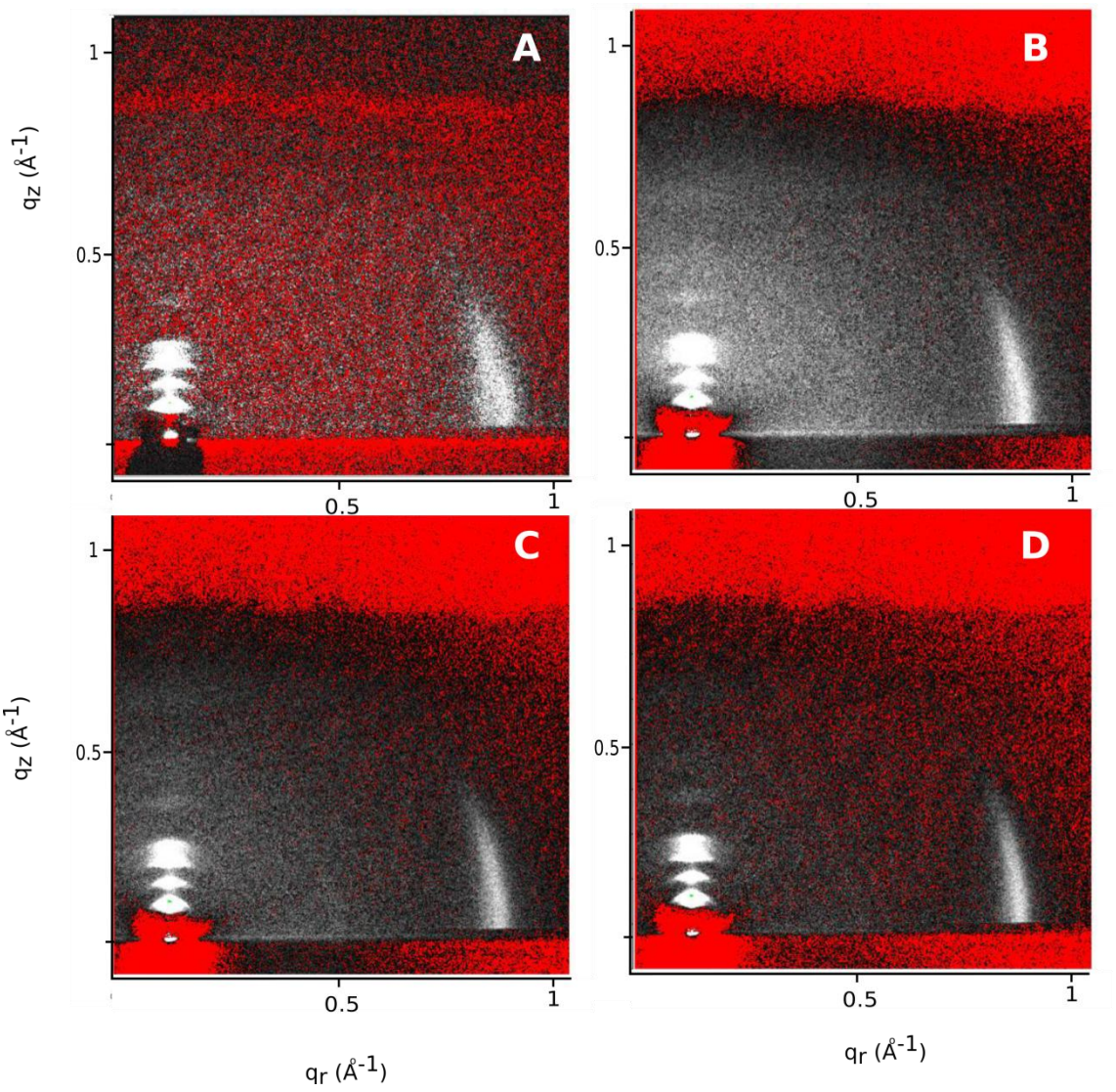

Figure 3.S25. Oriented eSM:eCer (85:15) at 3 °C (A), 10 °C (B), 15 °C (C), 20 °C (D), in a tilted gel phase, at 59.5 °C (F) in a fluid phase, collected after heating from the previous sample. D-spacing is 65.3 (A), 65.9 (B), 66.0 (C), 66.4 Å. (D).

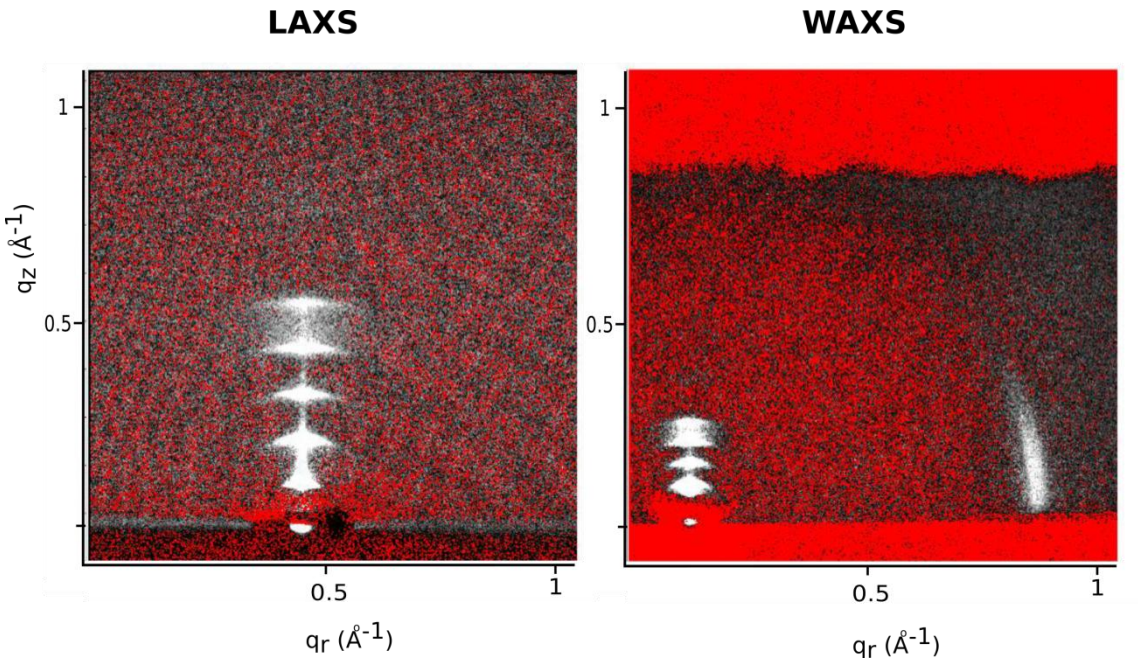

Figure 3.S26. Oriented eSM:eCer (70:30) at 30 °C in a tilted gel phase, collected after heating from 35 °C. D-spacing is 67.2 ± 0.2 Å.

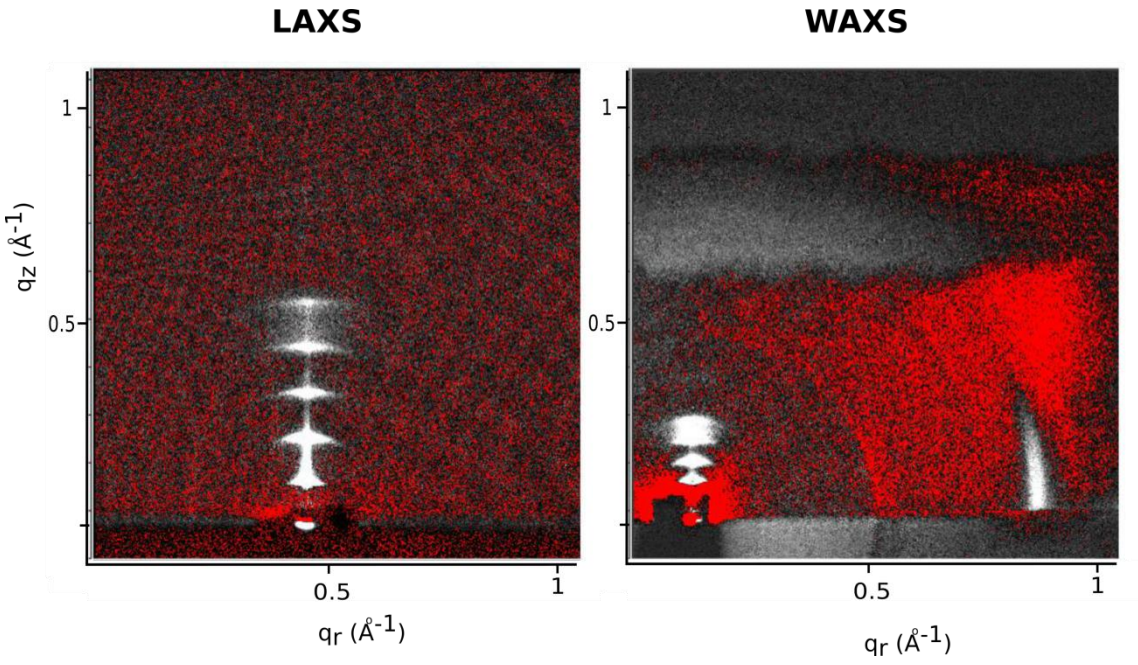

Figure 3.S27. Oriented eSM:eCer (70:30) at 35 °C in a tilted gel phase, collected after heating from 45 °C. D-spacing is 67.2 Å.

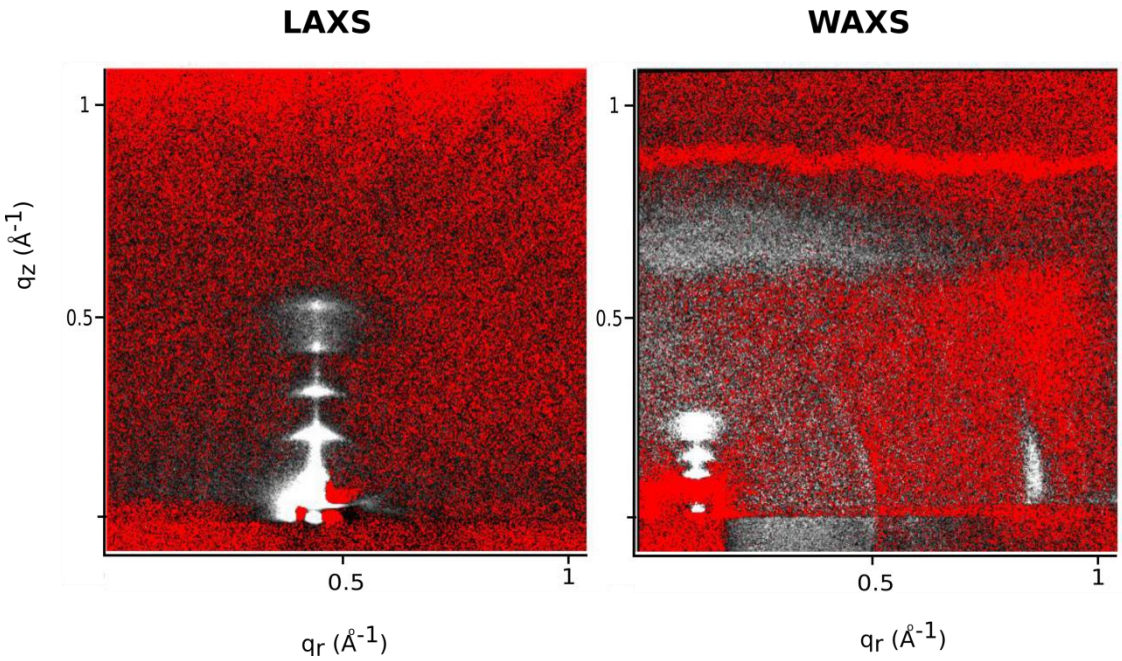

Figure 3.S28. Oriented eSM:eCer (70:30) at 45 °C in a tilted gel phase, collected after heating from 48 °C. D-spacing is 67.5 Å.

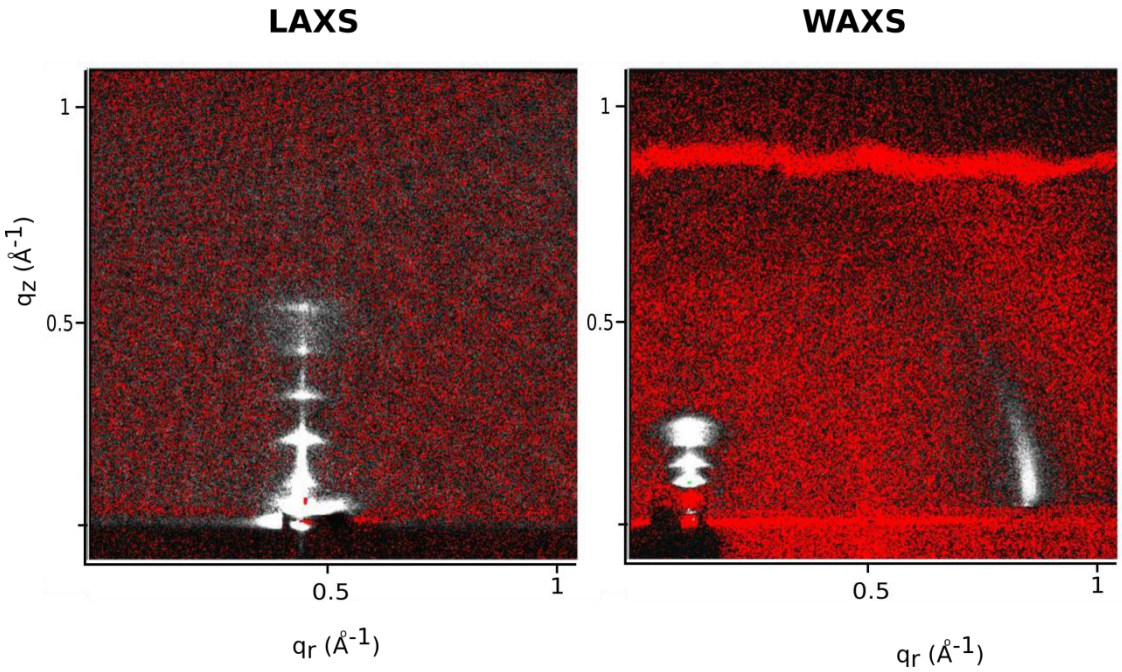

Figure 3.S29. Oriented eSM:eCer (70:30) at 48 °C in a tilted gel phase. D-spacing is 70.3 Å.

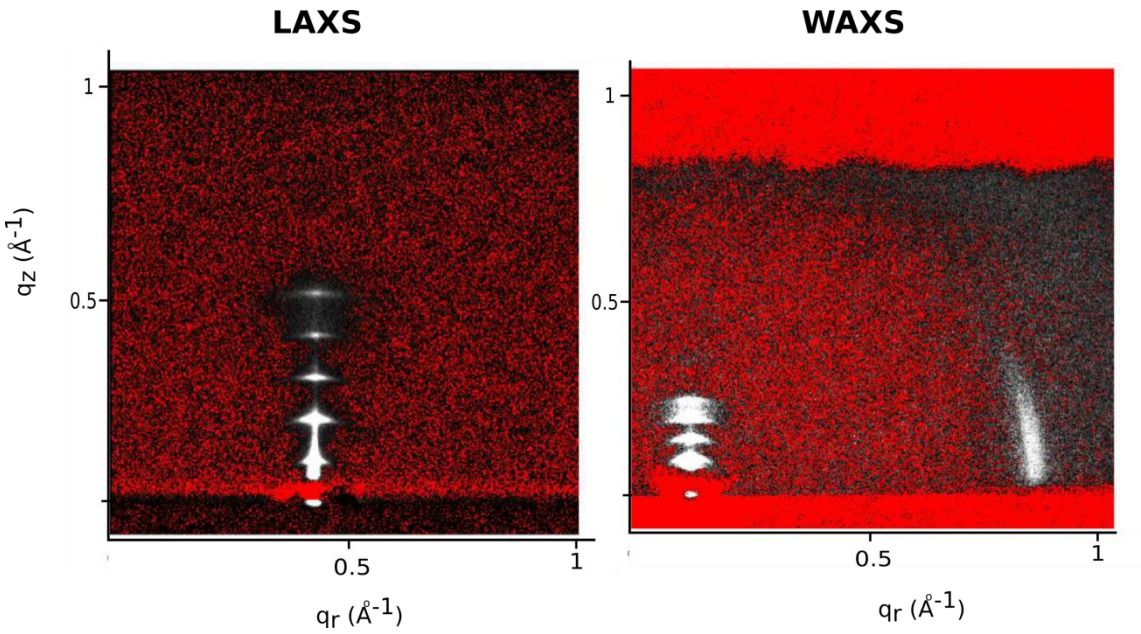

Figure 3.S30. Oriented eSM:eCer (70:30) at 55 °C in a tilted gel phase, collected after heating from 3 °C. D-spacing is 69.3 Å.

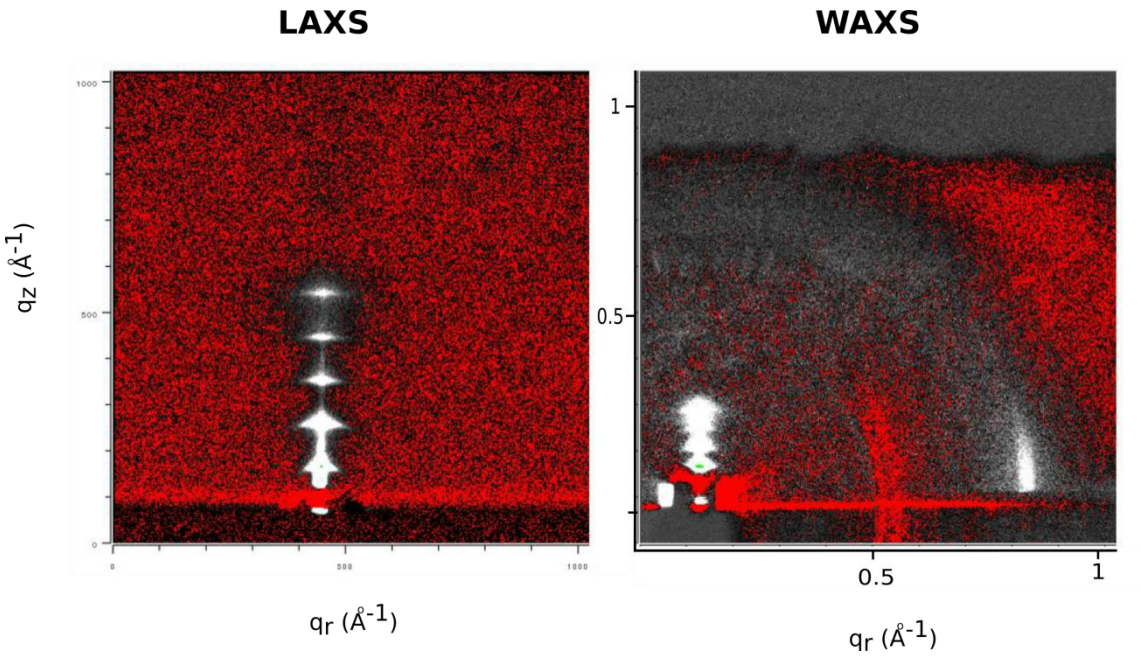

Figure 3.S31. Oriented eSM:eCer (70:30) at 59 °C in a tilted gel phase, collected after heating from 55 °C. D-spacing is 68.9 Å.

Table 3.S1a. Literature phase transition DSC results.

pSM Reference	Pretransition	T_P(ºC)	T_m(ºC)	Heating Rate (ºC/h)	Material
(Barenholz *et al.*, 1979)	Probably	25	41.3	15	[1]
(Barenholz *et al.*, 1979)	Yes	25	41.3	3-50	[1]
(Calhoun & Shipley, 1979a)	Yes (small)	31	40.5	300	D,L*
(Ahmad *et al.*, 1985)	No	-	41.5	150/300	[1]
(Sripada *et al.*, 1987)	No	-	41.0	300	D,L*
(Maulik & Shipley, 1996)	No	-	41.0	300	D,L*
(Bar *et al.*, 1997)	Yes (small)	29.6	41.1	20	Lipitek
(Ramstedt & Slotte, 1999)	Yes (small)	28.9	41.1	18	D-erythro
(Ramstedt & Slotte, 1999)	No	-	39.9	18	Racemic, D,L*
(Chemin *et al.*, 2008)	No	-	45	120	D-erythro
(Kodama *et al.*, 2012)	Yes (small)	27.5	40.4	45	D-erythro
(Jiménez-Rojo *et al.*, 2014)	Yes	30.9	41.7	45	Avanti
(Nyholm *et al.*, 2003)	Yes	27.4	40.9	30	D-erythro
(Estep *et al.*, 1979)	No	-	41	15	[1]

[1]Possibly stereospecificity is lacking

*D,L = D-erythro, L-threo SM

Table 3.S1b. Literature phase transition DSC results.

ESM Reference	Pretransition	T_P(ºC)	T_m(ºC)	Heating Rate (ºC/h)	Material
(Calhoun & Shipley, 1979a)	No	-		300	Avanti
(Ahmad *et al.*, 1985)	No	-	39-40	150/300	Sigma
(Mckeone *et al.*, 1986)	No	-	37.7	30	Avanti
(Chien & Huang, 1991)	No	-	37.5	300	Avanti
(Mannock *et al.*, 2003)	No	-	39.1	10	Avanti
(Filippov & Ora, 2006)	No	-	38.8	20	Avanti
(Chemin *et al.*, 2008)	No	-	39.3	30	Avanti
(Jiménez-Rojo *et al.*, 2014)	Yes?	-	38.1	45	Avanti
(García-Arribas *et al.*, 2016c)	No	-	36	45	Avanti

[1]Possibly stereospecificity is lacking

*D,L = D-erythro, L-threo SM

Table 3.S2. Summary of structural parameters from PSM experiments.

	T(°C)	DPP(Å)	A_L (Å^2)	Volume (Å^3)	DB (Å)	DC (Å)	Tilt (°)	d-space (Å)	<S_{CD}>
(Calhoun & Shipley, 1979b)	10	-	54.8*		38.4*		47*	4.14	
	50		59.4*		35.4*			4.6	
(Maulik *et al.*, 1986)	50	36.5	64.3*	1173*					
(Maulik & Shipley, 1996)	29	48	41*	1103*	54*			4.2	
	55	42	46*	1181*	51*			4.6	
(Li *et al.*, 2000) (monolayer)	10		46.3						
(Mehnert *et al.*, 2006)	<30						0		
	48								0.258
	48								0.214 (DPPC)
	3 (DPPC)	-	47 (DPPC)	1128 (DPPC)	48 (DPPC)		34 (DPPC)	4.27 (d20) 4.03 (d11) (DPPC)	
(Guler *et al.*, 2009)	48 (DPPC)		64 (DPPC)	1229 (DPPC)	38.4 (DPPC)				
(Bunge *et al.*, 2008)	40					16.2*			0.221
(Bartels *et al.*, 2008)	20		43.8+			19.8			
	30					19.1			
	45					16.2			~0.25
	60					14.9			~0.22
(Arsov *et al.*, 2018)	3	-	44.5	1099*	49.4	-	30.4	3.95 (d20) 4.14 (d11)	
(Arsov *et al.*, 2018)	45	37.6	64	1172*	36.6	13.3			

*Some assumptions, or calculated from other quantities,

+Assumed tilt = 0 degrees.

Table 3.S3. Summary of structural parameters from ESM experiments.

	T(°C)	DPP(Å)	A_L (Å^2)	Volume (Å^3)	DB (Å)	DC (Å)	Tilt (°)	d-space (Å)	<S_{CD}>
(Chachaty *et al.*, 2005)	20							4.2	
	50							4.6	
(Chemin *et al.*, 2008)	20		40.2+					4.17	
	55				~48				
(Quinn & Wolf, 2009a)	20	42.1 (ave)						4.21	
	50	39.6 (ave)				17.3	0		
(Leftin *et al.*, 2014)	48		53.2 (ave)		49.9 (DB) (ave)	17.0 (ave)			~0.32
(Arsov *et al.*, 2018)	45	38.6	64	1187	37.1	13.6			

+Assumed tilt = 0 degrees

CHAPTER 4:

BILAYERS OF TERNARY LIPID COMPOSITIONS CONTAINING EQUIMOLAR CERAMIDE AND CHOLESTEROL

CHAPTER 4: BILAYERS OF TERNARY LIPID COMPOSITIONS CONTAINING EQUIMOLAR CERAMIDE AND CHOLESTEROL

4.1 Introduction

Sphingolipids are important biomolecules, some of them acting as second messengers in cellular processes such as cell proliferation, signal transduction, and apoptosis (Hannun & Obeid, 2008). A number of findings in the last decade suggest that cellular membranes are laterally heterogeneous at the submicrometer scale, sphingolipids acting as lateral segregation inducers (Goñi, 2019; Sezgin *et al.*, 2017). Lateral segregation of liquid-ordered (L_o) domains has been observed with cholesterol (Chol) in saturated and unsaturated phospholipids such as 1,2-dipalmitoyl-*sn*-glycero-3-phosphocholine (DPPC) or 1-palmitoyl-2-oleoyl-*sn*-glycero-3-phosphocholine (POPC), but sphingosine-based lipids, such as sphingomyelin (SM), seem to enhance the phospholipid:Chol interaction mainly through hydrogen bonding (García-Arribas *et al.*, 2016b; Ramstedt & Slotte, 2006). The formation of (SM + Chol)-enriched domains in the L_o phase is well known (Veiga *et al.*, 2001; Quinn & Wolf, 2009b), and may be related to nanodomain (lipid raft) formation (Lingwood & Simons, 2010). A further lipid with the ability to segregate laterally together with SM is ceramide (Cer) (Busto *et al.*, 2009). Cer consists of a fatty acid linked to a sphingosine base through an amide bond. Normally Cer levels in cell membranes are quite low (0.1-1 mol % of total phospholipid), however higher concentrations can be found under cellular stress conditions, e.g. apoptotic cells (Castro *et al.*, 2014). Previous studies in model and cell membranes containing Cer revealed its capacity to induce membrane permeability (Ruiz-Argüello *et al.*, 1996), transbilayer flip-flop lipid motion (Contreras *et al.*, 2003), and lateral domain segregation (Veiga *et al.*, 1999). In fact, Cer can give rise to highly ordered gel-like domains (Sot *et al.*, 2006), which could in turn act as 'membrane platforms' clustering receptor molecules and mediating signal transduction processes (Cremesti *et al.*, 2001; Zhang *et al.*, 2009).

Cer are generated in cells under stress conditions primarily through SM hydrolysis by sphingomyelinases (Goñi & Alonso, 2002). Because of the abundance

of Chol in plasma membranes, sphingomyelinase-generated Cer could give rise to the formation of platforms enriched in SM, Chol and Cer. On that account, Chol-Cer interaction was studied and it was proposed that Cer displaces Chol from tightly packed SM/Chol liquid-ordered (L_o) phases (Megha & London, 2004; Chiantia *et al.*, 2006a). However, high concentrations of Chol are needed to induce Cer depletion from Cer-enriched domains (Silva *et al.*, 2007, 2009). Furthermore, Cer and Chol interact even in the absence of SM (Castro *et al.*, 2009b). These findings led to our studies of mixtures of Chol and Cer with N-palmitoylsphingomyelin (pSM) or DPPC in the absence of a disordered phase. In particular the phospholipid:Chol:pCer (54:23:23 mol ratio) mixture was found to originate apparently homogeneous ternary phases with unique thermotropic and nanomechanical properties (Busto *et al.*, 2014; Garcia-Arribas *et al.*, 2015), although the presence of a minor fraction of pCer-enriched nanodomains was detected using confocal microscopy (Busto *et al.*, 2010).

The purpose of this work is to further characterize bilayers composed of ternary mixtures including a saturated phospholipid (pSM or DPPC), Chol, and pCer, varying the proportions of (Chol + Cer) between 46 and 30% while keeping constant their 1:1 mol ratio. We have used differential scanning calorimetry (DSC) to study how the proportion of (Chol + pCer) affects their thermotropic behavior, trans-parinaric acid (tPA) and 1,6-diphenyl-1,3,5-hexatriene (DPH) fluorescence to study membrane order and thermostability of the ordered bilayers, DiI_{C18} and NAP to analyze the existence of segregated phases in giant unilamellar vesicles (GUV), and atomic force microscopy (AFM) to study their topology and nanomechanical properties. Fluorescence spectroscopy results agree with previous studies, which support the formation of a ternary phase, while AFM and confocal microscopy confirm the existence of pCer-enriched nanodomains that largely increase in size as the proportion of phospholipid increases.

4.2 Material and methods

4.2.1 Materials

DPPC, pSM, pCer and Chol were purchased from Avanti Lipid Products (Alabaster, AL, USA). 1,6-diphenyl-1,3,5-hexatriene (DPH) and 1,1'-dioctadecyl-3,3,3'3'-tetramethylindocarbocyanine perchlorate (DiI_{C18}) was from Molecular Probes (Eugene, OR). Naphtho[2,3-a]pyrene (NAP) was from Sigma-Aldrich (St. Louis, MO). Colloidal silica (Ludox) was supplied by Sigma (St. Louis, MO). *Trans*-parinaric acid (tPA) was kindly provided by Prof. J. P. Slotte (Åbo Akademi University, Turku, Finland). Due to its labile nature this fluorophore was stored dried in a N_2 atmosphere at -80 °C. Methanol and chloroform were from Fisher

(Suwanee, GA). Buffer solution, unless otherwise stated, was 20 mM PIPES, 1 mM EDTA, 150 mM NaCl, pH 7.4. All other reagents (salts and organic solvents) were of analytical grade.

4.2.2 Liposome preparation

Lipid vesicles were prepared by mixing the desired lipids dissolved in chloroform/methanol (2:1, v/v) and drying the solvent under a stream of nitrogen. The lipid film was kept under high vacuum for 90 min to ensure the removal of undesired organic solvent. Multilamellar vesicles (MLV) were formed by hydrating the lipid film with the buffer solution at 90 °C, helping the dispersion with a glass rod. The samples were finally sonicated for 10 min in a bath sonicator at the same temperature in order to facilitate homogenization.

4.2.3 Differential scanning calorimetry (DSC)

The measurements were performed in a VP-DSC high-sensitivity scanning microcalorimeter (MicroCal, Northampton, MA, USA). MLV to a final concentration of 1 mM were prepared as described above with a slightly different hydration step: instead of adding the buffer solution at once, increasing amounts of the solution were added, helping the dispersion by stirring with a glass rod. Then the vesicles were homogenized by forcing the sample 50-100 times between two syringes through a narrow tube (0.5 mm internal diameter, 10 cm long) at a temperature above the transition temperature of the lipid mixture. Before loading the MLV sample into the appropriate cell both lipid and buffer solutions were degassed. 0.5 mL of suspension containing 1 mM total lipid concentration was loaded into the calorimeter, performing 8 heating scans at a 45 °C/h rate, between 10 and 100 °C for all samples. Phospholipid concentration was determined as lipid phosphorus, and used together with data from the last scan to obtain normalized thermograms. The software Origin 7.0 (MicroCal), provided with the calorimeter, was used to determine the different thermodynamic parameters from the scans.

4.2.4 Confocal microscopy of giant unilamellar vesicles (GUV)

GUVs are prepared as described previously, using the electroformation method developed by Angelova and Dimitrov (Angelova *et al.*, 1992; Angelova & Dimitrov, 1986). Lipid stock solutions were prepared in 2:1 (v/v) chloroform/methanol and appropriate volumes of each preparation were mixed. Labelling was carried out by pre-mixing the desired fluorescent probe (NAP or DiI_{C18}) with the lipids in organic solvent. Fluorescent probe concentration was 0.4 mol % DiI_{C18} or 0.5 mol % NAP. The samples were deposited onto the surface of

platinum (Pt) wires attached to specially designed polytetrafluoroethylene (PTFE)-made cylindrical units, which were placed under vacuum for 2 h to completely remove the organic solvent. The sample was covered to avoid light exposure. Then, the units were fitted into specific holes within a specially designed chamber, to which a glass cover slip had been previously attached with epoxy glue. Once fitted, the platinum wires stayed in direct contact with the glass cover slip. The chamber was then equilibrated at the desired temperature by an incorporated water bath. 400 µL sucrose, prepared with high-purity water (SuperQ, Millipore, Billerica, MA) and heated at 90 °C, were added until the solution covered the Pt wires. The chambers were stopped with tightly fitting caps, and the latter were connected to a TG330 function generator (Thurlby Thandar Instruments, Huntingdon, UK). The alternating current field was applied with a frequency of 10 Hz and an amplitude of 940 mV for 120 min. The temperatures used for GUV formation were over the gel to liquid phase transition in all cases. The generator and the water bath were switched off, and vesicles were left to equilibrate at room temperature for 30 min. A slow cooling was needed to observe large enough domains in fluorescence microscopy (Castro *et al.*, 2007). After GUV formation, the chamber was placed onto an inverted confocal fluorescence microscope (Nikon D-ECLIPSE C1, Nikon, Melville, NY). The excitation wavelength was 458 nm for NAP, and 543 nm for DiI_{C18}. Emission was recovered between 478–520 nm for NAP, and 563–700 nm for DiI_{C18}. Image treatment and quantitation were performed using the software EZ-C1 3.20 (Nikon). No difference in domain size, formation, or distribution was detected in the vesicles during the observation period or after laser exposure.

4.2.5 Measuring non-stained areas in GUV

The percent area of non-stained domains in GUV was calculated using ImageJ software in four steps as follows (see Supplementary Figure 4.S1). (i) Images were processed and converted from RGB to a binary image (black and white). Thus, non-stained domains appeared in white while the more fluid phase appeared in black. (ii) GUV total area, and the fluid phase area (in black, A_B) in the image were measured. A_B percentage could then be computed. (iii) The non-stained domain area (A_W) was measured following the same procedure. (iv) The non-stained domain percentage was obtained from the ratio: % non-stained domains = $A_W/(A_W + A_B)$ (Artetxe, 2017).

4.2.6 Time-resolved tPA fluorescence

Time-resolved measurements of tPA fluorescence were performed as follows. MLV with the desired lipid composition were prepared at 0.2 mM plus 1 mol% tPA and incubated at the desired temperature before performing the measurements. tPA intensity decays were measured in a Fluoromax-3 spectrofluorometer with a time-correlated single-photon counting (TCSPC) accessory (Horiba Jobin Yvon, Edison, NY) connected to a water bath for temperature control and under continuous stirring. The samples were excited with a pulsed 289 nm LED and the emission was recorded at 430 nm. The emission slit was adjusted so that the count rate was always 0.6-0.3% (0.6-0.3 photons detected per 100 excitation pulses). The instrument response function was measured for each sample at each temperature at an emission of 289 nm using a scattering solution of colloidal silica. Data were analyzed with the DAS6 software using the nonlinear least squares analysis method (Lakowicz, 2006; Wolber & Hudson, 1981) and the intensity decays measured were fitted to a bi-exponential decay model:

$$I(t) = \alpha_1^{\left(\frac{-t}{\tau_1}\right)} + \alpha_2^{\left(\frac{-t}{\tau_2}\right)}$$

where τ_1 and τ_2 are the lifetime components and α_1 and α_2 their respective pre-exponential factors. When $\sum\alpha_i$ is normalized to unity, α_1 and α_2 represent the fractional amplitude of their corresponding lifetimes. Since the radiative decay rate of tPA is independent of the environment, the fractional amplitudes can be considered proportional to the mole fraction of tPA exhibiting the corresponding lifetime (Wolber & Hudson, 1981). In our case the data could be fitted to bi-exponential decays.

The author thanks Dr. I. Artetxe for his help with these experiments.

4.2.7 Fluorescence anisotropy

Anisotropy measurements were carried out with MLV at 0.1 mM plus 1 mol% tPA or DPH using a QuantaMaster 40 spectrofluorometer (Photon Technology International, Lawrenceville, NJ), under continuous stirring. Samples were equilibrated for 5 min at the desired temperature before the anisotropy measurements. tPA was excited at 305 nm and its emission recovered at 410 nm, while DPH was excited at 360 nm and its emission recovered at 430 nm. The anisotropy was calculated by the instrument software (PTI FelixGX) from an

average of measurements for each experimental point, automatically correcting for the G factor, which was measured for every sample at each temperature.

The author thanks Dr. I. Artetxe for his help with these experiments.

4.2.8 Supported planar bilayer (SPB) formation

SPB were prepared on high V-2 quality scratch-free mica substrates (Asheville-Schoonmaker Mica Co., Newport News, VA, USA) previously attached to round 24-mm glass coverslips with a two-component optical epoxy resin (EPO-TEK 301-2FL, Epoxy Technology Inc., Billerica, MA). SPB were prepared by the vesicle spin coating method (Simonsen & Bagatolli, 2004). Samples were dissolved at the desired ratio in an isopropanol/hexane/H_2O (3:1:1) solution at 10 mM total lipid concentration. 0.4 mol% DiI_{C18} was included. 10 µl of the lipid mixture were directly pipetted onto a freshly cleaved mica substrate and rotated at 3000 rpm for 40 s using a KW-4A spin-coater (Chemat Technology, Northridge, CA). The substrate was left under high vacuum overnight, mounted onto a Biocell sample holder (JPK Instruments, Berlin, Germany), and hydrated with 250 µl assay buffer. Multiple bilayers were then generated. The temperature was raised to 70 °C for 30 min and the sample washed 10 times throughout with assay buffer at 70 °C. In this way bilayers not directly adhered to the mica substrate were discarded. Bilayers were then left to equilibrate at room temperature for 1 hour prior to measurements. Finally, the BioCell was set to 23 °C for the AFM measurements.

4.2.9 AFM imaging

The measurements were performed with a NanoWizard II AFM (JPK Instruments, Berlin, Germany) at 23 °C, using MLCT Si_3N_4 cantilevers (Bruker, Billerica, MA) with a nominal spring constant of 0.1-0.5 N/m in contact mode scanning (constant vertical deflection). Sample temperature was controlled with the BioCell sample holder. 512x512 pixel resolution images were collected at a scanning rate between 1 and 1.5 Hz and line-fitted using the JPK Image Processing software as required.

4.2.10 Force measurements

The thermal noise method was used to calibrate the MLCT Si_3N_4 cantilevers in a lipid-free mica substrate in assay buffer. Force spectroscopy was performed at a speed of 1 µm/sec in no less than 500 x 500 nm bilayer areas in the form of 10x10 or 15x15 grids. Force steps were determined for each of the indentation curves as reproducible jumps within the extended traces. The resulting values

were obtained from at least 3 independent sample preparations with at least 3 independently calibrated cantilevers. Control indentations were always performed in lipid-free areas before and after bilayer indentations to ascertain the formation of a single bilayer and the absence of artifacts or debris on the tip, assessed by the lack of any force-distance step on both trace and retrace curves.

4.3 Results

4.3.1 Time-resolved tPA fluorescence

tPA is a fluorescent lipid, highly informative on the molecular order and lateral heterogeneity of bilayers. It is known to show two lifetimes in isotropic solvents and in bilayers in either fluid or gel state (Wolber & Hudson, 1981; Ruggiero & Hudson, 1989; De Almeida *et al.*, 2002; Artetxe *et al.*, 2013; Maula *et al.*, 2012). The main advantage of this fluorescent probe is its high preference towards gel domains that, even at very low fractions, will give rise to a fingerprint long-lifetime component above 30 ns (Castro *et al.*, 2007; Silva *et al.*, 2007).

Before studying how tPA was incorporated into the ternary mixtures, both Chol and Cer effects were individually studied in binary mixtures with a saturated phospholipid. The long and short lifetimes of tPA intensity decays in the various mixtures are collected in the Supplementary Figure 4.S2. The intensity decay of tPA was also measured at different temperatures (Supplementary Figure 4.S3). The results are in good agreement with published DSC data (Busto *et al.*, 2009).

4.3.2 DPH and tPA anisotropy

The various **s**amples were studied using DPH anisotropy as a tool for measuring bilayer order (Figure 4.1). Both pure DPPC and pure pSM liposomes show high anisotropy values below their gel-fluid transition temperatures, typical of bilayers in the gel phase, while low anisotropy values are recorded above their T_m, indicative of fluid bilayers (Figure 4.1 A, B, squares). In the binary mixtures with pCer, the anisotropy shows a clear melting profile (Figure 1 A, B, triangles). At low temperatures the anisotropy stays unchanged at a value similar to pure DPPC or pSM; it then starts to drop at ~45 °C for DPPC:pCer and at ~55 °C for pSM:pCer until the bilayer appears to become fluid (similar anisotropies than for pure DPPC or pSM in fluid state) at around 70 °C (Figure 4.1 A, B), similarly to what was seen with tPA lifetimes (Figure 4.S3). In the binary mixtures with Chol, the anisotropy values at low T are slightly below the values of the pure bilayers but decrease

slowly and remain significantly higher than those of pure bilayers or binary mixtures with pCer at high temperatures (Figure 4.1 A, B, circles).

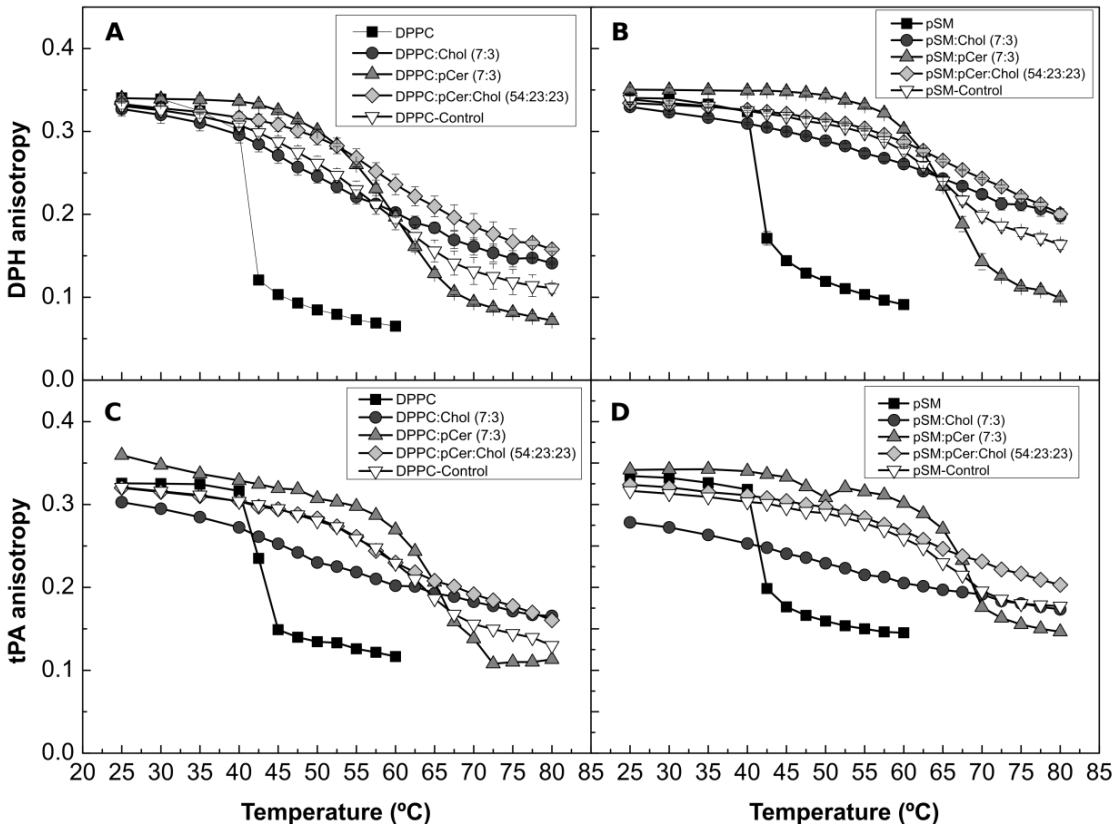

Figure 4.1. Fluorescence anisotropy of DPH (A, B) and tPA (C, D) as a function of temperature in MLV of varying compositions. Bilayer compositions are given in the insets. Values shown are averages of three separate experiments ± SD, but for the controls (a single experiment). The controls were a mixture of equal amounts of liposomes of each binary mixture, either (DPPC:Chol 7:3 + DPPC:pCer 7:3) or (pSM:Chol 7:3 + pSM:pCer 7:3).

The anisotropy of the ternary mixture at 25 °C exhibits a value intermediate between those of the binary mixtures with Chol and pCer, then it slowly decreases without a clear melting profile but in a similar way to the Chol-containing binary mixtures (Figure 4.1 A, B, diamonds). Again, the anisotropy at high temperatures is kept at higher values than those of typical disordered bilayers. The anisotropy values of the controls are at all temperatures intermediate between those of the binary mixtures with Chol or pCer (Figure 4.1 A, B inverted triangles). This is an expected result for a mixture of equal amounts of liposomes of both binary mixtures. The profile is also clearly different from that of the ternary mixture. The results are quite similar for both DPPC- and pSM-containing bilayers, the only noticeable difference being a slightly higher thermostability of ordered bilayers containing pSM as compared to those with DPPC (Figure 4.1 A, B).

DPH and tPA can be considered as complementary probes in studies with bilayers containing pCer, since the former fluorophore is excluded from pCer-rich domains whereas the latter presents a high preference for such domains (Castro *et al.*, 2007; Silva *et al.*, 2007). Therefore, fluorescence anisotropy of tPA was also measured in the same lipid mixtures to confirm the results obtained with DPH (Figure 4.1 C, D). Overall, the results with tPA anisotropy resemble those of DPH, the main differences being: lower anisotropy values for binary mixtures with Chol, higher values for pure bilayers and binary bilayers with pCer in the fluid phase, and higher thermostability of the ordered phase of DPPC:pCer bilayers (Figure 4.1), all of them probably due to the higher affinity of this probe to gel and pCer-rich domains.

4.3.3 Differential scanning calorimetry

In order to study how the lipid composition influences the formation of a gel ternary phase, pSM:pCer:Chol and DPPC:pCer:Chol ternary bilayers with decreasing amounts of (pCer + Chol) were studied by DSC (Figure 4.2). At high (pCer + Chol) concentrations (≥40 mol%) the SM-containing ternary mixture exhibits a symmetric endotherm centered at 60 °C, as previously reported (Busto *et al.*, 2010). In the DPPC-based mixture, the transition temperature is slightly lower and its endotherm is centered at 55 °C. Both pSM- and DPPC-containing samples present an increase in transition enthalpy as (pCer + Chol) decreases, while their transition temperatures decrease slightly (Table 4.1). Also with the decrease in (pCer + Chol) the thermograms become clearly asymmetric, as confirmed upon fitting the endotherms with Gaussian functions: while two components are obtained for the samples at 54:23:23 and 60:20:20 ratios, a third small component appears at 66:17:17, becoming more noticeable in 70:15:15 samples (Figure 4.2). The overall shape of the endotherms for the latter samples was similar to that observed in previous DSC studies of the pSM:pCer:Chol mixture at low Chol proportions (Busto *et al.*, 2010).

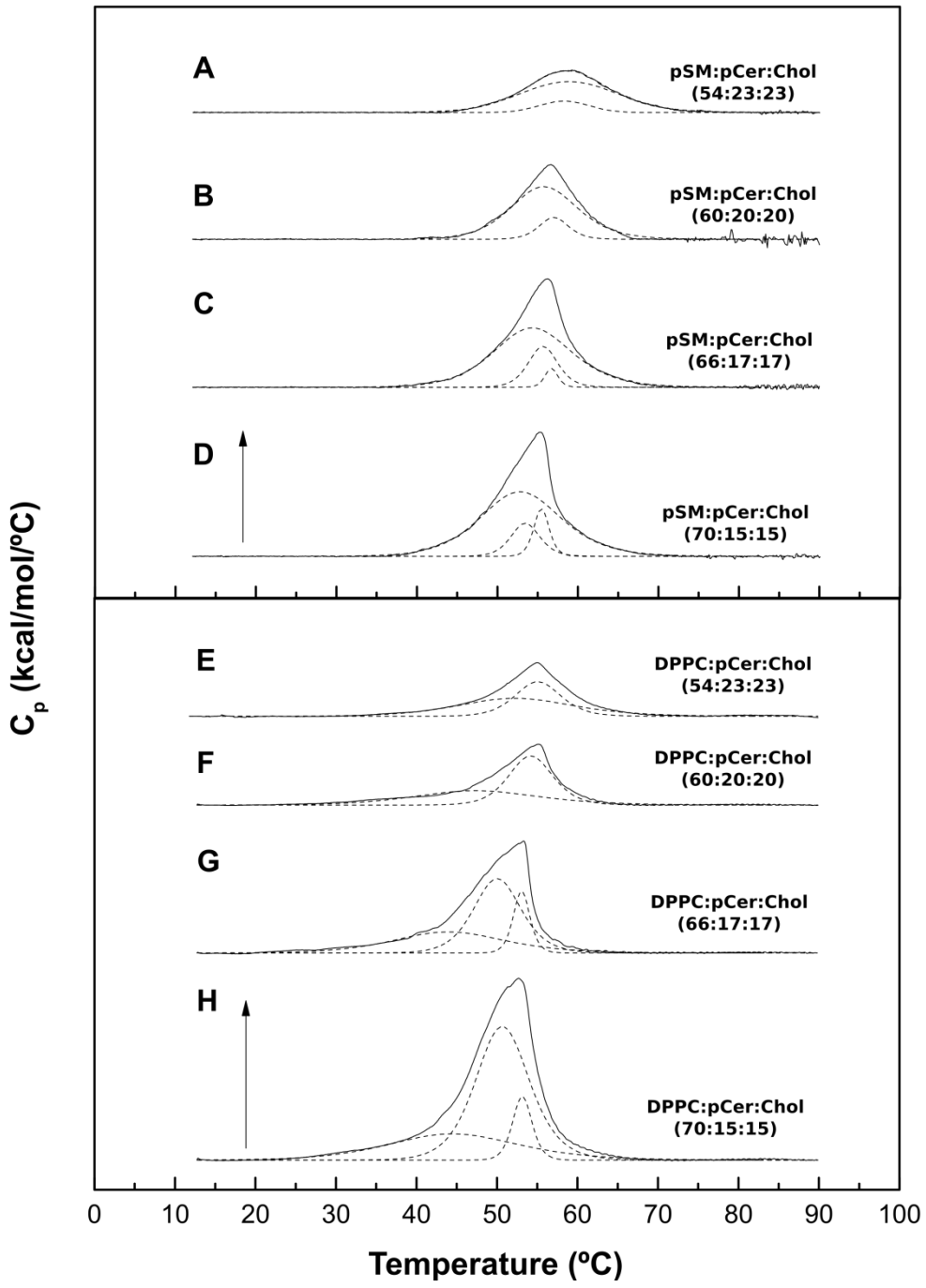

Figure 4.2. DSC of aqueous dispersions of pSM:pCer:Chol and DPPC:pCer:Chol at different mol ratios. The endotherms can be fitted with 2 or 3 Gaussian curves (dotted lines). The arrows correspond to 0.5 kcal/mol/°C.

Table 4.1. Thermodynamic parameters of DSC endotherms of pSM:pCer:Chol and DPPC:pCer:Chol liposomes at different mol ratios. Data from thermograms of Figure 4.2. Averages ± SD (n = 3) are given.

Bilayer composition	ΔH (cal/mol)	T_m (°C)	$\Delta T_{1/2}$ (°C)
pSM:pCer:Chol (54:23:23)	2800 ± 210	59.0 ± 0.5	11.5 ± 0.4
pSM:pCer:Chol (60:20:20)	3260 ± 70	56.7 ± 0.1	7.2 ± 1.0
pSM:pCer:Chol (66:17:17)	4900 ± 190	56.2 ± 0.1	6.9 ± 0.3
pSM:pCer:Chol (70:15:15)	5500 ± 200	55.3 ± 0.1	7.3 ± 0.5
DPPC:pCer:Chol (54:23:23)	1878 ± 177	54.92 ± 0.1	8.3 ± 0.3
DPPC:pCer:Chol (60:20:20)	2239 ± 94	55.07 ± 0.1	7.2 ± 0.2
DPPC:pCer:Chol (66:17:17)	3574 ± 406	53.3 ± 0.1	7.9 ± 0.1
DPPC:pCer:Chol (70:15:15)	6360 ± 1324	52.2 ± 0.7	9.5 ± 1.0

4.3.4 DiI_{C18} and NAP in the study of ternary phases

To further characterize the ternary mixtures, giant unilamellar vesicles (GUV) stained with DiI_{C18} or NAP were examined by confocal fluorescence microscopy. DiI_{C18} is a dye with a saturated long-chain hydrocarbon that favors its partition into fluid areas, besides being a suitable tool in fluorescence microscopy due to its high brightness and photostability (Klymchenko & Kreder, 2014). NAP is a polycyclic aromatic fluorescence molecule with a high affinity for cholesterol-enriched areas (Juhasz *et al.*, 2010). pSM:pCer:Chol bilayers at 54:23:23 mol ratio are differently stained with DiI_{C18} and NAP, although the heterogeneity is hardly noticeable when DiI_{C18} alone is used (Figure 4.3), as previously described (Busto *et al.*, 2010). This situation can be explained by the coexistence of two ternary mixtures with slightly different lipid proportions, or by the coexistence of immiscible binary and ternary mixtures or other similar combinations (Busto *et al.*, 2010). When ternary mixtures at a 60:20:20 ratio are studied, the presence of clearly visible DiI_{C18}-depleted areas is observed. These domains appear to be roughly circular, and the border of their areas appears enriched in DiI_{C18}-stainable material. As a consequence the DiI_{C18}-depleted areas appear surrounded by a (cholesterol-poor) red rim in the merged image (Figure 4.3). When SM proportion is 66 or 70 mol%, larger unstained areas are seen, that could arise from the partial coalescence of smaller domains. DPPC ternary mixtures appear in general more

homogeneous than their SM counterparts, with non-stained domains being clearly visible only in the 70:15:15 composition (Figure 4.4), which suggests that the ternary phase is more stable with DPPC than with SM, i.e. that a high affinity of pCer and Chol for SM is not the main factor for ternary gel phase formation.

The proportion of non-stained domains in the GUV was estimated as shown in the Supplementary Figure 4.S1. The results are given in Figure 4.5. The proportion of GUV surface covered by non-stained domains increases with the proportion of phospholipid, either SM or DPPC. The effect is detected above 60 mol% phospholipid. At the lower phospholipid concentrations the non-stained surface for DiI_{C18} was smaller than that for NAP. However, as the proportion of (pCer + Chol) decreases, the percentage of both DiI_{C18}- and NAP-depleted areas becomes very similar. The increase in DiI_{C18}- and NAP-depleted areas seems to be related to the formation of tightly-packed gel-like pSM:pCer domains containing a relatively low Chol amount, Chol at these low ratios not being able to displace Cer from SM.

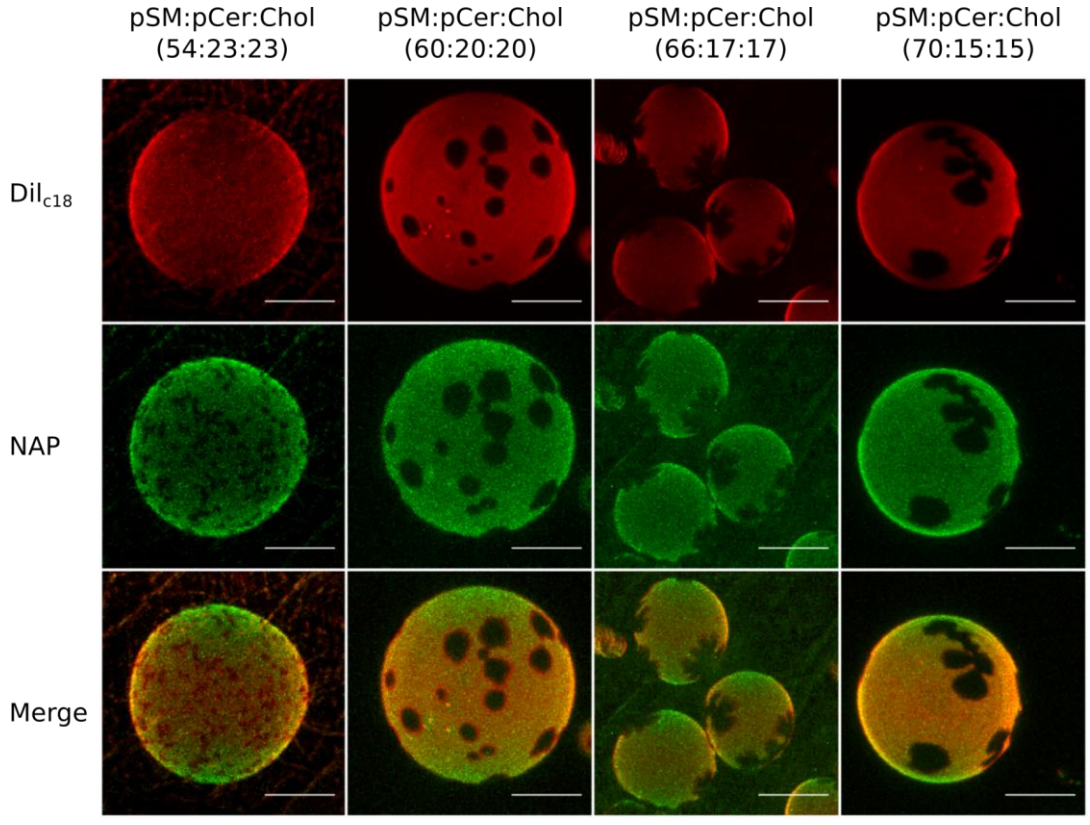

Figure 4.3. Confocal microscopy 3D (z-stack) images of pSM:pCer:Chol fluorescent giant unilamellar vesicles at different mol ratios, stained with 0.4 mol% DiI_{C18} and 0.5 mol% NAP.

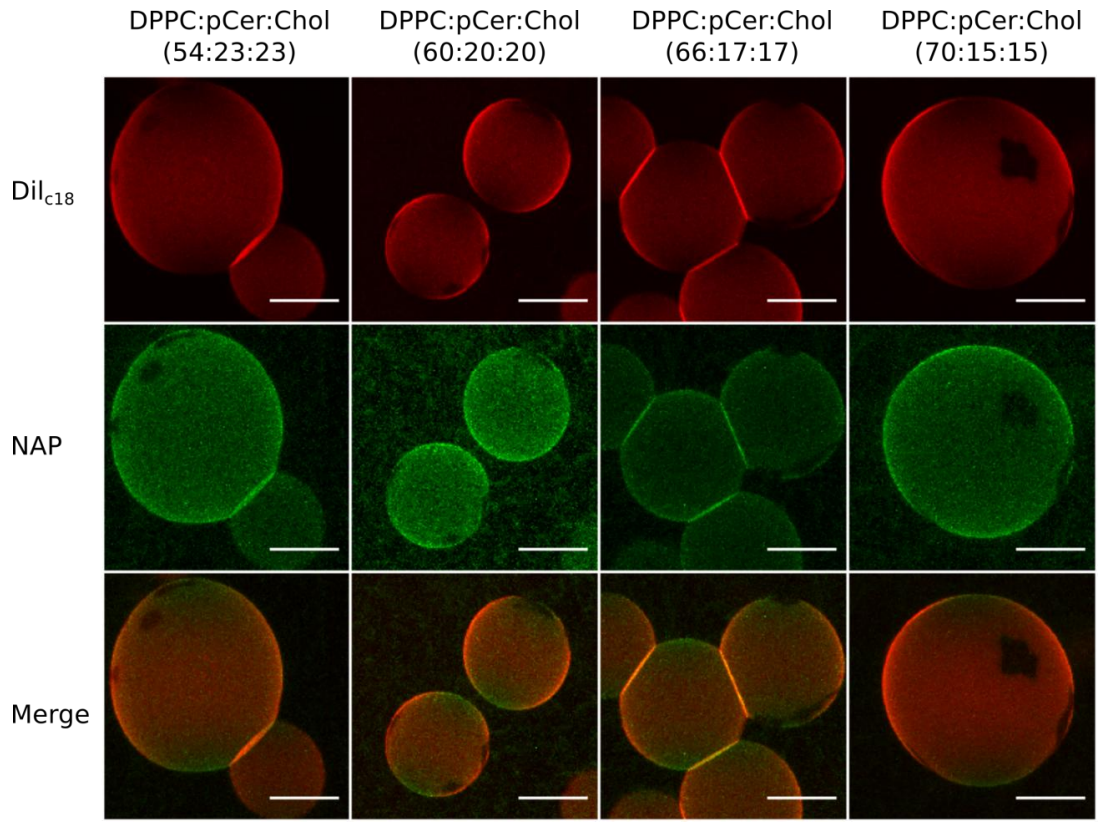

Figure 4.4. Confocal microscopy 3D (z-stack) images of DPPC:pCer:Chol fluorescent giant unilamellar vesicles at different mol ratios, stained with 0.4 mol% DiI_{C18} and 0.5 mol% NAP.

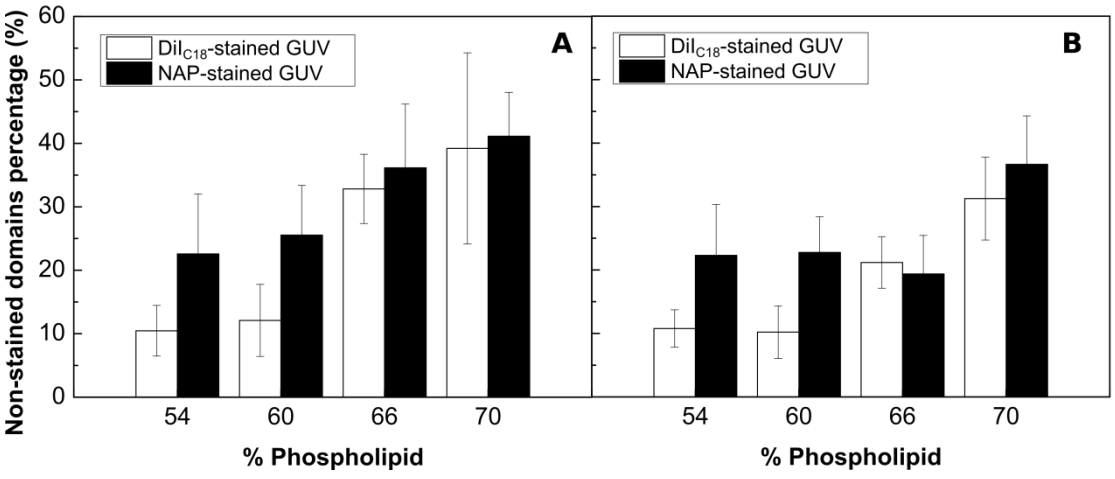

Figure 4.5. Non-stained domain percentage (%) in pSM:pCer:Chol (A) and DPPC:pCer:Chol (B) fluorescent GUV of different phospholipid mol ratios, stained with 0.4 mol % DiI_{C18} and 0.5 mol % NAP. Average values ± S.D. (n = 25-27).

4.3.5 Atomic force microscopy

In order to examine the possible pCer displacement or other effects due to Chol incorporation supported planar bilayers of the above compositions were examined. pSM- and DPPC-based samples were prepared by spin-coating, the use of this procedure being due to the high transition temperature of pCer (93.2 °C) (Jiménez-Rojo *et al.*, 2014), [note that no significant differences were detected either in topography images or force spectroscopy results when SUV adsorption and spin-coating methods were compared (Garcia-Arribas *et al.*, 2015)]. pSM and DPPC bilayers were left to equilibrate for 1 h in order to avoid artifacts due to rapid cooling (Attwood *et al.*, 2013) and to ensure that samples had reached equilibrium, because changes in topography were detected during the first hour after cooling the sample.

In previous studies from our laboratory the pSM:pCer:Chol (54:23:23) mixture was found to be slightly heterogeneous (Busto *et al.*, 2014), i.e. containing a major and a minor gel phase, at least when examined by confocal fluorescence microscopy using the NAP probe, but not when $DiIC_{18}$ was used. This partially unclear result has been confirmed by our present, detailed AFM studies. Segregated domains have been found (Figure 4.6) with clearly different topographic and nanomechanical properties. A ring-shaped segregated phase is observed (Figure 4.6 A) that could correspond to the narrow, elongated minor phase detected by NAP fluorescence [Figure 4 of ref. (Busto *et al.*, 2014)].

This ring-shaped phase divides the bilayer in two regions, inside and outside the ring (Figure 4.6 A). The continuous (outside) region presents an average bilayer thickness of 5.30 nm (Table 4.2) compared to 5.24 nm obtained previously (Garcia-Arribas *et al.*, 2015), which is in the range of thicknesses measured for supported phospholipid-based bilayers in a gel phase (Domènech *et al.*, 2007), Note however that supported gel phases commonly present slightly higher thicknesses (> 5.5 nm). The segregated (ring-shaped) phase has a thickness of 5.7 nm, while thickness is the same in the inner and the continuous phase. pSM:pCer:Chol (60:20:20) shows a similar behavior, and bilayer thickness inside and outside is also quite similar (5.0 ± 0.6 nm) (Figure 4.6 B). The measured thicknesses in the various samples/domains are summarized in Table 4.2.

A notable change is observed in bilayer topography when pSM:pCer:Chol (66:17:17) is used. Under these conditions domains of a discontinuous phase are interspersed in a continuous phase. In this case domain thickness is lower than that of the continuous phase (Figure 4.6 C), respectively 4.5 and 6.4 nm. Finally, the behavior of pSM:pCer:Chol (70:15:15) is quite similar to that of pSM:pCer:Chol

(66:17:17), again showing two different areas with a remarkable difference in thickness (see Table 4.2).

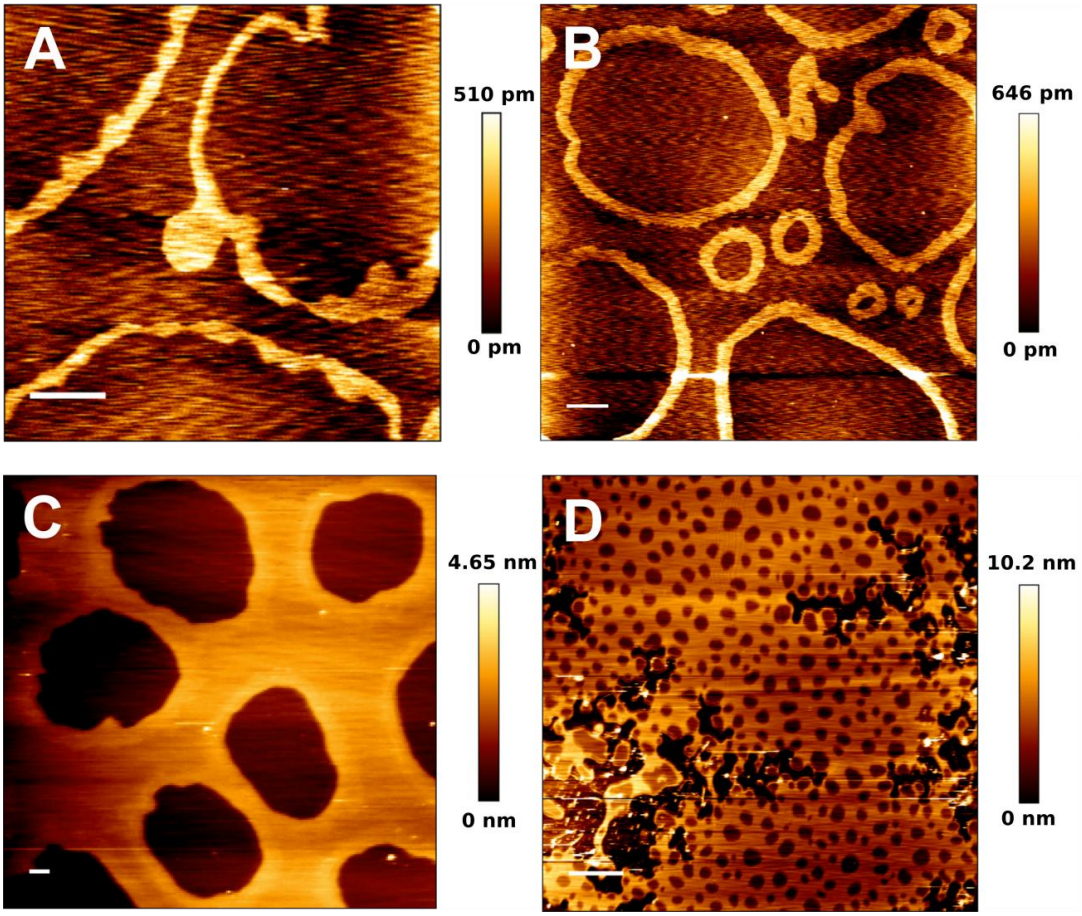

Figure 4.6. AFM images of pSM:pCer:Chol-based SPB at different mol ratios. pSM:pCer:Chol (54:23:23) (A), (60:20:20) (B), (66:17:17) (C) and (70:15:15) (D). Scale bars: 1 μm.

Next, we studied the DPPC:pCer:Chol (54:23:23) ternary mixture, which gives rise to a homogeneous phase from the point of view of height (Figure 4.7 A) as described previously (Garcia-Arribas *et al.*, 2015). The bilayer presents an average thickness of 4.5 ± 0.5 nm, as compared to 5.3 ± 0.2 nm of the pSM-based continuous phase, although the difference is not statistically significant. However, the observed homogeneity does not correlate with the result obtained by GUV fluorescence microscopy (Busto *et al.*, 2014), that showed a narrow, filamentous minor phase. It is possible that the segregation shown in GUV reflects the generation of two ternary phases of similar but not identical compositions. DPPC:pCer:Chol (60:20:20) samples look very similar to the 54:23:23 ones (Figure 4.7 B). Moreover, when the pCer + Chol amount is decreased, in DPPC:pCer:Chol (66:17:17) samples, micron-sized segregated domains of thickness 5.7 ± 0.6 nm appear (Figure 4.7 C). Domains show a different behavior in DPPC:pCer:Chol (66:17:17) and in pSM:pCer:Chol (66:17:17) because DPPC bilayers do not

undergo a Cer-induced reduction in thickness as the pSM-based ones (Garcia-Arribas *et al.*, 2015). Domain thickness reaches 6.2 nm against 4.1 nm in the continuous phase with DPPC:pCer:Chol (70:15:15) (Figure 4.7 D; Table 4.2).

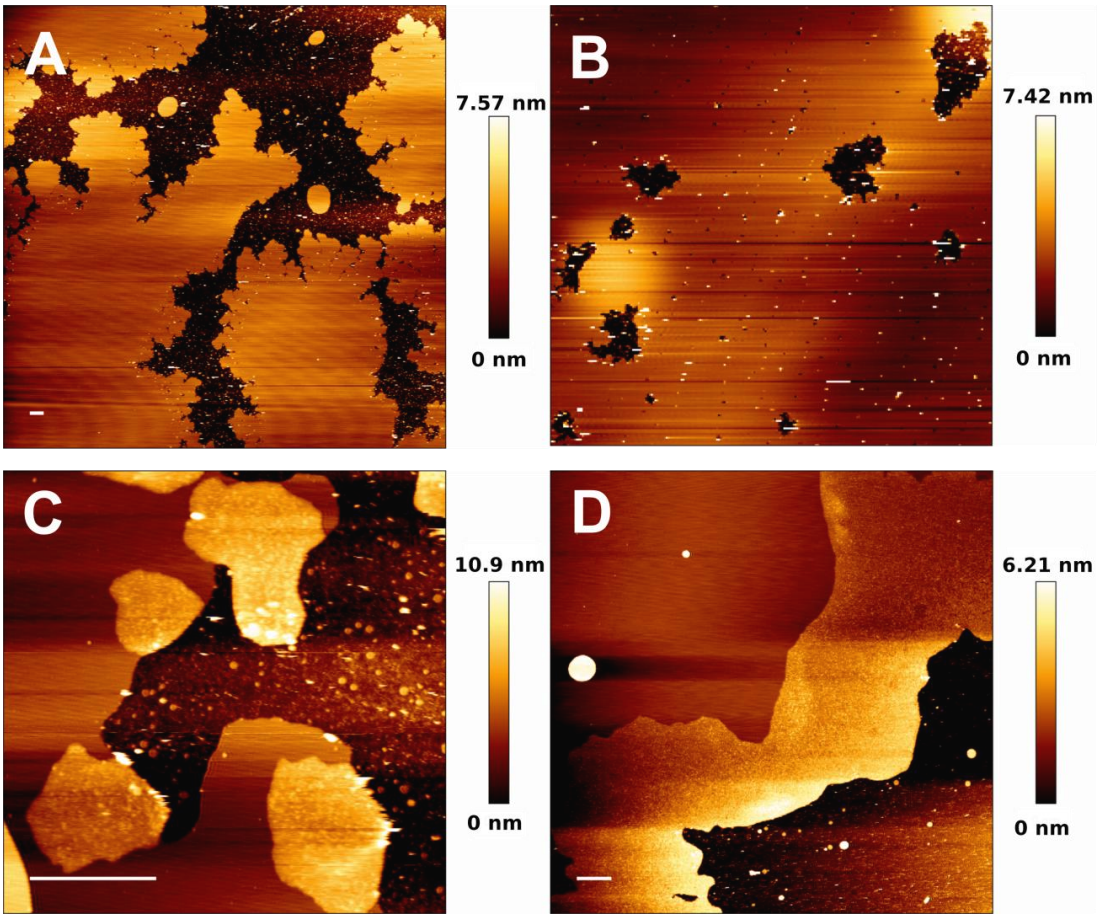

Figure 4.7. AFM images of DPPC:pCer:Chol-based SPB at different mol ratios. DPPC:pCer:Chol (54:23:23) (A), (60:20:20) (B), (66:17:17) (C) and (70:15:15) (D). Scale bars: 1 μm.

4.3.6 Force spectroscopy of ternary mixtures

Force spectroscopy-based indentations were performed to characterize the interaction between these lipids through measurements of the nanomechanical resistance of the bilayer. Usually the force-distance obtained is a jump of 4-6 nm, depending on bilayer thickness (Alessandrini *et al.*, 2012). A region of SPB was imaged and a series of force curves were performed, using the topographical images as a guide. This jump reflects the force with which the tip pierces through the bilayers, the so-called breakthrough force (F_b) (Unsay *et al.*, 2015). In our experiments, force spectroscopy is used to follow the intermolecular packing of

pSM- and DPPC-based ternary SPB through F_b measurements (Figures 4.8 and 4.9 respectively, Table 4.2). pSM:pCer:Chol (54:23:23) shows three different nanomechanical behaviors, confirming the topographic result. In summary, the continuous phase presents the same F_b value (35.4 ± 9.1 nN) as the homogeneous phase found in our previous analysis (Garcia-Arribas *et al.*, 2015), with a very high increase for the ring-shape-segregated phase value (96.3 ± 9.6 nN), while we have been unable to break through the inner phase with the maximum available applied force (130 nN). This fact supports the high intermolecular packing of the inner phase. pSM:pCer:Chol was analyzed at all proportions tested by AFM topography and a number of F_b values equal to the number of phases observed in imaging was obtained (Figure 4.8). Bilayer breakthrough events occur as smooth steps or changes in the slope of the curve, rather than in sharp peaks in most cases, showing that the tip does not undergo a violent and quick punch-through process between lipids but a slower and more difficult flattening of the lipid molecules in order to find a way across the membrane. This speaks in favor of a great degree of intermolecular packing. The F_b values decrease with (pCer + Chol) concentration for the pSM-based ternaries under study. Breakthrough force data can be found in Table 4.2. Moreover, DPPC:pCer:Chol (54:23:23) and (60:20:20) each show two smooth reproducible steps centered at ≈24 and ≈40 nN, respectively (Figure 4.9 A, B, Table 4.2 C1 and C2). It has been shown that the two-step piercing process is related to the distal and proximal leaflets of the bilayer (Alessandrini *et al.*, 2012), and it has been described previously for DPPC:pCer:Chol (54:23:23) (Garcia-Arribas *et al.*, 2015). A higher F_b value (73 - 75 nN) is obtained when DPPC:pCer:Chol mixtures are studied, respectively (66:17:17) and (70:15:15) (Figure 9 C, D), related to the appearance of scattered micron-sized domains in the topographic image. For DPPC-based ternaries, F_b values increase along with (pCer + Chol) concentration, reversing the trend of the pSM-based ones (Table 4.2). However this is heavily influenced by the fact that the DPPC-based ternaries (54:23:23) and (60:20:20) do not exhibit micron-sized domains (Fig 4.7 A, B).

Table 4.2. Bilayer thickness and bilayer nanomechanical resistance of the different SPB under study. Thickness measurements have been made by cross-section height analysis (n = 50–100) of the AFM images taken from each sample. Breakthrough force (F_b) values have been obtained by force spectroscopy (n=800-1300). Continuous phase (C), Segregated phase (S), Inner phase (I). Average values ± SD are shown.

Bilayer composition	Bilayer thickness (nm)	Breakthrough Force (nN)
pSM:pCer:Chol (54:23:23)	C: 5.3 ± 0.3 S: 5.7 ± 0.1	C: 35.4 ± 9.1 S: 96.3 ± 9.6
pSM:pCer:Chol (60:20:20)	C: 5.0 ± 0.6 S: 5.4 ± 0.2	C: 29.17 ± 7.7 S: 67.5 ± 6.9 I: 82.3 ± 7.8
pSM:pCer:Chol (66:17:17)	C: 6.4 ± 0.5 S: 4.5 ± 0.8	C: 45.0 ± 8.1 S: 74.0 ± 6.2
pSM:pCer:Chol (70:15:15)	C: 6.5 ± 0.5 S: 4.4 ± 0.9	C: 42.6 ± 11.4 S: 78.6 ± 10.3
DPPC:pCer:Chol (54:23:23)	C: 4.5 ± 0.5	C1: 24.6 ± 5.7 C2: 40.5 ± 2.6
DPPC:pCer:Chol (60:20:20)	C: 4.3 ± 0.4	C1: 23.1 ± 4.1 C2: 39.2 ± 4.8
DPPC:pCer:Chol (66:17:17)	C: 4.31 ± 0.6 S:5.67 ± 0.56	C:38.3 ± 9.1 S: 75.5 ± 4.4
DPPC:pCer:Chol (70:15:15)	C: 4.1 ± 0.6 S: 6.2 ± 0.25	C: 39.9 ± 3.5 S: 72.7 ± 5.7

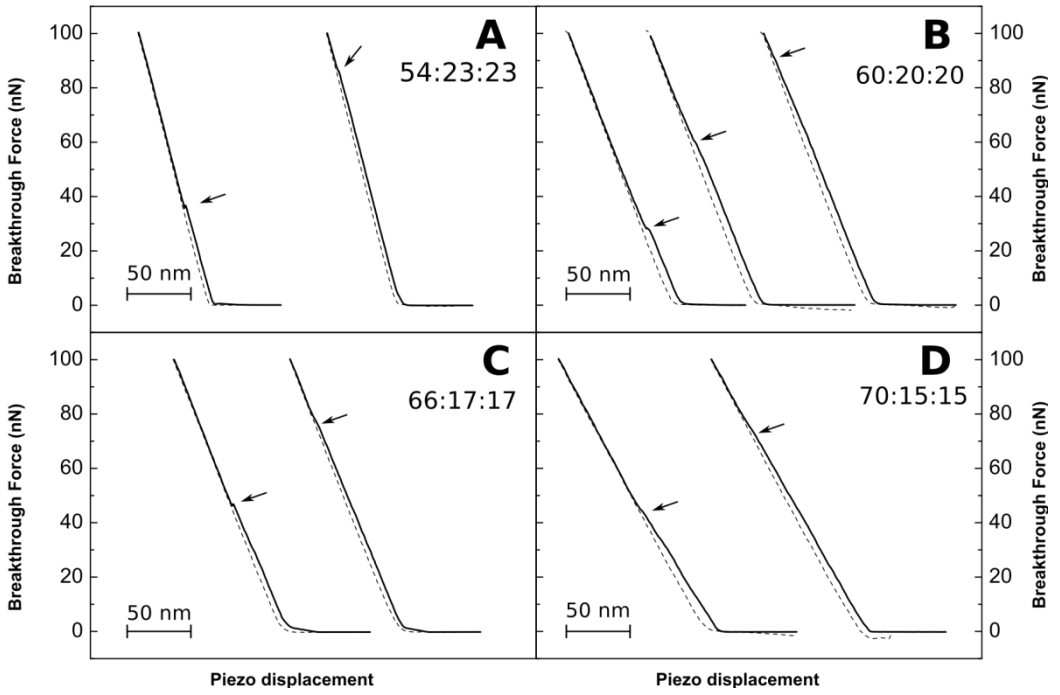

Figure 4.8. Representative AFM tip indentation curves. Representative force curves from the different nanomechanical behaviors detected in pSM:pCer:Chol (54:23:23) (A), pSM:pCer:Chol (60:20:20) (B), pSM:pCer:Chol (66:17:17) (C), pSM:pCer:Chol (70:15:15) (D). The retraction curves are shown as dotted lines. Arrows point to breakthrough events.

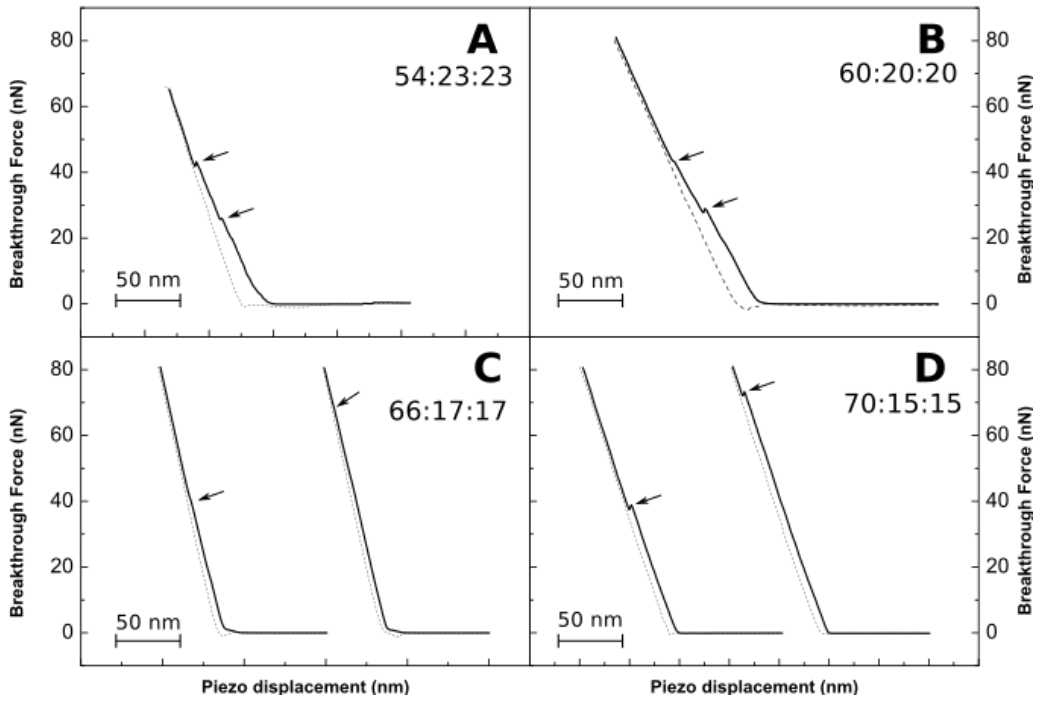

Figure 4.9. Representative AFM tip indentation curves. Representative force curves from the different nanomechanical behaviors detected in DPPC:pCer:Chol (54:23:23) (A), DPPC:pCer:Chol (60:20:20) (B), DPPC:pCer:Chol (66:17:17) (C), DPPC:pCer:Chol (70:15:15) (D). The retraction curves are shown as dotted lines. Arrows point to breakthrough events.

4.4 Discussion

This work was aimed at extending our understanding of SM:Chol:Cer ternary phases in which Chol:Cer exist at equimolar ratios. The origins of our investigation are, on one hand, the capacity of cholesterol and Cer to displace each other in tightly packed bilayers (Megha & London, 2004). On the other hand, we had described the gel phase properties of the ternary mixtures SM:Chol:Cer and DPPC:Chol:Cer at the 54:23:23 mol ratio (Busto *et al.*, 2014).

Cer and Chol are both highly hydrophobic molecules with a small polar headgroup. They both have a tendency to intercalate between phospholipid acyl chains, occupying the same spaces and opening the possibility for mutual displacement. This was first described by Megha and London (2004) (Megha & London, 2004). Alanko et al.. (2005) (Alanko *et al.*, 2005) showed that, in liquid-ordered bilayers consisting of pSM and Chol, Cer would displace Chol from SM if the concentration of both Cer and Chol were in the 10–20 mol% range. The resulting gel phase formed by Cer and SM had a higher packing than the original liquid-ordered phase, thus its nanomechanical properties and thickness were strongly affected (Chiantia *et al.*, 2007, 2006c; Garcia-Arribas *et al.*, 2015; Sullan *et al.*, 2009, 2010).

The Cer-enriched gel phase in phospholipid:Cer binary systems (i.e. in the absence of Chol) seems to be stoichiometrically constant, as a higher content in Cer does not affect its nanomechanical resistance or thickness, but only domain size (Garcia-Arribas *et al.*, 2015). Conversely, when the lipid system is highly saturated in cholesterol, Cer is not able to displace the former (Castro *et al.*, 2009b; Silva *et al.*, 2009; Busto *et al.*, 2010, 2014). This suggests that Cer–Chol displacement is not a matter of a particular affinity, but rather depends on the relative ratio of both molecules, as both have a tendency to occupy the spaces between the lipid acyl chains of phospholipids. Further molecular dynamics simulations showed that for both 54:23:23 ternaries ceramide molecules displace themselves several angstroms from the lipid tails zone towards the lipid tails-heads interphase of the bilayer to accommodate and facilitate Cer-Chol interactions (García-Arribas *et al.*, 2016c). This molecular behaviour could enhance interdigitation events which could cause stronger lipid-lipid hydrophobic interactions, such as van der Waals interactions, which are distance-dependant. This would explain the rather low bilayer thickness detected for the ternary mixtures.

The above observations and hypotheses led to the question on what would be the case if both lipids were present at saturating concentrations in the system, at an equimolar Cer:Chol mol ratio. To achieve maximum saturation, phospholipid:Chol mol ratio should be around 70:30 (Maulik & Shipley, 1996)

while for phospholipid:Cer the maximum stable ratio would be 67:33 (Busto *et al.*, 2009). Thus a simple model to study this phenomenon would be a 54:23:23 (a 70:30:30 system recalculated on a 100-basis) phospholipid:Chol:Cer mol ratio, with a Cer:Chol ratio of 1:1. This system would contain a phospholipid being equally and simultaneously saturated by both Cer and Chol. As mentioned above, Cer and Chol are actually able to coexist in a 54:23:23 single gel phase with intermediate properties between Cer- enriched domains and Chol-driven liquid-ordered phases (Busto *et al.*, 2014; Garcia-Arribas *et al.*, 2015) and the phase would probably be stabilized by direct Cer–Chol interactions. This phase is probably non-stoichiometrically constant (as opposed to SM:Cer domains) and the properties would depend on its composition. In this work, using tPA and DPH fluorescence measurements, we have provided further evidence that the 54:23:23 ternary mixtures have unique properties that cannot be reproduced by a mixture of phospholipid:Chol (70:30) and phospholipid:Cer (70:30) vesicles (Figure 4.1). Furthermore we have observed the properties of a series of mixtures in which the phospholipid mol ratio has been varied, while keeping constant the 1:1 Cer:Chol mol ratio.

The main observation in this paper is that in ternary mixtures of pSM (or DPPC):Cer:Chol at a mol ratio X:Y:Y, for X=54% the corresponding bilayers appear largely homogeneous, while for higher values of X, e.g. 60, 66, or 70 mol%, macroscopic heterogeneity becomes obvious. A comment on the concept of 'homogeneity' might be pertinent here. At least in the context of this study, the words homogeneity/heterogeneity apply to direct observations of bilayers using mainly confocal microscopy, AFM, or DSC. They should not be confused with the thermodynamic concepts of ideal or non-ideal mixing. Ideal mixing of membrane lipids is rarely observed, particularly when different lipid classes are mixed. Yet non-ideal mixing may occur at the nanoscopic level, with apparent homogeneity being observed at the micrometre scale. An additional caveat on 'homogeneity': a GUV bilayer may appear homogeneous when stained with one particular dye, but not when another dye is used, see e.g. DiI_{C18} and NAP stains in Busto et al.. (2014) (Busto *et al.*, 2014), or in Figure 4.3, 54:23:23 mixture in this paper.

Homogeneity can also be observed with one technique, but not with another, e.g. the 54:23:23 mixture in Figures 4.3 (DiI_{C18}) and 4.6 (AFM). The latter case is interesting because AFM detects three different phases: a continuous phase, ring-shaped segregated domains, and the domains inside the rings. This segregated phase did not appear in our previous AFM analysis, and it was only visible with NAP staining, in the form of thin filaments (Garcia-Arribas *et al.*, 2015), we attribute the difference to our recent improvements in the AFM Nanowizard II z-piezo components. Force spectroscopy measurements (Table 4.2) have shown that the continuous phase has the lowest breakthrough force (F_b), while the inner

phase could not be pierced with the maximum available applied force (130 nN). These results point to a very tight lipid packing inside the rings, although we cannot provide quantitative data on their mechanical resistance properties. A similar situation was described previously by Zou's laboratory, who were unable to break through SM:Cer-rich domains using DNP-S cantilevers with spring constants of 0.06 – 0.28 N/m (Sullan *et al.*, 2009). It is possible that the ring-shape segregated phase that surrounds the inner phase further limits its mobility, thus increasing its mechanical resistance. pSM:pCer:Chol (60:20:20) shows a similar behavior, although in this sample we were able to pierce through the inner phase (see values in Table 4.2). The fact that the inner phase shows the highest F_b value suggests again the 'fence' role of the ring-shaped segregated phase.

Noticeable differences are however found in pSM:pCer:Chol (66:17:17) and (70:15:15). DSC thermograms are displaced to higher temperatures showing clearly asymmetric endothermic transitions (Figure 4.2 Table 4.2), and giant unilamellar vesicles show an increase in the area occupied by NAP- and DiI_{C18}-depleted phases (Figure 4.5), perhaps because cholesterol concentration is not enough to abolish pSM:pCer-enriched domains. This would also explain the coexistence of segregated pSM:pCer domains in SPBs (Figure 4.6) when the saturated phospholipid concentration increases. pSM:pCer-enriched domains show a decrease in bilayer thickness compared to the surrounding DiI_{C18}-continuous phase, perhaps related to lipid interdigitation, as previously mentioned (Garcia-Arribas *et al.*, 2015).

The effect of replacing pSM with DPPC in ternary mixtures was investigated to characterize the different affinities of pCer and Chol for DPPC and for pSM. In general, DPPC:pCer:Chol ternary mixtures follow the same trend as pSM-based ones in DSC and confocal microscopy experiments. DSC shows an endothermic transition which is displaced to higher temperatures when (Chol + pCer) concentration decreases. Giant unilamellar vesicles show an increase in DiI_{C18}- and NAP-depleted areas when (pCer + Chol) decreases (Figure 4.5). However DPPC:pCer:Chol (54:23:23) and DPPC:pCer:Chol (60:20:20) appear homogeneous when SPB are imaged with AFM. The formation of a homogeneous bilayer can be related to the pCer and Chol lower degree of packaging with DPPC, which allows a higher freedom of motion to these lipids. When (pCer + Chol) decreases in DPPC:pCer:Chol (66:17:17) or particularly in DPPC:pCer:Chol (70:15:15), DPPC:pCer-enriched domains appear (Figures 4.4, .4.5, 4.7). These domains show an increase in bilayer thickness compared to the surrounding DiI_{C18}-continuous phase, due to a lower degree of lipid interdigitation as described previously (Garcia-Arribas *et al.*, 2015). Again, a lower degree of lipid interdigitation in DPPC:pCer-enriched domains is perhaps at the origin of the lower mechanical resistance of these domains when they are compared to pSM:pCer at lower (pCer +

Chol) amounts (Table 4.2). These results are in agreement with the suggestions that pCer or Chol, individually considered, have a higher affinity for pSM than for DPPC, which can be due to the amide and hydroxyl groups of pSM acting as hydrogen bond acceptors and donors while the DPPC polar head presents only hydrogen bond-accepting groups (García-Arribas *et al.*, 2016b). Moreover the existence of a (near)-homogeneous ternary phase at DPPC:pCer:Chol at 60:20:20, while the corresponding pSM-based bilayers show lateral phase separation (Figures 4.3, 4.4, 4.6, 4.7) indicates that the high affinities of Cer and Chol for SM are not an essential factor in the formation of the gel ternary phase.

It is difficult to ascertain at present whether or not these observations are directly applicable to the situation in the cell membranes. It is well-known that the plasma membrane is rich in SM and Chol, and that SM is partly hydrolyzed to ceramide and phosphorylcholine by an acid sphingomyelinase under stress conditions. Thus the three main molecules in our study could well coexist in a very small area under certain conditions. Note that ternary-like domains (i.e. enriched in both Cer and Chol) have been detected in fluid model bilayers, such as red blood cell lipid extracts (García-Arribas *et al.*, 2016a). The currently available technology does not allow the *in vivo* direct observation of transient nanodomains, as SM, Chol and Cer would probably form in the cellular environment, but fast progress is being made in this area, so that our hypothesis might become amenable to direct testing very soon (Goñi, 2019; Sezgin *et al.*, 2017).

In conclusion, we have found that, for bilayers consisting of mixtures of composition phospholipid:Chol:pCer at X:Y:Y mol ratios, the phospholipid being either pSM or DPPC, mixtures close to 54:23:23 give rise to a pure (or at least a highly predominant) gel phase, as detected by DSC, GUV confocal fluorescence microscopy, or AFM. However when the proportion of phospholipid increases beyond 60 mol%, i.e. in 66:17:17 or 70:15:15 mixtures, a clear lateral phase separation occurs at the microscopic (i.e. μm) scale. Heterogeneity, or lateral phase separation, occurs more easily with pSM than with DPPC. These data can be interpreted in terms of a pCer:Chol interaction, that would predominate at low phospholipid concentrations, while at the higher phospholipid concentrations pSM:pCer and pSM:Chol interactions would become more important, giving rise to coexisting gel and liquid-ordered phases respectively. The lower hydrogen-bonding capacity of DPPC with respect to pSM would explain the lower tendency towards macroscopic phase separation of the DPPC-based mixtures.

4.5 Supplementary data

4.5.1 Supplementary methods

Measuring non-stained areas in GUV. The Supplementary Figure 4.S1 shows two examples of the non-stained areas quantification procedure, respectively for GUV containing micro- and nano-domains.

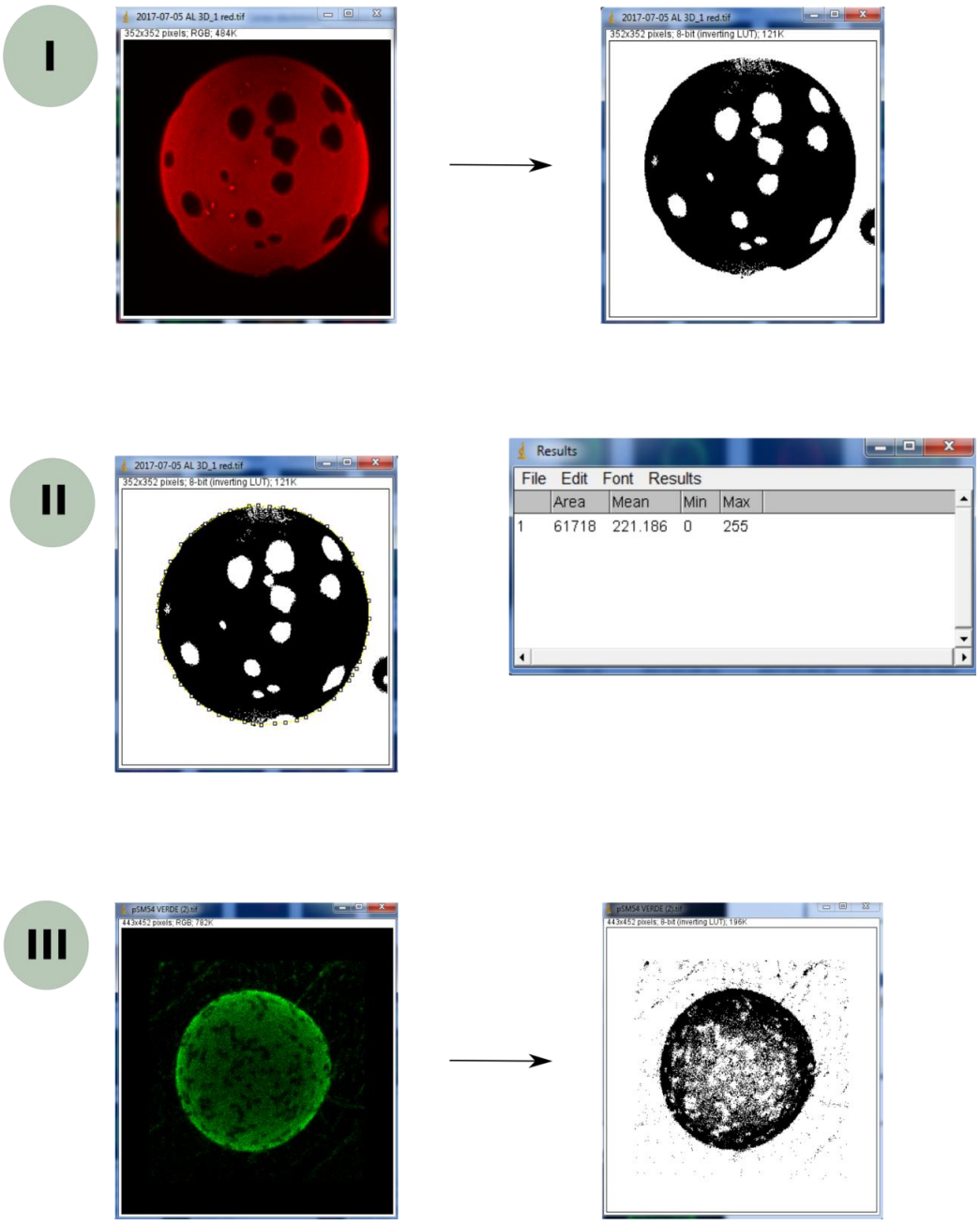

Figure 4.S1. Measuring non-stained areas in GUV method.

4.5.2 Supplementary results

tPA fluorescence lifetimes. In bilayers of pure pSM or DPPC, tPA showed a bi-exponential intensity decay with a long lifetime component of 45-50 ns and a shorter lifetime around 15 ns. Addition of 30 mol% Chol led to a decrease in the longest lifetime component and its fractional amplitude as described in (Wolber & Hudson, 1981), while addition of 30 mol% pCer resulted in an increase in the longest lifetime component, probably due to the gel-phase forming effect of the latter lipid. All binary mixtures exhibited bi-exponential decays, in accordance with studies supporting the presence of a single phase in bilayers with those compositions: an L_o phase in the case of Chol-containing bilayers (Busto *et al.*, 2010) and a highly rigid gel-like phase in the case of membranes with Cer (Busto *et al.*, 2009). The longest lifetime component of the ternary mixtures containing both Chol and pCer showed an intermediate value as compared to those of the binary mixtures, although the fractional amplitude was more similar to that of the Chol-containing binary mixtures. Similarly to the other compositions, the ternary mixture also showed a bi-exponential intensity decay. However, when a control sample containing a mixture of equal amounts of DPPC:Chol and DPPC:pCer liposomes was studied, the recovered intensity decay was still well adjusted to a bi-exponential decay. Therefore, the intensity decay of tPA seemed to be unable to distinguish between different ordered domains, so that the result obtained was just an average of the longest lifetimes of such domains and of their corresponding fractional amplitudes. It must be noted, however, that while the longest lifetimes of the control and the corresponding ternary mixture were identical, that was not the case for their fractional amplitudes (Supplementary Figure 4.S2).

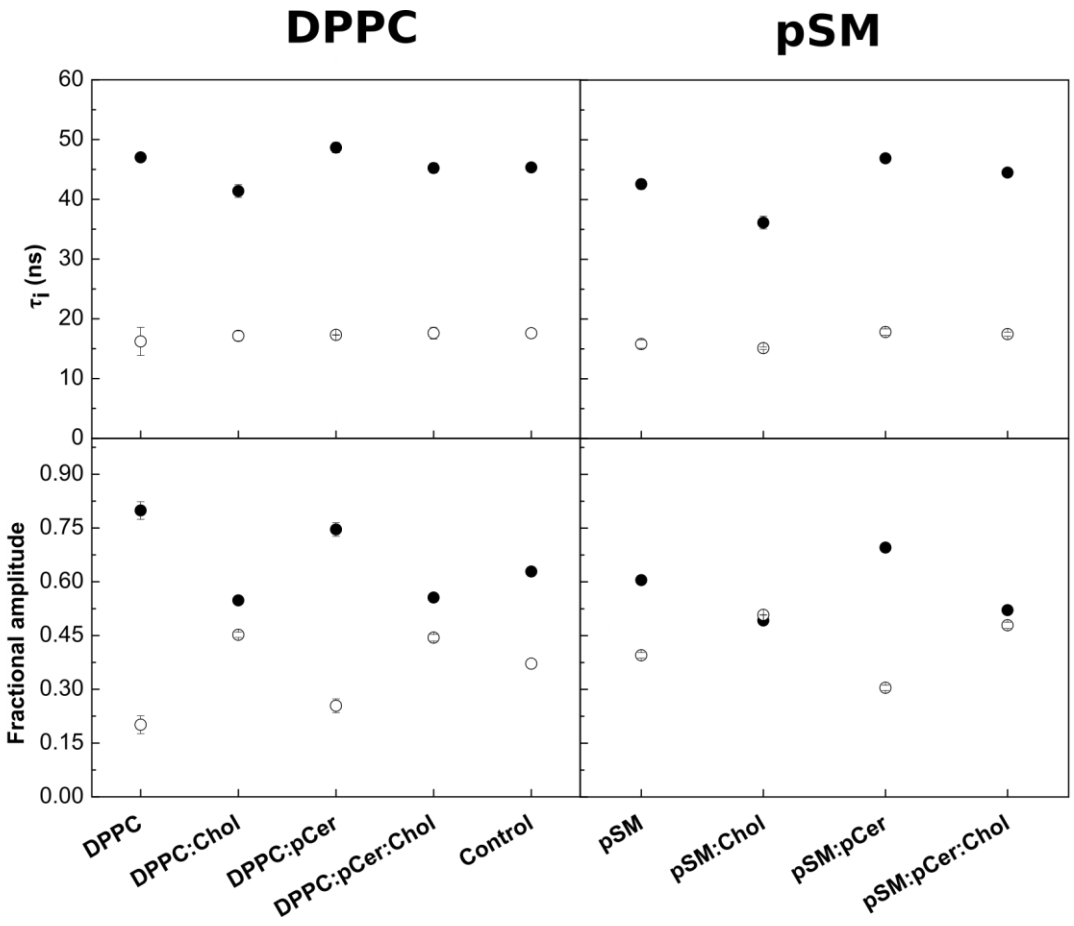

Figure 4.S2. tPA fluorescence lifetimes. Effect of Chol and/or pCer incorporation into pSM or DPPC bilayers at room temperature. tPA intensity decays were fitted to obtain two lifetime components (top panels, filled circles and empty circles). The bottom panels show the fractional amplitudes corresponding to the long lifetime (filled circles) and the short lifetime (empty circles). The binary mixtures were 7:3 (mol ratio) and the ternary mixtures were 54:23:23 (mol ratio). The control was a mixture of equal amounts of liposomes of both DPPC binary mixtures (DPPC:Chol 7:3 and DPPC:pCer 7:3). Values shown are averages of three separate experiments ± SD, but for the control (a single experiment).

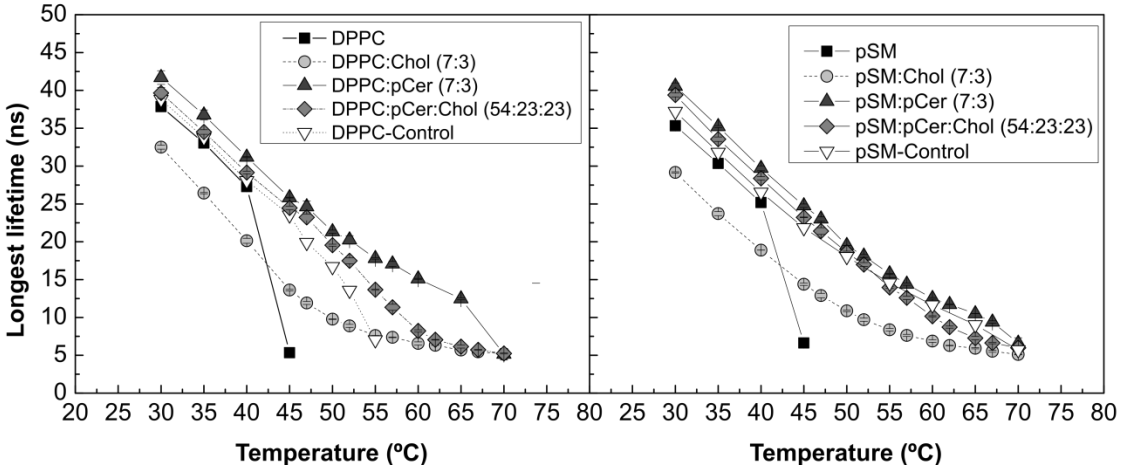

Figure 4.S3. Shortening of the tPA longest lifetimes with increasing temperatures. Bilayer compositions are given in the insets. Values shown are averages of three separate experiments ± SD, but for the controls (a single experiment). The controls were a mixture of equal amounts of liposomes of each binary mixture, either (DPPC:Chol 7:3 + DPPC:pCer 7:3) or (pSM:Chol 7:3 + pSM:pCer 7:3).

As temperature was increased, the longest tPA lifetime component was shortened (Figure 4.S3). Both pure pSM and DPPC bilayers showed a sharp decrease of the longest lifetime to < 10 ns at 45 ºC, when both bilayers became fluid (Figure 4.S3, squares). Binary mixtures with pCer showed a nearly linear decrease of the longest lifetime with a drop below 10 ns at 70 ºC (Figure 4.S3, triangles). This is in good agreement with the DSC thermograms (Busto *et al.*, 2009) where the gel-fluid transition was completed around that temperature. Binary mixtures with Chol exhibited a different trend with no sudden drop but a gradual change of slope when reaching the range of short lifetimes (<10 ns) at 50-55 ºC (Figure 4.S3, circles). An intermediate behavior was observed in ternary mixtures: at low T, the longest lifetime values were similar to those of the binary mixtures with pCer, then the trend of the decrease resembled that of the Chol-containing mixtures, and the low lifetime regime was reached at an intermediate temperature of 60-65 ºC (Figure 4.S3, diamonds). Controls containing a mixture of equal amounts of DPPC:Chol (or pSM:Chol) and DPPC:pCer (or pSM:pCer) liposomes showed a similar behavior to that of the pSM:pCer binary, or of the ternary mixtures (Figure 4.S3, inverted triangles).

CHAPTER 5:

COMPLEX EFFECTS OF 24:1 SPHINGOLIPIDS IN MEMBRANES CONTAINING DIOLEIOYL PHOSPHATIDYLCHOLINE AND CHOLESTEROL

CHAPTER 5: COMPLEX EFFECTS OF 24:1 SPHINGOLIPIDS IN MEMBRANES CONTAINING DIOLEIOYL PHOSPHATIDYLCHOLINE AND CHOLESTEROL

5.1 Introduction

The role of sphingolipids as second messengers in diverse cellular processes has attracted the attention of biophysicists and biochemists in recent years (Futerman & Hannun, 2004; Hannun & Obeid, 2011; Castro *et al.*, 2014). Ceramides are among the most studied sphingolipids due to their proposed role in cell death processes (Obeid *et al.*, 1993; Kolesnick, 2002; Taha *et al.*, 2006; Chipuk *et al.*, 2012; Zhu *et al.*, 2014; Lang *et al.*, 2015) and their capacity to induce bilayer heterogeneity, i.e. domain segregation of ceramide-enriched areas within the membrane (Stancevic & Kolesnick, 2010). Long chain ceramides are also able to modify the biophysical properties of membranes as they induce lipid flip-flop (Contreras *et al.*, 2003) and enhance solute efflux across the membrane (Montes *et al.*, 2002; Siskind *et al.*, 2002). Most of the aforementioned studies focus on C16:0 ceramide (palmitoyl ceramide, pCer) since pCer has been considered paradigmatic among long chain ceramides.

However recent studies in lipidomics show that nervonoyl sphingolipids (C24:1) are also abundant and, in some cases, concentration levels are on par with their C16:0 counterparts (Quinn *et al.*, 2005; Maté *et al.*, 2014). Very few studies have been performed to characterize the effect of C24:1 sphingolipids in lipid membranes and while comparative experiments between C16:0 and C24:1 sphingolipids as pure lipids are common in the literature (Pinto *et al.*, 2008, 2011; Slotte, 2013; Jiménez-Rojo *et al.*, 2014; Pinto *et al.*, 2014), studies of their effects in multicomponent bilayers are scarce (Maté *et al.*, 2014; Maula *et al.*, 2015), and the effects of different combinations of C16:0 and C24:1 sphingolipids of different class (e.g. sphingomyelin, ceramide) are virtually unexplored.

Bilayers in the gel (L_β) phase present low fluidity and increased lipid chain order. They typically exhibit higher nanomechanical resistance (Garcia-Manyes *et al.*, 2010; Garcia-Arribas *et al.*, 2015) and cause a significant increase in bilayer thickness (Nagle & Tristram-Nagle, 2000; Domènech *et al.*, 2007). In turn the 'lipid raft' hypothesis is focused on liquid-ordered phases (which are often defined as a middle ground between gel and fluid phases) enriched in sphingolipids and cholesterol (Simons & Ikonen, 1997; Simons & Gerl, 2010). However, sphingolipids such as ceramides are able to segregate into highly packed gel domains that could serve as signaling platforms in vivo for ceramide-related signaling cascades, such as those involved in cell death processes (Cremesti *et al.*, 2001, 2002; Kornhuber *et al.*, 2014). Ceramide-rich platforms would also facilitate protein clustering and membrane reorganization (Kolesnick *et al.*, 2000; Cremesti *et al.*, 2002; Gulbins & Li, 2006; Kornhuber *et al.*, 2014), thus being a strong governing factor of protein-based interactions. This hypothesis is supported by some in vivo experiments regarding the effects of ceramide-rich domains (Grassmé *et al.*, 2001; Grassme *et al.*, 2002). However, the complete confirmation of this hypothesis is hampered by problems such as the large number of components present in cell signaling cascades and, particularly, in the cell-death machinery.

The effect of cholesterol has been reported as a modulator of the generation of ceramide-enriched domains by displacing ceramide from mixtures with other lipids (Castro *et al.*, 2009b; Busto *et al.*, 2014) and ceramide generation can also cause disassembly of liquid-ordered phases enriched in cholesterol by sphingomyelin recruitment (Megha & London, 2004; Chiantia *et al.*, 2006a, 2007; Sot *et al.*, 2008). Therefore the presence of cholesterol could indeed have effects on the cell death-inducing capacities of ceramide (Montero *et al.*, 2008; Garcia-Ruiz *et al.*, 2009). Even in some situations non-stoichiometrically constant gel phases enriched in both ceramide and cholesterol can also appear, caused by direct ceramide-cholesterol interaction (García-Arribas *et al.*, 2016c, 2016a), thus ceramide:cholesterol ratios could be managed by living cells to fine tune membrane properties (García-Arribas *et al.*, 2016b). These studies are though focused on C16:0 sphingolipids, particularly C16:0 ceramide, and no further studies have been performed on C24:1 sphingolipids.

In the present study we aim to describe the effects of different combinations of C16:0 and C24:1 sphingolipids in model membranes composed of DOPC:SM:Chol (2:1:1) + Cer in order to recreate a L_α-L_o cell membrane environment in the presence of ceramide, where SM can be nervonoyl sphingomyelin (nSM), palmitoyl sphingomyelin (pSM) or an equimolecular mixture of both, and Cer can be nervonoyl ceramide (nCer), pCer o an equimolecular mixture of both. For this purpose, a combination of techniques was used: atomic force microscopy (AFM), confocal microscopy, and differential scanning calorimetry (DSC).

5.2 Materials and methods

5.2.1 Materials

1,2-dioleoyl-sn-glycero-3-phosphocholine (DOPC), N-palmitoyl-D-erythro-sphingosylphosphorylcholine (16:0 SM, pSM), N-nervonoyl-D-erythro-sphingosyl-phosphorylcholine (24:1 SM, nSM), N-palmitoyl-D-erythro-sphingosine (16:0 Cer, pCer), N-nervonoyl-D-erythro-sphingosine (24:1 SM, nCer) and lipophilic fluorescent probe 1,2-dioleoyl-sn-glycero-3-phosphoethanolamine-N-(lissamine rhodamine B sulfonyl) (Rho-PE) were purchased from Avanti Polar Lipids (Alabaster, AL, USA). Buffer solution ('assay buffer') for experiments was 20 mM PIPES, 1 mM EDTA, 150 mM NaCl, pH 7.4. All other reagents were of analytical grade.

5.2.2 Differential scanning calorimetry (DSC)

The measurements were performed in a VP-DSC high-sensitivity scanning microcalorimeter (MicroCal, Northampton, MA, USA). Both lipid and buffer solutions were degassed prior to loading into the appropriate cell in the form of MLVs. MLVs were prepared as described previously, but in assay buffer (NaCl 150 mM, 20 mM PIPES, 1 mM EDTA) and at a 1 mM concentration. 0.5 ml at 1 mM total lipid concentration was loaded into the calorimeter, performing 3-9 heating scans at a 45 °C/h rate, between 10 and 100 °C for all samples. Phospholipid concentration was determined as lipid phosphorus, and used together with data from any of the reproducible scans, to obtain normalized thermograms. The software Origin 7.0 (MicroCal), provided with the calorimeter, was used to determine the different thermodynamic parameters from the scans. The software PeakFit (Systat Software Inc., Chicago, IL, USA) was used for endotherm deconvolution.

5.2.3 Confocal microscopy of giant unilamellar vesicles (GUV)

Giant vesicles were prepared at 60 °C by electroformation on a pair of platinum (Pt) wires by a method first developed by Angelova and Dimitrov, modified as described previously (Angelova & Dimitrov, 1986; Dimitrov & Angelova, 1988; Montes *et al.*, 2007). Lipid stock solutions were prepared in 2:1 (v/v) chloroform/methanol at 0.27 mg/mL, and appropriate volumes of each preparation were mixed. Labeling was carried out by premixing the desired fluorescent probe (Rho-PE) with the lipids in organic solvent. Fluorescent probe concentration was 0.4 mol % Rho-PE. The samples were deposited on platinum (Pt) wires. The Pt wires were placed under vacuum for 2 h to completely remove

the organic solvent. The sample was covered to avoid light exposure and allowed to precipitate onto the Pt wires for 5 min. One side of the chamber was then sealed with a coverslip. We added 500 mL assay buffer, prepared with high-purity water (SuperQ, Millipore, Billerica, MA) heated at 75 °C, until it covered the Pt wires and the latter were connected to a TG330 function generator (Thurlby Thandar Instruments, Huntingdon, UK). The alternating current field was applied in three steps, all performed at 60 ºC: 1), frequency 500 Hz, amplitude 220 mV (35 V/m) for 5 min; 2), frequency 500 Hz, amplitude 1900 mV (313 V/m) for 20 min; and 3), frequency 500 Hz, amplitude 5.3 V (870 V/m) for 90 min. The temperatures used for GUV formation correspond to those at which the different membranes display a single fluid phase. The generator and the water bath were switched off, and vesicles were left to equilibrate at room temperature for 1 h. After GUV formation, the chamber was placed onto an inverted confocal fluorescence microscope (Nikon D-ECLIPSE C1, Nikon, Melville, NY). The excitation wavelength for Rho-PE was 561 nm, and the images were collected using a band-pass filter of 593 ± 20 nm. Image treatment and quantitation were performed using the software EZ-C1 3.20 (Nikon). No difference in domain size, formation, or distribution was detected in the vesicles during the observation period or after laser exposure.

5.2.4 Supported planar bilayer (SPB) formation

SPB were prepared on high V-2 quality scratch-free mica substrates (Asheville-Schoonmaker Mica Co., Newport News, VA, USA) previously attached to round 24 mm glass coverslips by the use of a two-component optical epoxy resin (EPO-TEK 301-2FL, Epoxy Technology Inc., Billerica, MA, USA). SPB are prepared by the vesicle adsorption method (McConnell *et al.*, 1986; Jass *et al.*, 2000). Multilamellar vesicles (MLV) were initially prepared by mixing the appropriate amounts of synthetic pure lipids in chloroform:methanol (2:1, v/v) solutions, including 0.4 mol% Rho-PE. Samples were then dried by evaporating the solvent under a stream of nitrogen and placing them under vacuum for 2 h. The samples were then hydrated in assay buffer and vortexed at a temperature above that of the sample lipids highest phase transition. After complete lipid detachment from the test tube bottom, formed MLV were introduced in a FB-15049 (Fisher Scientific Inc., Waltham, MA, USA) bath sonicator and kept at 70 °C for 1 h. In this way a proportion of small unilamellar vesicles (SUV) were generated. Thereafter, 120 µl assay buffer containing 3 mM $CaCl_2$ were added onto previously prepared 1.2 cm^2 freshly cleaved mica substrate mounted onto a BioCell coverslip-based liquid cell for atomic force microscopy (AFM) measurements (JPK Instruments, Berlin, Germany). 60 µl sonicated vesicles were then added on top of the mica. Divalent cations such as Ca^{2+} or Mg^{2+} have been described as enhancers of the vesicle adsorption process onto mica substrates (Attwood *et al.*, 2013). Final lipid concentration was 150 µM. Vesicles were left to adsorb and extend for 30 min

keeping the sample temperature at 60 °C. In order to avoid sample evaporation and ion concentration, after the first 5 min the buffer was constantly exchanged with assay buffer without $CaCl_2$ at 60 °C for the remaining time. Additional 30 min were left for the samples to equilibrate at room temperature, discarding the non-adsorbed vesicles by washing the samples 10 times with assay buffer without $CaCl_2$, in order to remove remaining Ca^{2+} cations from the solution which are reported to drastically affect the breakthrough force (F_b) results of lipid bilayer nanoindentation processes (Garcia-Manyes *et al.*, 2010). The efficiency of rinsing processes to obtain proper and clean supported lipid bilayers has been reported (Oncins *et al.*, 2005). This extension and cleaning procedure allowed the formation of bilayers that did not cover the entire substrate surface. The presence of lipid-depleted areas helped with the quantification of bilayer thicknesses and the performance of proper controls for force-spectroscopy measurements. Planar bilayers were then left to equilibrate at room temperature for 1 h prior to measurements in order to avoid the presence of possible artifacts as segregated domains appear at high temperatures (over the T_m) (Garcia-Manyes *et al.*, 2005) and could still be present at lower temperatures if the cooling process was too fast (> 1 °C/min) (Attwood *et al.*, 2013). Finally, the BioCell was set to 23 °C to start the AFM measurements.

5.2.5 AFM imaging

Planar bilayer topography was performed under contact mode AFM scanning (constant vertical deflection) in a NanoWizard II AFM (JPK Instruments, Berlin, Germany). For proper measurements the AFM was coupled to a Leica microscope and mounted onto a Halcyonics Micro 40 anti-vibration table (Halcyonics, Inc., Menlo Park, CA, USA) and inside an acoustic enclosure (JPK Instruments). The BioCell liquid sample holder (JPK Instruments) was used in order to control the assay temperature at 23 °C. V-shaped MLCT Si_3N_4 cantilevers (Bruker, Billerica, MA, USA) with nominal spring constants of 0.1 or 0.5 N/m were used for bilayer imaging, always keeping the minimum possible force (0.5 – 1 nN). 512 x 512 pixel resolution images were collected at a scanning rate between 1 and 1.5 Hz and line-fitted using the JPK Data Processing software as required prior to topography-related data collection. In this regard, bilayer thicknesses were calculated by cross-section height analysis (n=50-100) from no less than 3 images of at least 3 independent sample preparations with individual cantilevers.

5.2.6 Epifluorescence microscopy

Direct AFM-coupled inverted epifluorescence microscopy was performed in a Leica DMI 4000B microscope (Leica Microsystems, Wetzlar, Germany) using an

appropriate filter cube for Rho-PE fluorochrome (excitation filter HQ545/30x, dichroic mirror Q570LP and emission filter HQ610/75m) (Chroma Tech., Bellows Falls, VT, USA). Images were acquired using a 40X/0.60 LD objective (Leica Microsystems) with a high resolution ORCA-R2 digital CCD camera (Hamamatsu Photonics, Shizuoka, Japan).

5.2.7 Force spectroscopy

Prior to imaging, V-shaped MLCT Si_3N_4 cantilevers (Bruker, Billerica, MA, USA) with nominal spring constants of 0.1 or 0.5 N/m were individually calibrated in a lipid-free mica substrate in assay buffer using the thermal noise method. After proper bilayer area localization by means of AFM topography and direct epifluorescence microscopy, force spectroscopy was performed at a speed of 1 μm/sec in no less than 500 x 500 nm bilayer areas in the form of 10x10 or 15x15 grids. Force steps were determined for each of the indentation curves as reproducible jumps within the extended traces. The resulting histograms were generated from at least 3 independent sample preparations with at least 3 independently calibrated cantilevers (n=350-1800). Control indentations were always performed in lipid-free areas before and after bilayer indentations to ascertain the formation of a single bilayer and the absence of artifacts or debris on the tip, assessed by the lack of any force-distance step on both trace and retrace curves.

5.3. Results

Lipid gel phases surrounded by a fluid phase are identifiable using fluorescence techniques involving lipid fluorophores. Throughout this study the lipid fluorophore is Rho-PE, which partitions preferentially into fluid phases and tends to be excluded from the more ordered phases. In some cases, only a relative partition is observed, which means that the fluidity of the various phases differs but only to a certain degree. Rho-PE is used for confocal fluorescence visualization of GUV (Figure 5.1) and for epifluorescence visualization of supported planar bilayers, coupled with atomic force microscopy. In turn, AFM allows the direct detection of segregated phases either by imaging (segregated ordered phases tend to have increased thickness, and they appear with brighter colors on the images) or by force spectroscopy (ordered phases present higher nanomechanical resistance when force indentation curves are applied). By combining the above data the lipid bilayer can be characterized and different lipid compositions can be comparatively studied.

5.3.1 pSM-based samples

DOPC:pSM:Chol (2:1:1) samples containing additional 30 mol% ceramide were prepared (either 30 mol% pCer, or 30 mol% nCer, or 15 mol% pCer + 15 mol% nCer) in order to study the effects of nCer as compared to those of pCer. The 30 mol% pCer and the 30 mol% nCer mixtures present both a clear gel/fluid phase segregation that can be identified by fluorescence-depleted areas in GUV (Figures 5.1 A and 5.1 B respectively) and SPB (Figures 5.2 B and 5.2 D respectively), while AFM imaging also reveals phase segregation, as gel phase domains protrude out of the membrane with an increased thickness (Figures 5.2 A and 5.2 C respectively). Force spectroscopy data (Table 5.1) reveal that pCer domains are much stiffer than nCer domains, and DSC thermograms (Figure 5.3 A, 5.3 C) also point in the same direction, as T_m values are lower for nCer samples.

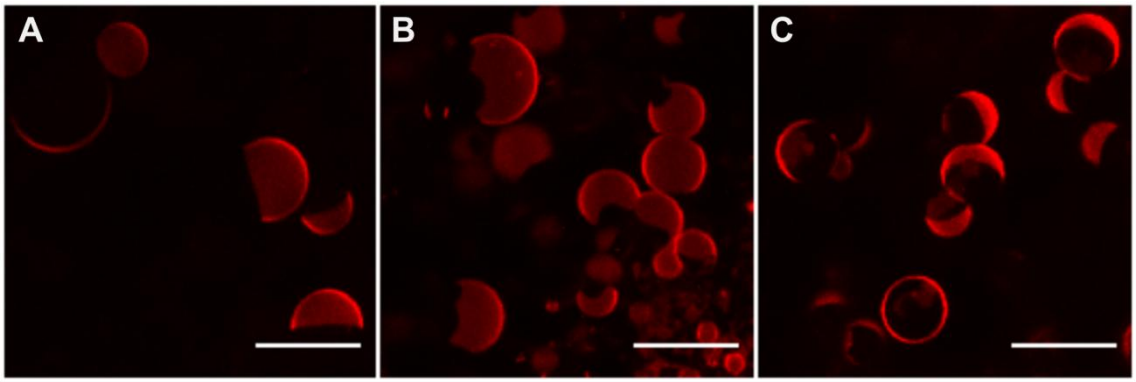

Figure 5.1. Confocal microscopy 3D (z-stack) images of fluorescent giant unilamellar vesicles containing 0.4% Rho-PE. DOPC:pSM:Chol (2:1:1) + 30% pCer (A), + 30% nCer (B), +15% pCer & 15% nCer (C). Scale bars: 10 µm.

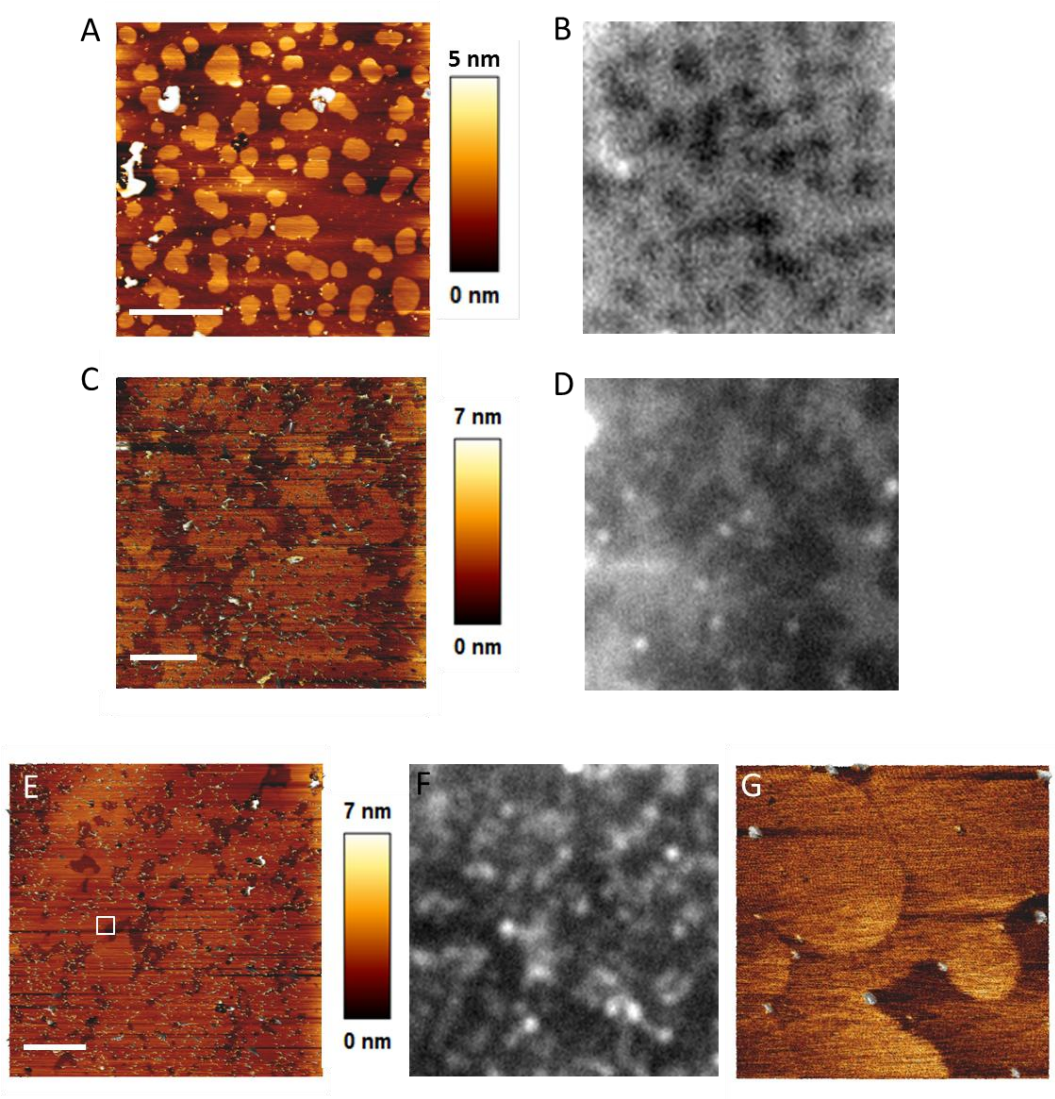

Figure 5.2. AFM and epifluorescence images of DOPC:pSM:Chol-based SPB containing 0.4% Rho-PE. DOPC:pSM:Chol (2:1:1) + 30% pCer (A & B), + 30% nCer (C & D), +15% pCer & 15% nCer (E, F) and zoom-in of the highlighted area in E (G). Scale bars: 5 µm.

Table 5.1. Bilayer nanomechanical resistance and bilayer thickness of the different SPB under study. Data expressed as mean ± SD, n= 300 – 1000.

Samples		Breakthrough Force (nN)		Bilayer Thickness (nm)	
		Continuous phase	*Segregated domains*	*Continuous phase*	*Segregated domains*
DOPC:pSM:Chol	pCer	6.5 ± 2.9	57.4 ± 2.3	4.57 ± 0.20	5.40 ± 0.13
	nCer	3.4 ± 1.5	17.3 ± 2.0	5.23 ± 0.17	5.95 ± 0.14
	pCer + nCer	2.4 ± 0.6	3.7 ± 0.8 20.9 ± 2.5	4.94 ± 0.20	5.32 ± 0.28 5.73 ± 0.16

The pSM sample containing 15 mol% of each ceramide displays a thermogram (Figure 5.3 B) which is close to the nCer-containing sample (Figure 5.3 C), although the T_m is slightly higher than the nCer- and clearly lower than the pCer-containing one (Figure 5.3 A). However, a close inspection of the data reveals an additional segregated phase, which can be identified both by confocal microscopy (Figure 5.1 C) and AFM imaging. In the zoom-in of Figure 5.2 G three lipid phases can be observed, with a clear difference in thickness (AFM image color), quantified in Table 5.1. Confocal microscopy visualization of this additional gel phase is revealed by a different degree of enrichment of Rho-PE (Figure 5.1 C), as some areas are completely devoid of fluorescence (first segregated phase) but others are only partially depleted (second segregated phase), while the continuous phase is clearly more fluorescent. This indicates that the second segregated phase is compositionally closer to the continuous fluid phase, as Rho-PE is present in both phases. This is corroborated by force spectroscopy data, as their breakthrough forces are much lower than for the fluorescence-depleted gel phase (Table 5.1).

Force spectroscopy data (Table 5.1, representative force curve in Supp. Fig. 5.S1 A) shows that gel domains exhibit lower nanomechanical resistance when nCer is present, in accordance with a noticeable decrease in T_m measured by DSC (Figure 5.3 for thermograms, Table 5.2 for quantitative results). In addition, the presence of nCer increases the overall bilayer thickness of every phase present, as measured by AFM imaging (Table 5.1). This could be a direct consequence of the longer N-acyl chain (C24:1 vs. C16:0) of nCer.

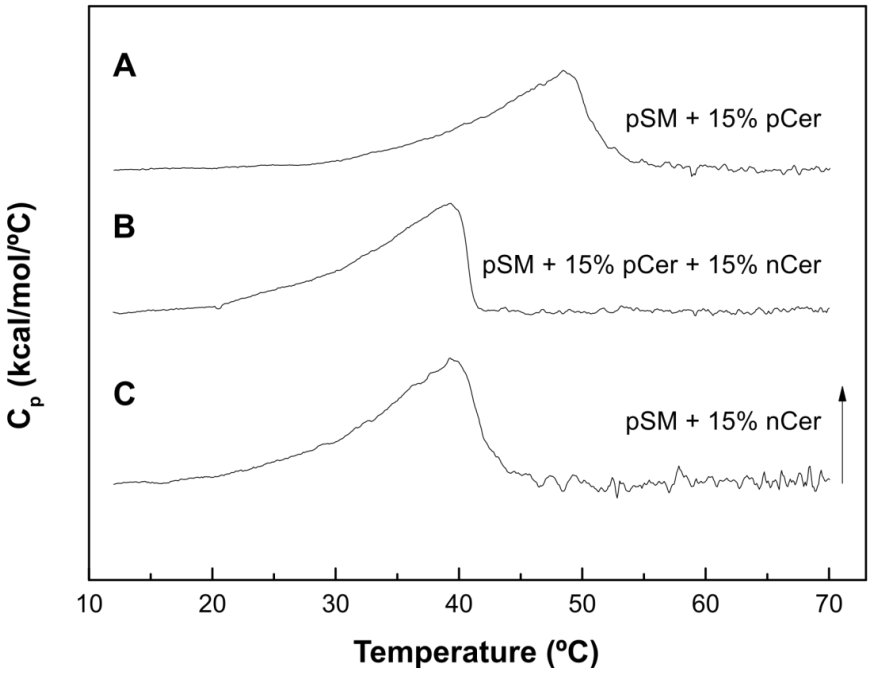

Figure 5.3. DSC thermograms. DOPC:pSM:Chol (2:1:1) + 30% pCer (A), + 15% pCer & 15% nCer (B), + 30% nCer (C). Arrow represents 0.5 kcal/mol·°C.

Table 5.2. Thermodynamic parameters of the gel-fluid transition, as obtained from DSC experiments. Average ± values SD (n=3).

Samples		ΔH (kJ/mol)	T_m (°C)	$T_{1/2}$ (°C)
DOPC:pSM:Chol	pCer	35.6 ± 16.9	48.5 ± 0.1	9.5 ± 0.4
	nCer	24.4 ± 0.8	39.0 ± 0.4	8.4 ± 0.5
	pCer + nCer	28.6 ± 1.7	39.5 ± 0.3	9.5 ± 0.6

ΔH: transition enthalpy change.

$\Delta T_{1/2}$: transition width at half-height

Confocal microscopy also points to both segregated phases sharing a part of the interphase boundary (instead of being completely separated by the continuous phase) and AFM data suggest, accordingly, that the thickest segregated phase could indeed be surrounded by the second segregated phase, and not by the continuous fluid phase. The potential composition of each phase will be discussed later. The thickest phase exhibits a slight increase in nanomechanical resistance when compared to nCer-enriched domains (20.9 nN vs. 17.3 nN), while it is still significantly lower than the resistance of pCer-enriched domains (Table 5.1), following the same trend as T_m values (Figure 5.3, Table 5.2). Moreover, pCer-

enriched domains present the same thickness and stiffness than in pure pSM:pCer mixtures in the same buffer (57 nN according to previous reports (Garcia-Arribas *et al.*, 2015)), which, as expected (Chiantia *et al.*, 2006b), indicates an almost complete displacement of DOPC and Chol from this phase to the continuous phase in the DOPC:pSM:Chol:pCer sample.

In summary, these results point to both ceramides as gel phase-inducing agents, pCer being much more effective than nCer for that purpose as pCer-induced gel phases are clearly stiffer.

5.3.2 nSM-based samples

Following the same procedure, similar experiments were performed on DOPC:nSM:Chol (2:1:1) + 30% ceramide (pCer, nCer or an equimolar mixture pCer/nCer). As with pSM (previous section), ceramides were able to generate segregated domains in a gel phase, although Rho-PE fluorescent probe is not completely excluded from the domains (Figure 5.4 A for pCer, Figure 5.4 B for nCer and Figure 5.4 C for the mixture of both ceramides), which points to domains being less ordered (or less packed) than in pSM-based samples. This case is of special interest as nSM is reportedly able to override phase segregation for liquid-ordered phases (Maté *et al.*, 2014) but to the best of our knowledge this had not been tested for ceramide-enriched gel phases.

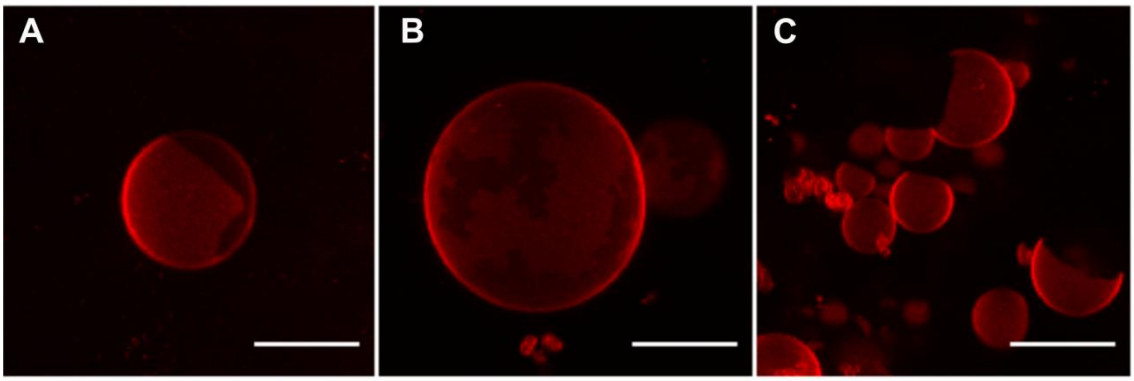

Figure 5.4. Confocal microscopy 3D (z-stack) images of fluorescent giant unilamellar vesicles containing 0.4% Rho-PE. DOPC:nSM:Chol (2:1:1) + 30% pCer (A), + 30% nCer (B), +15% pCer & 15% nCer (C). Scale bars: 10 μm.

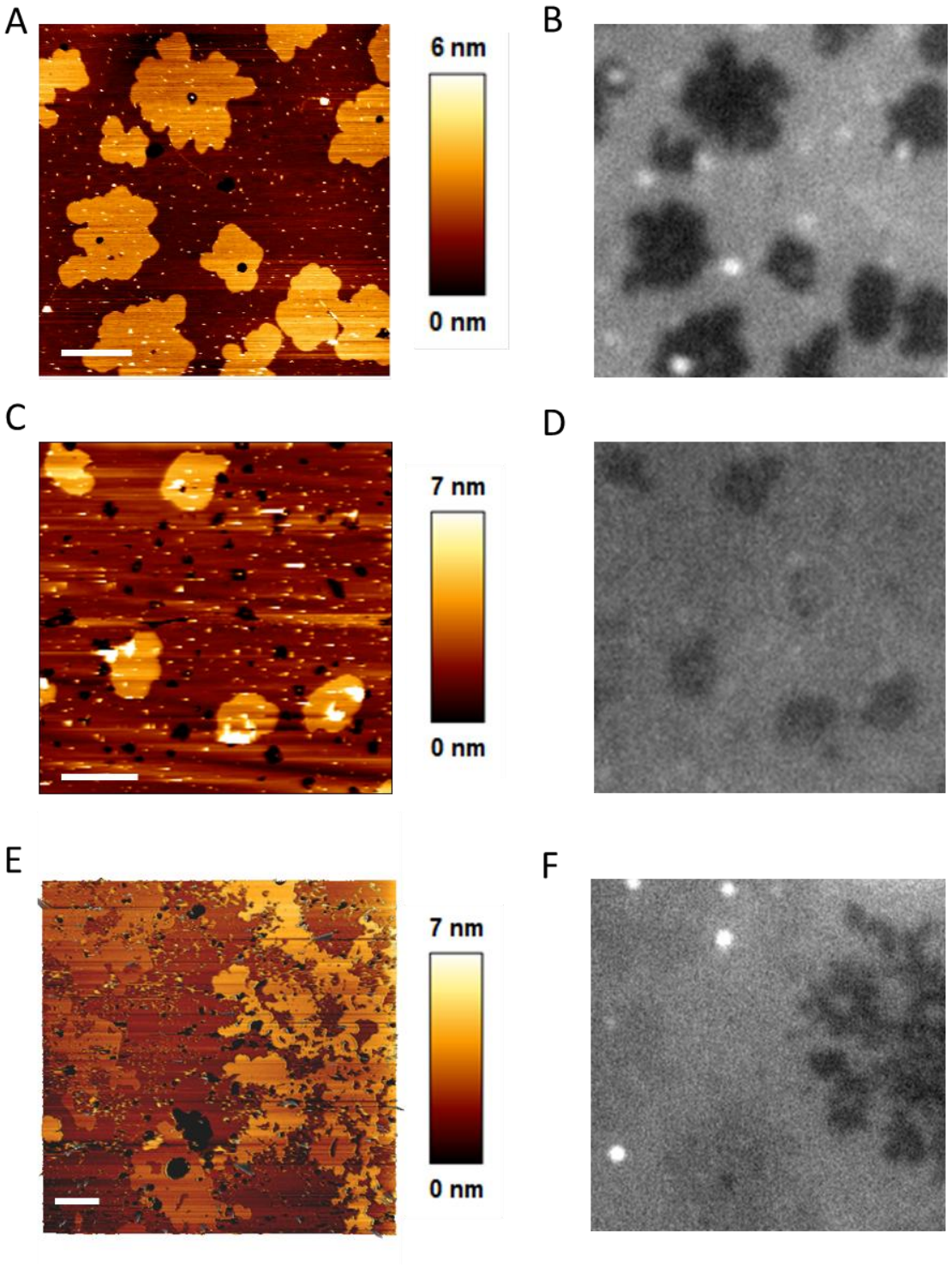

Figure 5.5. AFM and epifluorescence images of DOPC:nSM:Chol-based SPB containing 0.4% Rho-PE. DOPC:nSM:Chol (2:1:1) + 30% pCer (A & B), + 30% nCer (C & D), +15% pCer & 15% nCer (E & F). Scale bars: 5 μm.

AFM imaging and epifluorescence (Figure 5.5) corroborate confocal microscopy data as segregated gel domains can be detected in all three cases, due to their higher thickness and stiffness (Table 5.2). AFM results for the pCer+nCer

sample reveal two types of different segregated phases, while fluorescence reveals only one. This is discussed in the paragraph below. The presence of black areas in AFM images, such as in Figure 5.5 E, is caused by bare mica zones that are not covered by lipid bilayer. These zones are common in vesicle-adsorption SPB preparation and they are useful for bilayer thickness quantization (from mica, zero height, to the top surface of the lipid bilayer).

Table 5.3. Bilayer nanomechanical resistance and bilayer thickness of the different SPB under study. Data expressed as mean ± SD, n= 300 – 1000.

Samples		Breakthrough Force (nN)		Bilayer Thickness (nm)	
		Continuous phase	*Segregated domains*	*Continuous phase*	*Segregated domains*
DOPC:nSM:Chol	pCer	2.5 ± 0.4	10.2 ± 0.7	4.31 ± 0.45	5.07 ± 0.51
	nCer	1.8 ± 0.4	7.8 ± 2.7*	4.51 ± 0.22	6.31 ± 0.38
	pCer + nCer	2.4 ± 0.9	13.1 ± 1.1 10.7 ± 1.5*	4.04 ± 0.32	4.94 ± 0.42 5.86 ± 0.55

*Force curves present adhesion during tip retraction.

Additional differences exist between the two data sets (nSM- and pSM-based). The presence of nSM instead of pSM caused a sharp reduction in bilayer stiffness measured by AFM for every phase present (Table 5.3). As previously stated in the paragraph above, when both ceramides are present two kinds of domains appear, but in this case these two segregated phases cannot be distinguished through fluorescence as Rho-PE barely reveals the second one. This could be caused by the domains being compositionally close (inefficient fluorescent probe partition between the domains). Another difference with the two-domain pSM-based sample is that, in the case of nSM, these two segregated phases are separated from each other (i.e. they are both completely surrounded by the continuous phase, as seen in Figure 5.5 E) and, more importantly, both exhibit a higher nanomechanical resistance than the single-Cer samples (Table 5.3), which points to both phases being in a gel state. The possible nature of these domains will be further assessed in the Discussion section.

DSC data (Figure 5.6, Table 5.4) show that T_m decreases again in the order T_mpCer > T_mpCer+nCer > T_mnCer, although all three values are around 6 °C below the corresponding pSM-based samples (Table 5.2) and moreover in this case the

T_mpCer+nCer is intermediate between the other two and not particularly close to any of them, while in the pSM-based results the T_mpCer+nCer was closer to T_m nCer.

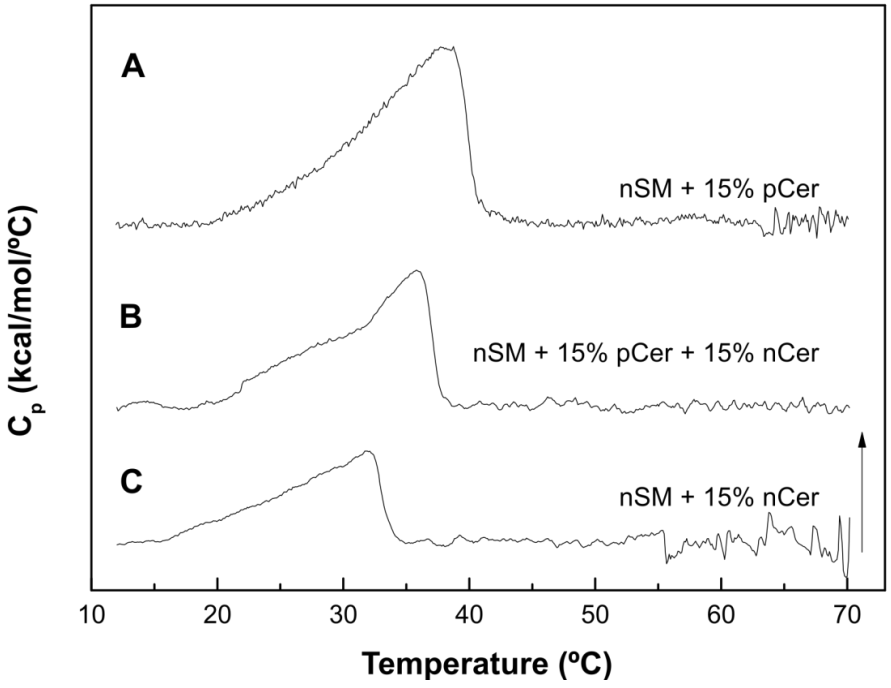

Figure 5.6. DSC thermograms. DOPC:nSM:Chol (2:1:1) + 30% pCer (A), + 15% pCer & 15% nCer (B), + 30% nCer (C). Arrow represents 0.5 kcal/mol·°C.

Table 5.4. Thermodynamic parameters of the gel-fluid transition, as obtained from DSC experiments. Average ± values SD (n=3).

Samples		ΔH (kJ/mol)	T_m (°C)	$T_{1/2}$ (°C)
DOPC:nSM:Chol	pCer	31.0 ± 0.9	38.8 ± 0.1	8.7 ± 0.2
	nCer	13.0 ± 1.1	31.2 ± 0.8	8.0 ± 0.3
	pCer + nCer	21.8 ± 1.0	35.8 ± 0.1	9.4 ± 1.6

ΔH: transition enthalpy change.

$\Delta T_{1/2}$: transition width at half-height

5.3.3 Samples containing both nSM and pSM

The case of DOPC:nSM:pSM:Chol (2:0.5:0.5:1) + 30% ceramide represents the most complex sample set of our study. As in the previous cases, segregated gel phases are observed using confocal microscopy (Figure 5.7 A for pCer, Figure 5.7 B for nCer and Figure 5.7 C for the mixture of both ceramides). When one kind of ceramide is present, segregated domains generated are shown as completely depleted areas using Rho-PE, however, when both ceramides are present exhibits a partial partition of the fluorescent probe, i.e. the latter is not completely excluded from any domain.

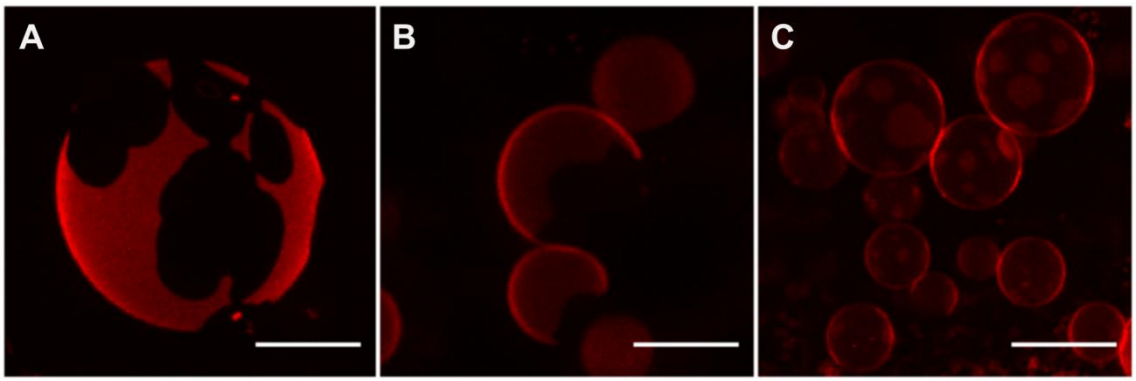

Figure 5.7. Confocal microscopy 3D (z-stack) images of fluorescent giant unilamellar vesicles containing 0.4% Rho-PE. DOPC:nSM:pSM:Chol (2:1:1) + 30% pCer (A), + 30% nCer (B), +15% pCer & 15% nCer (C). Scale bars: 10 μm.

DSC data follows the same trend as in the pSM sample set (Figure 5.8), although the three T_m are around 3 °C lower (Table 5.5), and higher than the nSM sample set.

Table 5.5. Thermodynamic parameters of the gel-fluid transition, as obtained from DSC experiments. Average ± values SD (n=3).

Samples		ΔH (kJ/mol)	T_m (°C)	$T_{1/2}$ (°C)
DOPC:nSM:pSM:Chol	pCer	25.1 ± 9.1	44.3 ± 0.3	8.8 ± 0.4
	nCer	19.5 ± 0.6	36.9 ± 0.8	8.6 ± 0.1
	pCer + nCer	23.3 ± 0.1	37.2 ± 1.0	10.2 ± 0.3

ΔH: transition enthalpy change.

$\Delta T_{1/2}$: transition width at half-height

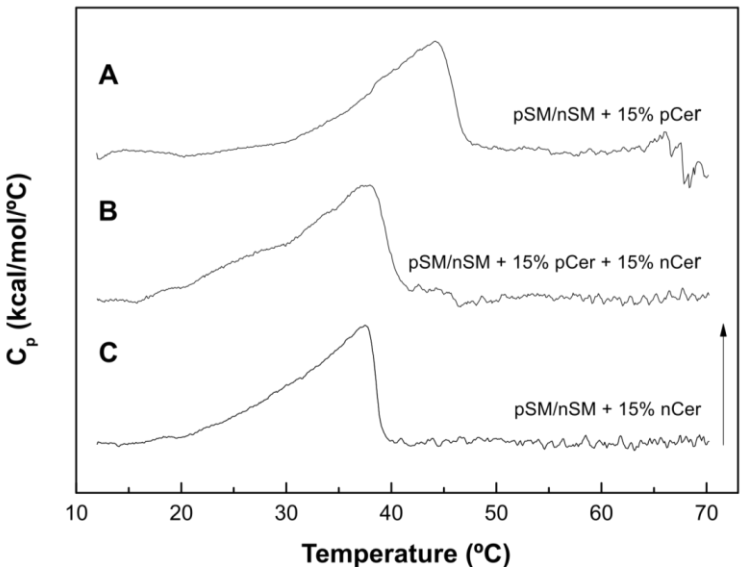

Figure 5.8. DSC thermograms. DOPC:nSM:pSM:Chol (2:1:1) + 30% pCer (A), + 15% pCer & 15% nCer (B), + 30% nCer (C). Arrow represents 0.5 kcal/mol·°C.

AFM imaging (Figure 5.9) reveals that there is only one single segregated gel phase for every case, even when both ceramides are present. Force spectroscopy (Table 5.6) correlates with DSC data, as breakthrough forces decrease for pCer and nCer, although the nCer + pCer exhibits the same stiffness as the highest domain of DOPC:pSM:Chol + both ceramides. This information is helpful for a better understanding of the nature of each phase, which will be addressed in the Discussion. In summary, these data suggest that the presence of nSM and pSM gives rise to a trend governed mainly by pSM, although the lipid phases tend to lose stiffness by the effect of nSM.

Table 5.6. Bilayer nanomechanical resistance and bilayer thickness of the different SPB under study. Data expressed as mean ± SD, n= 300 – 1000.

Samples		Breakthrough Force (nN)		Bilayer Thickness (nm)	
		Continuous phase	*Segregated domains*	*Continuous phase*	*Segregated domains*
DOPC:nSM:pSM: Chol	pCer	5.3 ± 2.1	49.1 ± 3.6	4.82 ± 0.31	5.65 ± 0.16
	nCer	3.0 ± 1.1	15.8 ± 2.7	4.66 ± 0.48	6.59 ± 0.62
	pCer + nCer	2.7 ± 0.9	21.2 ± 3.0	4.53 ± 0.43	5.55 ± 0.52

*Force curves present adhesion during tip retraction.

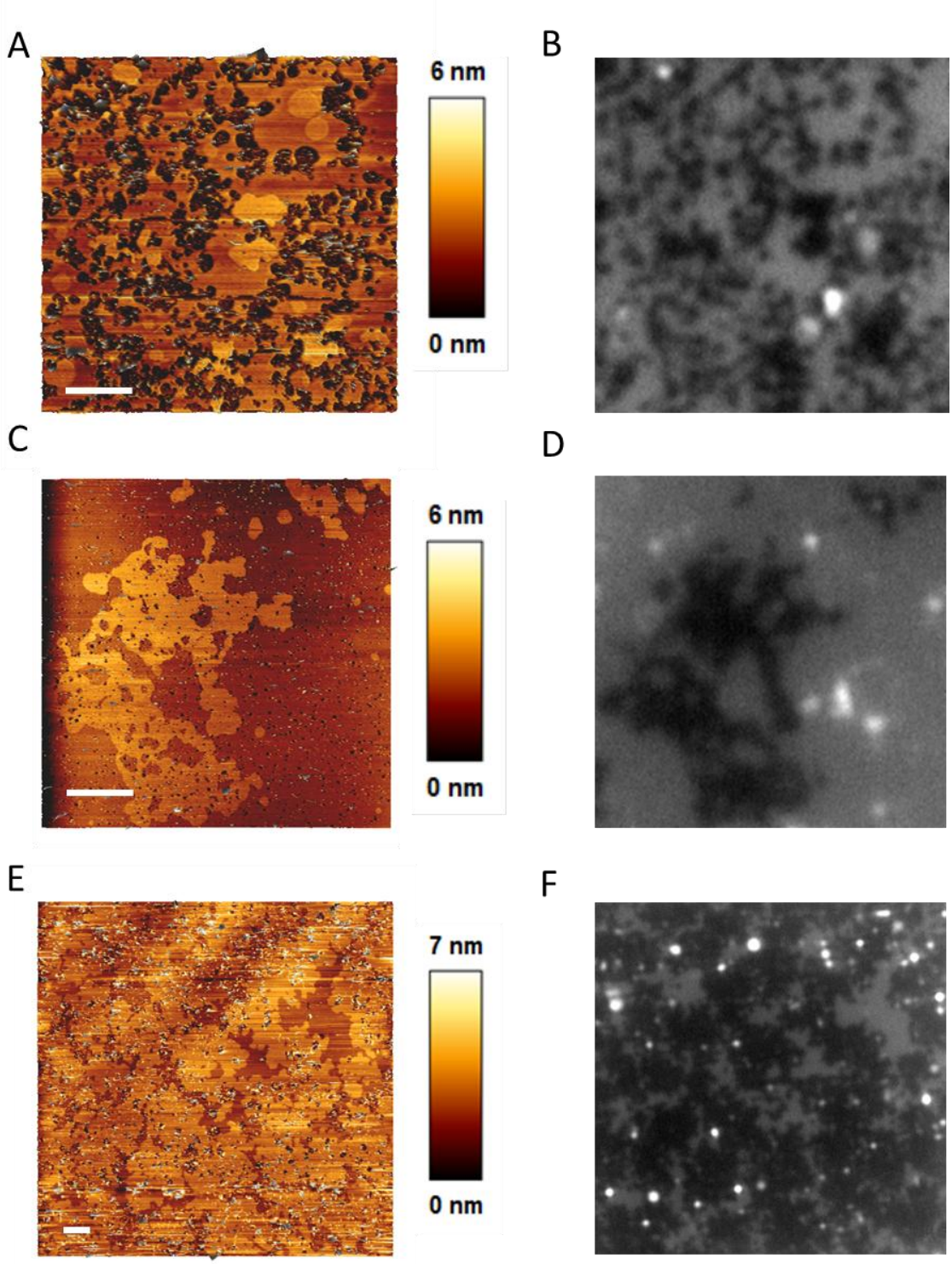

Figure 5.9. AFM and epifluorescence images of DOPC:pSM:nSM:Chol-based SPB containing 0.4% Rho-PE. DOPC:pSM:nSM:Chol (2:0.5:0.5:1) + 30% pCer (A & B), + 30% nCer (C & D), +15% pCer & 15% nCer (E & F). Scale bars: 5 µm.

5.4 Discussion

The presence of more than one kind of segregated phase in a lipid environment is a difficult issue to assess as different lipid phases present different degrees of lipid enrichment, but still a small concentration of every lipid is probably present in every phase. Moreover, the effects of different ceramides in the same lipid bilayer have not been studied previously, to the best of our knowledge. This increases the complexity of a complete analysis, but our data provide enough clues to at least suggest which lipids are the most abundant in each phase.

First, the comparison of the three techniques used for every sample provides consistent results, apart from small differences, e.g. when comparing confocal fluorescence of GUV with epifluorescence of SPB, as the latter is deposited onto a mica support. While the nature of supports has been shown to have an effect on lipid segregation, reducing the size of segregated phases in rough surfaces (Honigmann *et al.*, 2012, 2014), low-roughness supports such as mica (freshly cleaved and atomically flat) have drawn a good degree of consistency when compared to free, i.e. unsupported, vesicles, both in terms of phase segregation and fluorophore behavior. In our study, the only discrepancy observed is that the nSM-based sample with both Cer does not reveal two segregated phases in confocal microscopy but only one (Figure 5.4 C), epifluorescence barely reveals the second one (Figure 5.5 F), while atomic force microscopy clearly detects both segregated phases in terms of topography (Figure 5.5 E) and nanomechanical resistance (Table 5.3). This seems an exceptional case as both gel phases are compositionally close, but speaks in favor of force spectroscopic techniques in case of discrepancy.

Our experiments demonstrate that both ceramides (nCer and/or pCer) are able to form segregated gel phases even in a fluid environment and in presence of Chol. Most notably, the presence of nSM is not able to override gel phase segregation despite the reported capacity of this lipid to solubilize liquid-ordered phases in fluid environments (Maté *et al.*, 2014). However, nSM reduces the stiffness of Cer-enriched gel phases (Table 5.3), which could be caused by a partial destabilization of the phase, i.e. a lower degree of molecular packing. The possibility of interdigitation should also be taken into account, particularly in the case of nSM-based samples (Róg *et al.*, 2016), although this eventuality is hard to assess with our current methodologies.

For the complex cases where there are two ceramides present, the case of DOPC:nSM:Chol + both ceramides is probably the simplest to explain (Figure 5.5 E), as both segregated domains appear clearly separated from each other. A close

inspection of the force curves gives us further insights. For nCer domains, the curve presents an adhesion event on the retractive part (Supp. Fig. 5.S1 B), and this event also appears for one of the two domains of the nCer+pCer sample (Table 5.3). The simplest explanation is that each domain is enriched in one of the ceramides. However, domains grow stiffer in both cases when compared to pCer and nCer domains (Table 5.3), so the possibility of cooperation (i.e. synergic interaction) between ceramides seems plausible. Thus we consider that both ceramides are present in both domains, but the degree of enrichment of each ceramide varies as one domain (the stiffest one) would be enriched in pCer, while the other, more adhesive one, would be enriched in nCer. The continuous phases are enriched in DOPC and Chol, while nSM would also be present in the domains as SM has more preference for Cer than for Chol in non-saturated samples (Fidorra *et al.*, 2006; Chiantia *et al.*, 2007; Silva *et al.*, 2007; Sot *et al.*, 2008), although the presence of nSM in the continuous phase as well cannot be discarded.

One of the most surprising findings in our study is that the most complex sample, DOPC:pSM:nSM:Chol + both ceramides exhibits only one segregated domain (Figure 5.7), while the initially expected outcome should be that each ceramide would induce formation of a different domain (as in the previous sample), which could even be enriched in their respective SM as well. However, this is not the case as a single segregated domain is observed. As both ceramides are able to form segregated gel phases in a DOPC:pSM:nSM:Chol environment (Figure 5.9), the domain is necessarily enriched in both ceramides at the same time (otherwise we would have two types of different segregated domains), but in this case no cooperation between Cer is happening as the stiffness of the domain is intermediate when compared to single-ceramide DOPC:pSM:nSM:Chol samples. Thus, we can conclude that the presence of two ceramides in a single segregated phase can have two different and distinct effects: a cooperative effect with one ceramide enriched over the other where the stiffness grows for each domain or a non-cooperative effect (in the presence of pSM) where the stiffness is intermediate.

In DOPC:pSM:Chol + both ceramides, again two segregated phases appear (Figure 5.2), although in this case the thickest and stiffest phase appears surrounded by the other (Figure 5.1 C & Figure 5.2 G), acting as “domains within the domains”. Again, the presence of two ceramides could initially explain the existence of two segregated phases, one for each ceramide. However, force spectroscopy data (Table 5.1) points to a different explanation for the existence of these two domains, as one of them exhibits a very low breakthrough force, inappropriate for a gel phase under these ionic strength conditions (Garcia-Manyes *et al.*, 2010; Garcia-Arribas *et al.*, 2015), suggesting that both ceramides are present in the stiffest phase, and not in the second segregated phase. This implies

that a different ceramide arrangement is occurring and suggests instead another type of phase (probably liquid-ordered, which is supported in terms of nanomechanical resistance (García-Arribas *et al.*, 2016a). Interestingly, the stiffest phase shares the same breakthrough force ($p = 0.319$) and thickness ($p = 0.325$) than the DOPC:pSM:nSM:Chol + both ceramides single domain (Table 5.1), which points to a similar composition: the stiffest domain would be (partially) enriched in pSM, pCer and nCer, and the liquid ordered phase would be (partially) enriched in pSM and Chol. This conclusion is also supported by the absence of this liquid-ordered phase in the DOPC:pSM:nSM:Chol + both ceramides (Figure 5.9 5 E and Figure 5.9 F), as nSM has been reported to override liquid-ordered phase segregation, thus nSM would be excluded from the domain. The conclusions of the lipid phase compositional analysis have been summarized in Table 5.7 for clarity.

Table 5.7. Summary of the DOPC:X:Chol:pCer:nCer samples and the expected composition of the phases formed in each case.

		Main lipids present		
Brief Description		*Continuous phase*	*Domain 1*	*Domain 2*
X: pSM	L_o domain (1) with L_β subdomain (2)	DOPC, Chol	pSM, Chol	pSM, pCer, nCer
X: nSM	Separated L_β domains (1,2)	DOPC, Chol	nSM, nCer	nSM, pCer
X: nSM + pSM	L_β domain (1)	DOPC, Chol, nSM	pSM, pCer, nCer	-

A more difficult task would be to assess the effects of multiple ceramides present in smaller concentrations (i.e. with a total mol% Cer concentration far below the 30% used in our study) which is the case for actual cell membranes in living cells. Ceramide levels have been reported to increase up to 10 mol% during cell death processes, but there is no data available on how the levels of each ceramide species increase. A logical assumption, particularly after analysing the results in this study, is that the modulation of the ratio of each species of ceramide could be an essential tool for regulating the biophysical properties of the membrane and their functional effects. Furthermore, the presence of different sphingomyelins in the membrane is well known, but how sphingomyelinase activity is modulated by the presence of such a wide array of sphingomyelins, or if it presents any preference towards any specific sphingomyelin depending on the local composition of the membrane, are still unsolved questions. Our study opens the field for further studies on the possible cooperation (or displacement) between different ceramides in presence of a variety of lipids, including different sphingomyelins.

Finally, it is also worth mentioning that the presence of Chol in the bilayers could indeed be having an impact on the possible arrangements of different ceramides, as well as in the biophysical properties of the distinct phases present. Further studies with increasing (or decreasing) Chol content could give more information on the possibility of Chol-Cer displacements or interactions.

5.5 Supplementary data

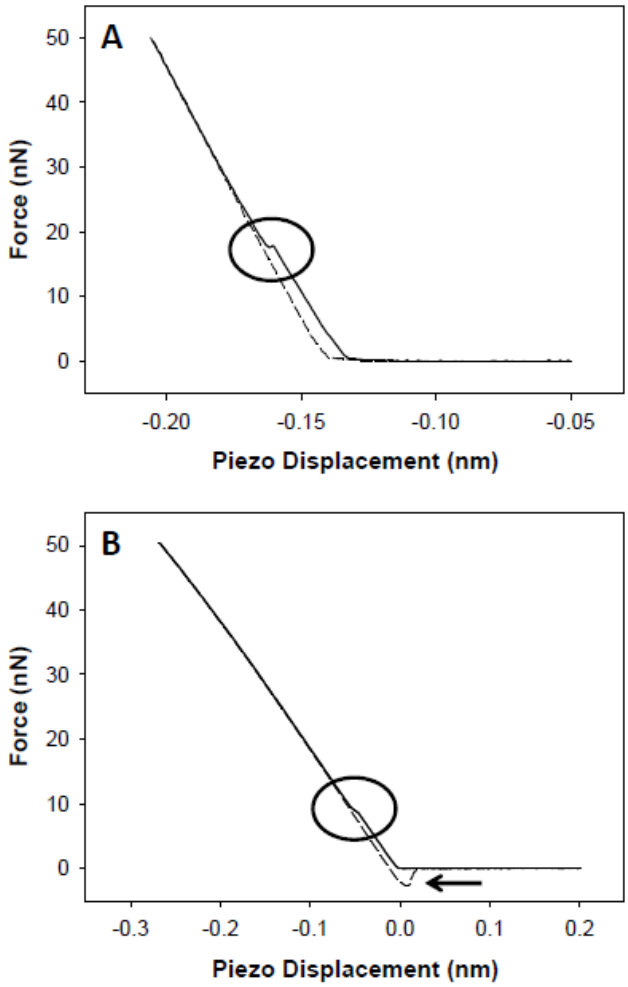

Figure 5.S1. Representative force curves. Extension (solid lines) and retraction (dashed lines) of a bilayer nanoindentation process on DOPC/pSM/Chol + nCer + pCer (A, gel phase), and on DOPC/nSM/Chol + nCer (B, gel phase). Breakthrough forces are identifiable by the step (circles) detected in the extension curves. B shows a reproducible adhesion event at the end of the rectraction curve (arrow).

CHAPTER 6:

MIXING BRAIN CEREBROSIDES WITH BRAIN CERAMIDES, CHOLESTEROL AND PHOSPHOLIPIDS

CHAPTER 6: MIXING BRAIN CEREBROSIDES WITH BRAIN CERAMIDES, CHOLESTEROL AND PHOSPHOLIPIDS.

6.1 Introduction

Glycosphingolipids (GSL) are components of most eukaryotic cell plasma membranes. They consist of a ceramide backbone linked to a saccharide polar headgroup through an *O*-glycosidic linkage to the C1-hydroxyl of ceramide (Cer) (Maggio *et al.*, 2006) (Supplementary Figure 6.S1). Total sphingolipids, mostly sphingomyelin (SM), constitute 15-20 mol% of the plasma membrane lipids, but the amount of GSL is usually much lower (Hoetzl *et al.*, 2007). Cerebrosides (Crb) are among the simplest GSL. Their polar head group consists of a hexose, commonly galactose (galactosylceramide, GalCer) or glucose (glucosylceramide, GlcCer) (Maggio *et al.*, 2006; Hoetzl *et al.*, 2007). Crb make up to 20 mol% of the lipids in myelin, and they occur in sizable amounts in epithelial cells from the small intestine and colon, apart from the skin epidermis (Van Meer *et al.*, 2003). They are known to be involved in cell division, growth, survival and membrane trafficking processes (Van Meer *et al.*, 2003). GlcCer has been shown to increase Ca^{2+} mobilization from intracellular stores (Lloyd-Evans *et al.*, 2003). Inborn enzyme defects may lead to cerebroside accumulation in cells, giving rise to Gaucher's and other diseases (Van Meer *et al.*, 2003; Lloyd-Evans *et al.*, 2003; Varela *et al.*, 2017; Holowka *et al.*, 2005).

GSL, and Crb in particular, are known to segregate laterally into membrane domains, at least in lipid mixtures and probably also in cell membranes. Presumed GSL-enriched domains in cells have been related to signaling by immune receptors and other signal transduction events (Varela *et al.*, 2017; Holowka *et al.*, 2005; Hakomori, 2002; Mayor *et al.*, 2006). A number of studies have been published on the properties of Crb mixtures with other membrane lipids (see review in (Maggio *et al.*, 2004)). Morrow et al.. (Morrow *et al.*, 1992) used ^{2}H-NMR to examine N-lignoceroyl (C24:0) GalCer in bilayers with 1-stearoyl-2-oleoyl phosphatidylcholine (PC). At glycolipid concentrations below 20 mol% the lipid components were miscible, both in

the fluid and the gel phases, while at higher concentrations separation of Crb-rich and PC-rich phases occurred under most conditions. Further studies have been published on this subject, with concurring results (Morrow *et al.*, 1992; Longo & Blanchette, 2010; Varela *et al.*, 2013; Blanchette *et al.*, 2006).

Cholesterol (Chol) has in common with GSL its relative abundance in plasma membranes, thus it is not surprising that Crb:Chol mixtures have attracted the attention of many investigators. In a relatively early study Slotte and co-workers (Slotte *et al.*, 1993), using Langmuir monolayers, observed that Chol did not induce significant condensation of monohexose Crb in binary mixtures, indicating that Chol did not increase the order of the acyl chains. However with dihexoside Crb, a Chol-induced condensing effect was observed. More recently Slotte and co-workers (Maunula *et al.*, 2007) examined bilayers composed of 1-palmitoyl-2-oleoyl PC (POPC), palmitoyl SM, Crb and Chol, at molar ratios close to 60:15:15:10, using differential scanning calorimetry (DSC), and fluorescence spectroscopy. They found that Crb was less effective than SM in forming laterally segregated domains with Chol, even if the various Crb tested associated with SM:Chol domains, i.e. Crb:Chol domains did not readily form, however mixed SM- and Chol-rich domains appeared to incorporate Crb. Also large differences in domain forming properties were seen between GlcCer and GalCer, the glucosyl derivative being more active in segregating with Chol (Maunula *et al.*, 2007; Westerlund & Slotte, 2009). Varela et al.. (Varela *et al.*, 2016) also studied the interactions of Crb (specifically GlcCer) with POPC and Chol, and provided ternary phase diagrams of the mixture at neutral and acidic (~5.5) pH. The phase diagrams are dominated by an extensive 3-phase coexistence region of fluid disordered (L_α, phospholipid-enriched), fluid ordered (L_o, Chol-enriched), and gel (L_β, Crb-enriched phases).

In the present contribution, the mixing properties of brain Crb (bCrb) with brain SM (bSM), brain Cer, Chol, and/or a lipid representing typical fluid bilayers (ePC) have been explored using DSC, Laurdan fluorescence spectroscopy, and confocal fluorescence microscopy of giant unilamellar vesicles (GUV). Using almost exclusively lipids of natural origin brings our studies closer to the biological situation, while the previous data on chemically-defined compounds are used to shed light on our results. In most previous studies Crb were minority components in the various mixtures, while we have explored mixtures in which Crb is usually >50 mol%, corresponding in the ternary phase diagrams of Varela et al.. (Varela *et al.*, 2016) to the lower, right-hand region of the triangle. This may reflect the overall cell membrane situation in Gaucher's or Krabbe's diseases, or the case of Crb-enriched microdomains expected to occur in healthy cell plasma membranes (Van Meer *et al.*, 2003; Lloyd-Evans *et al.*, 2003; Varela *et al.*, 2017). Moreover, some parallel studies in which the sphingolipid is either SM or Crb help us compare the role of two polar head groups in sphingolipids, namely hexose and phosphorylcholine.

6.2 Materials and methods

6.2.1 Materials

L-α-phosphatidylcholine (PC) from hen eggs was purchased from Lipid Products (South Nutfield, UK); main fatty acid distribution C16:0 33%, C18:0 12%, C18:1 32%, C18:2 17%. The following lipids were obtained from Avanti Polar Lipids (Alabaster, AL): porcine brain cerebrosides (bCrb) [main fatty acid distribution C16:0 6%, C18:0 7%, C22:0, 11%, C24:0 22%, C24:1 9%, others, predominantly hydroxylated, 42%], porcine brain sphingomyelin (bSM) [main fatty acid distribution C18:0 50%, C20:0 5%, C22:0 7%, C24:0 5%, C24:1 21%], porcine brain ceramide (bCer) [main fatty acid distribution C18:0 67%, C20:0 17%, C24:1 7%], cholesterol (Chol), N-palmitoyl Crb, N-palmitoyl Cer, N-palmitoyl SM, and the lipophilic fluorescent probe 1,2-dioleoyl-*sn*-glycero-3-phosphoethanolamine-N-(lissamine rhodamine B sulfonyl) (Rho-PE). 1,6-diphenyl-1,3,5-hexatriene (DPH), 8-aminonaphtalene-1,3,6-trisulfonic acid (ANTS), *p*-xylene-bis-pyridinium bromide (DPX) and (N-(7-nitrobenz-2-oxa-1,3-diazol-4-yl)-1,2-dihexadecanoyl-*sn*-glycero-3-phosphoethanolamine, triethylammonium salt) (NBD-PE) were from Molecular Probes (Eugene, OR). Methanol and chloroform were from Fisher (Suwanee, GA). Buffer solution for experiments was 20 mM PIPES, 1 mM EDTA, 150 mM NaCl, pH 7.4. All other materials (salts and organic solvents) were of analytical grade.

6.2.2 Differential scanning calorimetry (DSC)

DSC is commonly used in lipid studies to detect thermotropic phase transitions (most commonly of the gel-fluid sort) in fully hydrated lipid dispersions. Mid-point transition temperature (T_m), measured at the endotherm maximum, provides an indication of the stability of the gel phase, the higher T_m the more stable the gel phase. $\Delta T_{1/2}$ is the transition width at mid-height, this parameter being related to the transition cooperativity, more cooperative transitions giving rise to narrower endotherms, i.e. smaller $\Delta T_{1/2}$. ΔH, the change in transition enthalpy, is measured from the endotherm area (more specifically from the integration of C_P vs. T), and is highest for the transitions of a single component (Goñi & Alonso, 2006b). For DSC measurements lipid vesicles were prepared by mixing the desired lipids dissolved in chloroform:methanol (2:1, v/v) and drying the solvent under a steam of nitrogen. The lipid film was kept under high vacuum for 90 minutes to ensure the removal of undesired organic solvent. Multilamellar vesicles (MLV) were formed by hydrating the lipid film with the buffer solution at 90 °C, helping the dispersion with a glass rod. The measurements were performed

in a VP-DSC high-sensitivity scanning microcalorimeter (MicroCal, Northampton, MA, USA). Before loading the MLV sample into the appropriate cell both lipid and buffer solutions were degassed. 0.5 mL at 1 mM total lipid concentration was loaded into the calorimeter, performing 8–10 heating scans at a 45 °C/h rate, between 10 and 100 °C for all samples. bCrb concentration and sample volume were known for each sample, and used together with data from the last scan to obtain normalized thermograms. The software Origin 7.0 (MicroCal), provided with the calorimeter, was used to determine the different thermodynamic parameters (T_m, $\Delta T_{1/2}$ and ΔH, and the onset and completion temperatures of the transition) from the scans. Temperatures at the onset and completion of the endothermic phase transitions were used to build the phase diagrams.

6.2.3 Confocal Microscopy of Giant Unilamellar Vesicles (GUV)

GUV are prepared by the electroformation method described previously (Montes *et al.*, 2007; Angelova & Dimitrov, 1986; Angelova *et al.*, 1992). Lipid stock solutions were prepared in 2:1 (v/v) chloroform:methanol at 0.2 mg/mL, and appropriate volumes of each preparation were mixed. Labelling was carried out by premixing the desired fluorescent probe (Rho-PE) with the lipids in organic solvent. Fluorescent probe concentration was 0.4 mol % Rho-PE. The samples were added onto the surface of platinum (Pt) wires attached to specially designed polytetrafluoroethylene (PTFE)-made cylindrical units. The Pt wires were placed under vacuum for 2 h to completely remove the undesired organic solvent. The sample was covered to avoid light exposure. Then, the units were fitted into specific holes within a specially designed chamber to which a glass cover slip had been previously attached with epoxy glue. Once fitted, the platinum wires stayed in direct contact with the glass cover slip. The chamber was then equilibrated at the desired temperature by an incorporated water bath. 400 µL sucrose, prepared with high-purity water (SuperQ, Millipore, Billerica, MA) and heated at 90 °C were added, so that the solution covered the Pt wires. The cells were stopped with tightly fitting caps. The wires were connected to a TG330 function generator (Thurlby Thandar Instruments, Huntingdon, UK). The alternating current field was applied with a frequency of 10 Hz and an amplitude of 940 mV for 120 min. The temperatures used for GUV formation were above the gel to liquid phase transition in all cases. The generator and the water bath were switched off, and the vesicles were left to equilibrate at room temperature for 30 min. After GUV formation, the chamber was placed onto an inverted confocal fluorescence microscope (Nikon D-ECLIPSE C1, Nikon, Melville, NY). The excitation wavelength for Rho-PE was 561 nm, and the images were collected using a band-pass filter of 593 ± 20 nm. Image treatment and quantification were performed using the software EZ-C1 3.20 (Nikon). No difference in domain size, formation, or distribution was detected in the vesicles during the observation period or after laser exposure.

6.2.4 Laurdan fluorescence experiments

The experiments were performed in a QuantaMaster 40 spectrofluorometer (Photon Technology International, Lawrenceville, NJ) using Laurdan. Laurdan is a solvatochromic dye that exhibits an increase in charge separation when excited in polar solvents, which results in a larger dipole moment (Owen *et al.*, 2011). Laurdan shows different maximum emission intensities with liquid-ordered (440 nm) and liquid-disordered phases (490 nm). The emission spectrum changes in response to variations in the membrane environment, particularly in the glycerol backbone region in the phospholipid membrane. In order to quantify the spectral changes the generalized polarization function (GP) is used, that is obtained from measurements of wavelength displacements.

$$GP = \frac{I_{440} - I_{490}}{I_{440} + I_{490}}$$

GP measurements are performed using excitation light at 360 nm and recording emission intensities both at 440 and 490 nm. Multilamellar vesicles (MLV) were prepared as described above with 1 mol% Laurdan, and measurements were carried out at room temperature and constant stirring. Theoretically, GP values can vary from -1.0 (disordered) to +1.0 (ordered phases) but experimental values usually occur in the -0.3 to +0.6 range (Sanchez *et al.*, 2007).

6.2.5 DPH fluorescence polarization measurements

The experiments were performed in a QuantaMaster 40 spectrofluorometer (Photon Technology International, Lawrenceville, NJ) using DPH. DPH is a fluorescent membrane probe widely used to determine the molecular order of lipid bilayers. Anisotropy values will be near to 0.4 when DPH rotational diffusion is restricted in a gel state bilayer, however they will be quite lower above the phase transition temperature, when rotation diffusion of DPH increases. DPH was excited at 360 nm and its emission measured at 430 nm using the instrument software (PTIFelixGX), which computed the G factor before each measurement. Fluorescence intensities were recorded at an integration rate of 1 point/s for 60 s. The anisotropy (r) is obtained from measurements of emission intensities parallel (I_{VV}) and perpendicular (I_{VH}) to the polarization plane:

$$r = \frac{I_{VV} - G \cdot I_{VH}}{I_{VV} + 2 * G \cdot I_{VH}}$$

The grating factor *G* is an instrumental preference of the emission optics for the horizontal orientation to the vertical orientation. It can be computed as:

$$G = \frac{I_{HV}}{I_{HH}}$$

where I_{HV} and I_{HH} are the intensities of the vertically and horizontally polarized components of DPH emission.

6.2.6 Membrane permeabilization (leakage) assays

The permeabilizing effects of different lipids were tested following the release of vesicle-entrapped ANTS and its quencher DPX (Ellens *et al.*, 1985). A high DPX/ANTS ratio is used to ensure complete quenching inside the vesicles. Non-entrapped probes were removed by passing the vesicle suspension through a Sephadex G-25 column using an iso-osmotic buffer solution prepared with the help of a cryoscopic osmometer (Osmomat 030, Gonotec, Berlin, Germany) with NaCl. 10 mol% of the desired lipid is added to 0.1 mM ePE:Chol (3:1) vesicles in a 1-cm path lengt quartz cuvette and leakage is followed as the enhancement of ANTS fluorescence in a FluoroMax-3 spectrofluorometer (Horiba Jobin Yvon, Edison, NY), under continuous stirring. Excitation and emission wavelengths were 355 and 520 nm, respectively. An interference filter with a nominal cutoff value of 515 nm was placed in the emission light path to avoid the scattered-light contribution of the vesicles. When leakage reached equilibrium, 10% Triton X-100 was added to induce 100% release. To calculate the amount of leakage the following equation is used:

$$\text{Leakage (\%)} = \left(\frac{(\mathrm{F} - \mathrm{F}_0)}{(\mathrm{F}_{100} - \mathrm{F}_0)}\right) * 100$$

where F, F_0 and F_{100} are respectively the fluorescence at equilibrium, at time zero, and at maximum leakage.

6.2.7 Transbilayer (flip-flop) lipid motion assays

A fluorescent-labeled PE (NBD-PE) was used to study the transbilayer lipid motion across the membrane. ePE:Chol (3:1) LUV were prepared as described previously, including 0.6 mol% NBD-PE. The assay was performed in an Aminco-Bowman (Urbana, IL) AB-2 spectrofluorometer using a 1 mL quartz cuvette with

continuous stirring. NBD-PE was excited at 465 nm and emission wavelength was 530 nm. A cutoff filter at 515 nm was used to avoid scattered light. Sodium dithionite was used to reduce NBD in the outer leaflet, thus quenching its fluorescence. A decrease in fluorescence intensity of about one-half marked the reduction of NBD in the outer monolayer. Then the liposome suspension was passed through a Sephadex G-25 column for removing the excess dithionite. After 30 min incubation of LUV with the appropriate sphingolipids, 50 µL of 0.6 mM dithionite solution were added into the cuvette. Fluorescence intensity would decrease slowly as long as NBD-PE moved to the outer membrane leaflet. Flip-flop was estimated according to this equation:

$$\text{Flip} - \text{flop}\ (\%) = \left(1 - \frac{F_R}{F_0}\right) * 100$$

where F_R and F_0 are respectively the fluorescence at the end of the time course and at time zero (before the second dithionite addition).

6.3 Results

6.3.1 Gel-fluid transition of bCrb bilayers

According to X-ray diffraction data (Saxena *et al.*, 1999) aqueous dispersions of Crb (GlcCer or GalCer) give rise to bilayers. DSC measurements (Saxena *et al.*, 1999) show that N-palmitoyl GlcCer undergoes a gel-fluid transition at 87ºC, while N-palmitoyl GalCer does so at 85 °C. The transition enthalpy for the N-palmitoyl GalCer transition is ΔH = 17.9 kcal/mol. The natural bCrb used in the present study exhibits a calorimetric transition centered at T_m = 64.8 ± 0.07 °C (n = 3) (Figure 6.1). The transition enthalpy is ΔH = 3.15 ± 0.19 kcal/mol (n = 3). The fact that bCrb melts at a much lower temperature than the pure homologues is probably due to its mixed fatty acid composition (see Materials), since the glucose and galactose homologues have virtually the same T_m (Saxena *et al.*, 1999). The sugar composition of bCrb is galactose and glucose at a ~2.5 mol ratio (unpublished observation from the manufacturer). The smaller ΔH in bCrb has probably the same origin, i.e. mixed fatty acid composition. The bCrb endotherm is somewhat asymmetric, and in fact it can be decomposed into two Gaussian components (Figure 6.1). In the absence of specific proof, the two components might correspond to bCrb linked to hydroxylated and non-hydroxylated fatty acids. This would be supported by the behavior of hydroxylated vs. non-hydroxylated fatty acyl Cer (Saxena *et al.*, 1999). The former melts with a single, symmetric endotherm, while the latter exhibiting two well-resolved endotherms, one of them

several degrees below, and the other at T_m values comparable to those of the hydroxylated counterparts (Shah *et al.*, 1995b). Thus in the case of bCrb the lower-melting component would arise from the lower-melting of non-hydroxylated cerebroside molecules, while the higher-melting component would be originated by the higher-melting hydroxylated plus the whole of the non-hydroxylated molecules. Alternatively the observed asymmetry of the signals could be attributed to the asymmetrical shape of the region of the phase diagram where the gel and fluid phases coexist.

The gel-fluid transition of bCrb has also been monitored by Laurdan fluorescence emission GP (Figure 6.1, squares), it is centered at ~67 °C, in agreement with the DSC data. However, the transition as detected by Laurdan appears much broader than the calorimetric signal. This probably occurs because of the different phenomena measured by both techniques, Laurdan is monitoring events at the lipid-water interface, while DSC detects the cooperative melting of the hydrocarbon chains.

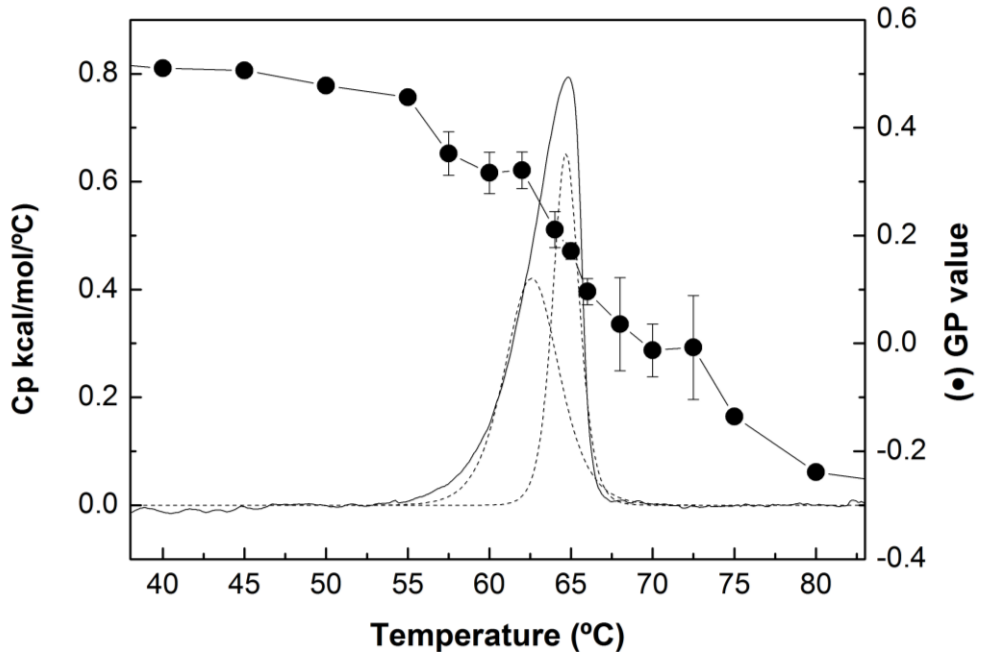

Figure 6.1. Gel-fluid thermothropic transition of bCrb in aqueous solution. Continuous line: DSC thermogram. The dotted curves correspond to the best fit of the endotherm to two Gaussian lines. Round symbols: Laurdan GP data (average ± S.D., triplicate).

6.3.2 Binary mixtures with ceramide (bCer)

DSC thermograms of bCrb/bCer mixtures, of compositions 100:0 to 60:40 mol ratios, are shown in Figure 6.2. The T_m of pure Cer are usually in the range of

80-90 °C (Shah *et al.*, 1995b, 1995a) thus it is not surprising that adding bCer shifts the bCrb gel-fluid transition to higher temperatures, at least up to 20% bCer (Figures 6.2 and 6.3 A). The two components of the bCrb thermogram observed in Figure 6.1 remain visible, and in apparently similar proportions, in all mixtures (Figure 6.2). The ΔH transition enthalpy of the mixture increases with addition of bCer (Figure 6.3 C), perhaps because Cer gel-fluid transitions have ΔH values above those of Crb (Saxena *et al.*, 1999; Jiménez-Rojo *et al.*, 2014). As a consequence of the above properties, the partial phase diagram for fully hydrated bCrb:bCer mixtures (Figure 6.3 D) is dominated by an extensive area of gel phase(s), below 55-60 °C. The system becomes fluid only above 70 °C.

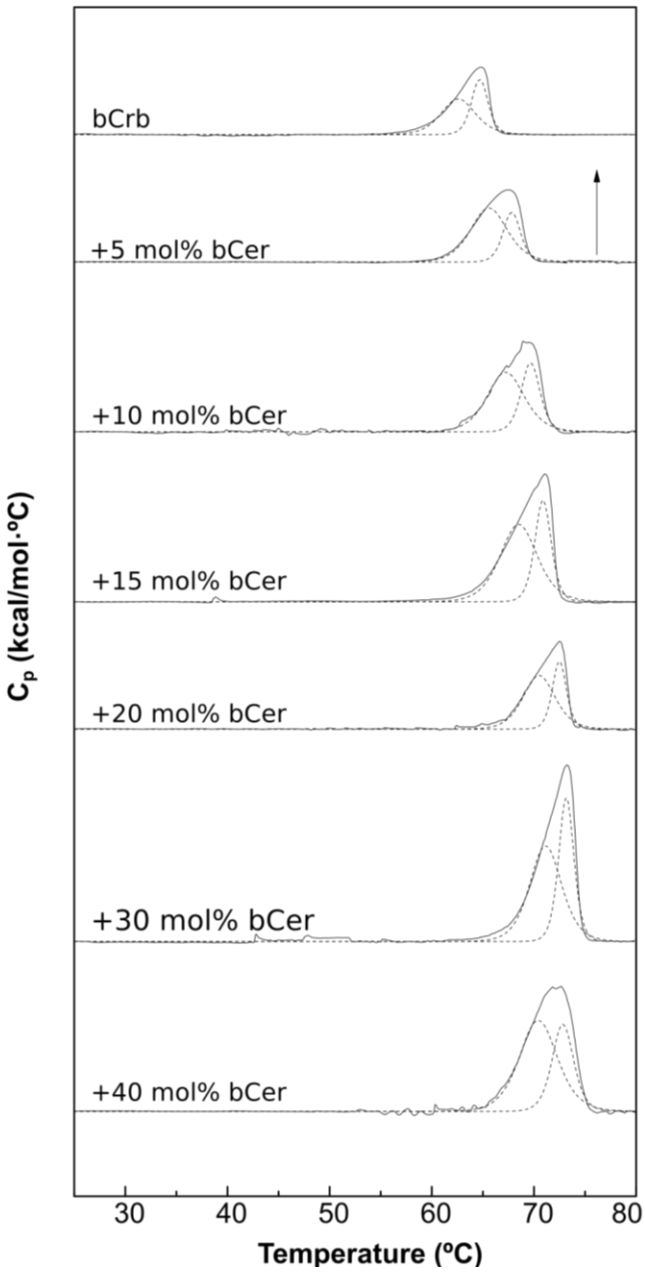

Figure 6.2. Representative DSC thermograms corresponding to the gel-fluid transition of pure bCrb and various bCrb:bCer mixtures in excess water. Mol percentage of bCer is indicated for each sample as a function of bCer concentration. Arrow: 1 kcal/mol/°C.

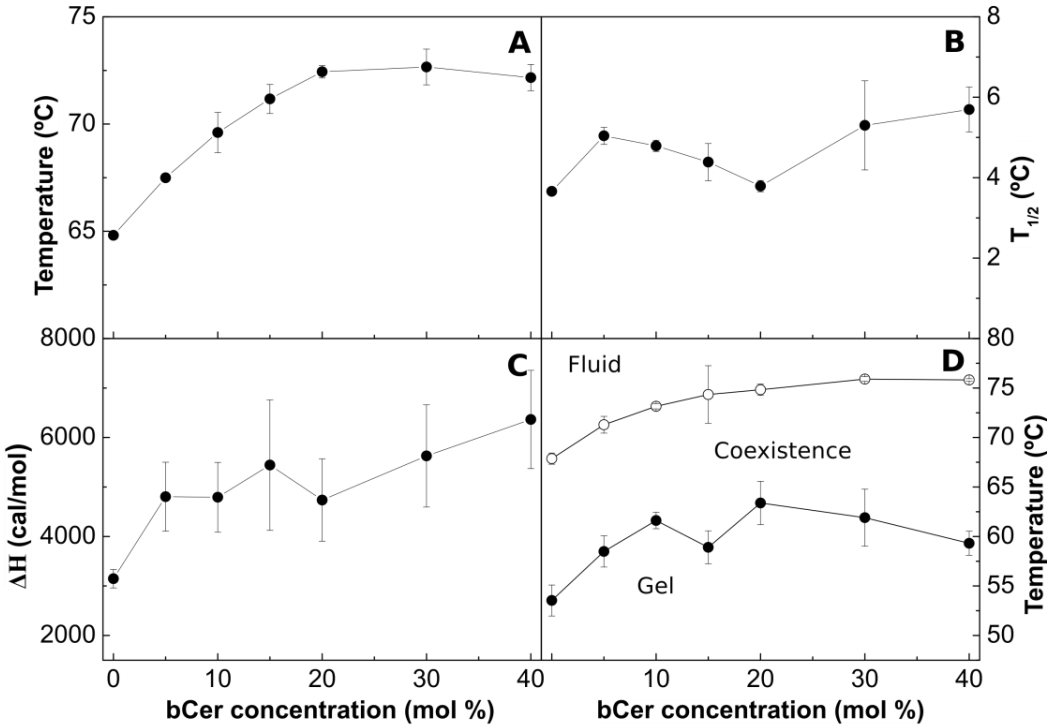

Figure 6.3. Thermodynamic parameters of bCrb:bCer mixtures. (A) Mid-point temperature of the gel-fluid transition. (B) Transition width at half-height. (C) Transition enthalpy, in cal/mol bCrb. (D) Temperature-composition diagram for the bCrb:bCer mixtures. The predominant phases are given for each area. (Average ± S.D., triplicate). Sometimes the errors are smaller than the symbols.

bCrb:bCer mixtures were also studied using Laurdan fluorescence GP. Bilayers containing 0, 15 and 30 mol% bCer were examined. The results in Figure 6.4 A are in agreement with the DSC data. Moreover, at room temperature (Supplementary Figure 6.S2 A, B), Laurdan shows that addition of increasing amounts of bCer hardly modify the polarity of the lipid-water interface in the bilayer the GP remaining at values typical of solid (gel) phases, in agreement with the above observations.

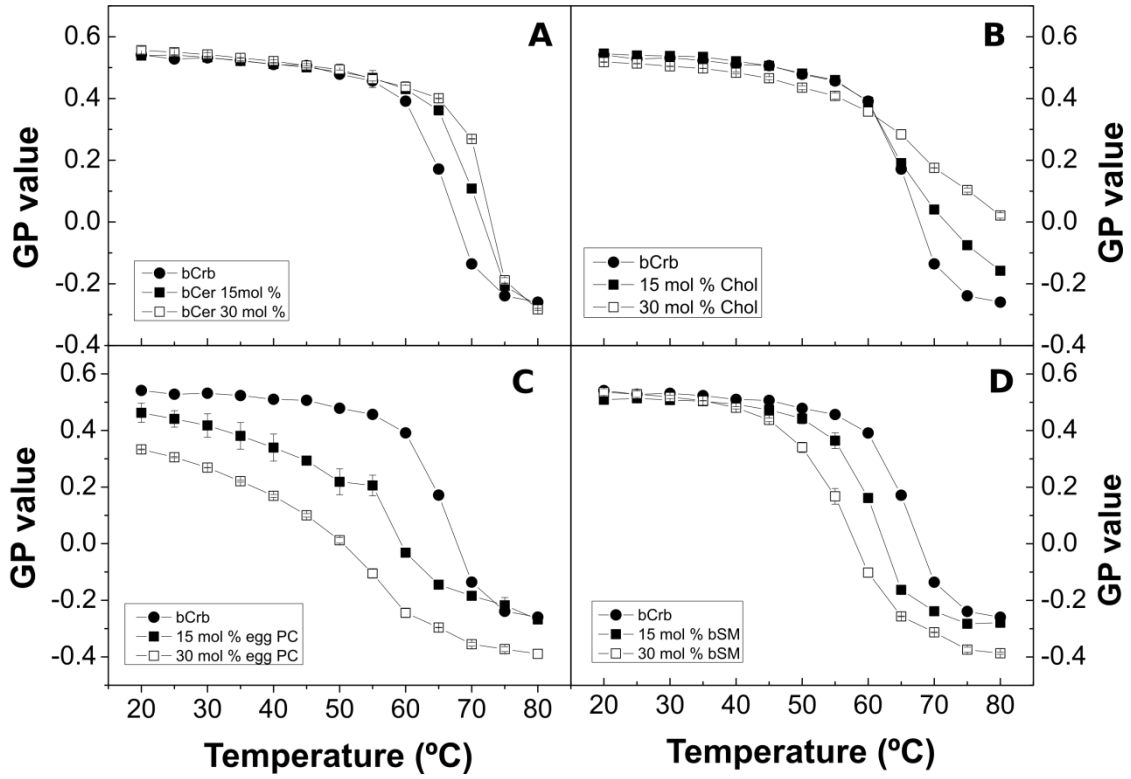

Figure 6.4. Thermotropic transitions of various bCrb-based bilayers, as detected through changes in Laurdan GP. Mixtures of bCrb with (A) bCer, (B) Chol, (C) ePC, (D) bSM. (Average ± S.D., triplicate). Sometimes the errors are smaller than the symbols.

6.3.3 Binary mixtures with cholesterol (Chol)

Several previous studies have been devoted to the Crb:Chol interactions (Varela *et al.*, 2017; Slotte *et al.*, 1993; Montes *et al.*, 2007), mainly with systems containing less than 50 mol% Crb. The influence of Chol on the gel-fluid transition of Crb has not been studied, to these authors' knowledge. This aspect of Crb behavior can be readily observed in the DSC thermograms in Figure 6.5. The calorimetric behavior of the mixture is very different from that of bCrb:bCer. With Chol the T_m transition temperature hardly changes, but the endotherm becomes progressively wider, until, at about 25 mol% Chol, it becomes hardly detectable. The marked widening and corresponding decrease in ΔH are clearly seen in the plots in Figure 6.6 B, C respectively. This is precisely the behavior of Chol in mixtures with phospholipids exhibiting a narrow gel-fluid phase transition, e.g. the saturated PC (Ladbrooke *et al.*, 1968; Mabrey *et al.*, 1978) or SM (Contreras *et al.*, 2004). The evolution of the two components found in the pure bCrb thermogram (Figure 6.1) is also interesting. With 5 mol% Chol (Figure 6.5) the two components are perfectly detectable. However already at 10 mol% Chol the endotherm is more symmetrical, and the two components observed are very different from the

previous ones: both are centered at the T_m, only one is much wider than the other. The situation is exactly the same as seen by Mabrey et al.. (Mabrey *et al.*, 1978) with DPPC:Chol thermograms. In our case we propose that, above a certain ratio, Chol interacts equally with the two Crb species (or sets of species) that gave origin to the asymmetric pure bCrb peak, the two novel components consisting presumably of Chol-poor and –rich domains. The partial phase diagram (Figure 6.6 D) is as expected quite similar to e.g. the one proposed for DMPC:Chol by Rivas and co-workers (Sáez-Cirión *et al.*, 2000; Vist & Davis, 1990).

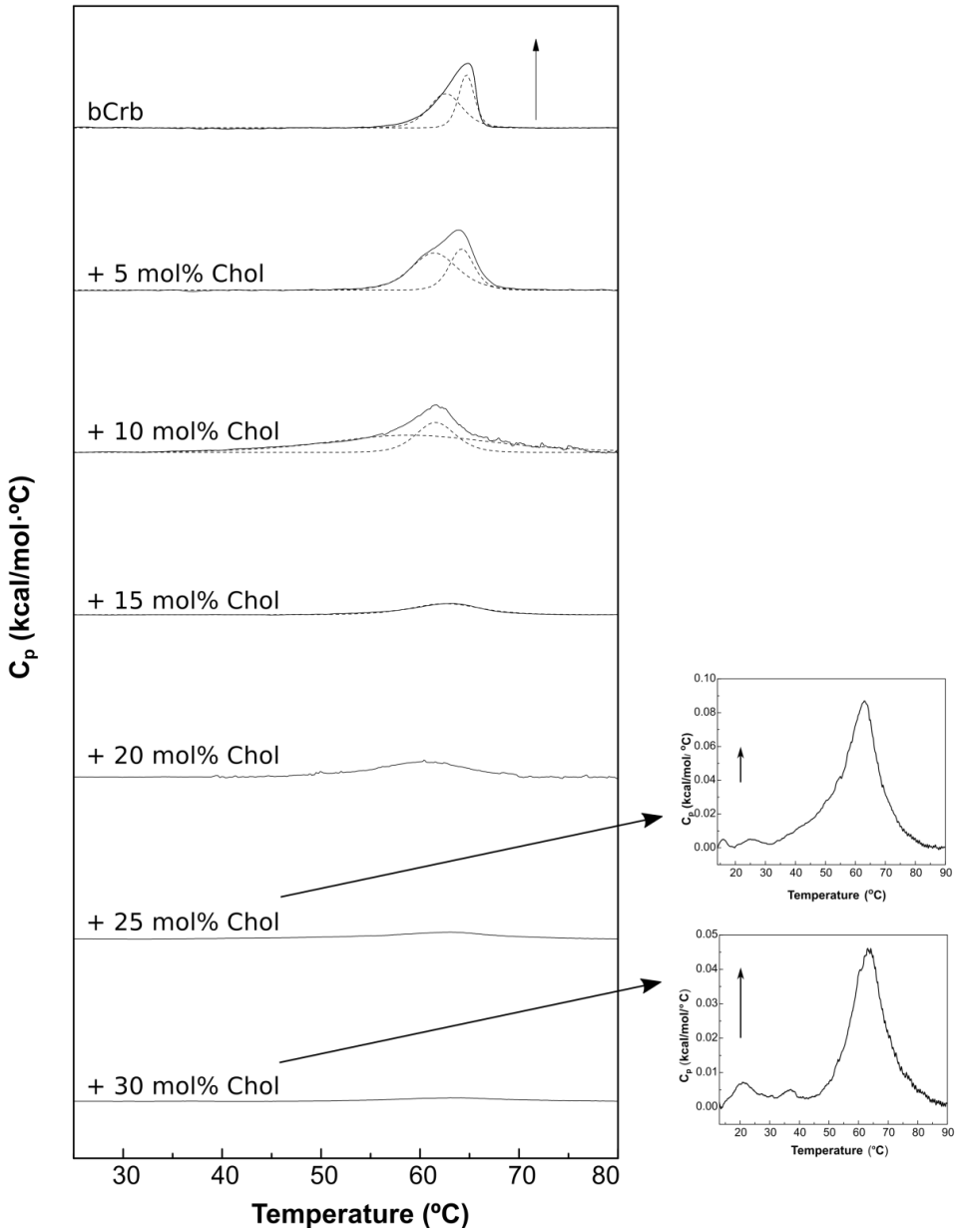

Figure 6.5. Representative DSC thermograms corresponding to the gel-fluid transition of pure bCrb and various bCrb:Chol mixtures in excess water. Mol percentage of Chol is indicated for each sample as a function of Chol concentration. Arrow: 1 kcal/mol/ºC. Arrow (insets, 25 and 30 mol% Chol): 0.02 kcal/mol/°C.

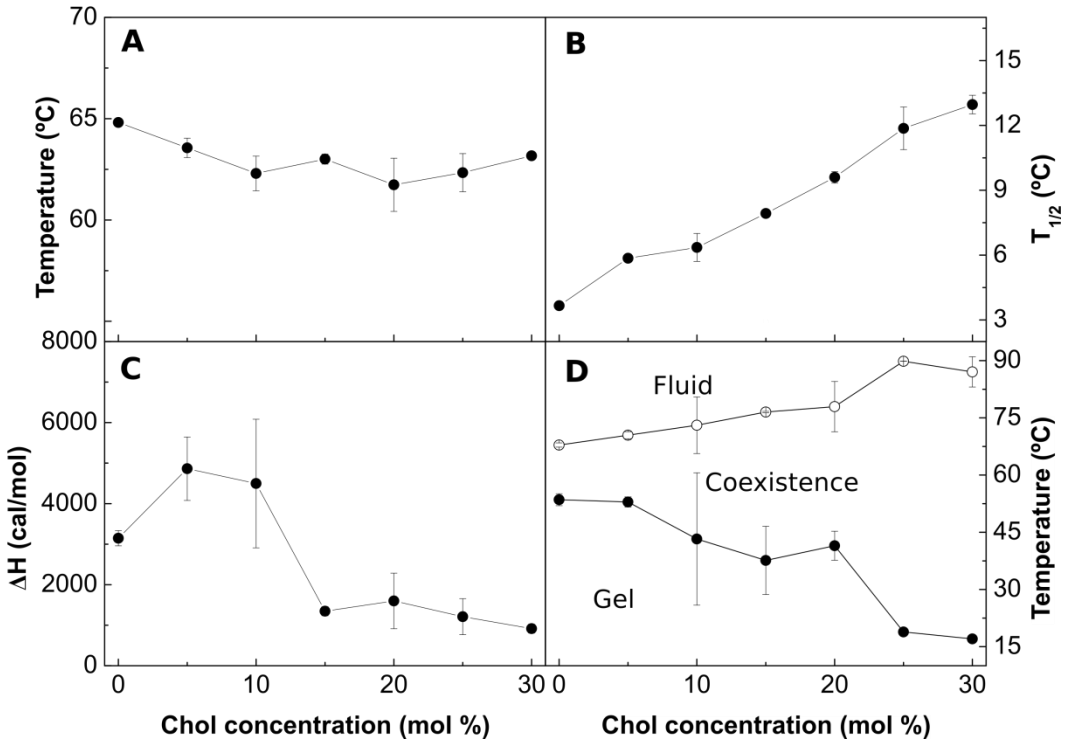

Figure 6.6. Thermodynamic parameters of bCrb:Chol mixtures. (A) Mid-point temperature of the gel-fluid transition. (B) Transition width at half-height. (C) Transition enthalpy, in cal/mol bCrb. (D) Temperature-composition diagram for the bCrb:Chol mixtures. The predominant phases are given for each area. (Average ± S.D., triplicate). Sometimes the errors are smaller than the symbols.

Laurdan GP studies of bCrb:Chol mixtures as a function of temperature (Figure 6.4 B) provide information complementary to the above. Essentially Chol exerts an ordering effect on the fluid bilayer chains, i.e. GP values at T>60 °C increase clearly with Chol concentration. A smaller, fluidifying effect is also seen at the lower temperatures. Studies of DPH fluorescence polarization in either pure bCrb or in 70:30 (mol ratio) bilayers over an extensive range of temperatures (Supplementary Figure 6.S3) also show the ordering properties of Chol on fluid bCrb bilayers and the smaller disordering effect at low temperatures. Once again the results are parallel to those obtained with the DMPC:Chol system (Harris *et al.*, 2002; Vist & Davis, 1990). This is an indication for the formation of liquid-ordered (L_o) phases. At room temperature (gel phase) Laurdan GP changes but little with a wide range of Chol concentrations, indicating only a small decrease in chain order (Supplementary Figure 6.S2 C, D).

6.3.4 Binary mixtures with egg PC (ePC)

In this series of experiments ePC is used as a typical lipid giving rise to a liquid-crystalline, or fluid (L_α) phase when fully hydrated at room temperature. Studies by previous authors have shown non-ideal miscibility of Crb and PC, both in monolayers and bilayers (Morrow *et al.*, 1992; Slotte *et al.*, 1993; Ali *et al.*, 1991; Maggio *et al.*, 1988, 1985). This is confirmed and expanded by the DSC thermograms in Figure 6.7. As expected from the low T_m of ePC (<0 ºC) increasing amounts of PC shift the bCrb transition towards lower temperatures. The two components seen in pure bCrb (Figure 6.1) remain distinct in all mixtures, but the low-T one appears to mix preferentially with the low-melting ePC, in agreement with the regular solution rule, with the outcome that, at a 60:40 bCrb:ePC mol ratio, the endotherm appears to arise exclusively from the high-T component (corresponding, according to our hypothesis, to hydroxylated bCer). In the hypothetical case of ideal miscibility of Crb and PC both Crb components would be equally affected by PC, and the asymmetry of the overall thermogram would not increase with PC concentration. The ePC-induced decrease in T_m and increase in $T_{1/2}$ (decrease in cooperativity) are quantitatively shown in Figure 6.8 A, B. Figure 6.8 C shows that, unlike Chol, ePC does not cause a decrease in transition enthalpy, perhaps even increases it, while 8B depicts an increase in $T_{1/2}$, i.e. a decrease in cooperativity. This may suggest that the bilayer is being fragmented into small domains (low cooperativity), but without extensive molecular mixing of bCrb and ePC (little change in ΔH). The above observations explain the partial phase diagram shown in Figure 6.8 D. Note that a major effect of ePC is to lower the onset of the transition, while its completion remains almost unchanged. This is also shown by the decrease in Laurdan GP with increasing concentrations of ePC, at room temperature (Supplementary Figure 6.S2 E, F): ePC is disordering the bCrb gel phase. Conversely additions of bCrb (in the 0-40 mol% range) increase linearly the order of fluid ePC bilayers at room temperature, according to Laurdan GP (Supplementary Figure 6.S4). Laurdan GPvalues as a function of T for different bCrb:ePC ratios (Figure 6.4 C) confirm the above observations.

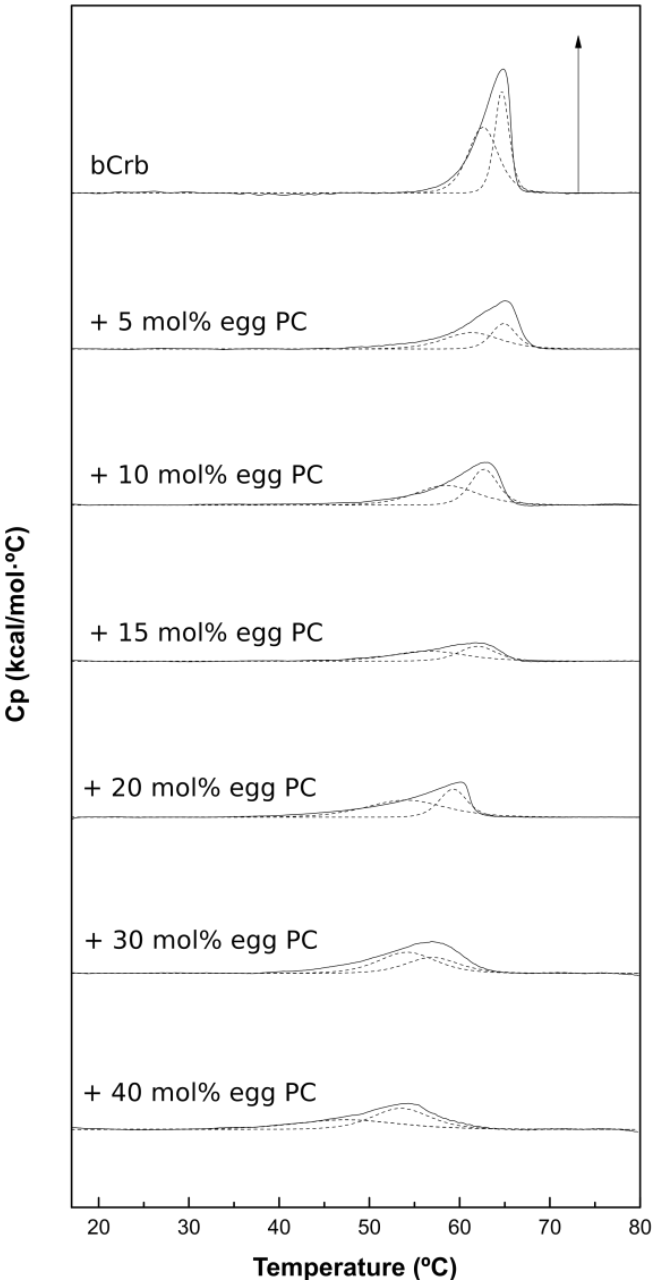

Figure 6.7. Representative DSC thermograms corresponding to the gel-fluid transition of pure bCrb and various bCrb:ePC mixtures in excess water. Mol percentage of ePC is indicated for each sample as a function of ePC concentration. Arrow: 1 kcal/mol/°C.

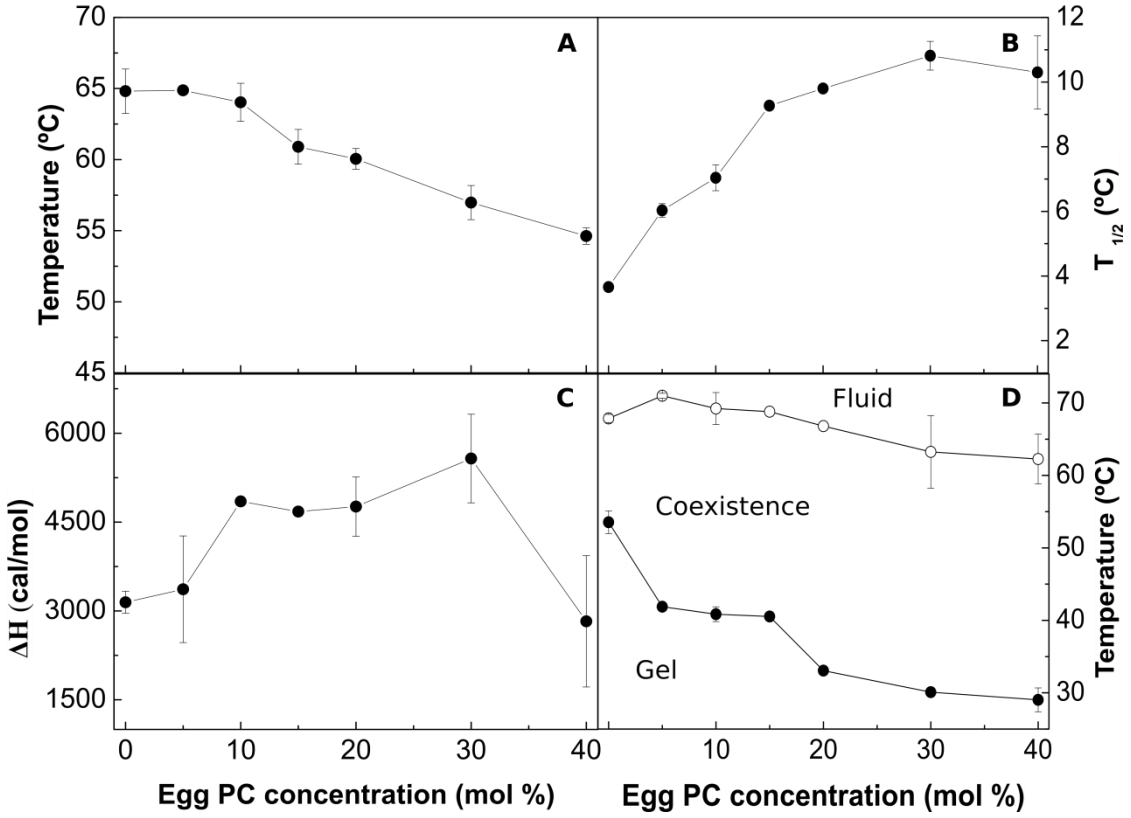

Figure 6.8. Thermodynamic parameters of bCrb:ePC mixtures. (A) Mid-point temperature of the gel-fluid transition. (B) Transition width at half-height. (C) Transition enthalpy, in cal/mol bCrb. (D) Temperature-composition diagram for the bCrb:ePC mixtures. The predominant phases are given for each area. (Average ± S.D., triplicate). Sometimes the errors are smaller than the symbols.

GUVs composed of bCrb:ePC could be formed and examined at room temperature by confocal fluorescence spectroscopy using Rho-PE, a probe that partitions preferentially into the more disordered domains. (Note that no GUV could be formed with either pure bCrb, or with bCrb:bCer or bCrb:Chol mixtures. Apparently bCrb requires mixing with some strongly bilayer-forming lipid, in our case ePC or bSM, to give rise to GUV under our conditions). A representative image of a vesicle containing bCrb:ePC at a 60:40 mol ratio is shown in Figure 6.9 A. Partially ordered (gel?), flower-like dark domains coexist with a continuous fluid disordered phase. The observed phase separation may be related to the different behavior of the two thermogram components seen in the DSC traces (Figure 6.7). This does not preclude the presence of the above-discussed microdomains in the overall fluid, continuous phase.

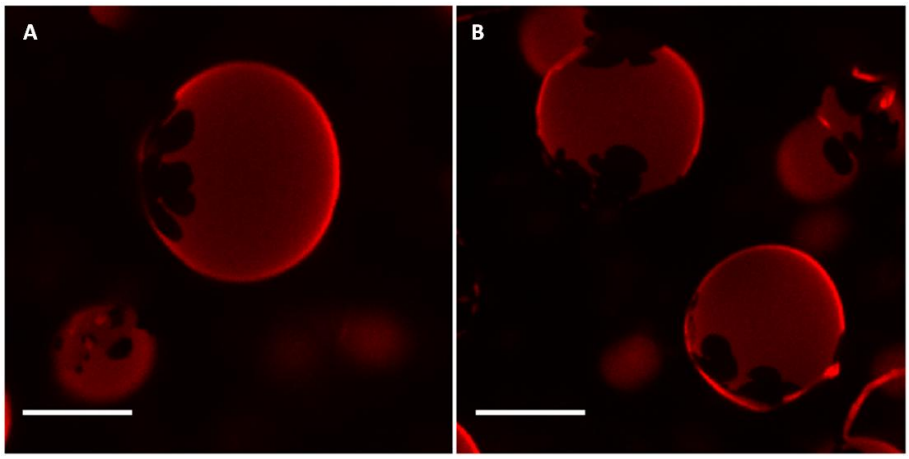

Figure 6.9. Confocal fluorescence microscopy of giant unilamellar vesicles of compositions: (A) bCrb:ePC (60:40 mol ratio) , (B) bCrb:bSM (60:40 mol ratio).

6.3.5 Binary mixtures with brain sphingomyelin (bSM)

Both Crb and SM are abundant in the myelin Schwann's cell membranes, thus their mixing properties are particularly relevant. bSM has a T_m transition temperature around 37 ºC (De Almeida *et al.*, 2003) *vs.* 64.8 ºC for bCrb (Figure 6.1). Consequently mixing of both lipids should lead to a decreased T_m of the mixture as bSM is included. This is what happens according to the DSC measurements (Figure 6.10). The endotherms are widened, particularly due to a decrease in the onset T above 20 mol% bSM (Figure 6.11 D). Many effects of bSM on bCrb are similar to those of ePC (Figure 6.8 and 6.12), perhaps because both bSM and ePC are phospholipids whose T_m are well below that of bCrb.

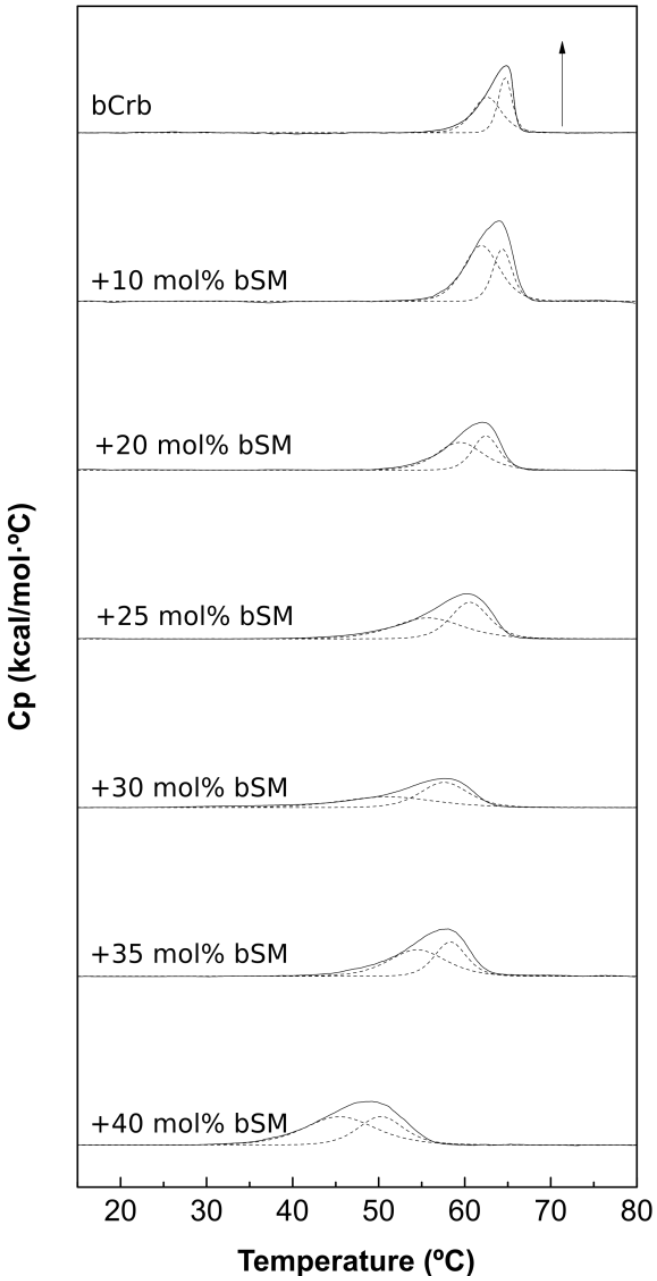

Figure 6.10. Representative DSC thermograms corresponding to the gel-fluid transition of pure bCrb and various bCrb:bSM mixtures in excess water. Mol percentage of bSM is indicated for each sample as a function of bSM concentration. Arrow: 1 kcal/mol/°C.

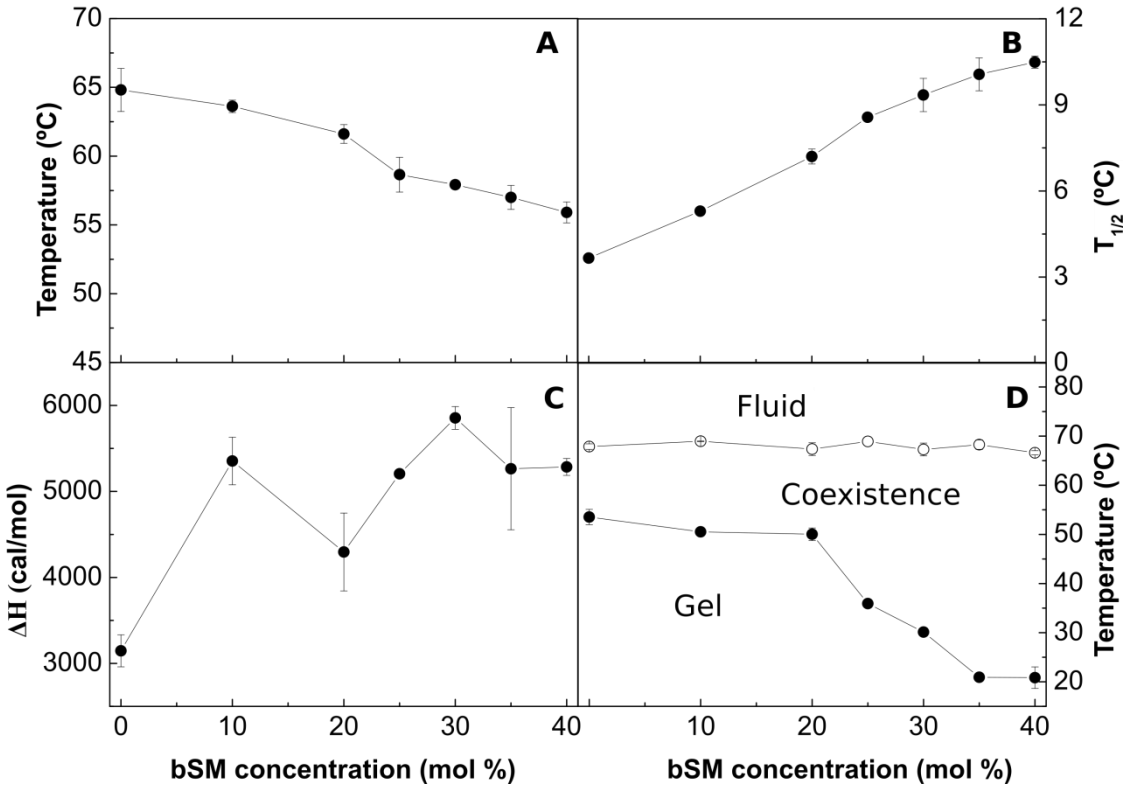

Figure 6.11: Thermodynamic parameters of bCrb:bSM mixtures. (A) Mid-point temperature of the gel-fluid transition. (B) Transition width at half-height. (C) Transition enthalpy, in cal/mol bCrb. (D) Temperature-composition diagram for the bCrb:bSM mixtures. The predominant phases are given for each area. (Average ± S.D., triplicate). Sometimes the errors are smaller than the symbols.

An important difference between both phospholipids is that, with bSM, little mixing appears to occur in the gel phase at and below 20 mol% concentration (Figure 6.11 D), while with ePC mixing starts as soon as some ePC molecules occur in the bCrb bilayer (Figure 6.8 D). This is most likely attributed to the higher T_m of bSM as compared to ePC. Similar results are found with Laurdan (Figure 6.4 C, D) in that ePC, but not bSM, causes a decrease in GP in the gel state. bSM is also unable to cause a dose-dependent decrease in Laurdan GP at room temperature, at variance with ePC (Supplementary Fig S2 E, G). All of the above data concur in showing that bSM and bCrb hardly mix at or below 20 mol% bSM. Some 60:40 (mol ratio) GUV vesicles, as seen by confocal fluorescence microscopy at room temperature, are shown in Figure 6.9 B. A lateral separation of more and less fluid domains (respectively bright and dark) is clearly seen. The dark patches display irregular contours, indicative of coexisting domains with little or no lipid intermixing, in agreement with the above data.

6.3.6 Crb induces very little membrane permeability or lipid transbilayer motion

Cer is known to make lipid bilayers and cell membranes permeable even to high molecular weight (protein-sized) solutes (Montes *et al.*, 2002). We have performed experiments in which either Cer or Crb in organic solvent are added to LUV composed of ePC:Chol (3:1 mol ratio) loaded with the water-soluble probes ANTS/DPX, as described in Montes et al.. (Montes *et al.*, 2002). N-palmitoyl Cer and N-palmitoyl Crb were tested separately, with N-palmitoyl SM as a control (Figure 6.12 A). The N-palmitoyl derivatives of all three lipids are used to facilitate comparison. Leakage values were recorded when an apparent equilibrium was achieved (30 min). Crb was clearly less active than Cer in promoting bilayer permeabilization.

An additional property of Cer is that they can induce lipid transbilayer (flip-flop) motion (De Almeida *et al.*, 2003). In this assay vesicles containing NBD-PE located in the inner monolayer were incubated with sodium dithionite, a fluorescence quencher for which the membranes are impermeable. Lipid flip-flop causes NBD-PE molecules to move to the outer monolayer, where they are quenched by dithionite. Thus transbilayer lipid motion was assayed as a decrease in NBD fluorescence (Contreras *et al.*, 2003). ePC:Chol (3:1 mol ratio) LUV were used, to which the appropriate sphingolipids (N-palmitoyl Cer, Crb or SM) are added at time 0. The decrease in NBD fluorescence was measured after an apparent equilibrium was reached. As seen in Figure 6.12 B Crb are again clearly less active than Cer in causing lipid flip-flop in bilayers.

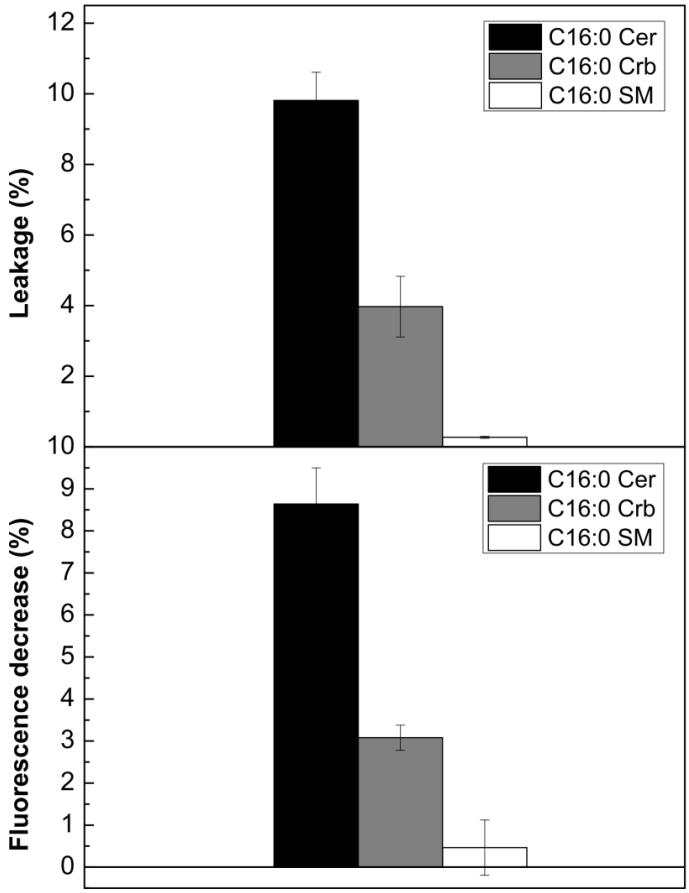

Figure 6.12. (A) Release of vesicular aqueous contents induced in LUV composed of ePC:Chol (3:1) by addition of C16:0 Cer, C16:0 Crb, or C16:0 SM. (B) Transbilayer (flip-flop) motion of lipids in LUV composed of ePC:Chol (3:1) by addition of C16:0 Cer, C16:0 Crb, or C16:0 SM. Average ± S.D (triplicate).

6.4 Discussion

6.4.1 The physical properties of bCrb in bilayers

From the combined experiments described above, one can conclude that the main relevant properties of bCrb are (i) its capacity to rigidify fluid bilayers, (ii) its relatively good mixing with both fluid phospholipids and ceramides, and (iii) its interaction with Chol. The rigidifying, or ordering capacity of bCrb is best seen when the calorimetric (Figure 6.8 A, 6.11 A) and Laurdan GP data (Figure 6.5 C, D) are seen for bCrb mixtures with ePC and bSM. The DSC data show that the higher the bCrb concentration, the higher the T_m. More clearly, the Laurdan data show that in mixtures with ePC (Figure 6.4 C), that is fluid at all temperatures, pure bCrb is more ordered than the bCrb:ePC mixtures at all T. With bSM, that is fluid only

above ~40 °C, the ordering effect of bCrb is only seen above that temperature. The rigidifying effect of bCrb is detectable at all concentrations. Supplementary Figure 6.S3 shows the Laurdan GP of ePC at room T with increasing bCrb concentrations (mol ratios 0-40%). This is in agreement with the data in (Morrow *et al.*, 1992; Longo & Blanchette, 2010; Varela *et al.*, 2013).

bCrb mixes (to some extent) and rigidifies fluid phospholipid bilayers. It also acts, conversely, disordering the highly rigid bCer bilayers. bCer cannot form, at least easily, bilayers when in pure form, it rather forms rigid patches in phospholipid bilayers, even at very low Cer:phospholipid ratios (Carrer & Maggio, 1999; Veiga *et al.*, 1999; Sot *et al.*, 2008; Goni & Alonso, 2009). However when bCrb is mixed with bCer under conditions when bilayers are formed, i.e. at high bCrb ratios, bCrb tends to increase bilayer fluidity, both lipids mixing even in the gel phase up to 20 mol% bCer concentration (Figure 6.3 A, D, Figure 6.4 A). bCrb miscibility with fluid phospholipid bilayers appears to be limited: several data report on phase separation at bCrb concentrations above 20 mol%. Nevertheless bCrb miscibility is clearly higher than that of Cer, for which < 5 mol% are sufficient to give rise to rigid domains (Sot *et al.*, 2006). However in GUVs containing 15 mol% bCrb in either bSM or ePC (Supplementary Figure 6.S4), no domains are detected

The data on bCrb:Chol mixtures provide the rather interesting observation that bCrb interacts with cholesterol in such a way that the main gel-fluid transition of bCrb is widened, and the associated ΔH decreases with increasing concentrations of Chol, while T_m remains essentially unchanged (Figure 6.5, 6.6). bCrb is acting like the saturated PC (DMPC, DPPC), or like many SM in mixtures with sterols (Ladbrooke *et al.*, 1968; Mabrey *et al.*, 1978; Contreras *et al.*, 2004; McMullen & McElhaney, 1995). In view of the very different head groups of SM and Crb, it appears that the observed behavior is mainly due to the presence of a two-chain, rigid lipid in the mixture with cholesterol. Note however the observation by Slotte et al.. (Slotte *et al.*, 1993) that Crb is weaker than SM in forming laterally segregated domains with Chol. Hall et al.. (Hall *et al.*, 2010), using atomistic molecular dynamics simulations in bilayers containing 5 mol% Crb, observed a specific interaction of the sphingolipid with Chol, in which Chol would be shielded from the water phase by Crb.

6.4.2 Cerebroside, ceramide, sphingomyelin: tamed tiger, wild tiger, caged tiger

These three lipids can exist in very different concentrations in cell membranes. Cer and Crb occur at <1% of the total membrane lipids in the average normal cell, while SM vary from 2 to 15%, depending on the tissue (Lloyd-Evans *et al.*, 2003). Cer concentration cannot increase much above the normal levels without irreversible damage to the cell, because Cer is a signal for apoptosis. Only in apoptotic cells can Cer levels reach values well above 1% (Reynolds *et al.*, 2004). In the relatively inert myelin membranes however, whose main role is that of acting as electrical insulators of the cell, Crb is found at up to 20% of the total lipids, and the bilayers are stable.

These different concentrations can be related to the different physical properties and physiological role of these lipids, as follows. (i) The simplest of them i.e. ceramide is also the one that is more disruptive for the bilayer: Cer hardly mixes with the other lipids, permeabilizes the cell membrane, destroys membrane asymmetry, and facilitates non-lamellar phase formation (Alonso & Goñi, 2018). Apart from being a metabolic intermediate, its main role in cell physiology appears to be as a pro-apoptotic signal. It is only natural that it is always found at very low concentrations in healthy cell membranes. (ii) At the other end of the sphingolipid spectrum SM occurs in large amounts, being one of the major phospholipids in all mammalian plasma membranes, forms very stable bilayers, and its main role appears to be largely structural. However SM is also the origin of Cer generation in the plasma membrane in response to stress conditions, through the action of acid sphingomyelinase (Merrill *et al.*, 1986; Kolesnick *et al.*, 2000). (iii) Crb has somewhat intermediate properties between Cer and SM. Its concentration in membranes may vary by two orders of magnitude without major changes in membrane stability or functionality. Crb can act as a metabolic intermediate just as readily as Cer, not only can it be at the origin of complex glycosphingolipid synthesis, but it can give rise to Cer through the glucosyl ceramidase reaction. As seen from the above results, Crb mixes much better than Cer with other membrane lipids, thus it can exist in high concentrations serving as a sphingolipid store, and it does not perturb the bilayer structure of the membrane. Using a fair amount of poetic licence, one could compare Cer to the wild tiger, SM to the caged tiger, waiting to be released through the sphingomyelinase reaction, and Crb to the tamed tiger, which can make itself useful in a variety of ways, relatively free of danger for its owner.

6.5 Supplementary data

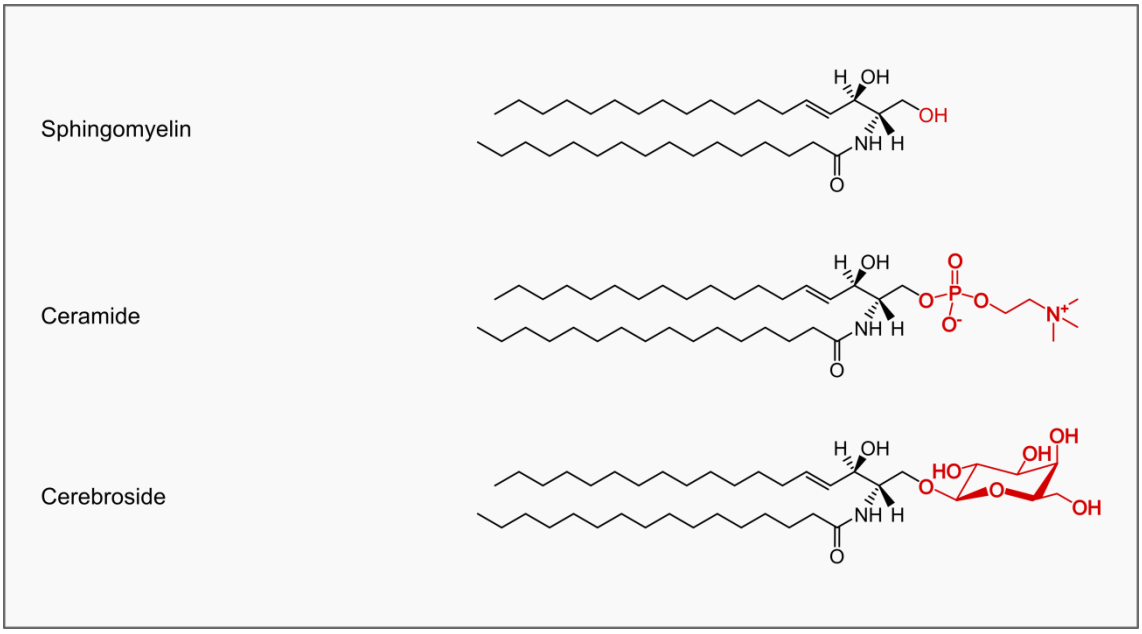

Figure 6.S1: Structures of the sphingolipids relevant to the present study.

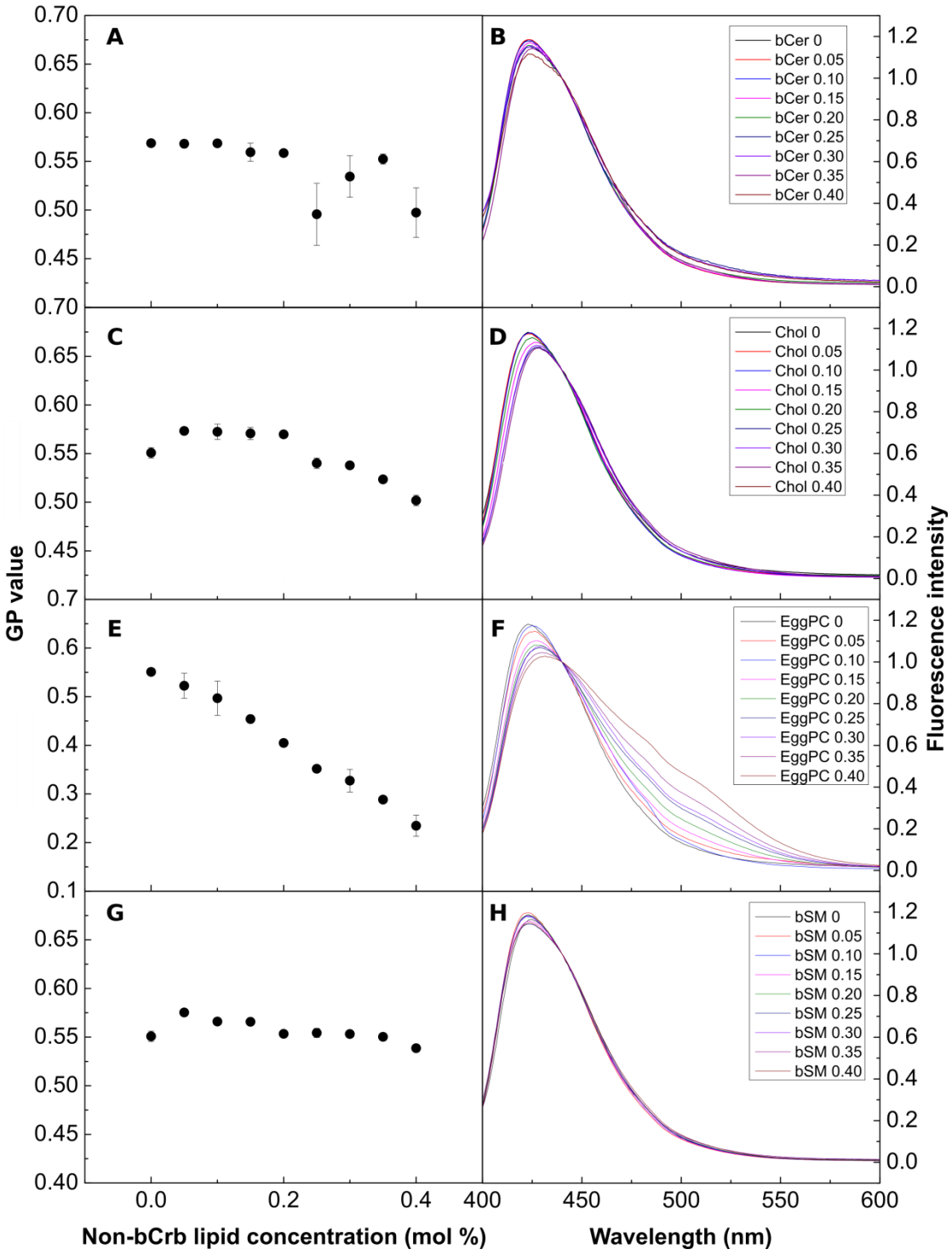

Figure 6.S2: Laurdan spectra and their corresponding GP values for mixtures of bCrb with additional lipids. Measurements were performed at room temperature. (A, B) bCrb + bCer. (C, D) bCrb + Chol. (E, F) bCrb + ePC. (G, H) bCrb + bSM. Average values ± S.D. (triplicate).

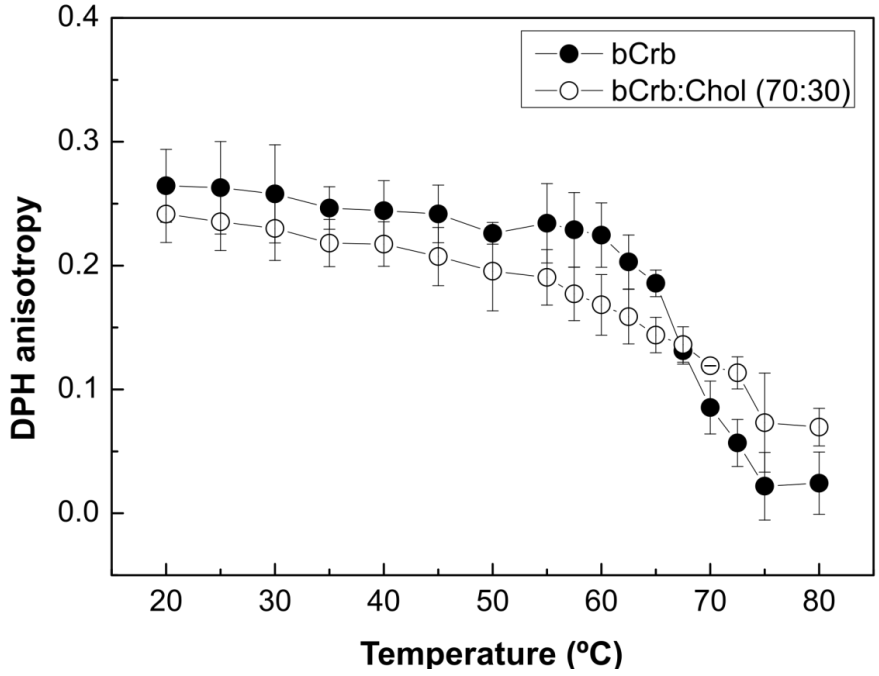

Figure 6.S3: DPH fluorescence anisotropy of bCrb and bCrb:Chol (70:30 mol ratio) as a function of temperature. Average values ± S.D. (triplicate).

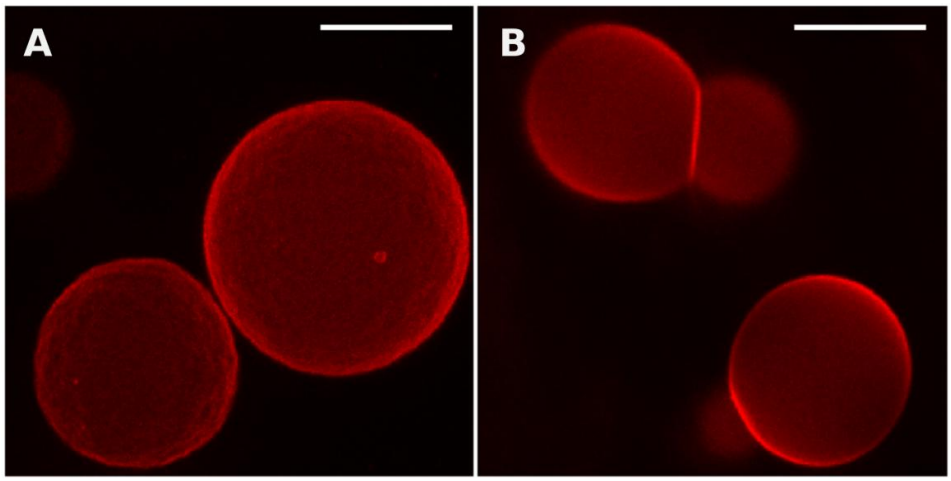

Figure 6.S4: Confocal fluorescence microscopy of giant unilamellar vesicles of compositions: (A) bCrb:bSM (15:85 mol ratio) , (B) bCer:ePC (15:85 mol ratio).

CHAPTER 7:

OVERVIEW AND CONCLUSIONS

CHAPTER 7: OVERVIEW AND CONCLUSIONS

The present thesis deals with the study of the lipid-lipid interactions associated to the lateral segregation of sphingolipids and cholesterol. These studies have been performed employing membrane model systems composed of three or four components, and using different biophysical techniques, mainly differential scanning calorimetry (DSC), fluorescence spectroscopy and microscopy, and atomic force microscopy (AFM), with the following aims:

- To characterize the structure of natural eSM and synthetic pSM phases below their main phase transition temperature.

- To analyze the behavior of Cer and Chol with a saturated phospholipid in three component systems.

- To study the effect of unsaturated sphingolipid incorporation into phospholipid model membranes.

- To describe the interaction of natural glycosphingolipids (Crb) in binary systems with sphingolipids, glycerolipids or Chol.

7.1 Phase behavior of palmitoyl and egg sphingomyelin

SM has become one of the most studied lipids in the last decades due to its role in Cer generation and to its interaction with Chol to form Chol-enriched domains. Our studies have characterized the phase behavior of natural SM (egg) and synthetic SM (palmitoyl) in a broad temperature interval with different results. Some of the previous studies observed a pretransition below the main phase transition, pointing to the existence of a ripple-gel phase transition, while others reported only one transition from the gel to the fluid phase.

In chapter 3 a structural characterization of both, egg and palmitoyl SM lamellar phases is performed, using X-ray scattering in a collaboration with S. Tristram-Nagle (Carnegie Mellon University, Pittsburgh, USA). The method developed by Dr. Tristram-Nagle is suitable to characterize the phase behavior of the lipids of interest.

Our results demonstrate that natural SM presents a stable ripple phase at all temperatures below its main phase transition, which is clearly identified as a ripple-fluid transition instead of a gel-fluid transition as previously reported. The stability of the ripple phase in this wide temperature range is associated with the presence of longer fatty acids in the sample. Otherwise, synthetic (N-palmitoyl) SM presents a pretransition from gel to ripple phase below its main phase transition.

The formation of highly ordered domains has been examined using oriented samples. The effects of Cer incorporation on eSM phases are observed, showing a change from ripple to gel phase. However, X-ray scattering requires a high proportion of Cer (≈ 30 mol%) to detect the formation of these domains, that may go unobserved at lower Cer concentrations.

7.2 Ceramide and cholesterol interaction with a saturated phospholipid

As previously described, SM has been widely studied due to its interaction with Chol; however, it also has an important role as a precursor of bioactive lipids such as Cer that also have a strong interaction with SM. The lateral segregation ability of both lipids has promoted several studies about their interactions, concluding: i) Cer displace Chol from tightly packed SM:Chol liquid-ordered (L_o) phases, ii) a high concentration of Chol is needed to induce Cer-enriched domain depletion, and iii) Cer and Chol interact even in the absence of SM. Additionally, previous studies in our laboratory have shown how Cer and Chol (at saturating concentrations) interact with a saturated-chain phospholipid giving rise to a homogeneous bilayer with unique properties.

In chapter 4 a study about the interaction between Cer and Chol with saturated phospholipids such as SM and DPPC is performed. Samples are prepared varying the concentration of both lipids but maintaining their ratio constant. This work intends to clarify if this interaction depends on the affinity between these lipids or their relative ratio, using atomic force microscopy (AFM), confocal microscopy and differential scanning calorimetry (DSC).

Our results show a predominant gel phase behavior (high molecular order and thermostability) of a ternary sample in which Cer and Chol are saturating the system. However, when the concentration of the phospholipid is increased, both lipids tend to segregate laterally. These observations are associated with the predominant lipid-lipid interaction in the sample, pCer:Chol being more important in the saturated sample (54:23:23), and pSM:pCer and pSM:Chol becomes detectable when the quantity of the phospholipid increases. Moreover, the lower affinity of Cer and Chol for DPPC over SM leads to a lower tendency towards macroscopic phase separation of the DPPC-based samples.

7.3 Unsaturated sphingolipid incorporation into phospholipid model membranes

Most studies on SM:Cer interaction have been focused on saturated sphingolipids; however recent studies have shown that the cell levels or unsaturated sphingolipids (C24:1) are higher than expected, and in some cases are on par with their C16:0 counterparts. Additionally, it has been described how C24:1 SM is not able to form liquid-ordered domains in the presence of DOPC and Chol.

In chapter 5 a four-component model system is used to characterize the effects of unsaturated sphingolipid incorporation into phospholipid membranes. DOPC, SM, Chol and Cer are used to replicate a L_α-L_o cell membrane environment. DOPC, SM and Chol are abundant in the plasma membrane, while Cer is obtained upon hydrolysis of SM. To characterize the biophysical properties of these model systems a number of techniques were used such as differential scanning calorimetry (DSC), confocal microscopy, and atomic force microscopy (AFM).

Our results conclude that unsaturated SM does not avoid the formation of highly ordered ceramide domains and tends to decrease the temperature phase transition in all cases studied. Moreover, we observe how saturated SM tends to accommodate both saturated and unsaturated Cer while unsaturated SM accommodates only partially Cer. This result is associated with a clear preference of Cer for palmitoyl SM. Our results also suggest that C24:1 SM favors the cooperation between Cer. In addition, it is confirmed that unsaturated Cer give rise to less ordered domains than their saturated counterparts.

7.4 Glycosphingolipid interaction with sphingolipids and cholesterol

The main difference between glycosphingolipids and SM is found in their polar headgroup, the former having a saccharide instead of a phosphorylcholine. Among them, Crb are the simplest glycosphingolipids and are components of most eukaryotic cell plasma membranes, although at a concentration considerably lower than SM. They are associated with cellular processes such as cell division, growth, survival and membrane trafficking. It has been demonstrated that the accumulation of Crb in cells gives rise to diseases such as Gaucher´s and Krabbe´s, however, most studies in the past have been performed with low Crb concentrations (5-10 mol%).

In chapter 6 the interaction between glycosphingolipids, sphingolipids and Chol is studied at high concentrations of Crb in binary mixtures, using mainly differential scanning calorimetry. In addition, the ability of Crb to induce membrane permeability and transbilayer movement is tested.

Our results show a relative good mixing between Crb and all sphingolipids tested, and with Chol. It is possible to observe how an increase in Chol concentration affects its main phase transition. Crb, as Cer, are not able to form lipid bilayers by themselves and tend to segregate laterally within a fluid lipid bilayer. However their miscibility is clearly higher (20 mol%) than that of Cer, which tend to segregate at concentrations below 5 mol%. Furthermore, Crb have somewhat intermediate properties between Cer and sphingomyelins. Their concentration in membranes may vary by two orders of magnitude without major changes in membrane stability or functionality. Crb can act as a metabolic intermediate just as readily as Cer, not only can they be at the origin of complex glycosphingolipid synthesis, but they can also give rise to Cer through the glucosyl ceramidase reaction. As seen from the above results, Crb mix much better than Cer with other membrane lipids, thus they can exist at high concentrations serving as a sphingolipid store, without perturbing the bilayer structure of the membrane.

7.5 Conclusions

The main conclusions of this work include:

- Egg SM forms a ripple phase below its main phase transition, in the 3 - 55 °C temperature range, while pSM presents a gel to ripple pretransition below its main phase transition, at ≈ 24 °C.

- (Cer + Chol) interaction in ternary mixtures with a saturated phospholipid depends on the phospholipid concentration of both lipids rather than on the Cer:Chol ratio.

- Unsaturated sphingolipids tend to decrease the stiffness of the sample. Specifically, unsaturated SM does not prevent the formation of Cer-enriched domains, and instead favors the cooperation between Cer.

- Crb have somewhat intermediate properties between Cer and SM. They mix much better than Cer with other membrane lipids and do not affect membrane stability or functionality as much as Cer.

CAPÍTULO 7:

RESUMEN Y CONCLUSIONES

CAPÍTULO 7: RESUMEN Y CONCLUSIONES

La presente tesis se ha centrado el estudio de las interacciones lípido-lípido asociadas a la segregación lateral de esfingolipidos y colesterol. Estos estudios se han llevado a cabo utilizando sistemas de membranas modelo compuestos por tres o cuatro componentes, y utilizando diferentes técnicas biofísicas, principalmente calorimetría diferencial de barrido, espectroscopia y microscopía de fluorescencia y microscopía de fuerza atómica, con los siguientes objetivos:

- Caracterizar la estructura de las fases de la eSM y la pSM por debajo de su temperatura de transición principal de fase.

- Analizar el comportamiento de la ceramida y el colesterol con un fosfolípido saturado en un sistema modelo de tres componentes.

- Estudiar el efecto de la incorporación de esfingolipidos insaturados en membranas fosfolipídicas modelo.

- Describir la interacción de glicoesfingolipidos naturales (cerebrósidos) en sistemas binarios con esfingolípidos, glicerolípidos o colesterol.

7.1 Comportamiento de fase de la SM de huevo y la pSM

La esfingomielina se ha convertido en uno de los lípidos más estudiados en las últimas décadas debido a su papel en la generación de ceramidas, y a su interacción con el colesterol para formar dominios enriquecidos en colesterol. Nuestros estudios han caracterizado el comportamiento de fase de la esfingomielina de huevo y la esfingomielina sintética (palmitil) en un amplio intervalo de temperaturas con diferentes resultados. En algunos estudios previos se había observado una pretransición por debajo de su transición de fase principal, apuntando a la existencia de una transición de fase ondulada a fase gel, mientras que otros solo observaron una transición de fase gel a fluida.

En el capítulo 3 se lleva a cabo una caracterización estructural de ambas esfingomielinas utilizando difracción de rayos X en colaboración con S. Tristram-Nagle (Carnegie Mellon University, Pittsburgh, United States). El método desarrollado por la Dra. Tristram-Nagle es adecuado para caracterizar el comportamiento de fase de los lípidos estudiados.

Nuestros resultados demuestran que la SM natural presenta una fase ondulada estable a todas las temperaturas estudiadas por debajo de su transición de fase principal, la cual es identificada como una transición de fase ondulada a fluida en lugar de ser una transición de fase gel a fluida como se había descrito previamente. La estabilidad de la fase ondulada en este amplio intervalo de temperaturas se asocia a la presencia de ácidos grasos de cadena larga. Por otro lado, la esfingomielina sintética presenta una pretransición de fase ondulada a fase gel por debajo de su transición principal.

Por último, se estudia la formación de dominios de ceramida altamente ordenados utilizando muestras orientadas. La incorporación de ceramida en la muestra provoca un cambio de fase ondulada a fase gel en la esfingomielina de huevo. Sin embargo, la difracción de rayos X requiere una gran cantidad de ceramida para detectar la formación de estos dominios, que probablemente aparecen a concentraciones de ceramida más bajas sin ser detectados.

7.2 Interacción de ceramida y colesterol con un fosfolípido saturado

La esfingomielina ha sido ampliamente estudiada debido a su interacción con el colesterol, sin embargo, tiene un papel importante como precursor de lípidos bioactivos tales como las ceramidas, que a su vez tienen una fuerte interacción con la esfingomielina. La capacidad de ambos lípidos de segregar lateralmente ha propiciado numerosos estudios sobre su interacción, concluyendo: i) la ceramida desplaza al colesterol de su interacción con la esfingomielina, ii) el colesterol regula la formación de dominios de ceramida, y iii) la ceramida y el colesterol interaccionan incluso en ausencia de esfingomielina. Además, estudios previos en nuestro laboratorio han demostrado cómo el colesterol y la ceramida (en concentraciones saturantes) interaccionan con fosfolipidos saturados dando lugar a una bicapa homogénea con propiedades singulares.

En el capítulo 4 se estudia la interacción entre la ceramida y el colesterol con fosfolípidos saturados tales como la esfingomielina y el DPPC. Se preparan muestras variando la concentración de ambos lípidos pero manteniendo constante su relación molar. En este capítulo se intenta aclarar si dicha interacción depende de la afinidad entre los lípidos o de su relación molar relativa, utilizando la

microscopía de fuerza atómica, la microscopía confocal y la calorimetría diferencial de barrido.

Nuestros resultados muestran un comportamiento de fase gel predominante (alto orden molecular y termoestabilidad) de una fase ternaria en la que el colesterol y la ceramida están saturando el sistema. Sin embargo, cuando la concentración del fosfolípido aumenta, ambos tienden a segregar lateralmente. Estas observaciones se asocian con la interacción lipídica predominante en la muestra, siendo la interacción ceramida-colesterol más importante en la muestra con menos fosfolípido (54:23:23), mientras que predomina la interacción de dichos lípidos con la esfingomielina por separado cuando la cantidad de fosfolípido aumenta. Además, la menor segregación lateral observada con el DPPC confirma la menor afinidad de la ceramida y el colesterol por el DPPC que por la esfingomielina.

7.3 Incorporación de esfingolipidos insaturados en membranas modelo fosfolipídicas

La mayoría de los estudios de interacción de SM:Cer se han enfocado en los esfingolipidos saturados, sin embargo, estudios recientes han demostrado que los niveles celulares de ciertos esfingolípidos insaturados como la esfingomielina 24:1 son más altos de los esperado. En algunos casos se encuentran muy igualados a otros esfingolipidos saturados como los esfingolipidos 16:0. Además, se ha observado que la esfingomielina 24:1 no segrega lateralmente en presencia de DOPC y colesterol.

En el capítulo 5 se utiliza un sistema modelo de cuatro componentes para caracterizar los efectos de la incorporación de esfingolipidos insaturados en membranas fosfolipídicas. Lipidos como el DOPC, la esfingomielina, el colesterol y la ceramida son utilizados para replicar la segregación de fases observada en las membranas celulares. El DOPC, la esfingomielina y el colesterol son abundantes en la membrana plasmática, mientras que la ceramida se obtiene mediante la hidrólisis de la esfingomielina. Para llevar a cabo una caracterización de las propiedades biofísicas de estas membranas se utilizan técnicas como la microscopía de fuerza atómica, la microscopía confocal y la calorimetría diferencial de barrido.

Nuestros resultados concluyen que la esfingomielina insaturada no evita la formación de dominios de ceramida altamente ordenados y tiende a disminuir la temperatura de transición de fase en todos los casos estudiados. Además, se observa cómo la esfingomielina saturada tiende a acomodar a ambas ceramidas,

saturada e insaturada, mientras que la esfingomielina insaturada solo acomoda parcialmente las ceramidas. Este resultado se asocia a una preferencia de ambas ceramidas por la palmitil esfingomielina. Nuestros resultados también sugieren que la esfingomielina 24:1 favorece la cooperación entre las ceramidas. Por último, se confirma que la ceramida insaturada forma dominios menos ordenados que la saturada.

7.4 Interacción de glicoesfingolipidos con esfingolipidos y colesterol

La diferencia principal entre los glicoesfingolípidos y la esfingomielina se encuentra en su cabeza polar, el primero tiene un grupo sacárido en lugar de una fosfocolina. Entre ellos, los cerebrósidos son los glicoesfingolípidos más simples, y son componentes de la membrana plasmática de la mayoría de las células eucariotas, aunque a una concentración considerablemente menor que la esfingomielina. Se asocian con procesos celulares como la división, el crecimiento, la supervivencia y el tráfico en la membrana. Además, se ha demostrado que la acumulación de cerebrósidos en las células provoca enfermedades como las de Gaucher y Krabbe, sin embargo, la mayoría de los estudios previos se han llevado a cabo a concentraciones muy bajas.

En el capítulo 6 se estudia la interacción entre los cerebrósidos (utilizando altas concentraciones) con esfingolipidos y colesterol en mezclas binarias, utilizando principalmente calorimetría diferencial de barrido. Además, se comprueba la habilidad de los cerebrósidos para inducir el movimiento transbicapa y la permeabilidad en la membrana.

Nuestros resultados muestran que los cerebrósidos se mezclan relativamente bien con todos los esfingolípidos e incluso el colesterol. Se puede observar cómo cambia su transición de fase principal a medida que se aumenta la concentración de colesterol. Los cerebrósidos, al igual que las ceramidas, no son capaces de formar estructuras lamelares por sí mismos y tienden a segregar lateralmente dentro de una bicapa lipídica fluida. Sin embargo su miscibilidad (20 % mol) es mucho más alta que la de las ceramidas, la cuales segregan a concentraciones menores (5 % mol). Además, los cerebrósidos tienen propiedades intermedias entre las ceramidas y las esfingomielinas, entre las que se encuentran: i) su concentración en las membranas puede variar en torno a dos órdenes de magnitud sin provocar grandes cambios en la estabilidad y la funcionalidad de las membranas, ii) pueden actuar como intermediarios metabólicos, al igual que las ceramidas, iii) pueden dar lugar a glicoesfingolipidos más complejos así como a ceramidas mediante la acción de la glucosil ceramidasa, iv) se mezclan mucho mejor que las ceramidas con otros lípidos de membrana, y v) pueden encontrarse a

altas concentraciones, sirviendo como precursor de esfingolípidos, sin perturbar la estructura de la membrana.

7.5 Conclusiones

Las conclusiones principales de este trabajo son:

- La esfingomielina de huevo muestra una fase lamelar ondulada por debajo de su transición de fase principal, en el rango de temperatura estudiado, mientras que la pSM presenta una pretransición de una fase gel a una fase ondulada por debajo de su transición principal.

- La interacción entre la ceramida y el colesterol en mezclas ternarias con fosfolípidos saturados depende de la concentración de ambos lípidos con respecto al fosfolípido, en lugar de su relación molar.

- Los esfingolípidos insaturados tienden a disminuir la rigidez de la muestra. Específicamente, la esfingomielina insaturada no impide la formación de dominios enriquecidos en ceramida, y en su lugar favorece la cooperación entre ceramidas.

- Los cerebrósidos presentan un comportamiento intermedio entre las ceramidas y las esfingomielinas. Estos se mezclan mucho mejor que las ceramidas con otros lípidos de membrana y no afectan a la estabilidad ni a la funcionalidad de la membrana como las ceramidas.

REFERENCES

REFERENCES

Ahmad TY, Sparrow JT & Morrisett JD (1985) Fluorine-labeled, pyrene-labeled, and nitroxide-labeled sphingomyelin - Semi-synthesis and thermotropic properties. *J Lipid Res* **26:** 1160–1165

Akabori K & Nagle JF (2015) Structure of the DMPC lipid bilayer ripple phase. *Soft Matter* **11:** 918–926 Available at: http://dx.doi.org/10.1039/C4SM02335H

Alanko SMK, Halling KK, Maunula S, Slotte JP & Ramstedt B (2005) Displacement of sterols from sterol/sphingomyelin domains in fluid bilayer membranes by competing molecules. *Biochim. Biophys. Acta - Biomembr.* **1715:** 111–121

Alessandrini A & Facci P (2005) AFM: A versatile tool in biophysics. *Meas. Sci. Technol.* **16:**

Alessandrini A, Seeger HM, Caramaschi T & Facci P (2012) Dynamic force spectroscopy on supported lipid bilayers: effect of temperature and sample preparation. *Biophys J* **103:** 38–47 Available at: http://www.ncbi.nlm.nih.gov/pubmed/22828330

Ali S, Brockman HL & Brown RE (1991) Structural Determinants of Miscibility in Surface Films of Galactosylceramide and Phosphatidylcholine: Effect of Unsaturation in the Galactosylceramide Acyl Chain. *Biochemistry* **30:** 11198–11205

De Almeida RFM, Fedorov A & Prieto M (2003) Sphingomyelin/phosphatidylcholine/cholesterol phase diagram: Boundaries and composition of lipid rafts. *Biophys. J.* **85:** 2406–2416

De Almeida RFM, Loura LMS, Fedorov A & Prieto M (2002) Nonequilibrium phenomena in the phase separation of a two-component lipid bilayer. *Biophys. J.* **82:** 823–834

Alonso A & Goñi FM (2018) The Physical Properties of Ceramides in Membranes. *Annu. Rev. Biophys.* **47:** 633–654 Available at: http://www.ncbi.nlm.nih.gov/pubmed/29618220

Anderle G & Mendelsohn R (1986) Fourier-Transform Infrared Studies of CaATPase / Phospholipid Interaction : Survey of Lipid Classes ? *Biochemistry* **25:** 5594–5598

Angelova MI & Dimitrov DS (1986) Liposome Electro formation. *Faraday Discuss. Chem. SOC* **81:** 303–311

Angelova MI, Soléau S, Méléard P, Faucon F & Bothorel P (1992) Preparation of giant vesicles by external AC electric fields. Kinetics and applications. *Trends Colloid Interface Sci. VI* **131:** 127–131 Available at: http://www.springerlink.com/index/10.1007/BFb0116295

Armen RS, Uitto OD & Feller SE (1998) Phospholipid Component Volumes : Determination and Application to Bilayer Structure Calculations. *Biophys. J.* **75:** 734–744 Available at: http://dx.doi.org/10.1016/S0006-3495(98)77563-0

Arsov Z, González-Ramírez EJ, Goñi FM, Tristram-Nagle S & Nagle JF (2018) Phase behavior of palmitoyl and egg sphingomyelin. *Chem. Phys. Lipids* **213:** 102–110 Available at: http://linkinghub.elsevier.com/retrieve/pii/S0009308417303341

Arsov Z & Quaroni L (2008) Detection of lipid phase coexistence and lipid interactions in sphingomyelin / cholesterol membranes by ATR-FTIR spectroscopy. *Biochim. Biophys. Acta* **1778:** 880–889

Artetxe I (2017) Doctoral Thesis Leioa

Artetxe I, Sergelius C, Kurita M, Yamaguchi S, Katsumura S, Slotte JP & Maula T (2013) Effects of sphingomyelin headgroup size on interactions with ceramide. *Biophys. J.* **104:** 604–612 Available at: http://dx.doi.org/10.1016/j.bpj.2012.12.026

Attwood SJ, Choi Y & Leonenko Z (2013) Preparation of DOPC and DPPC supported planar lipid bilayers for atomic force microscopy and atomic force spectroscopy. *Int. J. Mol. Sci.* **14:** 3514–3539

Bagatolli L a. (2006) To see or not to see: Lateral organization of biological membranes and fluorescence microscopy. *Biochim. Biophys. Acta - Biomembr.* **1758:** 1541–1556

Bagatolli LA (2003) Thermotropic Behavior of Lipid Mixtures Studied at the Level of Single Vesicles: Giant Unilamellar Vesicles and Two-Photon Excitation Fluorescence Microscopy. *Methods Enzymol.* **367:** 233–253

Bangham AD & Horne RW (1964) Negative staining of phospholipids and their structural modification by surface-active agents as observed in the electron microscope. *J. Mol. Biol.* **8:** IN2-IN10 Available at: http://dx.doi.org/10.1016/S0022-2836(64)80115-7

Bar LK, Barenholz Y & Thompson TE (1997) Effect of Sphingomyelin Composition on the Phase Structure of. *Biochemistry* **2960:** 2507–2516

Barenholz Y, Suurkuusk J, Mountcastle D, Thompson TE & Biltonen RL (1979) A Calorimetric Study of the Thermotropic Behavior of Aqueous Dispersions of Natural and Synthetic Sphingomyelins. *Biochem. J Biol* **15:** 2441–2447

Bartels T, Lankalapalli RS, Bittman R, Beyer K & Brown MF (2008) Raftlike Mixtures of Sphingomyelin and Cholesterol Investigated by Solid-State 2 H NMR Spectroscopy. *J Am Chem Soc***:** 14521–14532

Bartlett R, Bartlett R, Foundation R, Foundation R, Jolla L, Jolla L, Fiske T, Fiske T, Institutes N, Institutes N, Curve-the S & Curve-the S (1958) Phosphorus Assay in Column. *Solutions***:** 3–5

Basañez G (2002) Membrane fusion: the process and its energy suppliers. *C. Cell. Mol. Life Sci.* **59:** 1478–1490

Basañez G, Ruiz-Argüello MB, Alonso A, Goni FM, Karlsson G & Edwards K (1997) Morphological Changes Induced by Phospholipase C and by Sphingomyelinase on Large Unilamellar Vesicles : A Cryo-Transmission Electron Microscopy Study of Liposome Fusion. *Biophys. J.* **72:** 2630–2637

Baumgart T, Hunt G, Farkas ER, Webb WW & Feigenson GW (2007) Fluorescence probe partitioning between Lo/Ldphases in lipid membranes. *Biochim. Biophys. Acta - Biomembr.* **1768:** 2182–2194

Binnig G, Quate CF & Gerber C (1986) Atomic Force Microscope. *Phys. Rev. Lett.* **56:** 930–933

Björkbom A, Róg T, Kaszuba K, Kurita M, Yamaguchi S, Lo M & Bjo A (2010) Effect of Sphingomyelin Headgroup Size on Molecular Properties and Interactions with Cholesterol. *Biophys. J.* **99:** 3300–3308

Blanchette CD, Lin WC, Ratto T V. & Longo ML (2006) Galactosylceramide domain microstructure: Impact of cholesterol and nucleation/growth conditions. *Biophys. J.* **90:** 4466–4478

Böttcher CJF, Van gent CM & Pries C (1961) A rapid and sensitive sub-micro phosphorus determination. *Anal. Chim. Acta* **24:** 203–204

Bunge A, Herrmann A, Huster D, Sto M & Mu P (2008) Characterization of the Ternary Mixture of Sphingomyelin , POPC , and Cholesterol : Support for an Inhomogeneous Lipid Distribution at High Temperatures. *Biophys. J.* **94:**

2680–2690

Burger KNJ (2000) Greasing Membrane Fusion and Fission Machineries. *Traffic* **1:** 605–613

Busto J V, Fanani ML, De Tullio L, Sot J, Maggio B, Goni FM & Alonso A (2009) Coexistence of immiscible mixtures of palmitoylsphingomyelin and palmitoylceramide in monolayers and bilayers. *Biophys J* **97:** 2717–2726 Available at: http://www.ncbi.nlm.nih.gov/pubmed/19917225

Busto J V, García-Arribas AB, Sot J, Torrecillas A, Gómez-Fernández JC, Goñi FM & Alonso A (2014) Lamellar gel (lβ) phases of ternary lipid composition containing ceramide and cholesterol. *Biophys. J.* **106:** 621–30 Available at: http://www.sciencedirect.com/science/article/pii/S000634951305813X [Accessed February 2, 2016]

Busto J V, Sot J, Requejo-Isidro J, Goni FM & Alonso A (2010) Cholesterol displaces palmitoylceramide from its tight packing with palmitoylsphingomyelin in the absence of a liquid-disordered phase. *Biophys J* **99:** 1119–1128 Available at: http://www.ncbi.nlm.nih.gov/pubmed/20712995

Calhoun WI & Shipley GG (1979a) Fatty-acid composition and thermal-behavior of natural sphingomyelins. *Biochim. Biophys. Acta* **555:** 436–441

Calhoun WI & Shipley GG (1979b) Sphingomyelin-Lecithin Bilayers and Their Interaction with Cholesterolt. *Biochemistry* **18:** 1717–1722

Carrer DC & Maggio B (1999) Phase behavior and molecular interactions in mixtures of ceramide with dipalmitoylphosphatidylcholine. *J. Lipid Res.* **40:** 1978–89 Available at: http://www.ncbi.nlm.nih.gov/pubmed/10553001

Castro BM, De Almeida RFM, Silva LC, Fedorov A & Prieto M (2007) Formation of ceramide/sphingomyelin gel domains in the presence of an unsaturated phospholipid: A quantitative multiprobe approach. *Biophys. J.* **93:** 1639–1650

Castro BM, Prieto M & Silva LC (2014) Ceramide: A simple sphingolipid with unique biophysical properties. *Prog. Lipid Res.* **54:** 53–67 Available at: http://dx.doi.org/10.1016/j.plipres.2014.01.004

Castro BM, Silva LC, Fedorov A, de Almeida RFM & Prieto M (2009a) Cholesterol-rich fluid membranes solubilize ceramide domains: Implications for the structure and dynamics of mammalian intracellular and plasma membranes. *J. Biol. Chem.* **284:** 22978–22987

Castro BM, Silva LC, Fedorov A, de Almeida RFM & Prieto M (2009b) Cholesterol-

rich fluid membranes solubilize ceramide domains: Implications for the structure and dynamics of mammalian intracellular and plasma membranes. *J. Biol. Chem.* **284:** 22978–22987

Chachaty C, Rainteau D, Tessier C, Quinn PJ & Wolf C (2005) Building Up of the Liquid-Ordered Phase Formed by Sphingomyelin and Cholesterol. *Biophys. J.* **88:** 4032–4044

Chalfant CE & Spiegel S (2005) Sphingosine 1-phosphate and ceramide 1-phosphate : expanding roles in cell signaling. *J. Cell Sci.* **118:** 4605–4612

Chemin C, Pabst G, Bourgaux C, Jean-manuel P, Patrick W, Couvreur P & Ollivon M (2008) Consequences of ions and pH on the supramolecular organization of sphingomyelin and sphingomyelin / cholesterol bilayers. *Chem. Phys. Lipids* **153:** 119–129

Chiantia S, Kahya N, Ries J & Schwille P (2006a) Effects of ceramide on liquid-ordered domains investigated by simultaneous AFM and FCS. *Biophys J* **90:** 4500–4508 Available at: http://www.ncbi.nlm.nih.gov/pubmed/16565041

Chiantia S, Kahya N, Ries J & Schwille P (2006b) Effects of ceramide on liquid-ordered domains investigated by simultaneous AFM and FCS. *Biophys. J.* **90:** 4500–4508

Chiantia S, Kahya N & Schwille P (2007) Raft domain reorganization driven by short- and long-chain ceramide: A combined AFM and FCS study. *Langmuir* **23:** 7659–7665

Chiantia S, Ries J, Kahya N & Schwille P (2006c) Combined AFM and Two-Focus SFCS Study of Raft-Exhibiting Model Membranes **. **:** 2409–2418

Chien K & Huang W (1991) Fusion of Sphingomyelin Vesicles Induced by Proteins from Taiwan Cobra (Naja naja atra) Venom. *J. Biol. Chem.***:** 3252–3259

Chipuk JE, McStay GP, Bharti A, Kuwana T, Clarke CJ, Siskind LJ, Obeid LM & Green DR (2012) Sphingolipid metabolism cooperates with BAK and BAX to promote the mitochondrial pathway of apoptosis. *Cell* **148:** 988–1000 Available at: http://dx.doi.org/10.1016/j.cell.2012.01.038

Chu N, Liu Y, Tristram-nagle S & Nagle JF (2005) Anomalous swelling of lipid bilayer stacks is caused by softening of the bending modulus. *Phys Rev E* **71:** 1–8

Connell SD & Smith DA (2006) The atomic force microscope as a tool for studying

phase separation in lipid membranes (review). *Mol. Membr. Biol.* **23:** 17–28

Contreras F, Sánchez-magraner L, Alonso A & Goñi FM (2010) Transbilayer (flip-flop) lipid motion and lipid scrambling in membranes. *FEBS Lett.* **584:** 1779–1786 Available at: http://dx.doi.org/10.1016/j.febslet.2009.12.049

Contreras F, Sot J, Alonso A & Goñi FM (2004) Cholesterol modulation of sphingomyelinase activity at physiological temperatures. **130:** 127–134

Contreras FX, Basanez G, Alonso A, Herrmann A & Goñi FM (2005) Asymmetric addition of ceramides but not dihydroceramides promotes transbilayer (flip-flop) lipid motion in membranes. *Biophys. J.* **88:** 348–359

Contreras FX, Villar AV, Alonso A, Kolesnick RN & Goñi FM (2003) Sphingomyelinase activity causes transbilayer lipid translocation in model and cell membranes. *J. Biol. Chem.* **278:** 37169–37174

Cremesti A, Paris F, Grassmé H, Holler N, Tschopp J, Fuks Z, Gulbins E & Kolesnick R (2001) Ceramide Enables Fas to Cap and Kill. *J. Biol. Chem.* **276:** 23954–23961

Cremesti AE, Goni FM & Kolesnick R (2002) ScienceDirect - FEBS Letters : Role of sphingomyelinase and ceramide in modulating rafts: do biophysical properties determine biologic outcome? **531:** 47–53 Available at: https://vpn.ucsf.edu/,DanaInfo=www.sciencedirect.com+science?_ob=ArticleURL&_udi=B6T36-46WVR5X-3&_user=4430&_rdoc=1&_fmt=&_orig=search&_sort=d&view=c&_acct=C000059594&_version=1&_urlVersion=0&_userid=4430&md5=85d2cef68b8231fc5990ebe4867e5b04

Cullis PR & Kruijff B De (1979) Lipid polymorphismand the functional roles of lipids in biologicalmembranes. *Biochim. Biophys. Acta* **559:** 399–420

Danielli JF & Davson H. (1935) A contribution to the theory of permeability of thin films. *J. Cell. Comp. Physiol.* **5:** 495–508

Dervichian D & Macheboeuf M (1938) Sur l'existence d'une couche monomoléculaire de substances lipoidiques à la surface des globules rouges du sang. *Compt. Rend. l'Academie des Sci.* **206:** 1511–1514

Dimitrov DS & Angelova MI (1988) Lipid swelling and liposome formation in electric fields. *Bioelectrchemistry Bioenerg.* **19:** 323–336

Domènech Ò, Redondo L, Picas L, Morros A, Montero MT & Hernández-Borrell J (2007) Atomic force microscopy characterization of supported planar bilayers

that mimic the mitochondrial inner membrane. In *Journal of Molecular Recognition* pp 546–553.

Ellens H, Bentz J & Szoka FC (1985) H + - and Ca2 + -Induced Fusion and Destabilization of Liposomes. *Biochemistry* **24:** 3099–3106

Engelman DM (2005) Membranes are more mosaic than fluid. *Nature* **438:** 578–580

Epand RM (1998) Lipid polymorphism and protein- lipid interactions. *Biochim. Biophys. Acta* **1376:** 353–368

Epand RM & Epand RF (1980) Studies of thermotropic phospholipid phase transitions using scanning densitometry. *Chem. Phys. Lipids* **27:** 139–150

Estep TN, Mountcastle DB, Barenholz Y, Biltonen RL & Thompson TE (1979) Thermal Behavior of Synthetic Sphingomyelin-Cholesterol. *Biochemistry***:** 2112–2117

F. Szoka & Papahadjopoulos D (1980) COMPARATIVE PROPERTIES PREPARATION OF LIPID VESICLES (LIPOSOMES) l. *Annu. Rev. Biophys. Bioeng.* **9:** 467–508

Feigenson GW (2007) Phase Boundaries and Biological Membranes. *Annu. Rev. Biophys. Biomol. Struct.* **36:** 63–77 Available at: http://www.annualreviews.org/doi/10.1146/annurev.biophys.36.040306.132721

Fidorra M, Duelund L, Leidy C, Simonsen AC & Bagatolli LA (2006) Absence of fluid-ordered/fluid-disordered phase coexistence in ceramide/POPC mixtures containing cholesterol. *Biophys J* **90:** 4437–4451 Available at: http://www.ncbi.nlm.nih.gov/pubmed/16565051

Filippov A & Ora G (2006) Sphingomyelin Structure Influences the Lateral Diffusion and Raft Formation in Lipid Bilayers. *Biophys. J.* **90:** 2086–2092

Fiske and Subbarow Y (1925) THE COLORIMETRIC DETERMINATION OF PHOSPHORUS. *J. Biol. Chem.* **66:** 375–400

Futerman AH & Hannun YA (2004) The complex life of simple sphingolipids. *EMBO Rep.* **5:** 777–782

García-Arribas AB, Ahyayauch H, Sot J, López-González PL, Alonso A & Goñi FM (2016a) Ceramide-Induced Lamellar Gel Phases in Fluid Cell Lipid Extracts. *Langmuir* **32:** 9053–9063

García-Arribas AB, Alonso A & Goñi FM (2016b) Cholesterol interactions with ceramide and sphingomyelin. *Chem. Phys. Lipids* **199:** 26–34 Available at: http://linkinghub.elsevier.com/retrieve/pii/S0009308416300457 [Accessed March 26, 2018]

García-Arribas AB, Axpe E, Mujika JI, Mérida D, Busto J V., Sot J, Alonso A, Lopez X, García JÁ, Ugalde JM, Plazaola F & Goñi FM (2016c) Cholesterol-Ceramide Interactions in Phospholipid and Sphingolipid Bilayers As Observed by Positron Annihilation Lifetime Spectroscopy and Molecular Dynamics Simulations. *Langmuir* **32:** 5434–5444

Garcia-Arribas AB, Busto J V, Alonso A & Goñi FM (2015) Atomic force microscopy characterization of palmitoylceramide and cholesterol effects on phospholipid bilayers: a topographic and nanomechanical study. *Langmuir* **31:** 3135–3145 Available at: http://www.ncbi.nlm.nih.gov/pubmed/25693914

Garcia-Manyes S, Oncins G & Sanz F (2005) Effect of temperature on the nanomechanics of lipid bilayers studied by force spectroscopy. *Biophys. J.* **89:** 4261–4274 Available at: http://dx.doi.org/10.1529/biophysj.105.065581

Garcia-Manyes S, Redondo-Morata L, Oncins G & Sanz F (2010) Nanomechanics of lipid bilayers: heads or tails? *J Am Chem Soc* **132:** 12874–12886 Available at: http://www.ncbi.nlm.nih.gov/pubmed/20799688

Garcia-Manyes S & Sanz F (2010) Nanomechanics of lipid bilayers by force spectroscopy with AFM: A perspective. *Biochim. Biophys. Acta - Biomembr.* **1798:** 741–749 Available at: http://dx.doi.org/10.1016/j.bbamem.2009.12.019

Garcia-Ruiz C, Colell A, Morales A, Caballero F, Montero J, Terrones O, Basañez G & Fernández-checa JC (2009) Mitochondrial cholesterol in health and disease. **:** 117–132 Available at: http://digital.csic.es/bitstream/10261/32074/3/Mitochondrial cholesterol.pdf

Gennis RB (1989) Springer advanced texts in chemistry New York Available at: http://scholar.google.com/scholar?hl=en&btnG=Search&q=intitle:Springer+Advanced+Texts+in+Chemistry#0%5Cnhttp://scholar.google.com/scholar?hl=en&btnG=Search&q=intitle:Springer+advanced+texts+in+chemistry#0

Goldsbury CS, Scheuring S & Kreplak L (2009) Introduction to atomic force microscopy (AFM) in Biology. *Curr. Protoc. Protein Sci.***:** 1–19

Goñi FM (2014) The basic structure and dynamics of cell membranes: An update of the Singer-Nicolson model. *Biochim. Biophys. Acta - Biomembr.* **1838:** 1467–

1476 Available at: http://dx.doi.org/10.1016/j.bbamem.2014.01.006

Goñi FM (2019) " Rafts " : A nickname for putative transient nanodomains. *Chem. Phys. Lipids* **218:** 34–39 Available at: https://doi.org/10.1016/j.chemphyslip.2018.11.006

Goni FM & Alonso A (2009) Effects of ceramide and other simple sphingolipids on membrane lateral structure. *Biochim Biophys Acta* **1788:** 169–177 Available at: http://www.ncbi.nlm.nih.gov/pubmed/18848519

Goñi FM & Alonso A (2002) Sphingomyelinases: Enzymology and membrane activity. *FEBS Lett.* **531:** 38–46

Goñi FM & Alonso A (2006a) Biophysics of sphingolipids I. Membrane properties of sphingosine, ceramides and other simple sphingolipids. *Biochim Biophys Acta* **1758:** 1902–1921 Available at: http://www.ncbi.nlm.nih.gov/pubmed/17070498

Goñi FM & Alonso A (2006b) Differential Scanning Calorimetry in the Study of Lipid Structures. In *Chemical Biology: Applications and Techniques*, Larijani B Rosser CA & Woscholski R (eds) pp 47–66. London: John Wiley & Sons Ltd Available at: http://doi.wiley.com/10.1002/9780470319253

Goñi FM & Alonso A (2006c) Biophysics of sphingolipids I. Membrane properties of sphingosine, ceramides and other simple sphingolipids. *Biochim. Biophys. Acta - Biomembr.* **1758:** 1902–1921

Goñi FM, Sot J & Alonso A (2014) Biophysical properties of sphingosine , ceramides and other simple sphingolipids. *Biochem Soc Trans* **42:** 1401–1408

Goñi FM, Villar A V., Nieva JL & Alonso A (2003) Interaction of Phospholipases C and Sphingomyelinase with Liposomes. *Methods Enzymol.* **372:** 3–19

Gorter E. & Grendel F (1926) On bimolecular layers of lipoids on the chromo- cytes of the blood. *J Exp Med* **41:** 439–443

Grassmé H, Jekle A, Riehle A, Schwarz H, Berger J, Sandhoff K, Kolesnick R & Gulbins E (2001) CD95 Signaling via Ceramide-rich Membrane Rafts. *J. Biol. Chem.* **276:** 20589–20596

Grassme H, Jendrossek V, Bock J, Riehle A & Gulbins E (2002) Ceramide-Rich Membrane Rafts Mediate CD40 Clustering. *J. Immunol.* **168:** 298–307 Available at: http://www.jimmunol.org/cgi/doi/10.4049/jimmunol.168.1.298

Gulbins E & Li PL (2006) Physiological and pathophysiological aspects of ceramide. *Am. J. Physiol. Regul. Integr. Comp. Physiol.* **290:** R11-26 Available at: http://www.ncbi.nlm.nih.gov/pubmed/16352856

Guler SD, Ghosh DD, Pan J, Mathai JC, Zeidel ML, Nagle JF & Tristram-nagle S (2009) Effects of ether vs . ester linkage on lipid bilayer structure and water permeability. **160:** 33–44

Hakomori S -i. (2002) The glycosynapse. *Proc. Natl. Acad. Sci.* **99:** 225–232 Available at: http://www.pnas.org/cgi/doi/10.1073/pnas.012540899

Hall A, Róg T, Karttunen M & Vattulainen I (2010) Role of Glycolipids in Lipid Rafts: A View through Atomistic Molecular Dynamics Simulations with Galactosylceramide. *J. Phys. Chem. B* **114:** 7797–7807

Halling KK, Ramstedt B, Nyström JH, Slotte JP & Nyholm TKM (2008) Cholesterol interactions with fluid-phase phospholipids: Effect on the lateral organization of the bilayer. *Biophys. J.* **95:** 3861–3871

Hannun YA. & Obeid LM (2002) The Ceramide-centric Universe of Lipid-mediated Cell Regulation : Stress Encounters of the Lipid Kind *. *J. Biol. Chem.* **277:** 25847–25851

Hannun YA, Loomis CR, Merrill AH & Bell RM (1986) Sphingosine Inhibition of Protein Kinase C Activity and of Phorbol Dibutyrate Binding. *J. Biol. Chem.* **261:** 12604–12609

Hannun YA, Luberto C & Argraves KM (2001) Current topics enzymes of sphingolipid metabolism: from modular to integrative signaling. *Biochemistry* **40:** 4893–4903

Hannun YA & Obeid LM (2008) Principles of bioactive lipid signalling: Lessons from sphingolipids. *Nat. Rev. Mol. Cell Biol.* **9:** 139–150

Hannun YA & Obeid LM (2011) Many ceramides. *J. Biol. Chem.* **286:** 27855–27862

Harayama T & Riezman H (2018) Understanding the diversity of membrane lipid composition Takeshi. *Nat. Publ. Gr.* **19:** 281–296 Available at: http://dx.doi.org/10.1038/nrm.2017.138

Harris FM, Best KB & Bell JD (2002) Use of laurdan fluorescence intensity and polarization to distinguish between changes in membrane fluidity and phospholipid order. *Biochim. Biophys. Acta - Biomembr.* **1565:** 123–128

Hentschel MP & Rustichelli F (1991) Structure of the ripple phase P-beta' in hydrated phosphatidylcholine multimembranes. *Phys Rev Lett* **66:** 903–906

Hinkovska-Galcheva V, Boxer LA, Kindzelskii A, Hiraoka M, Abe A, Goparju S, Spiegel S, Petty HR & Shayman JA (2005) Ceramide 1-Phosphate , a Mediator of Phagocytosis *. *J. Biol. Chem.* **280:** 26612–26621

Hla T (2004) Physiological and pathological actions of sphingosine 1-phosphate. *Semin. Cell Dev. Biol.* **15:** 513–520

Hoetzl S, Sprong H & van Meer G (2007) The way we view cellular (glyco)sphingolipids. *J. Neurochem.* **103 Suppl:** 3–13

Holowka D, Gosse J a., Hammond AT, Han X, Sengupta P, Smith NL, Wagenknecht-Wiesner A, Wu M, Young RM & Baird B (2005) Lipid segregation and IgE receptor signaling: A decade of progress. *Biochim. Biophys. Acta - Mol. Cell Res.* **1746:** 252–259

Hölzl G & Dörmann P (2007) Structure and function of glycoglycerolipids in plants and bacteria. *Prog. Lipid Res.* **46:** 225–243

Honigmann A, Mueller V, Hell SW & Eggeling C (2012) STED microscopy detects and quantifies liquid phase separation in lipid membranes using a new far-red emitting fluorescent phosphoglycerolipid analogue. *Faraday Discuss.* **161:** 77–89

Honigmann A, Sadeghi S, Keller J, Hell SW, Eggeling C & Vink R (2014) A lipid bound actin meshwork organizes liquid phase separation in model membranes. *Elife* **2014:** 1–16

Huang J & Feigenson GW (1999) A Microscopic Interaction Model of Maximum Solubility of Cholesterol in Lipid Bilayers. *Biophys. J.* **76:** 2142–2157

Ira & Johnston LJ (2008) Sphingomyelinase generation of ceramide promotes clustering of nanoscale domains in supported bilayer membranes. *Biochim. Biophys. Acta - Biomembr.* **1778:** 185–197

Ira, Zou S, Ramirez DMC, Vanderlip S, Ogilvie W, Jakubek ZJ & Johnston LJ (2009) Enzymatic generation of ceramide induces membrane restructuring: Correlated AFM and fluorescence imaging of supported bilayers. *J. Struct. Biol.* **168:** 78–89 Available at: http://dx.doi.org/10.1016/j.jsb.2009.03.014

Israelachvili JN, Marcelja S, Horn RG & Introduction A (1980) Physical principles of membrane organization. *Q. Rev. Biophys.* **2:** 121–200

Jacobson K, Sheets ED & Simson R (1995) Revisiting the Fluid Mosaic Model of Membranes. *Sciencee* **268:** 1441–1442

Jass J, Tjarnhage T & Puu G (2000) From liposomes to supported, planar bilayer structures on hydrophilic and hydrophobic surfaces: an atomic force microscopy study. *Biophys J* **79:** 3153–3163 Available at: http://www.ncbi.nlm.nih.gov/pubmed/11106620

Jiménez-Rojo N, García-Arribas AB, Sot J, Alonso A & Goñi FM (2014) Lipid bilayers containing sphingomyelins and ceramides of varying N-acyl lengths: A glimpse into sphingolipid complexity. *Biochim. Biophys. Acta - Biomembr.* **1838:** 456–464 Available at: http://dx.doi.org/10.1016/j.bbamem.2013.10.010

Juhasz J, Davis JH & Sharom FJ (2010) Fluorescent probe partitioning in giant unilamellar vesicles of 'lipid raft' mixtures. *Biochem. J.* **430:** 415–423 Available at: http://biochemj.org/lookup/doi/10.1042/BJ20100516

Katsaras J, Liu Y, Headrick RL, Fontes E, Mason PC & Nagle JF (2000) Clarification of the ripple phase of lecithin bilayers using fully hydrated , aligned samples. *Phys Rev E* **61:** 5668–5677

Kleinzeller A (1997) Ernest Overton ' s to the Cell Membrane Concept : A Centennial Appreciation. *News Physiol. Sci.* **February 1:** 49–53

Klymchenko AS & Kreder R (2014) Fluorescent probes for lipid rafts: From model membranes to living cells. *Chem. Biol.* **21:** 97–113

Kodama M, Kawasaki Y & Ohtaka H (2012) Thermochimica Acta The main transition enthalpy of the gel-to-liquid crystal phases for a series of asymmetric chain length d - erythro (2S , 3R) sphingomyelins. *Thermochim. Acta* **532:** 22–27 Available at: http://dx.doi.org/10.1016/j.tca.2011.01.011

Kolesnick R (2002) The therapeutic potential of modulating the ceramide/sphingomyelin pathway. *J. Clin. Invest.* **110:** 3–8 Available at: http://www.jci.org/articles/view/16127

Kolesnick RN (1987) 1,2-Diacylglycerols but Not Phorbol Esters Stimulate Sphingomyelin Hydrolysis in GH, Pituitary Cells*. *J. Biol. Chem.* **262:** 16758–16762

Kolesnick RN, Goñi FM & Alonso A (2000) Compartmentalization of Ceramide Signaling: Physical Foundations and Biological Effects. *J. Cell. Physiol.* **184:** 285–300

Kornberg RD & Mcconnell HM (1971) Inside-Outside Transitions of Phospholipids in Vesicle Membranes. *Biochemistry* **10:** 1111–1120

Kornhuber J, Müller CP, Becker KA, Reichel M & Gulbins E (2014) The ceramide system as a novel antidepressant target. *Trends Pharmacol. Sci.* **35:** 293–304

Kucerka N, Nagle JF, Sachs JN, Feller SE, Pencer J, Jackson A & Katsaras J (2008) Lipid Bilayer Structure Determined by the Simultaneous Analysis of Neutron and X-Ray Scattering Data. *Biophys. J.* **95:** 2356–2367 Available at: http://dx.doi.org/10.1529/biophysj.108.132662

Ladbrooke BD, Williams RM & Chapman D (1968) Studies on lecithin-cholesterol-water interactions by differential scanning calorimetry and X-ray diffraction. *BBA - Biomembr.* **150:** 333–340

Lakowicz JR (2006) Time-Domain Lifetime Measurements. *Princ. Fluoresc. Spectrosc.* **1:** 97–155 Available at: d:%5Cliterature%5C_papers%5CLakowicz_PrincFSpectr_Ch4_Time-Domain Lifetime Measurements.pdf

Lang E, Bissinger R, Gulbins E & Lang F (2015) Ceramide in the regulation of eryptosis, the suicidal erythrocyte death. *Apoptosis* **20:** 758–767

Ledeen RW, Hakomori SI, Yates AJ, Schneider J. & Yu RK (1998) Sphingolipids as signaling modulators in the nervous system Annals of the New York Academy of Sciences (ed) New York

Leftin A, Molugu TR, Job C, Beyer K & Brown MF (2014) Article Area per Lipid and Cholesterol Interactions in Membranes from Separated. *Biophys. J.* **107:** 2274–2286 Available at: http://dx.doi.org/10.1016/j.bpj.2014.07.044

Lenard J & Singer SJ (1966) Protein conformation in cell membrane preparations as studied by optical rotatory dispersion and circular dichroism. *Proc Natl Acad Sci U S A* **56:** 1828–1835

Li X, Smaby JM, Momsen MM, Brockman HL & Brown RE (2000) Sphingomyelin Interfacial Behavior : The Impact of Changing Acyl Chain Composition. *Biophys. J.* **78:** 1921–1931 Available at: http://dx.doi.org/10.1016/S0006-3495(00)76740-3

Lingwood D & Simons K (2010) Lipid rafts as a membrane-organize principle. *Science (80-.).* **327:** 46–50

Lloyd-Evans E, Pelled D, Riebeling C, Bodennec J, De-Morgan A, Waller H,

Schiffmann R & Futerman AH (2003) Glucosylceramide and glucosylsphingosine modulate calcium mobilization from brain microsomes via different mechanisms. *J. Biol. Chem.* **278:** 23594–23599

Lombard J (2014) Once upon a time the cell membranes : 175 years of cell boundary research. *Biol. Direct* **9:** 1–35

Longo ML & Blanchette CD (2010) Imaging cerebroside-rich domains for phase and shape characterization in binary and ternary mixtures. *Biochim. Biophys. Acta - Biomembr.* **1798:** 1357–1367

Lönnfors M, Doux JPF, Killian JA, Nyholm TKM, Slotte JP & Lo M (2011) Sterols have higher affinity for sphingomyelin than for phosphatidylcholine bilayers even at equal acyl-chain order. *Biophys. J.* **100:** 2633–2641

Lubensky TC & Mackintosh FC (1993) Theory of 'Ripple' Phases of Lipid Bilayers. *Phys Rev Lett* **71:** 1565–1568

Luckey M (2008) Membrane Structural Biology: With Biochemical and Biophysical Foundations Cambridge: Cambridge University Press

Luzzati V & Tardieu A (1974) Lipid Phases: Structure and Structural Transitions. *Annu. Rev. Phys. Chem.* **25:** 79–94

Mabrey S, Mateo PL, Sturtevant JM, Mabrey S, Mateo PL & Sturtevant JM (1978) High-Sensitivity Scanning Calorimetric Study of Mixtures of Cholesterol with Dimyristoyl- and Dipalmitoylphosphatidylcholines. *Biochemistry* **17:** 2464–2468

Maddy AH. & Malcolm B. (1965) Protein conformations in the plasma membrane. *Science (80-.).* **150:** 1616–1618

Maggio B, Ariga T, Sturtevant JM & Yu RK (1985) Thermotropic behavior of binary mixtures of dipalmitoylphosphatidylcholine and glycosphingolipids in aqueous dispersions. *Biochim. Biophys. Acta* **818:** 1–12 Available at: http://www.ncbi.nlm.nih.gov/pubmed/19133760

Maggio B, Carrer DC, Fanani ML, Oliveira RG & Rosetti CM (2004) Interfacial behavior of glycosphingolipids and chemically related sphingolipids. *Curr. Opin. Colloid Interface Sci.* **8:** 448–458

Maggio B, Fanani ML, Rosetti CM & Wilke N (2006) Biophysics of sphingolipids II. Glycosphingolipids: An assortment of multiple structural information transducers at the membrane surface. *Biochim. Biophys. Acta - Biomembr.* **1758:** 1922–1944

Maggio B, Montich GG & Cumar FA (1988) Surface topography of sulfatide and gangliosides in unilamellar vesicles of dipalmitoylphosphatidylcholine. *Chem. Phys. Lipids* **46:** 137–146

Manni MM, Sot J, Arretxe E, Gil-redondo R, Falcón-pérez JM, Balgoma D, Alonso C, Goñi FM & Alonso A (2018) The fatty acids of sphingomyelins and ceramides in mammalian tissues and cultured cells : Biophysical and physiological implications. *Chem. Phys. Lipids* **217:** 29–34 Available at: https://doi.org/10.1016/j.chemphyslip.2018.09.010

Mannock DA, Mcintosh TJ, Jiang X, Covey DF & Mcelhaney RN (2003) Effects of Natural and Enantiomeric Cholesterol on the Thermotropic Phase Behavior and Structure of Egg Sphingomyelin Bilayer Membranes. *Biophys. J.* **84:** 1038–1046 Available at: http://dx.doi.org/10.1016/S0006-3495(03)74920-0

Mason PC & Gaulin BD (1999) Small-angle scattering studies of the fully hydrated phospholipid DPPC. *Phys Rev E* **59:** 921–928

Maté S, Busto JV, García-Arribas AB, Sot J, Vazquez R, Herlax V, Wolf C, Bakás L & Goñi FM (2014) N-Nervonoylsphingomyelin (C24:1) Prevents Lateral Heterogeneity in Cholesterol-Containing Membranes. *Biophys. J.* **106:** 2606–2616 Available at: http://linkinghub.elsevier.com/retrieve/pii/S0006349514005098

Matuoka S, Kato S & Hatta I (1994) Temperature Change of the Ripple Structure in Fully Hydrated Dimyristoylphosphatidylcholine / Cholesterol Multibilayers. *Biophys. J.* **67:** 728–736 Available at: http://dx.doi.org/10.1016/S0006-3495(94)80533-8

Maula T, Artetxe I, Grandell PM & Slotte JP (2012) Importance of the sphingoid base length for the membrane properties of ceramides. *Biophys. J.* **103:** 1870–1879 Available at: http://dx.doi.org/10.1016/j.bpj.2012.09.018

Maula T, Al Sazzad MA & Slotte JP (2015) Influence of Hydroxylation, Chain Length, and Chain Unsaturation on Bilayer Properties of Ceramides. *Biophys. J.* **109:** 1639–1651 Available at: http://dx.doi.org/10.1016/j.bpj.2015.08.040

Maulik PR, Atkinson D & Shipley GG (1986) X-ray-scattering of vesicles of N-acyl sphingomyelins - Determination of bilayer thickness. *Biophys. J.* **50:** 1071–1077 Available at: http://dx.doi.org/10.1016/S0006-3495(86)83551-2

Maulik PR & Shipley GG (1996) N -Palmitoyl Sphingomyelin Bilayers : Structure and Interactions with Cholesterol. *Biochemistry* **2960:** 8025–8034

Maunula S, Björkqvist YJE, Slotte JP & Ramstedt B (2007) Differences in the domain

forming properties of N-palmitoylated neutral glycosphingolipids in bilayer membranes. *Biochim. Biophys. Acta - Biomembr.* **1768:** 336–345

Mayer MJH and PRC (1986) V e s i c l e s of variable sizes produced by a rapid extrusion procedure L.D. Mayer, M.J. H o p e a n d P.R. Cullis. *Biochim. Biophys. Acta* **858:** 161–168

Mayor S, Viola A, Stan R V. & del Pozo M a. (2006) Flying kites on slippery slopes at Keystone. Symposium on Lipid Rafts and Cell Function. *EMBO Rep.* **7:** 1089–1093

McConnell HM, Watts TH, Weis RM & Brian a. a. (1986) Supported planar membranes in studies of cell-cell recognition in the immune system. *BBA - Rev. Biomembr.* **864:** 95–106

McIntyre JC & Sleight RG (1991) Fluorescence Assay for Phospholipid Membrane Asymmetry. *Biochemistry* **30:** 11819–11827

Mckeone BJ, Pownall HJ & Massey JB (1986) Ether Phosphatidylcholines: Comparison of Miscibility with Ester Phosphatidylcholines and Sphingomyelin, Vesicle Fusion, and Association with Apolipoprotein A-It. *Biochemistry***:** 7711–7716

McMullen TPW & McElhaney RN (1995) New aspects of the interaction of cholesterol with dipalmitoylphosphatidylcholine bilayers as revealed by high-sensitivity differential scanning calorimetry. *BBA - Biomembr.* **1234:** 90–98

van Meer G & de Kroon AIPM (2011) Lipid map of the mammalian cell. *J. Cell Sci.* **124:** 5–8 Available at: http://jcs.biologists.org/cgi/doi/10.1242/jcs.071233

Van Meer G, Voelker DR & Feigenson GW (2008) Membrane lipids: Where they are and how they behave. *Nat. Rev. Mol. Cell Biol.* **9:** 112–124

Van Meer G, Wolthoorn J & Degroote S (2003) The fate and function of glycosphingolipid glucosylceramide. *Philos. Trans. R. Soc. B Biol. Sci.* **358:** 869–873

Megha & London E (2004) Ceramide Selectively Displaces Cholesterol from Ordered Lipid Domains (Rafts): IMPLICATIONS FOR LIPID RAFT STRUCTURE AND FUNCTION. *J. Biol. Chem.* **279:** 9997–10004 Available at: http://www.jbc.org/cgi/doi/10.1074/jbc.M309992200

Mehnert T, Jacob K, Bittman R & Beyer K (2006) Structure and Lipid Interaction of N -Palmitoylsphingomyelin in Bilayer Membranes as Revealed by 2 H-NMR Spectroscopy. *Biophys. J.* **90:** 939–946

Merrill AH, Schmelz E., Dillehay D., Spiegel S, Shayman JA, Schroeder JJ, Riley RT, Voss KA, Wang E & Ang EW (1997) Sphingolipids - The enigmatic lipid class: biochemistry, physiology, and pathophysiology. *Toxicol. Appl. Pharmacol.* **225:** 208–225

Merrill AH, Sereni AM, Stevens VL, Hannun YA, Bell RM & Kinkade JM (1986) Inhibition of phorbol ester-dependent differentiation of human promyelocytic leukemic (HL-60) cells by sphinganine and other long-chain bases. *J. Biol. Chem.* **261:** 12610–12615

Metcalf R & Pandit SA (2012) Mixing Properties of Sphingomyelin Ceramide Bilayers : *J. Phys. Chem. B* **116:** 4500–4509

Mills TT, Toombes GES, Tristram-nagle S & Smilgies D (2008) Order Parameters and Areas in Fluid-Phase Oriented Lipid Membranes Using Wide Angle X-Ray Scattering. *Biophys. J.* **95:** 669–681

Montero J, Morales A, Llacuna L, Lluis JM, Terrones O, Basañez G, Antonsson B, Prieto J, García-Ruiz C, Colell A & Fernández-Checa JC (2008) Mitochondrial cholesterol contributes to chemotherapy resistance in hepatocellular carcinoma. *Cancer Res.* **68:** 5246–5256

Montes LR, Alonso A, Goñi FM & Bagatolli L a. (2007) Giant unilamellar vesicles electroformed from native membranes and organic lipid mixtures under physiological conditions. *Biophys. J.* **93:** 3548–3554

Montes LR, Ruiz-Argüello MB, Goñi FM & Alonso A (2002) Membrane restructuring via ceramide results in enhanced solute efflux. *J. Biol. Chem.* **277:** 11788–11794

Morrow MR, Singh D, Lu D & Grant CWM (1992) Glycosphingolipid phase behaviour in unsaturated phosphatidylcholine bilayers: a 2H NMR study. *Biochim. Biophys. Acta* **1106:** 85–93

Munro S (2003) Lipid Rafts : Elusive or Illusive? *Cell* **115:** 377–388

Nagle JF, Akabori K, Treece BW & Tristram-nagle S (2016) Determination of mosaicity in oriented stacks of lipid bilayers. *Soft Matter* **12:** 1884–1891

Nagle JF & Tristram-Nagle S (2000) Structure of lipid bilayers. *Biochim. Biophys. Acta - Rev. Biomembr.* **1469:** 159–195

Nagle JF & Wilkinson DA (1978) Lecithin bilayers density measurements and molecular interactions. *Biophys. J.* **23:** 159–175 Available at:

http://dx.doi.org/10.1016/S0006-3495(78)85441-1

Nielsen MMB & Simonsen AC (2013) Imaging ellipsometry of spin-coated membranes: Mapping of multilamellar films, hydrated membranes, and fluid domains. *Langmuir* **29:** 1525–1532

Niemela P, Hyvonen MT & Vattulainen I (2004) Structure and Dynamics of Sphingomyelin Bilayer : Insight Gained through Systematic Comparison to Phosphatidylcholine. *Biophys. J.* **87:** 2976–2989

Nieva JL, Goñi FM & Alonso A (1989) Liposome Fusion Catalytically Induced by Phospholipase C. *Biochemistry* **28:** 7364–7367

Nyholm TKM, Nylund M & Slotte JP (2003) A Calorimetric Study of Binary Mixtures of Dihydrosphingomyelin and Sterols , Sphingomyelin , or Phosphatidylcholine. *Biophys. J.* **84:** 3138–3146

Obeid LM, Linardic CM, Karolak LA & Hannun YA (1993) Programmed cell death induced by ceramide. *Science (80-.).* **259:** 1769–1771

Oncins G, Garcia-Manyes S & Sanz F (2005) Study of frictional properties of a phospholipid bilayer in a liquid environment with lateral force microscopy as a function of NaCl concentration. *Langmuir* **21:** 7373–7379

Overton E (1895) Über die osmotischen Eigenschaften der lebenden Pflanzen und Thierzelle. *Vierteljahrsschr Naturforsch Ges Zürich* **40:** 159–201

Owen DM, Rentero C, Magenau A, Abu-Siniyeh A & Gaus K (2011) Quantitative imaging of membrane lipid order in cells and organisms. *Nat. Protoc.* **7:** 24–35 Available at: http://www.nature.com/doifinder/10.1038/nprot.2011.419 [Accessed November 21, 2017]

Parasassi T, De Stasio G, d'Ubaldo A & Gratton E (1990) Phase fluctuation in phospholipid membranes revealed by Laurdan fluorescence. *Biophys. J.* **57:** 1179–1186

Perkovic S & Mcconnell HM (1997) Cloverleaf Monolayer Domains. *J. Phys. Chem. B* **5647:** 381–388

Pike LJ (2006) report Rafts defined : a report on the Keystone symposium on lipid rafts and cell function. *J. Lipid Res.* **47:** 1597–1598

Pinto SN, Laviad EL, Stiban J, Kelly SL, Merrill AH, Prieto M, Futerman AH & Silva LC (2014) Changes in membrane biophysical properties induced by

sphingomyelinase depend on the sphingolipid *N* -acyl chain. *J. Lipid Res.* **55:** 53–61 Available at: http://www.jlr.org/lookup/doi/10.1194/jlr.M042002

Pinto SN, Silva LC, De Almeida RFM & Prieto M (2008) Membrane domain formation, interdigitation, and morphological alterations induced by the very long chain asymmetric C24:1 ceramide. *Biophys. J.* **95:** 2867–2879 Available at: http://dx.doi.org/10.1529/biophysj.108.129858

Pinto SN, Silva LC, Futerman AH & Prieto M (2011) Effect of ceramide structure on membrane biophysical properties: The role of acyl chain length and unsaturation. *Biochim. Biophys. Acta - Biomembr.* **1808:** 2753–2760 Available at: http://dx.doi.org/10.1016/j.bbamem.2011.07.023

Plesofsky NS, Levery SB, Castle SA & Brambl R (2008) Stress-Induced Cell Death Is Mediated by Ceramide Synthesis in Neurospora crassa . *Eukaryot. cells* **7:** 2147–2159

Quinn PJ, Tessier C, Rainteau D, Koumanov KS & Wolf C (2005) Structure and thermotropic phase behaviour of detergent-resistant membrane raft fractions isolated from human and ruminant erythrocytes. *Biochim. Biophys. Acta - Biomembr.* **1713:** 5–14

Quinn PJ & Wolf C (2009a) Biochimica et Biophysica Acta Thermotropic and structural evaluation of the interaction of natural sphingomyelins with cholesterol. *BBA - Biomembr.* **1788:** 1877–1889 Available at: http://dx.doi.org/10.1016/j.bbamem.2009.07.005

Quinn PJ & Wolf C (2009b) The liquid-ordered phase in membranes. *Biochim. Biophys. Acta - Biomembr.* **1788:** 33–46 Available at: http://dx.doi.org/10.1016/j.bbamem.2008.08.005

Quinn PJ & Wolf C (2010) An X-ray diffraction study of model membrane raft structures. *FEBS J.* **277:** 4685–4698

Rahim N, Ahmat N, Norrizah JS, Fadhilah N, Aripin K, Hamid HAA & Saleh A (2018) A review on phase behaviour of glycolipids derived from plants. *Mater. Today Proc.* **5:** S180–S185 Available at: https://doi.org/10.1016/j.matpr.2018.08.063

Ramstedt B & Slotte JP (1999) Comparison of the Biophysical Properties of Racemic and d-Erythro-N -Acyl Sphingomyelins. *Biophys. J.* **77:** 1498–1506 Available at: http://dx.doi.org/10.1016/S0006-3495(99)76997-3

Ramstedt B & Slotte JP (2002) Membrane properties of sphingomyelins. *FEBS Lett.* **531:** 33–37

Ramstedt B & Slotte JP (2006) Sphingolipids and the formation of sterol-enriched ordered membrane domains. *Biochim. Biophys. Acta - Biomembr.* **1758:** 1945–1956

Rappolt M & Rapp G (1996) Structure of the stable and metastable ripple phase of dipalmitoylphosphatidylcholine. *Eur Biophys J Biophy* **24:** 381–386

Reeves JP & Dowben RM (1969) Formation and properties of thin-walled phospholipid vesicles. *J. Cell. Physiol.* **73:** 49–60

Reynolds CP, Maurer BJ & Kolesnick RN (2004) Ceramide synthesis and metabolism as a target for cancer therapy. *Cancer Lett.* **206:** 169–180

Robertson J. (1960) The molecular structure and contact relationships of cell membranes. *Prog. Biophyis Mol Biol* **10:** 343–418

Róg T, Orłowski A, Llorente A, Skotland T, Sylvänne T, Kauhanen D, Ekroos K, Sandvig K & Vattulainen I (2016) Interdigitation of long-chain sphingomyelin induces coupling of membrane leaflets in a cholesterol dependent manner. *Biochim. Biophys. Acta - Biomembr.* **1858:** 281–288

Ruggiero A & Hudson B (1989) Critical density fluctuations in lipid bilayers detected by fluorescence lifetime heterogeneity. *Biophys. J.* **55:** 1111–1124

Ruiz-Argüello MB, Basáñez G, Goñi FM & Alonso A (1996) Different Effects of Enzyme-generated Ceramides and Diacylglycerols in Phospholipid Membrane Fusion and Leakage *. **271:** 26616–26621

Rujanavech C, Henderson PA & Silbert DF (1986) Influence of Sterol Structure on Phospholipid Phase Behavior as Detected by Parinaric Acid Fluorescence Spectroscopy *. *J Biol Chem* **261:** 7204–7214

Sáez-Cirión A, Alonso A, Goñi FM, McMullen TPW, McElhaney RN & Rivas EA (2000) Equilibrium and kinetic studies of the solubilization of phospholipid-cholesterol bilayers by C12E8. The influence of the lipid phase structure. *Langmuir* **16:** 1960–1968

Sanchez SA, Tricerri MA, Gunther G & Gratton E (2007) Laurdan Generalized Polarization: from cuvette to microscope. *Mod. Res. Educ. Top. Microsc.* **2:** 1007–1014 Available at: http://www.formatex.org/microscopy3/pdf/pp1007-1014.pdf [Accessed November 21, 2017]

Saxena K, Duclos RI, Zimmermann P, Schmidt RR & Shipley GG (1999) Structure and properties of totally synthetic galacto- and gluco-cerebrosides. *J. Lipid Res.*

40: 839–849

Sezgin E, Levental I, Mayor S & Eggeling C (2017) The mystery of membrane organization: Composition, regulation and roles of lipid rafts. *Nat. Rev. Mol. Cell Biol.* **18:** 361–374 Available at: http://dx.doi.org/10.1038/nrm.2017.16

Shah J, Atienza JM, Duclos RI, Rawlings a V, Dong Z & Shipley GG (1995a) Structural and thermotropic properties of synthetic C16:0 (palmitoyl) ceramide: effect of hydration. *J. Lipid Res.* **36:** 1936–44 Available at: http://www.ncbi.nlm.nih.gov/pubmed/8558082

Shah J, Atienza JM, Rawlings a V & Shipley GG (1995b) Physical properties of ceramides: effect of fatty acid hydroxylation. *J. Lipid Res.* **36:** 1945–1955

Shaw KP, Brooks NJ, Clarke JA, Ces O, Seddon JM & Law R V (2012) Pressure – temperature phase behaviour of natural sphingomyelin extracts †. *Soft Matter* **8:** 1070–1078

Silva LC, De Almeida RFM, Castro BM, Fedorov A & Prieto M (2007) Ceramide-domain formation and collapse in lipid rafts: Membrane reorganization by an apoptotic lipid. *Biophys. J.* **92:** 502–516

Silva LC, Futerman AH & Prieto M (2009) Lipid raft composition modulates sphingomyelinase activity and ceramide-induced membrane physical alterations. *Biophys. J.* **96:** 3210–3222 Available at: http://dx.doi.org/10.1016/j.bpj.2008.12.3923

Simons K & Gerl MJ (2010) Revitalizing membrane rafts: New tools and insights. *Nat. Rev. Mol. Cell Biol.* **11:** 688–699 Available at: http://dx.doi.org/10.1038/nrm2977

Simons K & Ikonen E (1997) Functional rafts in cell membranes. *Nature* **387:** 569–572

Simons K & Meers G Van (1988) Perspectives in Biochemistry Lipid Sorting in Epithelial Cells. *Biochemistry* **27:** 6197–6202

Simonsen AC & Bagatolli LA (2004) Structure of spin-coated lipid films and domain formation in supported membranes formed by hydration. *Langmuir* **20:** 9720–9728 Available at: http://www.ncbi.nlm.nih.gov/pubmed/15491207

Singer JS. & Nicolson GL (1972) The Fluid Mosaic Model of the Structure of Cell Membranes. *Science (80-.).* **175:** 720–731

Siskind LJ, Kolesnick RN & Colombini M (2002) Ceramide channels increase the permeability of the mitochondrial outer membrane to small proteins. *J. Biol. Chem.* **277:** 26796–26803

Slotte JP (2013) Molecular properties of various structurally defined sphingomyelins- Correlation of structure with function. *Prog. Lipid Res.* **52:** 206–219

Slotte JP (2016) The importance of hydrogen bonding in sphingomyelin ' s membrane interactions with co-lipids. *Biochim. Biophys. Acta - Biomembr.* **1858:** 304–310 Available at: http://dx.doi.org/10.1016/j.bbamem.2015.12.008

Slotte JP, Östman AL, Kumar ER & Bittman R (1993) Cholesterol Interacts with Lactosyl and Maltosyl Cerebrosides but Not with Glucosyl or Galactosyl Cerebrosides in Mixed Monolayers. *Biochemistry* **32:** 7886–7892

Smith EB (1960) Intimal and medial lipids in human aortas. *Lancet***:** 799–803

Smith ER, Merrill H, Obeid LM & Hannun A (2000) Effects of Sphingosine and Other Sphingolipids on Protein Kinase C Elsevier Masson SAS Available at: http://dx.doi.org/10.1016/S0076-6879(00)12921-0

Sot J, Arand FJ, Collado MI, Goñi FM & Alonso A (2005a) Different Effects of Long- and Short-Chain Ceramides on the Gel-Fluid and Lamellar-Hexagonal Transitions of Phospholipids : A Calorimetric , NMR , and X-Ray Diffraction Study. *Biophys. J.* **88:** 3368–3380

Sot J, Bagatolli L a., Goñi FM & Alonso A (2006) Detergent-resistant, ceramide-enriched domains in sphingomyelin/ceramide bilayers. *Biophys. J.* **90:** 903–914

Sot J, Goñi FM & Alonso A (2005b) Molecular associations and surface-active properties of short- and long- N -acyl chain ceramides. *Biochim. Biophys. Acta* **1711:** 12–19

Sot J, Ibarguren M, Busto J V, Montes LR, Goni FM & Alonso A (2008) Cholesterol displacement by ceramide in sphingomyelin-containing liquid-ordered domains, and generation of gel regions in giant lipidic vesicles. *FEBS Lett* **582:** 3230–3236 Available at: http://www.ncbi.nlm.nih.gov/pubmed/18755187

Sripada PK, Maulik PR, Hamilton JA & Shipley GG (1987) Partial synthesis and properties of a series of N-acyl sphingomyelinsl. *J Lipid Res* **28:**

Stancevic B & Kolesnick R (2010) Ceramide-rich platforms in transmembrane

signaling. *FEBS Lett.* **584:** 1728–1740

Steinbauer B, Mehnert T & Beyer K (2003) Hydration and Lateral Organization in Phospholipid Bilayers Containing Sphingomyelin : A 2 H-NMR Study. *Biophys. J.* **85:** 1013–1024 Available at: http://dx.doi.org/10.1016/S0006-3495(03)74540-8

Stillwell W (2016) An Introduction to Biological Membranes: Composition, Structure and Function. 2nd editio. San Diego: Elsevier Science

Sullan RM, Li JK, Hao C, Walker GC & Zou S (2010) Cholesterol-dependent nanomechanical stability of phase-segregated multicomponent lipid bilayers. *Biophys J* **99:** 507–516 Available at: http://www.ncbi.nlm.nih.gov/pubmed/20643069

Sullan RMA, Li JK & Zou S (2009) Direct correlation of structures and nanomechanical properties of multicomponent lipid bilayers. *Langmuir* **25:** 7471–7477

Sun J, Tristram S, Sutert RM & Nagle JF (1996a) Structure of the ripple phase in lecithin bilayers. *P Natl Acad Sci USA* **93:** 7008–7012

Sun W., Suter M, Knewtson MA & Worthington C. (1994) Order and disorder in fully hydrated unoriented bilayers of gel phase DPPC. *Phys. Rev. E* **49:** 4665–4676

Sun W, Suter RM & Nagle JF (1996b) Structure of Gel Phase Saturated Lecithin Bilayers :. Temperature and Chain Length Dependence. *Biophys. J.* **71:** 885–891

Taha TA, Mullen TD & Obeid LM (2006) A house divided: Ceramide, sphingosine, and sphingosine-1-phosphate in programmed cell death. *Biochim. Biophys. Acta - Biomembr.* **1758:** 2027–2036

Thudichum JL. (1884) A Treatise on the Chemical Constitution of Brain London: Bailliere, Tindall, and Cox

Tristram-Nagle S, Liu Y, Legleiter J & Nagle JF (2002) Structure of Gel Phase DMPC Determined by X-Ray Diffraction. *Biophys. J.* **83:** 3324–3335

Tristram-Nagle S, R. Zhang, R.M. Suter, Worthington CR, Sun W. & Nagle JF (1994) Measurement of chain tilt order angle in fully hydrated bilyers of gel phase lecithins. *Biophys. J.* **64:** 1097–1109

Tristram-nagle SA (2007) NIH Public Access. **1993:** 63–75

Tristram-Nagle SA (2007) Preparation of oriented, fully hydrated lipid samples for structure determination using X-ray scattering. *Methods Mol. Biol.* **400:** 63–75

Unsay JD, Cosentino K & García-Sáez AJ (2015) Atomic Force Microscopy Imaging and Force Spectroscopy of Supported Lipid Bilayers. *J. Vis. Exp.*: 1–9 Available at: http://www.jove.com/video/52867/atomic-force-microscopy-imaging-force-spectroscopy-supported-lipid [Accessed October 31, 2017]

Vanier MT (1999) Lipid Changes in Niemann-Pick Disease Type C Brain : Personal Experience and Review of the Literature. *Neurochem. Res.* **24:** 481–489

Varela ARP, Couto AS, Fedorov A, Futerman AH, Prieto M & Silva LC (2016) Glucosylceramide Reorganizes Cholesterol-Containing Domains in a Fluid Phospholipid Membrane. *Biophys. J.* **110:** 612–622

Varela ARP, Gonçalves Da Silva AMPS, Fedorov A, Futerman AH, Prieto M & Silva LC (2013) Effect of glucosylceramide on the biophysical properties of fluid membranes. *Biochim. Biophys. Acta - Biomembr.* **1828:** 1122–1130

Varela ARP, Ventura AE, Carreira AC, Fedorov A, Futerman AH, Prieto M & Silva LC (2017) Pathological levels of glucosylceramide change the biophysical properties of artificial and cell membranes. *Phys. Chem. Chem. Phys.* **19:** 340–346 Available at: http://xlink.rsc.org/?DOI=C6CP07227E

Veiga MP, Arrondo JLR, Goñi FM & Alonso A (1999) Ceramides in phospholipid membranes: Effects on bilayer stability and transition to nonlamellar phases. *Biophys. J.* **76:** 342–350

Veiga MP, Arrondo JLR, Goñi FM, Alonso A & Marsh D (2001) Interaction of cholesterol with sphingomyelin in mixed membranes containing phosphatidylcholine, studied by spin-label ESR and IR spectroscopies. A possible stabilization of gel-phase sphingolipid domains by cholesterol. *Biochemistry* **40:** 2614–2622

Venable ME, Lee JY, Smyth MJ, Bielawska A & Obeid LM (1995) Role of Ceramide in Cellular Senescence *. *J. Biol. Chem.* **270:** 30701–30708

Venable RM, Sodt AJ, Rogaski B, Rui H, Hatcher E, Mackerell AD, Pastor RW & Klauda JB (2014) Article CHARMM All-Atom Additive Force Field for Sphingomyelin : Elucidation of Hydrogen Bonding and of Positive Curvature. *Biophys. J.* **107:** 134–145 Available at: http://dx.doi.org/10.1016/j.bpj.2014.05.034

Vist MR & Davis JH (1990) Phase Equilibria of Cholesterol/Dipalmitoylphosphatidylcholine Mixtures: 2H Nuclear Magnetic Resonance and Differential Scanning Calorimetry. *Biochemistry* **29:** 451–464

Wack DC & Webb WW (1989) Synchrotron x-ray study of the modulated lamellar phase P beta in the lecithin-water system. *Phys Rev A* **40:** 2712–2730

Weber G & Farris FJ (1979) Synthesis and Spectral Properties of a Hydrophobic Fluorescent Probe: 6-Propionyl-2-(dimethylamino)naphthalene. *Biochemistry* **18:** 3075–3078

Wertz PW & Downing DT (1983) Ceramides of pig epidermis: structure determination. *J. Lipid Res.* **24:** 759–765

Westerlund B & Slotte JP (2009) How the molecular features of glycosphingolipids affect domain formation in fluid membranes. *Biochim. Biophys. Acta - Biomembr.* **1788:** 194–201 Available at: http://dx.doi.org/10.1016/j.bbamem.2008.11.010

Wolber PK & Hudson BS (1981) Fluorescence Lifetime and Time-Resolved Polarization Anisotropy Studies of Acyl Chain Order and Dynamics in Lipid Bilayers. *Biochemistry* **20:** 2800–2810

Yabu T, Shiba H, Shibasaki Y, Nakanishi T, Imamura S, Touhata K & Yamashita M (2015) Stress-induced ceramide generation and apoptosis via the phosphorylation and activation of nSMase1 by JNK signaling. *Cell Death Differ.* **22:** 258–273 Available at: http://dx.doi.org/10.1038/cdd.2014.128

Yao H, Matuoka S, Tenchov B & Hatta I (1991) Metastable ripple phase of fully hydrated dipalmitoylphosphatidylcholine as studied by small angle x-ray scattering. *Biophys. J.* **59:** 252–255 Available at: http://dx.doi.org/10.1016/S0006-3495(91)82216-0

Yingchoncharoen P, Kalinowski DS & Richardson DR (2016) Lipid-Based Drug Delivery Systems in Cancer Therapy: What Is Available and What Is Yet to Come. *Pharmacol. Rev.* **68:** 701–787 Available at: http://pharmrev.aspetjournals.org/cgi/doi/10.1124/pr.115.012070

Zahler PH, Donald BY & Wallach FH (1966) Protein conformations in cellular membranes. *Biochemistry* **56:** 1552–1559

Zhang Y, Li X, Becker KA & Gulbins E (2009) Ceramide-enriched membrane domains-Structure and function. *Biochim. Biophys. Acta - Biomembr.* **1788:** 178–183 Available at: http://dx.doi.org/10.1016/j.bbamem.2008.07.030

Zhu W, Wang X, Zhou Y & Wang H (2014) C2-ceramide induces cell death and protective autophagy in head and neck squamous cell carcinoma cells. *Int. J. Mol. Sci.* **15:** 3336–3355

PUBLICATIONS

PUBLICATIONS

Publications related to this thesis:

- García-Arribas A.B., González-Ramírez E.J., Sot J., Areso I., Alonso A., Goñi F.M. 2017. Complex Effects of 24:1 Sphingolipids in Membranes Containing Dioleoylphosphatidylcholine and Cholesterol. *Langmuir.* 33(22):5545–5554. doi:10.1021/acs.langmuir.7b00162.

- Arsov Z., González-Ramírez E.J., Goñi F.M., Tristram-Nagle S., Nagle J.F. 2018. Phase behavior of palmitoyl and egg sphingomyelin. *Chem Phys Lipids*. 213(March):102–110. doi:10.1016/j.chemphyslip.2018.03.003.

- González-Ramírez E.J., Alonso A., Goñi F.M. Mixing brain cerebrosides with brain ceramides, cholesterol and phospholipids. *(Under 2nd revision).*

- González-Ramírez E.J., Artetxe I., García-Arribas A.B., Alonso A., Goñi F.M. Homogeneous and heterogeneous bilayers of ternary lipid compositions containing equimolar ceramide and cholesterol*. (Submitted).*

Publications not related to this thesis:

- Ahyayauch H., García-arribas A.B., Sot J., González Ramírez E.J., Busto J.V., Monasterio B.G., Jiménez-rojo N., Contreras F.X. 2018. Pb(II) Induces scramblase activation and ceramide-domain generation in red blood cells. Sci Rep. 8(September 2017):1–17. doi:10.1038/s41598-018-25905-8.

LANGMUIR

Article

pubs.acs.org/Langmuir

Complex Effects of 24:1 Sphingolipids in Membranes Containing Dioleoylphosphatidylcholine and Cholesterol

Aritz B. García-Arribas,*[,†,‡,§] Emilio J. González-Ramírez,[†,‡,§] Jesús Sot,[†,‡] Itziar Areso,[†,‡] Alicia Alonso,[†,‡] and Félix M. Goñi*[,†,‡]

[†]Instituto Biofisika (CSIC, UPV/EHU), 48940, Bilbao, Spain

[‡]Departamento de Bioquímica, University of the Basque Country (UPV/EHU), 48940, Bilbao, Spain

Supporting Information

ABSTRACT: The effects of C24:1 sphingolipids have been tested in phospholipid bilayers containing cholesterol. Confocal microscopy, differential scanning calorimetry, and atomic force microscopy imaging and force curves have been used. More precisely, the effects of C24:1 ceramide (nervonoyl ceramide, nCer) were evaluated and compared to those of C16:0 ceramide (palmitoyl ceramide, pCer) in bilayers composed basically of dioleoylphosphatidylcholine, sphingomyelin (either C24:1, nSM or C16:0, pSM) and cholesterol. Combination of equimolecular amounts of C24:1 and C16:0 sphingolipids were also studied under the same conditions. Results show that both pCer and nCer are capable of forming segregated gel domains. Force spectroscopy data point to nCer having a lower stiffening effect than pCer, while the presence of nSM reduces the stiffness. DSC reveals T_m reduction by nSM in every case. Furthermore, pSM seems to better accommodate both ceramides in a single phase of intermediate properties, while nSM partial accommodation of ceramides generates different gel phases with higher stiffnesses caused by interceramide cooperation. If both pSM and nSM are present, a clear preference of both ceramides toward pSM is observed. These findings show the sharp increase in complexity when membranes exhibit different sphingolipids of varying N-acyl chains, which should be a common issue in an actual cell membrane environment.

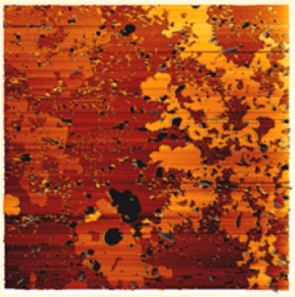

INTRODUCTION

The role of sphingolipids as second messengers in diverse cellular processes has attracted the attention of biophysicists and biochemists in recent years.[1−3] Ceramides are among the most studied sphingolipids due to their proposed role in cell death processes[4−9] and their capacity to induce bilayer heterogeneity, i.e., domain segregation of ceramide-enriched areas within the membrane.[10] Long chain ceramides are also able to modify the biophysical properties of membranes as they induce lipid flip-flop[11] and enhance solute efflux across the membrane.[12,13] Most of the aforementioned studies focus on C16:0 ceramide (palmitoyl ceramide, pCer) since pCer has been considered paradigmatic among long chain ceramides.

However, recent studies in lipidomics show that nervonoyl sphingolipids (C24:1) are also abundant and, in some cases, concentration levels are on par with their C16:0 counterparts.[14,15] Very few studies have been performed to characterize the effect of C24:1 sphingolipids in lipid membranes, and, while comparative experiments between C16:0 and C24:1 sphingolipids as pure lipids are common in the literature,[16−20] studies of their effects in multicomponent bilayers are scarce,[14,21] and the effects of different combinations of C16:0 and C24:1 sphingolipids of different class (e.g., sphingomyelin, ceramide) are virtually unexplored.

Bilayers in the gel (L_β) phase present low fluidity and increased lipid chain order. They typically exhibit higher nanomechanical resistance[22,23] and cause a significant increase in bilayer thickness.[24,25] In turn, the "lipid raft" hypothesis is focused on liquid-ordered phases (which are often defined as a middle ground between gel and fluid phases) enriched in sphingolipids and cholesterol.[26,27] However, sphingolipids such as ceramides are able to segregate into highly packed gel domains that could serve as signaling platforms *in vivo* for ceramide-related signaling cascades, such as those involved in cell death processes.[28−30] Ceramide-rich platforms would also facilitate protein clustering and membrane reorganization,[28,29,31,32] thus being a strong governing factor of protein-based interactions. This hypothesis is supported by some *in vivo* experiments regarding the effects of ceramide-rich domains.[33,34] However, the complete confirmation of this hypothesis is hampered by problems such as the large number of components present in cell signaling cascades and, particularly, in the cell-death machinery.

The effect of cholesterol has been reported as a modulator of the generation of ceramide-enriched domains by displacing ceramide from mixtures with other lipids,[35,36] and ceramide generation can also cause disassembly of liquid-ordered phases enriched in cholesterol by sphingomyelin recruitment.[37−40] Therefore, the presence of cholesterol could indeed have effects on the cell death-inducing capacities of ceramide.[41,42] Even in

Received: January 17, 2017
Revised: May 10, 2017
Published: May 16, 2017

DOI: 10.1021/acs.langmuir.7b00162
Langmuir 2017, 33, 5545−5554

some situations, nonstoichometrically constant gel phases enriched in both ceramide and cholesterol can also appear, caused by direct ceramide-cholesterol interaction,[23,43,44] thus ceramide:cholesterol ratios could be managed by living cells to fine-tune membrane properties.[45] These studies are though focused on C16:0 sphingolipids, particularly C16:0 ceramide, and no further studies have been performed on C24:1 sphingolipids.

In the present study we aim to describe the effects of different combinations of C16:0 and C24:1 sphingolipids in model membranes composed of DOPC:SM:Chol (2:1:1) + Cer in order to recreate a L_d–L_o cell membrane environment in the presence of ceramide, where SM can be nervonoyl sphingomyelin (nSM), palmitoyl sphingomyelin (pSM) or an equimolecular mixture of both, and Cer can be nervonoyl ceramide (nCer), pCer, or an equimolecular mixture of both. For this purpose, a combination of techniques was used: atomic force microscopy (AFM), confocal microscopy, and differential scanning calorimetry (DSC). The results point to C24:1 sphingolipids as having particular properties that clearly differentiate them from their C16:0 counterparts.

MATERIALS AND METHODS

Chemicals. Lipids and lipophilic fluorescent probe 1,2-dioleoyl-*sn*-glycero-3-phosphoethanolamine-*N*-(lissamine rhodamine B sulfonyl) (RhoPE) were purchased from Avanti Polar Lipids (Alabaster, AL, USA). Buffer solution ("assay buffer") for experiments was 20 mM PIPES, 1 mM EDTA, 150 mM NaCl, pH 7.4. All other reagents were of analytical grade.

Confocal Microscopy of Giant Unilamellar Vesicles (GUVs). Giant vesicles were prepared at 60 °C by electroformation on a pair of platinum (Pt) wires by a method first developed by Angelova and Dimitrov, modified as described previously.[46−48] Lipid stock solutions were prepared in 2:1 (v/v) chloroform/methanol at 0.27 mg/mL, and appropriate volumes of each preparation were mixed. Labeling was carried out by premixing the desired fluorescent probe (Rho-PE) with the lipids in organic solvent. Fluorescent probe concentration was 0.4 mol % Rho-PE. The samples were deposited on platinum (Pt) wires. The Pt wires were placed under vacuum for 2 h to completely remove the organic solvent. The sample was covered to avoid light exposure and allowed to precipitate onto the Pt wires for 5 min. One side of the chamber was then sealed with a coverslip. We added 500 mL assay buffer, prepared with high-purity water (SuperQ, Millipore, Billerica, MA) heated at 60 °C, until it covered the Pt wires, and the latter were connected to a TG330 function generator (Thurlby Thandar Instruments, Huntingdon, UK). The alternating current field was applied in three steps, all performed at 60 °C: (1) frequency 500 Hz, amplitude 220 mV (35 V/m) for 5 min; (2) frequency 500 Hz, amplitude 1900 mV (313 V/m) for 20 min; and (3) frequency 500 Hz, amplitude 5.3 V (870 V/m) for 90 min. The temperatures used for GUV formation correspond to those at which the different membranes display a single fluid phase. The generator and the water bath were switched off, and vesicles were left to equilibrate at room temperature for 1 h. After GUV formation, the chamber was placed onto an inverted confocal fluorescence microscope (Nikon D-ECLIPSE C1, Nikon, Melville, NY). The excitation wavelength for Rho-PE was 561 nm, and the images were collected using a band-pass filter of 593 ± 20 nm. Image treatment and quantitation were performed using the software EZ-C1 3.20 (Nikon). No difference in domain size, formation, or distribution was detected in the vesicles during the observation period or after laser exposure.

Supported Planar Bilayer (SPB) Formation. SPBs were prepared on high V-2 quality scratch-free mica substrates (Asheville-Schoonmaker Mica Co., Newport News, VA, USA) previously attached to round 24 mm glass coverslips by the use of a two-component optical epoxy resin (EPO-TEK 301−2FL, Epoxy Technology Inc., Billerica, MA, USA). SPB are prepared by the vesicle adsorption method.[49,50] Multilamellar vesicles (MLVs) were initially prepared by mixing the appropriate amounts of synthetic pure lipids in chloroform/methanol (2:1, v/v) solutions, including 0.4 mol % DiL_{C18}. Samples were then dried by evaporating the solvent under a stream of nitrogen and placing them under vacuum for 2 h. The samples were then hydrated in assay buffer and vortexed at a temperature above that of the sample lipids highest phase transition. After complete lipid detachment from the test tube bottom, formed MLVs were introduced in a FB-15049 (Fisher Scientific Inc., Waltham, MA, USA) bath sonicator and kept at 70 °C for 1 h. In this way a proportion of small unilamellar vesicles (SUVs) were generated. Thereafter, 120 μL assay buffer containing 3 mM $CaCl_2$ were added onto previously prepared 1.2 cm^2 freshly cleaved mica substrate mounted onto a BioCell coverslip-based liquid cell for atomic force microscopy (AFM) measurements (JPK Instruments, Berlin, Germany). Sonicated vesicles (60 μL) were then added on top of the mica. Divalent cations such as Ca^{2+} or Mg^{2+} have been described as enhancers of the vesicle adsorption process onto mica substrates.[51] Final lipid concentration was 150 μM. Vesicles were left to adsorb and extend for 30 min, keeping the sample temperature at 60 °C. In order to avoid sample evaporation and ion concentration, after the first 5 min the buffer was constantly exchanged with assay buffer without $CaCl_2$ at 60 °C for the remaining time. Additional 30 min were left for the samples to equilibrate at room temperature, discarding the nonadsorbed vesicles by washing the samples 10 times with assay buffer without $CaCl_2$, in order to remove remaining Ca^{2+} cations from the solution, which are reported to drastically affect the breakthrough force (F_b) results of lipid bilayer nanoindentation processes.[22] The efficiency of rinsing processes to obtain proper and clean supported lipid bilayers has been reported.[52] This extension and cleaning procedure allowed the formation of bilayers that did not cover the entire substrate surface. The presence of lipid-depleted areas helped with the quantification of bilayer thicknesses and the performance of proper controls for force-spectroscopy measurements. Planar bilayers were then left to equilibrate at room temperature for 1 h prior to measurements in order to avoid the presence of possible artifacts as segregated domains appear at high temperatures (over the T_m)[53] and could still be present at lower temperatures if the cooling process was too fast (>1 °C/min).[51] Finally, the BioCell was set to 23 °C to start the AFM measurements.

Differential Scanning Calorimetry (DSC). The measurements were performed in a VP-DSC high-sensitivity scanning microcalorimeter (MicroCal, Northampton, MA, USA). Both lipid and buffer solutions were degassed prior to loading into the appropriate cell in the form of MLVs. MLVs were prepared as described previously, but in assay buffer (NaCl 150 mM, 20 mM PIPES, 1 mM EDTA) and at a 1 mM concentration. 0.5 mL at 1 mM total lipid concentration was loaded into the calorimeter, performing 5−9 heating scans at a 45 °C/h rate, between 10 and 105 °C for all samples. Phospholipid concentration was determined as lipid phosphorus, and used together with data from any of the reproducible scans, to obtain normalized thermograms. The software Origin 7.0 (MicroCal), provided with the calorimeter, was used to determine the different thermodynamic parameters from the scans. The software PeakFit (Systat Software Inc., Chicago, IL, USA) was used for endotherm deconvolution.

AFM imaging. Planar bilayer topography was performed under contact mode AFM scanning (constant vertical deflection) in a NanoWizard II AFM (JPK Instruments, Berlin, Germany). For proper measurements the AFM was coupled to a Leica microscope and mounted onto a Halcyonics Micro 40 antivibration table (Halcyonics, Inc., Menlo Park, CA, USA) and inside an acoustic enclosure (JPK Instruments). The BioCell liquid sample holder (JPK Instruments) was used in order to control the assay temperature at 23 °C. V-shaped MLCT Si_3N_4 cantilevers (Bruker, Billerica, MA, USA) with nominal spring constants of 0.1 or 0.5 N/m were used for bilayer imaging, always keeping the minimum possible force (0.5−1 nN). 512 × 512 pixel resolution images were collected at a scanning rate between 1 and 1.5 Hz and line-fitted using the JPK Data Processing software as required prior to topography-related data collection. In this regard,

DOI: 10.1021/acs.langmuir.7b00162
Langmuir 2017, 33, 5545−5554

bilayer thicknesses were calculated by cross-section height analysis (n = 50−100) from no less than three images of at least three independent sample preparations with individual cantilevers.

Epifluorescence Microscopy. Direct AFM-coupled inverted epifluorescence microscopy was performed in a Leica DMI 4000B microscope (Leica Microsystems, Wetzlar, Germany) using an appropriate filter cube for Rho-PE fluorochrome (excitation filter HQ545/30x, dichroic mirror Q570LP and emission filter HQ610/75m) (Chroma Tech., Bellows Falls, VT, USA). Images were acquired using a 40X/0.60 LD objective (Leica Microsystems) with a high resolution ORCA-R2 digital CCD camera (Hamamatsu Photonics, Shizuoka, Japan).

Force Spectroscopy. Prior to imaging, V-shaped MLCT Si_3N_4 cantilevers (Bruker, Billerica, MA, USA) with nominal spring constants of 0.1 or 0.5 N/m were individually calibrated in a lipid-free mica substrate in assay buffer using the thermal noise method. After proper bilayer area localization by means of AFM topography and direct epifluorescence microscopy, force spectroscopy was performed at a speed of 1 μm/sec in no less than 500 × 500 nm bilayer areas in the form of 10 × 10 or 15 × 15 grids. Force steps were determined for each of the indentation curves as reproducible jumps within the extended traces. The resulting histograms were generated from at least three independent sample preparations with at least three independently calibrated cantilevers (n = 350−1800). Control indentations were always performed in lipid-free areas before and after bilayer indentations to ascertain the formation of a single bilayer and the absence of artifacts or debris on the tip, assessed by the lack of any force−distance step on both trace and retrace curves.

RESULTS

Lipid gel phases surrounded by a fluid phase are identifiable using fluorescence techniques involving lipid fluorophores. Throughout this study, the lipid fluorophore is RhoPE, which partitions preferentially into fluid phases and tends to be excluded from the more ordered phases. In some cases, only a relative partition is observed, which means that the fluidity of the various phases differs but only to a certain degree. RhoPE is used for confocal fluorescence visualization of GUV (Figure 1) and for epifluorescence visualization of supported planar bilayers, coupled with AFM. In turn, AFM allows the direct detection of segregated phases either by imaging (segregated ordered phases tend to have increased thickness, and they appear with brighter colors on the images) or by force spectroscopy (ordered phases present higher nanomechanical resistance when force indentation curves are applied). By combining the above data, the lipid bilayer can be characterized and different lipid compositions can be comparatively studied.

pSM-Based Samples. DOPC:pSM:Chol (2:1:1) samples containing additional 30 mol % ceramide were prepared (either 30 mol % pCer, or 30 mol % nCer, or 15 mol % pCer +15 mol % nCer) in order to study the effects of nCer as compared to those of pCer. The 30 mol % pCer and the 30 mol % nCer mixtures present both a clear gel/fluid phase segregation that can be identified by fluorescence-depleted areas in GUV (Figure 1A,B, respectively) and SPB (Figure 2B,D respectively), while AFM imaging also reveals phase segregation, as gel phase domains protrude out of the membrane with an increased thickness (Figure 2A,C respectively). Force spectroscopy data (Table 1) reveal that pCer domains are much stiffer than nCer domains, and DSC thermograms (Figure 3A,C) also point in the same direction, as T_m values are lower for nCer samples.

The pSM sample containing 15 mol % of each ceramide displays a thermogram (Figure 3B), which is close to the nCer-containing sample (Figure 3C), although the T_m is slightly

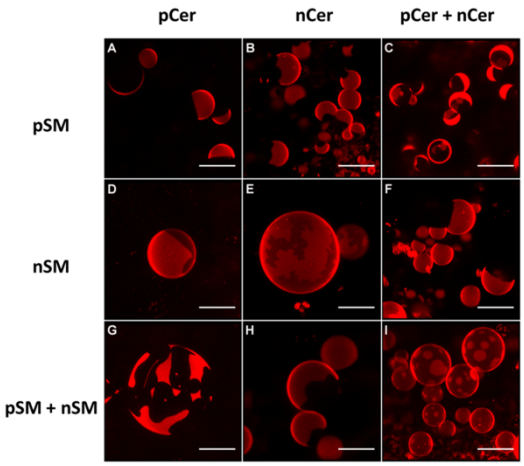

Figure 1. Confocal microscopy 3D (z-stack) images of fluorescent giant unilamellar vesicles containing 0.4% RhoPE. DOPC:pSM:Chol (2:1:1) + 30% pCer (A), + 30% nCer (B), + 15% pCer and 15% nCer (C); DOPC:nSM:Chol (2:1:1) + 30% pCer (D), + 30% nCer (E), + 15% pCer and 15% nCer (F); DOPC:nSM:pSM:Chol (2:0.5:0.5:1) + 30% pCer (G), + 30% nCer (H), + 15% pCer and 15% nCer (I). Scale bars: 10 μm.

higher than the nCer- and clearly lower than the pCer-containing one (Figure 3A). However, a close inspection of the data reveals an additional segregated phase, which can be identified both by confocal microscopy (Figure 1C) and AFM imaging. In the zoom-in of Figure 2G, three lipid phases can be observed, with a clear difference in thickness (AFM image color), quantified in Table 3. Confocal microscopy visualization of this additional gel phase is revealed by a different degree of enrichment of RhoPE (Figure 1C), as some areas are completely devoid of fluorescence (first segregated phase) but others are only partially depleted (second segregated phase), while the continuous phase is clearly more fluorescent. This indicates that the second segregated phase is compositionally closer to the continuous fluid phase, as RhoPE is present in both phases. This is corroborated by force spectroscopy data, as their breakthrough forces are much lower than for the fluorescence-depleted gel phase (Table 1).

Force spectroscopy data (Table 1, representative force curve in Supporting Figure S1A) shows that gel domains exhibit lower nanomechanical resistance when nCer is present, in accordance with a noticeable decrease in T_m measured by DSC (Figure 3A,B,C for thermograms, Table 2 for quantitative results). In addition, the presence of nCer increases the overall bilayer thickness of every phase present, as measured by AFM imaging (Table 3). This could be a direct consequence of the longer N-acyl chain (C24:1 vs C16:0) of nCer.

Confocal microscopy also points to both segregated phases sharing a part of the interphase boundary (instead of being completely separated by the continuous phase) and AFM data suggest, accordingly, that the thickest segregated phase could indeed be surrounded by the second segregated phase, and not by the continuous fluid phase. The potential composition of each phase will be discussed later. The thickest phase exhibits a slight increase in nanomechanical resistance when compared to nCer-enriched domains (20.9 nN vs 17.3 nN), while it is still

DOI: 10.1021/acs.langmuir.7b00162
Langmuir 2017, 33, 5545−5554

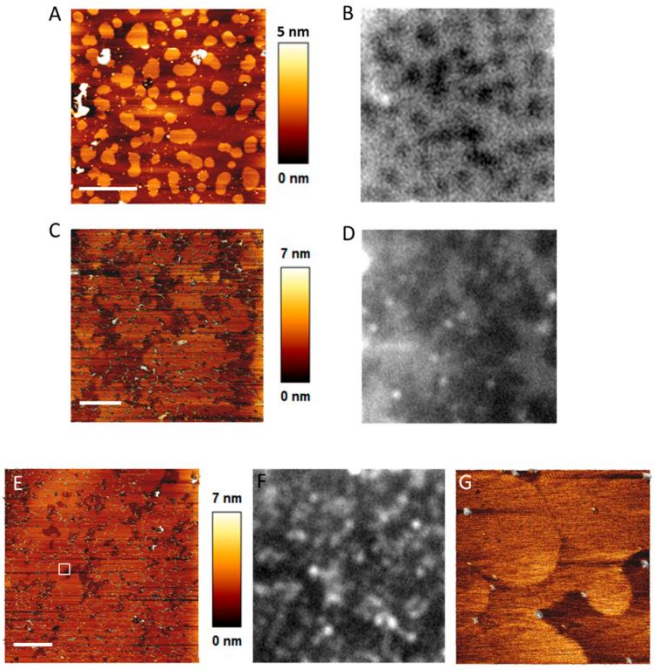

Figure 2. AFM and epifluorescence images of DOPC:pSM:Chol-based SPB containing 0.4% RhoPE. DOPC:pSM:Chol (2:1:1) + 30% pCer (A,B), + 30% nCer (C,D), + 15% pCer and 15% nCer (E,F) and zoom-in of the highlighted area in E (G). Scale bars: 5 μm.

Table 1. Bilayer Nanomechanical Resistance of the Different SPBs under Study[a]

		breakthrough force (nN)	
		continuous phase	segregated domains
DOPC:pSM:Chol	+ pCer	6.5 ± 2.9	57.4 ± 2.3
	+ nCer	3.4 ± 1.5	17.3 ± 2.0
	+ pCer + nCer	2.4 ± 0.6	3.7 ± 0.8
			20.9 ± 2.5
DOPC:nSM:Chol	+ pCer	2.5 ± 0.4	10.2 ± 0.7
	+ nCer	1.8 ± 0.4	7.8 ± 2.7[b]
	+ pCer + nCer	2.4 ± 0.9	13.1 ± 1.1
			10.7 ± 1.5[b]
DOPC:pSM:nSM:Chol	+ pCer	5.3 ± 2.1	49.1 ± 3.6
	+ nCer	3.0 ± 1.1	15.8 ± 2.7
	+ pCer + nCer	2.7 ± 0.9	21.2 ± 3.0

[a]Data expressed as mean ± SD, n = 300−1000. [b]Force curves present adhesion during tip retraction.

significantly lower than the resistance of pCer-enriched domains (Table 1), following the same trend as T_m values (Figure 3, Table 2). Moreover, pCer-enriched domains present the same thickness and stiffness than in pure pSM:pCer mixtures in the same buffer (57 nN according to previous reports[23]), which, as expected,[39] indicates an almost complete displacement of DOPC and Chol from this phase to the continuous phase in the DOPC:pSM:Chol:pCer sample.

In summary, these results point to both ceramides as gel phase-inducing agents, pCer being much more effective than nCer for that purpose, as pCer-induced gel phases are clearly stiffer.

nSM-Based Samples. Following the same procedure, similar experiments were performed on DOPC:nSM:Chol (2:1:1) + 30% ceramide (pCer, nCer, or an equimolar mixture pCer/nCer). As with pSM (previous section), ceramides were able to generate segregated domains in a gel phase, although RhoPE fluorescent probe is not completely excluded from the domains (Figure 1D for pCer, Figure 1E for nCer and Figure 1F for the mixture of both ceramides), which points to domains being less ordered (or less packed) than in pSM-based samples. This case is of special interest, as nSM is reportedly able to override phase segregation for liquid-ordered phases[14] but to the best of our knowledge this had not been tested for ceramide-enriched gel phases.

AFM imaging and epifluorescence (Figure 4) corroborate confocal microscopy data as segregated gel domains can be detected in all three cases, due to their higher thickness and stiffness (Table 1). AFM results for the pCer+nCer sample reveal two types of different segregated phases, while fluorescence reveals only one. This is discussed in the paragraph below. The presence of black areas in AFM images, such as in Figure 2E, is caused by bare mica zones that are not covered by lipid bilayer. These zones are common in vesicle-adsorption SPB preparation, and they are useful for bilayer thickness quantitation (from mica, zero height, to the top surface of the lipid bilayer). DSC data (Figure 3G,H,I, Table 2) show that T_m decreases again in the order T_mpCer > T_mpCer +nCer > T_mnCer, although all three values are around 6 °C

DOI: 10.1021/acs.langmuir.7b00162
Langmuir 2017, 33, 5545−5554

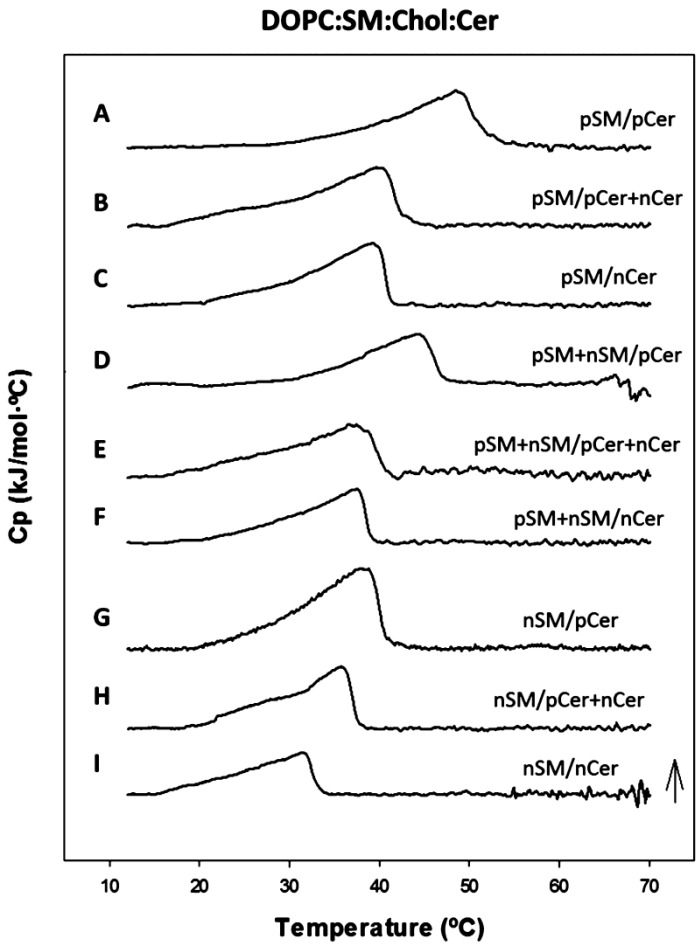

Figure 3. DSC thermograms. DOPC:pSM:Chol (2:1:1) + 30% pCer (A), + 15% pCer and 15% nCer (B), + 30% nCer (C); DOPC:pSM:nSM:Chol (2:0.5:0.5:1) + 30% pCer (D), +15% pCer and 15% nCer (E), + 30% nCer (F); DOPC:nSM:Chol (2:1:1) + 30% pCer (G), + 15% pCer and 15% nCer (H), + 30% nCer (I). Arrow represents 2 kJ/mol·°C.

Table 2. Thermodynamic Parameters of the Gel−Fluid Transition, As Obtained from DSC Experiments[a]

		ΔH (kJ/mol°C)	T_m (°C)	$T_{1/2}$ (°C)
DOPC:pSM:Chol	+ pCer	35.6 ± 16.9	48.5 ± 0.1	9.5 ± 0.4
	+ nCer	24.4 ± 0.8	39.0 ± 0.4	8.4 ± 0.5
	+ pCer + nCer	28.6 ± 1.7	39.5 ± 0.3	9.5 ± 0.6
DOPC:nSM:Chol	+ pCer	31.0 ± 0.9	38.8 ± 0.1	8.7 ± 0.2
	+ nCer	13.0 ± 1.1	31.2 ± 0.8	8.0 ± 0.3
	+ pCer + nCer	21.8 ± 1.0	35.8 ± 0.1	9.4 ± 1.6
DOPC:pSM:nSM:Chol	+ pCer	25.1 ± 9.1	44.3 ± 0.3	8.8 ± 0.4
	+ nCer	19.5 ± 0.6	36.9 ± 0.8	8.6 ± 0.1
	+ pCer + nCer	23.3 ± 0.1	37.2 ± 1.0	10.2 ± 0.3

[a]Average ± values SD (n = 3).

below the corresponding pSM-based samples (Table 2) and moreover, in this case, the T_mpCer+nCer is intermediate between the other two and not particularly close to any of them, while in the pSM-based results, the T_mpCer+nCer was closer to T_mnCer.

Additional differences exist between the two data sets (nSM- and pSM-based). The presence of nSM instead of pSM caused a sharp reduction in bilayer stiffness measured by AFM for every phase present (Table 1). As previously stated in the paragraph above, when both ceramides are present, two kinds of domains appear, but in this case these two segregated phases

DOI: 10.1021/acs.langmuir.7b00162
Langmuir 2017, 33, 5545−5554

Table 3. Bilayer Thickness of the Different SPBs under Study[a]

		bilayer thickness (nm)	
		continuous phase	segregated domains
DOPC:pSM:Chol	+ pCer	4.57 ± 0.20	5.40 ± 0.13
	+ nCer	5.23 ± 0.17	5.95 ± 0.14
	+ pCer + nCer	4.94 ± 0.20	5.32 ± 0.28
			5.73 ± 0.16
DOPC:nSM:Chol	+ pCer	4.31 ± 0.45	5.07 ± 0.51
	+ nCer	4.51 ± 0.22	6.31 ± 0.38
	+ pCer + nCer	4.04 ± 0.32	4.94 ± 0.42
			5.86 ± 0.55
DOPC:pSM:nSM:Chol	+ pCer	4.82 ± 0.31	5.65 ± 0.16
	+ nCer	4.66 ± 0.48	6.59 ± 0.62
	+ pCer + nCer	4.53 ± 0.43	5.55 ± 0.52

[a]Data expressed as mean ± SD, n = 30−100.

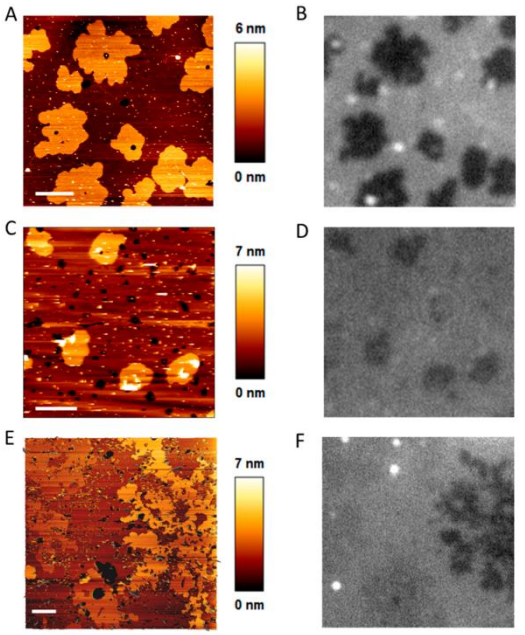

Figure 4. AFM and epifluorescence images of DOPC:nSM:Chol-based SPB containing 0.4% RhoPE. DOPC:nSM:Chol (2:1:1) + 30% pCer (A,B), + 30% nCer (C,D), + 15% pCer and 15% nCer (E,F). Scale bars: 5 μm.

cannot be distinguished through fluorescence, as RhoPE barely reveals the second one. This could be caused by the domains being compositionally close (inefficient fluorescent probe partition between the domains). Another difference with the two-domain pSM-based sample is that, in the case of nSM, these two segregated phases are separated from each other (i.e., they are both completely surrounded by the continuous phase, as seen in Figure 2E) and, more importantly, both exhibit a higher nanomechanical resistance than the single-Cer samples (Table 1), which points to both phases being in a gel state. The possible nature of these domains will be further assessed in the Discussion section.

Samples Containing Both nSM and pSM. The case of DOPC:nSM:pSM:Chol (2:0.5:0.5:1) + 30% ceramide represents the most complex sample set of our study. As in the previous cases, segregated gel phases are observed using confocal microscopy (Figure 1G for pCer, Figure 1H for nCer and Figure 1I for the mixture of both ceramides). The kind of domain observed when both ceramides are present exhibits a partial partition of the fluorescent probe, i.e., the latter is not completely excluded from any domain. DSC data follows the same trend as in the pSM sample set (Figure 3D,E,F), although the three T_m are around 3 °C lower (Table 2), and higher than the nSM sample set. AFM imaging (Figure 5) reveals that there is only one single segregated gel phase for

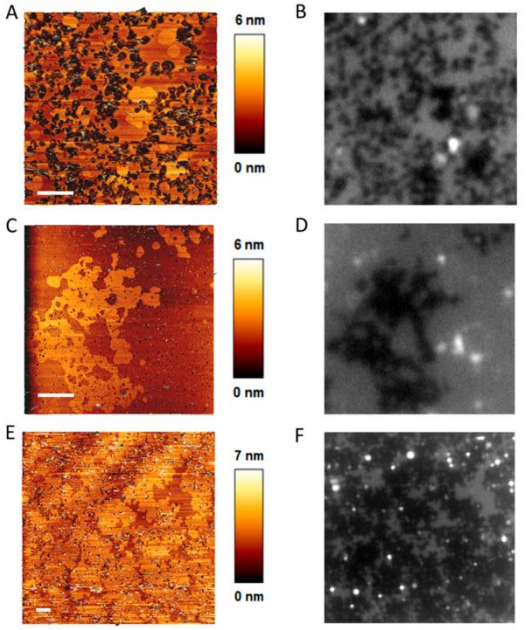

Figure 5. AFM and epifluorescence images of DOPC:pSM:nSM:Chol-based SPB containing 0.4% RhoPE. DOPC:pSM:nSM:Chol (2:0.5:0.5:1) + 30% pCer (A,B), + 30% nCer (C,D), + 15% pCer and 15% nCer (E,F). Scale bars: 5 μm.

every case, even when both ceramides are present. Force spectroscopy (Table 1) correlates with DSC data, as breakthrough forces decrease for pCer and nCer, although the nCer + pCer exhibits the same stiffness as the highest domain of DOPC:pSM:Chol + both ceramides. This information is helpful for a better understanding of the nature of each phase, which will be addressed in the Discussion. In summary, these data suggest that the presence of nSM and pSM gives rise to a trend governed mainly by pSM, although the lipid phases tend to lose stiffness by the effect of nSM.

■ DISCUSSION

The presence of more than one kind of segregated phase in a lipid environment is a difficult issue to assess as different lipid phases present different degrees of lipid enrichment, but still a

DOI: 10.1021/acs.langmuir.7b00162
Langmuir 2017, 33, 5545−5554

small concentration of every lipid is probably present in every phase. Moreover, the effects of different ceramides in the same lipid bilayer have not been studied previously, to the best of our knowledge. This increases the complexity of a complete analysis, but our data provide enough clues to at least suggest which lipids are the most abundant in each phase.

First, the comparison of the three techniques used for every sample provides consistent results, apart from small differences, e.g., when comparing confocal fluorescence of GUV with epifluorescence of SPB, as the latter is deposited onto a mica support. While the nature of supports has been shown to have an effect on lipid segregation, reducing the size of segregated phases in rough surfaces,[54,55] low-roughness supports such as mica (freshly cleaved and atomically flat) have drawn a good degree of consistency when compared to free, i.e., unsupported, vesicles, both in terms of phase segregation and fluorophore behavior. In our study, the only discrepancy observed is that the nSM-based sample with both Cer does not reveal two segregated phases in confocal microscopy but only one (Figure 1F), epifluorescence barely reveals the second one (Figure 3F), while AFM clearly detects both segregated phases in terms of topography (Figure 3E) and nanomechanical resistance (Table 1). This seems an exceptional case as both gel phases are compositionally close, but speaks in favor of force spectroscopic techniques in the case of discrepancy.

Our experiments demonstrate that both ceramides (nCer and/or pCer) are able to form segregated gel phases even in a fluid environment and in the presence of Chol. Most notably, the presence of nSM is not able to override gel phase segregation (Figure 1, Figure 4, and Figure 5) despite the reported capacity of this lipid to solubilize liquid-ordered phases in fluid environments.[14] However, nSM reduces the stiffness of Cer-enriched gel phases (Table 1), which could be caused by a partial destabilization of the phase, i.e., a lower degree of molecular packing. The possibility of interdigitation should also be taken into account, particularly in the case of nSM-based samples,[56] although this eventuality is hard to assess with our current methodologies.

For the complex cases where there are two ceramides present, the case of DOPC:nSM:Chol + both ceramides is probably the simplest to explain (Figure 4), as both segregated domains appear clearly separated from each other. A close inspection of the force curves gives us further insights. For nCer domains, the curve presents an adhesion event on the retractive part (Supporting Figure S1B), and this event also appears for one of the two domains of the nCer+pCer sample (Table 1). The simplest explanation is that each domain is enriched in one of the ceramides. However, domains grow stiffer in both cases when compared to pCer and nCer domains (Table 1), so the possibility of cooperation (i.e., synergic interaction) between ceramides seems plausible. Thus, we consider that both ceramides are present in both domains, but the degree of enrichment of each ceramide varies as one domain (the stiffest one) would be enriched in pCer, while the other, more adhesive one, would be enriched in nCer. The continuous phases are enriched in DOPC and Chol, while nSM would also be present in the domains, as SM has more preference for Cer than for Chol in nonsaturated samples,[38,40,57,58] although the presence of nSM in the continuous phase as well cannot be discarded.

One of the most surprising findings in our study is that the most complex sample, DOPC:pSM:nSM:Chol + both ceramides exhibits only one segregated domain (Figure 1I, 5E and 5F), while the initially expected outcome should be that each ceramide would induce formation of a different domain (as in the previous sample), which could even be enriched in their respective SM as well. However, this is not the case, as a single segregated domain is observed. As both ceramides are able to form segregated gel phases in a DOPC:pSM:nSM:Chol environment (Figure 5A and Figure 5C), the domain is necessarily enriched in both ceramides at the same time (otherwise we would have two types of different segregated domains), but in this case, no cooperation between Cer is happening, as the stiffness of the domain is intermediate when compared to single-ceramide DOPC:pSM:nSM:Chol samples. Thus, we can conclude that the presence of two ceramides in a single segregated phase can have two different and distinct effects: a cooperative effect with one ceramide enriched over the other where the stiffness grows for each domain, or a noncooperative effect (in the presence of pSM) where the stiffness is intermediate.

In DOPC:pSM:Chol + both ceramides, again two segregated phases appear (Figure 2E and more clearly in Figure 2G), although in this case the thickest and stiffest phase appears surrounded by the other (Figure 1C and Figure 2G), acting as "domains within the domains". Again, the presence of two ceramides could initially explain the existence of two segregated phases, one for each ceramide. However, force spectroscopy data (Table 1) points to a different explanation for the existence of these two domains, as one of them exhibits a very low breakthrough force, inappropriate for a gel phase under these ionic strength conditions,[22,23] suggesting that both ceramides are present in the stiffest phase, and not in the second segregated phase. This implies that a different ceramide arrangement is occurring and suggests instead another type of phase (probably liquid-ordered, which is supported in terms of nanomechanical resistance[43]). Interestingly, the stiffest phase shares the same breakthrough force ($p = 0.319$) and thickness ($p = 0.325$) than the DOPC:pSM:nSM:Chol + both ceramides single domain (Table 1 and Table 3), which points to a similar composition: the stiffest domain would be (partially) enriched in pSM, pCer, and nCer, and the liquid ordered phase would be (partially) enriched in pSM and Chol. This conclusion is also supported by the absence of this liquid-ordered phase in the DOPC:pSM:nSM:Chol + both ceramides (Figure 5E and Figure 5F), as nSM has been reported to override liquid-ordered phase segregation,[14] thus nSM would be excluded from the domain. The conclusions of the lipid phase compositional analysis have been summarized in Table 4 for clarity.

A more difficult task would be to assess the effects of multiple ceramides present in smaller concentrations (i.e., with a total

Table 4. Summary of the DOPC:X:Chol:pCer:nCer Samples and the Expected Composition of the Phases Formed in Each Case

		main lipids present		
	brief description	continuous phase	domain 1	domain 2
X: pSM	L_o domain (1) with L_β subdomain (2)	DOPC, Chol	pSM, Chol	pSM, pCer, nCer
X: nSM	separated L_β domains (1,2)	DOPC, Chol	nSM, nCer	nSM, pCer
X: nSM + pSM	L_β domain (1)	DOPC, Chol, nSM	pSM, pCer, nCer	-

DOI: 10.1021/acs.langmuir.7b00162
Langmuir 2017, 33, 5545−5554

mol % Cer concentration far below the 30% used in our study) which is the case for actual cell membranes in living cells. Ceramide levels have been reported to increase up to 10 mol % during cell death processes, but there is no data available on how the levels of each ceramide species increase. A logical assumption, particularly after analyzing the results in this study, is that the modulation of the ratio of each species of ceramide could be an essential tool for regulating the biophysical properties of the membrane and their functional effects. Furthermore, the presence of different sphingomyelins in the membrane is well-known, but how sphingomyelinase activity is modulated by the presence of such a wide array of sphingomyelins, or if it presents any preference toward any specific sphingomyelin depending on the local composition of the membrane, are still unsolved questions. Our study opens the field for further studies on the possible cooperation (or displacement) between different ceramides in the presence of a variety of lipids, including different sphingomyelins.

Finally, it is also worth mentioning that the presence of Chol in the bilayers could indeed have an impact on the possible arrangements of different ceramides, as well as in the biophysical properties of the distinct phases present. Further studies with increasing (or decreasing) Chol content could give more information on the possibility of Chol−Cer displacements or interactions.

■ CONCLUSION

The above results point to nCer having a lower stiffening effect than pCer, while the presence of nSM reduces the stiffness and T_m in every case. While previous reports point to nSM as a better agent to prevent phase separation (of liquid-ordered samples), it does not seem to present the same capacity with ceramide-enriched gel phases, as both pCer and nCer are capable of forming segregated gel domains. Furthermore, pSM seems to better accommodate both ceramides in a single phase of intermediate properties, while nSM only accommodates them partially. This reveals that both ceramides have a preference toward the saturated N-acyl C16:0 chain of pSM which facilitates accommodation. This is further confirmed when both nSM and pSM are present. Moreover, nSM partial accommodation of ceramides generates different gel phases with higher stiffnesses caused, probably, by some kind of interceramide cooperation mediated by nSM, as this cooperative effect does not happen with pSM. Therefore, the N-acyl C24:1 chain of nSM, although less efficient in terms of ceramide accommodation, is essential to allow ceramides to interact in a cooperative way. These findings show the sharp increase in complexity when membranes exhibit different sphingolipids of varying N-acyl chains, which should be a common issue in an actual cell membrane environment.

■ ASSOCIATED CONTENT

Supporting Information

The Supporting Information is available free of charge on the ACS Publications website at DOI: 10.1021/acs.langmuir.7b00162.

(PDF)

■ AUTHOR INFORMATION

Corresponding Authors

*Address: Instituto Biofisika (CSIC, UPV/EHU) Leioa 48940, Basque Country, Spain. E-mail: felix.goni@ehu.eus.

*Address: Instituto Biofisika (CSIC, UPV/EHU) Leioa 48940, Basque Country, Spain. E-mail: aritz.garcia@ehu.eus.

ORCID

Félix M. Goñi: 0000-0001-6270-9216

Author Contributions

§These two authors contributed equally to the experimental part of this work. A.G.A. planned the experiments and performed and analyzed the AFM experiments. E.G.R. planned, performed, and analyzed DSC and confocal microscopy experiments. J.S. gave advice and helped with DSC and confocal microscopy samples. I.A. helped with AFM samples. A.G.A., A.A., and F.M.G. supervised and designed the overall research and wrote the manuscript.

Notes

The authors declare no competing financial interest.

■ ACKNOWLEDGMENTS

A.G.A. was a postdoctoral scientist supported by the Basque Government and later by the University of the Basque Country (UPV/EHU). E.G.R. was a predoctoral student supported by the UPV/EHU. This work was also supported in part by grants from the Spanish Government (FEDER/MINECO BFU 2015-66306-P to F.M.G. and A.A.) and the Basque Government (IT849-13 to F.M.G. and IT838-13 to A.A.).

■ REFERENCES

(1) Hannun, Y. A.; Obeid, L. M. Many ceramides. *J. Biol. Chem.* **2011**, *286*, 27855−27862.

(2) Futerman, A. H.; Hannun, Y. A. The complex life of simple sphingolipids. *EMBO Rep.* **2004**, *5*, 777−82.

(3) Castro, B. M.; Prieto, M.; Silva, L. C. Ceramide: a simple sphingolipid with unique biophysical properties. *Prog. Lipid Res.* **2014**, *54*, 53−67.

(4) Lang, E.; Bissinger, R.; Gulbins, E.; Lang, F. Ceramide in the regulation of eryptosis, the suicidal erythrocyte death. *Apoptosis* **2015**, *20*, 758−67.

(5) Zhu, W.; Wang, X.; Zhou, Y.; Wang, H. C2-ceramide induces cell death and protective autophagy in head and neck squamous cell carcinoma cells. *Int. J. Mol. Sci.* **2014**, *15*, 3336−3355.

(6) Taha, T. A.; Mullen, T. D.; Obeid, L. M. A house divided: ceramide, sphingosine, and sphingosine-1-phosphate in programmed cell death. *Biochim. Biophys. Acta, Biomembr.* **2006**, *1758*, 2027−36.

(7) Obeid, L. M.; Linardic, C. M.; Karolak, L. A.; Hannun, Y. A. Programmed cell death induced by ceramide. *Science* **1993**, *259*, 1769−71.

(8) Kolesnick, R. The therapeutic potential of modulating the ceramide/sphingomyelin pathway. *J. Clin. Invest.* **2002**, *110*, 3−8.

(9) Chipuk, J. E.; McStay, G. P.; Bharti, A.; Kuwana, T.; Clarke, C. J.; Siskind, L. J.; Obeid, L. M.; Green, D. R. Sphingolipid metabolism cooperates with BAK and BAX to promote the mitochondrial pathway of apoptosis. *Cell* **2012**, *148*, 988−1000.

(10) Stancevic, B.; Kolesnick, R. Ceramide-rich platforms in transmembrane signaling. *FEBS Lett.* **2010**, *584*, 1728−40.

(11) Contreras, F. X.; Villar, A. V.; Alonso, A.; Kolesnick, R. N.; Goñi, F. M. Sphingomyelinase activity causes transbilayer lipid translocation in model and cell membranes. *J. Biol. Chem.* **2003**, *278*, 37169−74.

(12) Montes, L. R.; Ruiz-Arguello, M. B.; Goñi, F. M.; Alonso, A. Membrane restructuring via ceramide results in enhanced solute efflux. *J. Biol. Chem.* **2002**, *277*, 11788−94.

(13) Siskind, L. J.; Kolesnick, R. N.; Colombini, M. Ceramide channels increase the permeability of the mitochondrial outer membrane to small proteins. *J. Biol. Chem.* **2002**, *277*, 26796−803.

(14) Maté, S.; Busto, J. V.; García-Arribas, A. B.; Sot, J.; Vazquez, R.; Herlax, V.; Wolf, C.; Bakás, L.; Goñi, F. M. N-Nervonoyl-

DOI: 10.1021/acs.langmuir.7b00162
Langmuir 2017, 33, 5545−5554

sphingomyelin (C24:1) prevents lateral heterogeneity in cholesterol-containing membranes. *Biophys. J.* **2014**, *106*, 2606−2616.
(15) Koumanov, K. S.; Tessier, C.; Momchilova, A. B.; Rainteau, D.; Wolf, C.; Quinn, P. J. Comparative lipid analysis and structure of detergent-resistant membrane raft fractions isolated from human and ruminant erythrocytes. *Arch. Biochem. Biophys.* **2005**, *434*, 150−158.
(16) Jiménez-Rojo, N.; García-Arribas, A. B.; Sot, J.; Alonso, A.; Goñi, F. M. Lipid bilayers containing sphingomyelins and ceramides of varying N-acyl lengths: A glimpse into sphingolipid complexity. *Biochim. Biophys. Acta, Biomembr.* **2014**, *1838*, 456−464.
(17) Pinto, S. N.; Laviad, E. L.; Stiban, J.; Kelly, S. L.; Merrill, A. H., Jr.; Prieto, M.; Futerman, A. H.; Silva, L. C. Changes in membrane biophysical properties induced by sphingomyelinase depend on the sphingolipid N-acyl chain. *J. Lipid Res.* **2014**, *55*, 53−61.
(18) Pinto, S. N.; Silva, L. C.; Futerman, A. H.; Prieto, M. Effect of ceramide structure on membrane biophysical properties: the role of acyl chain length and unsaturation. *Biochim. Biophys. Acta, Biomembr.* **2011**, *1808*, 2753−60.
(19) Pinto, S. N.; Silva, L. C.; de Almeida, R. F.; Prieto, M. Membrane domain formation, interdigitation, and morphological alterations induced by the very long chain asymmetric C24:1 ceramide. *Biophys. J.* **2008**, *95*, 2867−79.
(20) Slotte, J. P. Molecular properties of various structurally defined sphingomyelins−correlation of structure with function. *Prog. Lipid Res.* **2013**, *52*, 206−219.
(21) Maula, T.; Al Sazzad, M. A.; Slotte, J. P. Influence of hydroxylation, chain length, and chain unsaturation on bilayer properties of ceramides. *Biophys. J.* **2015**, *109*, 1639−1651.
(22) Garcia-Manyes, S.; Redondo-Morata, L.; Oncins, G.; Sanz, F. Nanomechanics of lipid bilayers: heads or tails? *J. Am. Chem. Soc.* **2010**, *132*, 12874−12886.
(23) García-Arribas, A. B.; Busto, J. V.; Alonso, A.; Goñi, F. M. Atomic force microscopy characterization of palmitoylceramide and cholesterol effects on phospholipid bilayers: a topographic and nanomechanical study. *Langmuir* **2015**, *31*, 3135−45.
(24) Nagle, J. F.; Tristram-Nagle, S. Structure of lipid bilayers. *Biochim. Biophys. Acta, Rev. Biomembr.* **2000**, *1469*, 159−95.
(25) Domenech, O.; Redondo, L.; Picas, L.; Morros, A.; Montero, M. T.; Hernández-Borrell, J. Atomic force microscopy characterization of supported planar bilayers that mimic the mitochondrial inner membrane. *J. Mol. Recognit.* **2007**, *20*, 546−553.
(26) Simons, K.; Gerl, M. J. Revitalizing membrane rafts: new tools and insights. *Nat. Rev. Mol. Cell Biol.* **2010**, *11*, 688−99.
(27) Simons, K.; Ikonen, E. Functional rafts in cell membranes. *Nature* **1997**, *387*, 569−572.
(28) Kornhuber, J.; Müller, C. P.; Becker, K. A.; Reichel, M.; Gulbins, E. The ceramide system as a novel antidepressant target. *Trends Pharmacol. Sci.* **2014**, *35*, 293−304.
(29) Cremesti, A. E.; Goni, F. M.; Kolesnick, R. Role of sphingomyelinase and ceramide in modulating rafts: do biophysical properties determine biologic outcome? *FEBS Lett.* **2002**, *531*, 47−53.
(30) Cremesti, A.; Paris, F.; Grassme, H.; Holler, N.; Tschopp, J.; Fuks, Z.; Gulbins, E.; Kolesnick, R. Ceramide enables fas to cap and kill. *J. Biol. Chem.* **2001**, *276*, 23954−61.
(31) Kolesnick, R. N.; Goni, F. M.; Alonso, A. Compartmentalization of ceramide signaling: physical foundations and biological effects. *J. Cell. Physiol.* **2000**, *184*, 285−300.
(32) Gulbins, E.; Li, P. L. Physiological and pathophysiological aspects of ceramide. *American Journal of Physiology-Regulatory, Integrative and Comparative Physiology* **2006**, *290*, R11−R26.
(33) Grassmé, H.; Jendrossek, V.; Bock, J.; Riehle, A.; Gulbins, E. Ceramide-rich membrane rafts mediate CD40 clustering. *J. Immunol.* **2002**, *168*, 298−307.
(34) Grassmé, H.; Jekle, A.; Riehle, A.; Schwarz, H.; Berger, J.; Sandhoff, K.; Kolesnick, R.; Gulbins, E. CD95 signaling via ceramide-rich membrane rafts. *J. Biol. Chem.* **2001**, *276*, 20589−20596.
(35) Castro, B. M.; Silva, L. C.; Fedorov, A.; de Almeida, R. F.; Prieto, M. Cholesterol-rich fluid membranes solubilize ceramide domains: implications for the structure and dynamics of mammalian intracellular and plasma membranes. *J. Biol. Chem.* **2009**, *284*, 22978−87.
(36) Busto, J. V.; Garcia-Arribas, A. B.; Sot, J.; Torrecillas, A.; Gomez-Fernandez, J. C.; Goñi, F. M.; Alonso, A. Lamellar gel (L_{β}) phases of ternary lipid composition containing ceramide and cholesterol. *Biophys. J.* **2014**, *106*, 621−30.
(37) Megha; London, E. Ceramide selectively displaces cholesterol from ordered lipid domains (rafts): implications for lipid raft structure and function. *J. Biol. Chem.* **2004**, *279*, 9997−10004.
(38) Chiantia, S.; Kahya, N.; Schwille, P. Raft domain reorganization driven by short- and long-chain ceramide: a combined AFM and FCS study. *Langmuir* **2007**, *23*, 7659−65.
(39) Chiantia, S.; Kahya, N.; Ries, J.; Schwille, P. Effects of ceramide on liquid-ordered domains investigated by simultaneous AFM and FCS. *Biophys. J.* **2006**, *90*, 4500−4508.
(40) Sot, J.; Ibarguren, M.; Busto, J. V.; Montes, L.; Goñi, F. M.; Alonso, A. Cholesterol displacement by ceramide in sphingomyelin-containing liquid-ordered domains, and generation of gel regions in giant lipidic vesicles. *FEBS Lett.* **2008**, *582*, 3230−3236.
(41) Garcia-Ruiz, C.; Mari, M.; Colell, A.; Morales, A.; Caballero, F.; Montero, J.; Terrones, O.; Basañez, G.; Fernandez-Checa, J. C. Mitochondrial cholesterol in health and disease. *Histol Histopathol* **2009**, *24*, 117−32.
(42) Montero, J.; Morales, A.; Llacuna, L.; Lluis, J. M.; Terrones, O.; Basañez, G.; Antonsson, B.; Prieto, J.; Garcia-Ruiz, C.; Colell, A.; Fernandez-Checa, J. C. Mitochondrial cholesterol contributes to chemotherapy resistance in hepatocellular carcinoma. *Cancer Res.* **2008**, *68*, 5246−56.
(43) García-Arribas, A. B.; Ahyayauch, H.; Sot, J.; López-González, P. L.; Alonso, A.; Goñi, F. M. Ceramide-induced lamellar gel phases in fluid cell lipid extracts. *Langmuir* **2016**, *32*, 9053−9063.
(44) García-Arribas, A. B.; Axpe, E.; Mujika, J. I.; Mérida, D.; Busto, J. V.; Sot, J.; Alonso, A.; Lopez, X.; García, J. Á.; Ugalde, J. M.; Plazaola, F.; Goñi, F. M. Cholesterol−Ceramide Interactions in Phospholipid and Sphingolipid Bilayers As Observed by Positron Annihilation Lifetime Spectroscopy and Molecular Dynamics Simulations. *Langmuir* **2016**, *32*, 5434−5444.
(45) García-Arribas, A. B.; Alonso, A.; Goñi, F. M. Cholesterol interactions with ceramide and sphingomyelin. *Chem. Phys. Lipids* **2016**, *199*, 26−34.
(46) Dimitrov, D.; Angelova, M. Lipid swelling and liposome formation mediated by electric fields. *J. Electroanal. Chem. Interfacial Electrochem.* **1988**, *253*, 323−336.
(47) Angelova, M. I.; Dimitrov, D. S. Liposome electroformation. *Faraday Discuss. Chem. Soc.* **1986**, *81*, 303−311.
(48) Montes, L. R.; Ahyayauch, H.; Ibarguren, M.; Sot, J.; Alonso, A.; Bagatolli, L. A.; Goñi, F. M. Electroformation of giant unilamellar vesicles from native membranes and organic lipid mixtures for the study of lipid domains under physiological ionic-strength conditions. *Methods Mol. Biol.* **2010**, *606*, 105−14.
(49) Jass, J.; Tjarnhage, T.; Puu, G. From liposomes to supported, planar bilayer structures on hydrophilic and hydrophobic surfaces: an atomic force microscopy study. *Biophys. J.* **2000**, *79*, 3153−63.
(50) McConnell, H.; Watts, T.; Weis, R.; Brian, A. Supported planar membranes in studies of cell-cell recognition in the immune system. *Biochim. Biophys. Acta, Rev. Biomembr.* **1986**, *864*, 95−106.
(51) Attwood, S. J.; Choi, Y.; Leonenko, Z. Preparation of DOPC and DPPC Supported Planar Lipid Bilayers for Atomic Force Microscopy and Atomic Force Spectroscopy. *Int. J. Mol. Sci.* **2013**, *14*, 3514−39.
(52) Oncins, G.; Garcia-Manyes, S.; Sanz, F. Study of frictional properties of a phospholipid bilayer in a liquid environment with lateral force microscopy as a function of NaCl concentration. *Langmuir* **2005**, *21*, 7373−7379.
(53) Garcia-Manyes, S.; Oncins, G.; Sanz, F. Effect of temperature on the nanomechanics of lipid bilayers studied by force spectroscopy. *Biophys. J.* **2005**, *89*, 4261−74.

DOI: 10.1021/acs.langmuir.7b00162
Langmuir 2017, 33, 5545−5554

(54) Honigmann, A.; Sadeghi, S.; Keller, J.; Hell, S. W.; Eggeling, C.; Vink, R. A lipid bound actin meshwork organizes liquid phase separation in model membranes. *eLife* **2014**, 3, e01671.
(55) Honigmann, A.; Mueller, V.; Hell, S. W.; Eggeling, C. STED microscopy detects and quantifies liquid phase separation in lipid membranes using a new far-red emitting fluorescent phosphoglycerolipid analogue. *Faraday Discuss.* **2013**, *161*, 77−89 discussion 113-50..
(56) Rog, T.; Orlowski, A.; Llorente, A.; Skotland, T.; Sylvanne, T.; Kauhanen, D.; Ekroos, K.; Sandvig, K.; Vattulainen, I. Interdigitation of long-chain sphingomyelin induces coupling of membrane leaflets in a cholesterol dependent manner. *Biochim. Biophys. Acta, Biomembr.* **2016**, *1858*, 281−8.
(57) Silva, L. C.; de Almeida, R. F.; Castro, B. M.; Fedorov, A.; Prieto, M. Ceramide-domain formation and collapse in lipid rafts: membrane reorganization by an apoptotic lipid. *Biophys. J.* **2007**, *92*, 502−16.
(58) Fidorra, M.; Duelund, L.; Leidy, C.; Simonsen, A. C.; Bagatolli, L. A. Absence of fluid-ordered/fluid-disordered phase coexistence in ceramide/POPC mixtures containing cholesterol. *Biophys. J.* **2006**, *90*, 4437−51.

DOI: 10.1021/acs.langmuir.7b00162
Langmuir 2017, 33, 5545−5554

Chemistry and Physics of Lipids 213 (2018) 102–110

Contents lists available at ScienceDirect

Chemistry and Physics of Lipids

journal homepage: www.elsevier.com/locate/chemphyslip

Phase behavior of palmitoyl and egg sphingomyelin

Zoran Arsov[a,1], Emilio J. González-Ramírez[b,1], Felix M. Goñi[b], Stephanie Tristram-Nagle[c], John F. Nagle[c,*]

[a] Department of Condensed Matter Physics, Laboratory of Biophysics, Jozef Stefan Institute, 1000 Ljubljana, Slovenia
[b] Instituto Biofísika (CSIC, UPV/EHU) and Departamento de Bioquímica, Universidad del País Vasco, 48080 Bilbao, Spain
[c] Physics Department, Carnegie Mellon University, Pittsburgh, PA 15213, United States

ARTICLE INFO

Keywords:
X-ray diffraction
X-ray diffuse scattering
Volume determination
Ripple phase
Gel phase
Fluid phase
Ripple wavelength

ABSTRACT

Despite the biological significance of sphingomyelins (SMs), there is far less structural information available for SMs compared to glycerophospholipids. Considerable confusion exists in the literature regarding even the phase behavior of SM bilayers. This work studies both palmitoyl (PSM) and egg sphingomyelin (ESM) in the temperature regime from 3 °C to 55 °C using X-ray diffraction and X-ray diffuse scattering on hydrated, oriented thick bilayer stacks. We observe clear evidence for a ripple phase for ESM in a large temperature range from 3 °C to the main phase transition temperature (T_M) of ~38 °C. This unusual stability of the ripple phase was not observed for PSM, which was in a gel phase at 3 °C, with a gel-to-ripple transition at ~24 °C and a ripple-to-fluid transition at ~41 °C. We also report structural results for all phases. In the gel phase at 3 °C, PSM has chains tilted by ~30° with an area/lipid ~45 Å^2 as determined by wide angle X-ray scattering. The ripple phases for both PSM and ESM have temperature dependent ripple wavelengths that are ~145 Å near 30 °C. In the fluid phase, our electron density profiles combined with volume measurements allow calculation of area/lipid to be ~64 Å^2 for both PSM and ESM, which is larger than that from most of the previous molecular dynamics simulations and experimental studies. Our study demonstrates that oriented lipid films are particularly well-suited to characterize ripple phases since the scattering pattern is much better resolved than in unoriented samples.

1. Introduction

The major lipids in biological membranes are glycerophospholipids, sphingolipids and sterols. While sphingolipids include glycosphingolipids and sphingomyelins (SMs), the latter are the most abundant sphingolipids in mammalian cells (van Meer et al., 2008) reaching concentrations of 15% of the total phospholipid content in the outer leaflet of the plasma membranes (Shaw et al., 2012). Structurally, SMs are similar to phosphatidylcholines (PCs) in that both lipids have phosphatidylcholine as the polar headgroup and both have long hydrocarbon tails, but there are considerable differences in the linkages between these parts of the lipids (Ramstedt and Slotte, 2002).

Recent interest in SMs arises from their interaction with cholesterol in generating cholesterol-rich lateral membrane domains, their specific binding to and regulation of particular membrane proteins, and their involvement as precursors to simpler sphingolipids in cell signaling events (Goni and Alonso, 2006; Slotte, 2013). The preferential mixing of sterols with SMs over PCs is mainly attributed to two properties: Firstly, SMs usually have saturated or *trans*-unsaturated tails and they apparently pack more tightly (van Meer et al., 2008); secondly, the amide and hydroxyl groups in SMs can act as hydrogen bond donors and acceptors, so they can form both intra- and intermolecular hydrogen bonding (Slotte, 2016; Venable et al., 2014).

Since pure SMs are more expensive than pure PCs, many experimental studies of systems involving them are performed using natural SM extracts e.g., egg, brain and milk SMs, which have mixtures of hydrocarbon chains. On the other hand, simulation studies use pure SM lipids with homogeneous chains. Egg SM (ESM) stands out as the most homogeneous of the natural SMs; it has predominantly 86% N-palmitoyl (16:0) acyl chain (Filippov et al., 2006) with 93% of the sphingosine (18:1) long-chain base (Ramstedt et al., 1999). Therefore from the viewpoint of composition, ESM is the closest natural extract to the pure palmitoyl sphingomyelin (PSM), so experimental properties using ESM are frequently compared to simulation studies using PSM (Niemela et al., 2004); such comparisons should be made carefully, especially as the main transition temperature of PSM (T_M = 41 °C) (Barenholz et al., 1976) is somewhat higher than for ESM (T_M = 38 °C) (Jimenez-Rojo et al., 2014). This paper will further address differences between ESM

* Corresponding author.
E-mail address: nagle@cmu.edu (J.F. Nagle).
[1] Contributed equally as first co-authors.

https://doi.org/10.1016/j.chemphyslip.2018.03.003
Received 14 December 2017; Received in revised form 2 February 2018; Accepted 6 March 2018
Available online 22 April 2018

and PSM.

Even the nature of the generic SM main transition has been unclear. By analogy with saturated PC lipids, the transition is often inferred to be from ripple phase to fluid (liquid-crystalline or liquid-disordered) phase if a pretransition is observed and gel-to-fluid phase if it is not. Many thermotropic studies did not observe a pretransition, either in PSM (de Almeida et al., 2003; Maulik and Shipley, 1996), or in ESM (Anderle and Mendelsohn, 1986; Arsov and Quaroni, 2008; Chien et al., 1991; Epand and Epand, 1980; Garcia-Arribas et al., 2016; Jimenez-Rojo et al., 2014; Mannock et al., 2003; Mckeone et al., 1986; Rujanavech et al., 1986; Steinbauer et al., 2003; Veiga et al., 2001), and have described the transition as from a gel-to-fluid (liquid-crystalline or liquid-disordered) phase.

Other PSM studies (Barenholz et al., 1976; Calhoun and Shipley, 1979) observed a pretransition using DSC. Turning to structural studies one of the first low- and wide-angle X-ray scattering (LAXS and WAXS) studies on PSM reported a gel phase structure below T_M despite observing a pretransition using DSC (Calhoun and Shipley, 1979). (Maulik and Shipley, 1996) also reported no X-ray evidence for a ripple phase in PSM. However, other X-ray studies have reported that ESM is in a ripple phase below T_M (Chemin et al., 2008; Quinn and Wolf, 2009; Shaw et al., 2012). All of these X-ray studies employed unoriented MLV samples where ripple reflections are either small or weak. By contrast, X-ray diffraction from oriented lipid samples is particularly well suited to differentiate between flat gel or interdigitated phases and the ripple phase (Akabori and Nagle, 2015; Guler et al., 2009; Katsaras et al., 2000; Sun et al., 1996b). To clarify the above mentioned differences in the literature for both ESM and PSM individually, as well as what the actual differences are between ESM and PSM, the aim of this work is to characterize the structure of the phases, particularly for $T < T_M$, using oriented hydrated samples.

A broad temperature interval was investigated and our results show that ESM persists in a ripple phase at all studied temperatures below T_M (3–35 °C), i.e., no gel phase or gel-to-ripple phase pretransition was observed. This persistence enabled us to study the temperature dependence of the ESM ripple phase structural parameters. In contrast, we find that PSM is in a gel phase below 24 °C and in a ripple phase between 24 °C and the main transition. Our study confirms that it is particularly valuable to study oriented lipid films, especially for ripple phases, since their scattering patterns are much better resolved than in unoriented MLV samples. It will also serve to alleviate a relative dearth in structural studies of PSM and ESM.

2. Materials & methods

2.1. Reagents & lipids

Egg sphingomyelin (ESM) (Lot Egg-SM 860061-01-115) and palmitoyl sphingomyelin (PSM) (Lot 860584-01-017) were purchased from Avanti Polar Lipids (Alabaster, AL) and used as received. Avanti estimates 1–1.5% L-erythro impurity, no D- or L-threo impurity, and greater than 99% purity with respect to total sphingomyelin content in PSM, whereas as much as 10% L-threo may occur when synthesizing by hydrolysis of natural SM. HPLC organic solvents were purchased from Sigma/Aldrich (St. Louis, MO).

2.2. Sample preparation

2.2.1. Oriented samples

4 mg of lyophilized lipid was dissolved in 200 mL chloroform:TFE (1:1) (v/v) and plated onto a silicon wafer (15 × 30 × 1 mm) via the rock and roll method (Tristram-Nagle, 2007) to produce stacks of ~1800 aligned bilayers (Tristram-Nagle et al., 2002). Solvents were removed by evaporation in a fume hood, followed by 2 h under vacuum at room temperature. The oriented samples were prehydrated at close to 100% RH in a polypropylene hydration chamber at 60 °C for 2 h and allowed to slowly cool to room temperature. Thin layer chromatography indicated no degradation due to this annealing procedure. Approximately 10 μm thick samples were trimmed to leave 5 mm (in the direction of the X-ray beam) by 30 mm (to provide many locations for the ~1 mm wide beam to minimize radiation damage).

2.2.2. Unoriented samples

2–10 mg of lyophilized lipid was mixed with 100 μL of MilliQ water. Samples were hydrated by vortexing and temperature cycling 3 times between 60 °C and 0 °C to form multilamellar vesicles (MLVs). Hydrated lipids were mildly centrifuged using a desk-top centrifuge in a glass test tube at 1000 rpm for 10 min and the concentrated lipid was loaded into 1 mm diameter thin-walled X-ray capillaries (Charles Supper Company, Natick, MA) and flame-sealed. The X-ray capillaries were centrifuged in a capillary holder at 1000 rpm for an additional 2 min to further concentrate the lipid in the beam. The final ratio of water to lipid was at least 2:1 so the MLVs were fully hydrated as evidenced by their contact with excess water in the capillary.

2.2.3. Volumetric samples

48.9 mg lyophilized ESM was added to 1.204 g MilliQ water and hydrated by vortexing and cycling three times between 60 and 0 °C. ~10 mg lyophilized PSM was added to ~1.1 g MilliQ water and hydrated by vortexing and cycling three times between 60 and 0 °C.

2.3. Methods

2.3.1. X-ray scattering

Oriented stacks of membrane mimics were hydrated through the vapor phase in a temperature-controlled hydration chamber described in (Kučerka et al., 2005). Low angle X-ray scattering (LAXS) and wide angle X-ray scattering (WAXS) were obtained from a Rigaku RUH3R rotating anode as described in (Tristram-Nagle et al., 2002; Tristram-Nagle et al., 1993). Wavelength was 1.5418 Å, and sample-to-detector (*S*)-distance was 280.6 mm (LAXS) and 133.7 mm (WAXS). Data were collected using a Rigaku (The Woodlands, TX) Mercury CCD array detector (1024 × 1024, 68 μm pixels) during 5- or 10 min dezingered scans. Temperature was controlled using a Julabo Model F25 circulating water bath. Data analysis for the ripple phase was performed as in (Sun et al., 1996b; Akabori and Nagle, 2015) using our proprietary TiffView software.

2.3.2. Volume measurements

The 4.1% aqueous ESM or ~1% aqueous PSM suspension was loaded into the Anton-Paar 5000 M DMA scanning density meter and heated at 12°/h.

3. Results

Fig. 1A shows the typical X-ray pattern obtained for ESM. Oriented samples clearly show off-specular peaks below T_M, indicated by white arrows; such peaks are required for in-plane periodicity that occurs for the ripple phase. The peaks are arranged symmetrically around the meridian because the sample is a powder average, in-plane only. This rippled pattern was present at every temperature investigated in this work from 3 to 35 °C. Additional oriented ESM data are shown in the Supplementary material (Figs. S1–S8). Following the literature (Akabori and Nagle, 2015; Sun et al., 1996b; Wack and Webb, 1989) these peaks can be indexed as (h,k) where the (h,0) peaks are the usual lamellar peaks that occur on the meridian with $q_r = 0$. The ripple side peaks are labeled with the k index. In Fig. 1A, the visible side peaks are, from the top, (4,−2), (3,−1), (3,−2), (2,−1), (1,−1) and a weak (1,1). Fig. 1B shows that ESM is also in the ripple phase at 35 °C.

Fig. 2 shows LAXS data for PSM. At 37 °C (Fig. 2B) PSM is clearly in the ripple phase, however, at 3 °C (Fig. 2A) the absence of side peaks is consistent with a gel phase. In Fig. 2A, arcs, instead of spots, are due to

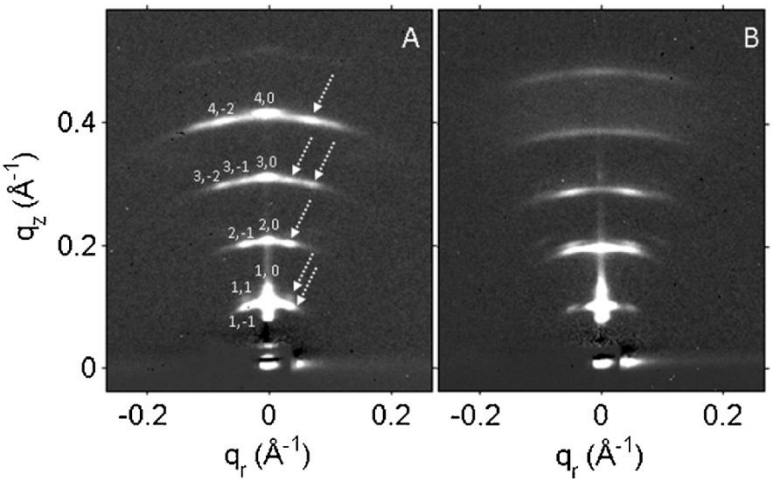

Fig. 1. LAXS data from oriented ESM. A. Overnight equilibration at 3 °C, followed by B. equilibration at 35 °C. White arrows in A. point to the off-specular peaks. D-spacing in A. is 60.3 Å and in B. is 65.8 Å.

mosaicity (Nagle et al., 2016). Additional oriented PSM data are shown in the Supplementary material (Figs. S9–S15).

In order to describe our structural results, a diagram of some of the basic structural parameters of ripple phases is shown in Fig. 3. The usual lamellar D-spacing in the z direction perpendicular to the substrate and the stack of bilayers includes the average bilayer thickness and the water spacing; it was obtained from the q_z positions of the specular (h,0) peaks. Following previous studies (Akabori and Nagle, 2015; Sun et al., 1996b; Wack and Webb, 1989), the in-plane spacing λ_r is the length of the rippled repeat distance; it was obtained from the q_r positions of the off-specular (h,k) peaks. γ is the angle in the two dimensional unit cell; it was obtained from the angle of the lines joining the central (h,0) peaks to the (h,k < 0) side peaks (Akabori and Nagle, 2015; Sun et al., 1996b).

Fig. 4 shows results for λ_r and γ. The result that γ values differ from 90° requires that the ripple be asymmetric unlike the symmetric ripple phases that occur metastably in DPPC and which have λ_r greater than 200 Å (Katsaras et al., 2000; Mason et al., 1999; Rappolt and Rapp,

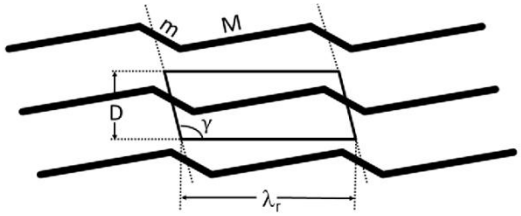

Fig. 3. Diagram of structural parameters characterizing the ripple phase. The bold solid lines represent the centers of three adjacent bilayers. M represents the major arm and m the minor arm in a typical saw-toothed asymmetric ripple (Akabori and Nagle, 2015; Katsaras et al., 2000; Sun et al., 1996b). D is the usual lamellar repeat D-spacing, λ_r is the ripple wavelength and γ the ripple offset angle in the unit cell indicated by the parallelogram containing the middle of the 2nd bilayer.

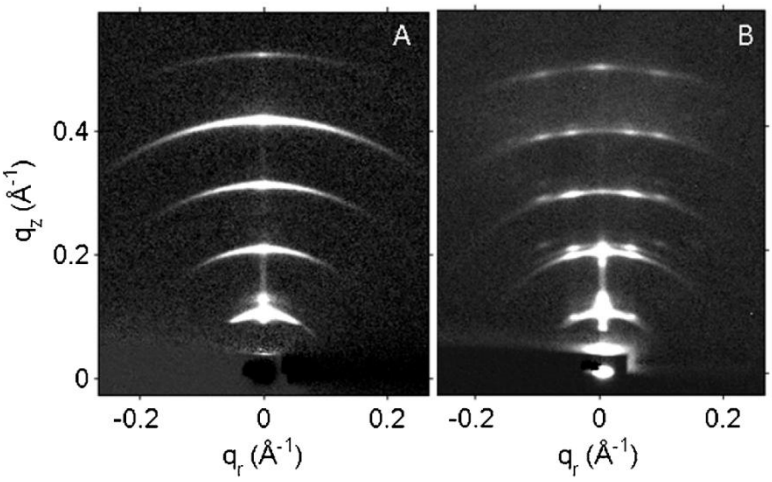

Fig. 2. LAXS data from oriented PSM. A. After overnight equilibration at 3 °C and B. at 37 °C. D-spacing in A is 60.0 Å, and in B is 63.6 Å.

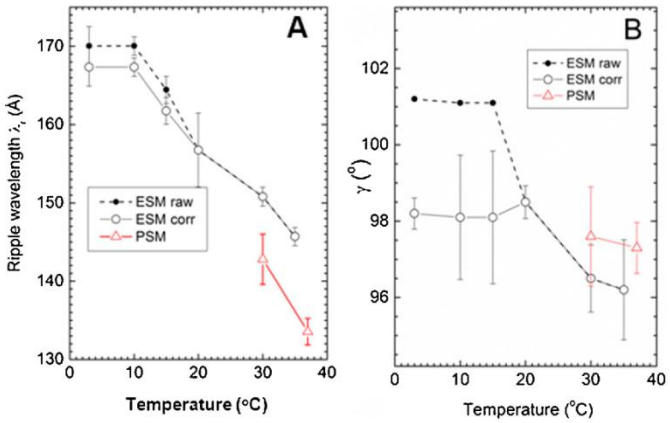

Fig. 4. Temperature dependence of A. λ_r of the ripple phase and B. the γ angle for ESM (open black circles) and PSM (open red triangles). The solid symbols show values before correction for hydration level (*vide infra*).

1996; Yao et al., 1991). Furthermore, the stronger intensity of the negative k peaks compared to the positive k peaks means that the asymmetry for $\gamma > 90°$ is as drawn in Fig. 3 (Akabori and Nagle, 2015; Sun et al., 1996b).

Fig. 5 shows wide-angle WAXS scattering for the same PSM sample as in Fig. 2. With the longer exposure time appropriate for the WAXS scattering, Fig. 5A shows LAXS orders h = 1-4 that are overexposed and weak h = 5, 7 and 9 LAXS orders. The WAXS scattering in Fig. 5A looks similar to the WAXS pattern from the $L_{\beta I}$ gel phase in DMPC (Tristram-Nagle et al., 2002), where tilted chains cause the (1,1) peak to be lifted up off the equator near $q_z = 1.4\ Å^{-1}$. Also visible at the same q_z and smaller q_z is a satellite that comes from modulation of the continuous form factor along the (1,1) Bragg rod (Sun et al., 1994). The wide angle scattering in Fig. 5B is consistent with the much higher resolution WAXS from DMPC in the ripple phase (Akabori and Nagle, 2015) suggesting that there is a stronger Bragg rod centered near $q_r = 1.5\ Å^{-1}$ and $q_z \sim 0.3\ Å^{-1}$ and a weaker Bragg rod at smaller q_r and q_z, although such a separation is not visible in Fig. 5B. Figs. S3–S5 for ESM are more suggestive of such a wide angle pattern.

WAXS data shown in Fig. 5A were used to determine the gel phase chain tilt angle for PSM, $\theta_{tilt} = 30.4$, the area/chain perpendicular to the chains, $A_C = 19.2\ Å^2$, and the area/lipid $A_L = 2A_C/\cos\theta_{tilt}$ following (Tristram-Nagle et al., 2002; Tristram-Nagle et al., 1993).

Although data from oriented samples are the more important, unoriented MLV samples are also informative. Fig. 6 shows X-ray scattering from ESM MLVs. In the WAXS regime, a single sharper ring is observed below the transition temperature, indicating chain ordering, and this becomes broad at 50 °C, indicating chain melting. PC lipids have a single sharp WAXS ring in their ripple phase, whereas in their gel phase there are two separate WAXS rings, one sharp and one broader, due to chain tilt. It is important to note that the single WAXS ring below T_M in Fig. 6 does not prove, contrary to what is commonly assumed, that ESM is in a ripple phase. Separation of the two rings in PC lipids is just due to orthorhombic splitting of the hexagonal packing of the chains. A gel phase does not require such splitting, in which case one would also observe a single ring that would be misidentified with a ripple phase.

Several peaks are observed in the LAXS regime in Fig. 6, but these can be satisfactorily indexed as lamellar peaks with no obvious off-specular reflections that would indicate that the sample is in the ripple phase. To further illustrate the difficulty of verifying a ripple phase in unoriented samples, we have taken the oriented data in Fig. 1A and powder averaged it into isotropic rings (Fig. 7); this blurs the relatively weak but clearly separated off-specular peaks in Fig. 1A with the lamellar orders and gives intensity plots similar to the isotropic data in Fig. 6B.

There is one advantage of unoriented MLV samples, which are immersed in excess water and are therefore fully hydrated, over our oriented samples, which are hydrated from the vapor. While it is an advantage to be able to hydrate oriented samples to different D-spacings, it is time consuming to achieve the preferred full hydration. As we have shown previously, D-spacing is extremely sensitive to humidity close to

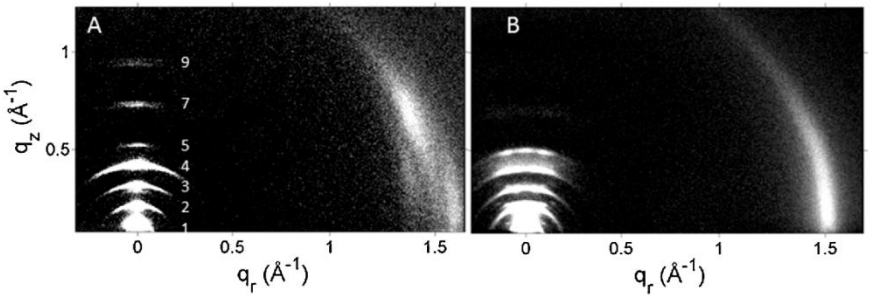

Fig. 5. Wide angle WAXS intensity together with overexposed LAXS for the same sample and temperatures as in Fig. 2. A. PSM at 3 °C, B. PSM at 37 °C. D-spacing in A is 59.2 Å, and in B it is 63.0 Å.

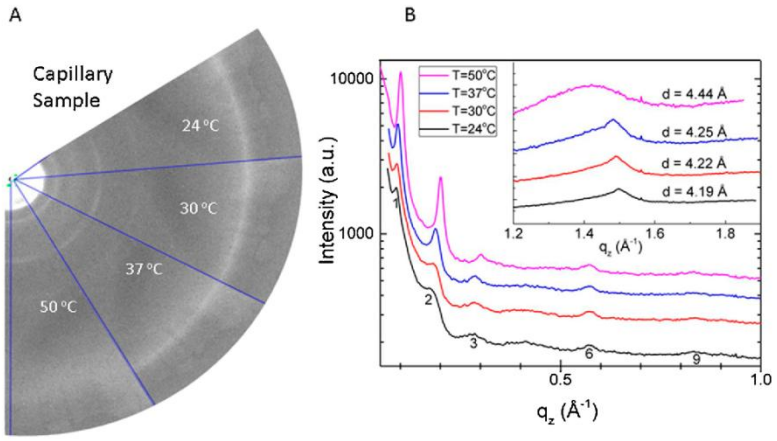

Fig. 6. A. X-ray scattering data from ESM MLVs in a glass capillary collected on a 2D CCD detector at the temperatures indicated. The rings close to the beam (white center) are in the LAXS regime, while the single ring close to the edge of the pie sectors is in the WAXS regime. **B.** Intensity plots of capillary data shown in A. Small black numbers indicate lamellar orders, h = 1,2,3,6,9. Inset: zoomed WAXS region.

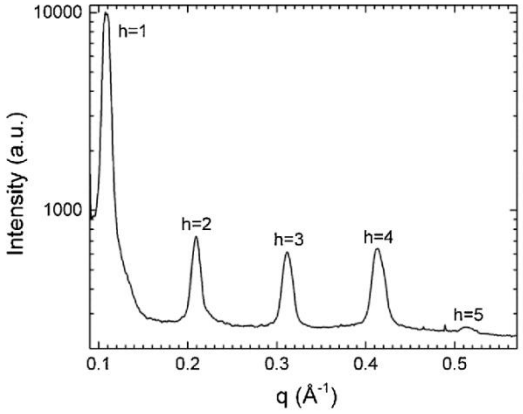

Fig. 7. Powder average of LAXS data shown in Fig. 1A, ESM at 3 °C. As shown, off-specular side peaks are difficult to distinguish from the background scattering between lamellar peaks (numbered). D-spacing is 60.3 Å.

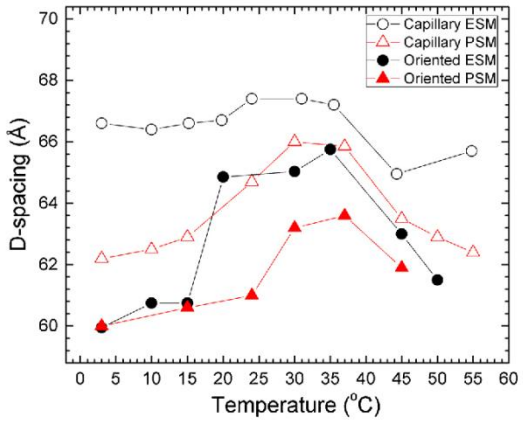

Fig. 8. D-spacings of capillary and oriented samples as a function of temperature (see legend for details).

100% relative humidity (Chu et al., 2005). Fig. 8 compares the actual D-spacings of our oriented samples with those of the fully hydrated MLV samples. Although we did not achieve full hydration for all temperatures in the oriented samples, our experience has been that this amount of dehydration is small enough that the basic properties of fluid and gel phase bilayers are little changed. In Supplementary material, it is shown how our capillary data compare to capillary D-spacings from the literature (Fig. S16).

However, relative humidity affects the values of the ripple phase unit cell parameters as is shown in Fig. 9 for PSM. This impacts the temperature dependence of the raw data in Fig. 4 because those values are affected by both temperature and relative humidity. Fig. 8 shows how much the hydration level differed from full hydration in terms of the D-spacing for our samples at different temperatures. Fig. 9 shows how much λ_r and γ change as a function of D-spacing at the same temperature. Combining these two sets of data allows us to estimate the effect of temperature alone, as is shown by the corrected values in Fig. 4.

Density data yielded a molecular volume for ESM as shown in Fig. 10A. The main phase transition was centered at T_M = 38.3 °C, but it was broad (~4°) as expected for a mixture of chain lengths. No pretransition was observed for ESM. Similar density traces were obtained for PSM, but the absolute molecular volumes are not accurate because the amount of material was much smaller and was not quantitated

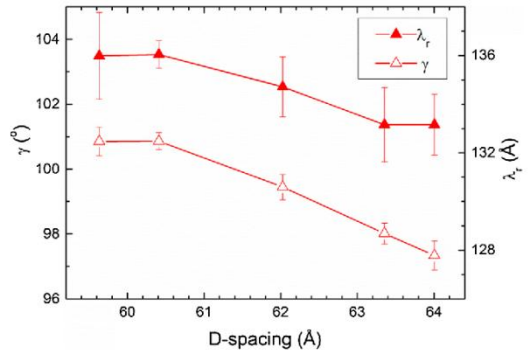

Fig. 9. Effect of hydration level, as indicated by D-spacing, upon unit cell parameters λ_r (solid red triangles, right axis) and γ (open red triangles, left axis). Sample was PSM at 37 °C.

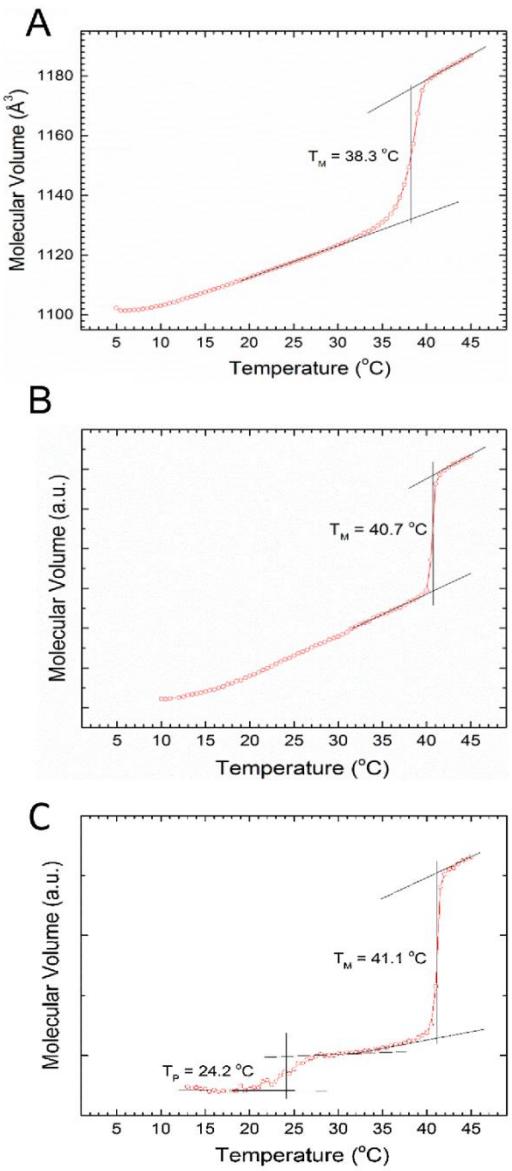

Fig. 10. A. Densitometer scan of ESM immediately after cooling to 3 °C. B. Densitometer scan of PSM immediately after cooling to 3 °C. C. Densitometer scan of PSM after incubating the sample at 3 °C for 4-1/2 days. The T_M was determined as the midpoint of the straight line connecting the extensions of the upper and lower slopes. The heating rate was 12 °C/h.

precisely. The scan in Fig. 10B gave T_M = 40.7 °C for PSM with a smaller width of ~2°, but no pretransition was visible. However, when the sample was held at 3 °C for 4.5 days, a pretransition was readily visible at T_P = 24.2 °C in Fig. 10C, which is a similar value to the DSC literature results for T_P shown in Table S1.

For the fluid phase, the form factors (Fig. S17) that result from diffuse LAXS (Figs. S8 and S15) and the measured volume data were

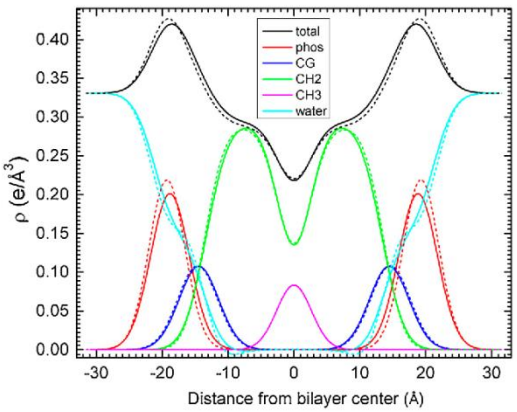

Fig. 11. Electron density profiles of PSM (solid lines) and ESM (dashed lines) in the fluid phase at 45 °C. Bilayer components are: total (black), phosphocholine headgroup (red), glycerol backbone linkage (blue), CH2 groups (green), terminal CH3 groups (magenta) and water (cyan). (For interpretation of the references to colour in this figure legend, the reader is referred to the web version of this article.)

used to construct electron density profiles (Fig. 11) which were then used to obtain A_L at 45 °C by fitting to a model of the electron density of a bilayer (Scattering Density Profile program) (Kučerka et al., 2008). One input into the SDP program is the headgroup volume with the volume ratio of the two headgroup components (phosphocholine and sphingosine linkage). To estimate these, we subtracted the hydrocarbon chain volume from the total lipid volume (see 4.5); the sphingosine linkage volume was obtained by subtracting the phosphocholine volume from the total headgroup volume (Armen et al., 1998).

4. Discussion

4.1. Identification of phases

The most important result from this work is the difference in phase behavior between ESM and PSM at $T < T_M$. We clearly find that the ripple phase in ESM is the stable phase below the main transition at least down to 3 °C. Our result that there is no phase transition below the main transition at T_M agrees with many previous investigations that have reported only a single transition in ESM at 36–39.5 °C by differential scanning calorimetry (Calhoun and Shipley, 1979; Chien et al., 1991; Filippov et al., 2006; García-Arribas et al., 2016; Jiménez-Rojo et al., 2014; Mannock et al., 2003; Mckeone et al., 1986), scanning densitometry (Epand and Epand, 1980), fluorescence spectroscopy (Rujanavech et al., 1986), ^{2}H NMR spectroscopy (Steinbauer et al., 2003) and FTIR spectroscopy (Anderle and Mendelsohn, 1986; Arsov and Quaroni, 2008; Veiga et al., 2001). (Additional DSC literature results are summarized in Table S1). However, in all of these studies, the transition at T_M was interpreted as a gel-to-fluid transition, whereas our results clearly identify the main transition as a ripple-to-fluid transition. Our result agrees with previous X-ray studies that have reported a ripple phase for ESM. The SAXS data of (Chemin et al., 2008) showed weak (0,1) and (1,1) ripple reflections. Using X-ray diffraction, (Shaw et al., 2012) found that the SAXS pattern below T_M in ESM showed a number of broad peaks which could not be resolved from each other. These peaks fit within the same envelope as the ripple phase peaks of bovine brain sphingomyelin which they were able to resolve, so they concluded that ESM was also likely to be in a ripple phase below T_M. A third X-ray investigation reported that after prolonged equilibration at 20 °C, bilayers of ESM formed a ripple structure with a somewhat

Table 1
Elastic and structural results for gel and fluid phases.

Sample	$K_C \times 10^{-20}$ (J)[a]	S_{xray}	A_L (Å^2)	Tilt Angle θ_{tilt} (°)	D_B (Å)
PSM (fluid, 45 °C)	8.3 ± 0.1	0.54 ± 0.02	64 ± 2	–	36.6 ± 1.2
ESM (fluid, 45 °C)	6.7 ± 0.4	0.48 ± 0.02	64 ± 2	–	37.1 ± 1.2
DPPC (fluid, 50 °C)[b]	6.7 ± 0.7	0.41 ± 0.03	64 ± 1[b]	–	38.5 ± 0.5[b]
			63 ± 1[c]		39 ± 0.5[c]
PSM (gel, 3 °C)	–	–	44.5 ± 0.5	30.4 ± 0.6	49.4 ± 0.3
DPPC (gel, 3 °C)[d]	–	–	47.0 ± 0.3	34.0 ± 0.4	48.0 ± 0.2

[a] Results without including a tilt degree of freedom (Nagle, 2017).
[b] (Guler et al., 2009).
[c] (Kučerka et al., 2008).
[d] (Sun et al., 1996a).

smaller periodicity of 125 Å that was obtained from the (0,1) in-plane reflection (Quinn and Wolf, 2009). Based on this peak and on their WAXS results, the authors suggested that at 20 °C ESM showed a phase coexistence of a ripple phase with an interdigitated phase, but it appears that they misinterpreted the higher order ripple peaks. Unlike these previous X-ray works which studied isotropic MLV samples, our oriented samples much more clearly show a rippled phase that is stable from 35 down to 3 °C. This is because oriented samples have clear separations between lamellar and off-specular peaks (Hentschel and Rustichelli, 1991), that are easily measured using a two-dimensional detector.

In contrast to ESM, in PSM the ripple phase is only stable down to about 24 °C and below that the stable phase is a flat gel phase. Previous structural studies (Calhoun and Shipley, 1979; Maulik and Shipley, 1996) found no evidence for a ripple phase in PSM. Some calorimetric studies (Maulik and Shipley, 1996) did not observe a pre-transition in PSM and concluded that PSM is in the gel phase below T_M. Other calorimetric studies reported a pre-transition (Barenholz and Shinitzky, 1976; Calhoun and Shipley, 1979), and those are consistent with our PSM structural results. It has been suggested that this difference in results may be due to the synthesis of PSM yielding a fraction in the L-threo form instead of the D-erythro form (Ramstedt and Slotte, 1999; Venable et al., 2014). In contrast, the Avanti supplied lipid is greater than 98% D-erythro PSM. In any case, we believe that we have now established the PSM phase behavior and that it differs from ESM.

What could be the origin of the stability of the ripple phase in ESM? Recall that the fatty acid composition of Avanti Polar Lipid ESM is 86% 16:0, 6% 18:0, 3% 22:0, 3% 24:0 and 2% unknown. We suggest that it is the presence of a small percentage of longer chain length lipids (18, 22 and 24 carbons) that stabilize the ripple phase in ESM, perhaps by locating in the major arm (M), since the major arm has been shown to be thicker than the minor arm (m), at least in DMPC (Akabori and Nagle, 2015; Sun et al., 1996b). Adding longer chain lipids to the M arm would then increase the disparity between the M and m arms, which would have the tendency to stabilize the ripple phase in ESM to lower temperature. Future experiments on well-defined mixtures could test this suggestion.

4.2. Ripple phase wavelength λ_r

The temperature change is the primary modulator of the ripple structure in our study. As shown in Fig. 4A for ESM, the ripple wavelength λ_r decreases from ~170 to 145 Å over a 32 ° increase. This result is in the same direction, but not as dramatic, as that observed using X-ray diffraction for DMPC, where the ripple repeat decreased from 135 to 120 Å when the temperature increased from 15.2 to 20 °C (Matuoka et al., 1994).

4.3. Ripple phase gamma angle γ

Hydration is the primary modulator of the stacking angle γ which is an indicator of the asymmetry of ripples (Lubensky and Mackintosh, 1993). Asymmetric ripples are defined by the length of the M arm being different from the length of the m arm. Then, interbilayer interactions establish different thickness of the water layers between adjacent bilayers and the stacking of adjacent unit cells may be shifted along the x axis as well as along the z axis, thereby resulting in a value of γ not necessarily equal to 90°. In contrast, if the ripples were symmetric, γ would necessarily be 90°. In *l*-DPPC and *dl*-DPPC (Katsaras et al., 2000) as well as in DMPC (Wack and Webb, 1989) γ decreases as a function of increasing D-spacing. In *l*-DPPC, γ decreased from ~98° at 64 Å to ~90° at 68 Å, and then decreased further to 85° at 73 Å lamellar D-spacing (Katsaras et al., 2000). In ESM, we find that γ > 90° at our largest D-spacings close to T_M, although these D-spacings are not as large as those for *l*-DPPC. In PSM γ decreases from 101 to 98° at lamellar D from 59.5 to 64 Å (Fig. 9). For the same level of hydration, Fig. 4B indicates little effect of temperature on γ.

4.4. Gel and fluid phase properties

Results for PSM and ESM are summarized in Table 1, including bending modulus K_C and the order parameter S_{xray} (Mills et al., 2008) in the fluid phase, area/lipid A_L, bilayer thickness ($D_B = V_L/A_L$) and tilt angle θ_{tilt} in the gel phase. As shown, there was little difference in fluid phase structure between ESM and PSM, although PSM was stiffer than ESM and somewhat more ordered as determined by S_{xray}. Literature results for DPPC are shown for comparison. Except for the considerably smaller value of S_{xray}, which agrees with NMR(S_{CD}) result of (Mehnert et al., 2006), differences are small. Further comparison of these results with X-ray and NMR studies from the literature can be found in Tables S2 and S3.

Results for the gel phase of PSM are also compared in Table 1 to results for DPPC extrapolated to 3 °C. Not shown in Table 1 are values for the area/chain A_C perpendicular to the chains. That value is 19.2 ± 0.2 Å^2 for PSM and for DPPC it is 19.5 ± 0.2 Å^2 (Sun et al., 1996a). This indicates a slightly tighter packing of PSM than DPPC. The other primary difference is the smaller tilt angle in PSM. Those two differences make the area/lipid of PSM noticeably smaller through the relation $A_L = 2A_C/\cos\theta_{tilt}$.

4.5. Contact with MD simulations

Simulations are generally very poor for ripple phases and even problematic for gel phases. However, it is appropriate to compare to MD simulations of sphingomyelins in the fluid phase. One point of contact we can make presently is with our most accurately obtained volume of 1187 ± 1 Å^3 at 45 °C for ESM in the fluid phase. To compare to simulations of PSM at 50 °C, we added 6 Å^3 for thermal expansion using (Nagle and Wilkinson, 1978) and subtracted 27 Å^3 per extra methylene to account for the longer chains in the ESM mixture to obtain 1178 Å^3. Lipid volumes from GROMACS MD simulations of PSM at 50 °C yielded 1168 ± 12 Å^3 (Metcalf and Pandit, 2012) and

1180 ± 10 Å^3 (Niemela et al., 2004). Another point of contact is our A_L of 64 Å^2 for both ESM and PSM. Our area in Table 1 is significantly larger than the average 54 ± 3 Å^2 obtained in several MD simulations (Venable et al., 2014) (and references therein), which suggests that the SM force fields might have to be re-evaluated.

4.6. General comment

Our results address the question of whether the less expensive ESM mixture is likely to be a suitable replacement for the more specific PSM lipid in raft studies that assume that ESM is a single component or when comparing simulations that use PSM to compare to experimental data obtained using ESM. Our result that the lipid areas are essentially the same is encouraging that such replacements can be used in the fluid phase, which is where simulations are most reliable. However, for phase behavior, our results show different propensities to form ripple versus gel phases. While ripple phases are unlikely to form in ternary mixtures, the different propensity to form ripple phases shows that PSM and ESM have different interactions that could affect the stability of liquid ordered phases in lipid raft mixtures, depending on which lipid is used. However, this difference occurs only for temperatures substantially below the main transition temperature, which is itself different by a few degrees between ESM and PSM. Probably, these differences would only be significant for the most careful studies of phase behavior.

Author contributions

Felix Goñi and Stephanie Tristram-Nagle conceived this project, which is part of a larger study of SM mixtures. John Nagle and Stephanie Tristram-Nagle instructed Emilio González-Ramírez in X-ray and densitometer data collection and analysis. Emilio González-Ramírez and Zoran Arsov collected and analyzed X-ray and densitometer data. Zoran Arsov, Stephanie Tristram-Nagle and John Nagle wrote the paper. John Nagle takes responsibility for the integrity of the work as a whole, from inception to finished article.

Acknowledgements

We thank Dr. Steve Burgess at Avanti Polar Lipids for providing detailed information regarding the purity of PSM. Z.A. acknowledges financial support by the Slovenian Research Agency (research program No. P1-0060) and the Fulbright Visiting Scholar Program. E.J.G.-R. acknowledges the University of the Basque Country for a pre-doctoral grant. F.M.G. acknowledges the Spanish Ministry of Economy (BFU 2015-66306-P) and the Basque Government (IT-849-13). S.T.-N. acknowledges financial support from the Samuel and Emma Winters Foundation.

Appendix A. Supplementary data

Supplementary data associated with this article can be found, in the online version, at https://doi.org/10.1016/j.chemphyslip.2018.03.003.

References

Akabori, K., Nagle, J.F., 2015. Structure of the DMPC lipid bilayer ripple phase. Soft Matter 11, 918–926.
Anderle, G., Mendelsohn, R., 1986. Fourier-transform infrared studies of CaATPase phospholipid interaction – survey of lipid classes. Biochemistry-Us 25, 2174–2179.
Armen, R.S., Uitto, O.D., Feller, S.E., 1998. Phospholipid component volumes: determination and application to bilayer structure calculations. Biophys. J . 75, 734–744.
Arsov, Z., Quaroni, L., 2008. Detection of lipid phase coexistence and lipid interactions in sphingomyelin/cholesterol membranes by ATR-FTIR spectroscopy. Biochim. Biophys. Acta 1778, 880–889.
Barenholz, Y., Shinitzky, M., 1976. Effect of sphingomyelin level on membrane dynamics. Israel J. Med. Sci. 12, 1362–1363.
Barenholz, Y., Suurkuusk, J., Mountcastle, D., Thompson, T.E., Biltonen, R.L., 1976. A calorimetric study of thermotropic behavior of aqueous dispersions of natural and synthetic sphingomyelins. Biochemistry-Us 15, 2441–2447.
Calhoun, W.I., Shipley, G.G., 1979. Fatty-acid composition and thermal-behavior of natural sphingomyelins. Biochim. Biophys. Acta 555, 436–441.
Chemin, C., Bourgaux, C., Pean, J.M., Pabst, G., Wuthrich, P., Couvreur, P., Ollivon, M., 2008. Consequences of ions and pH on the supramolecular organization of sphingomyelin and sphingomyelin/cholesterol bilayers. Chem. Phys. Lipids 153, 119–129.
Chien, K.Y., Huang, W.N., Jean, J.H., Wu, W.G., 1991. Fusion of sphingomyelin vesicles induced by proteins from Taiwan cobra (Naja–Naja Atra) venom – Interactions of zwitterionic phospholipids with cardiotoxin analogs. J. Biol. Chem. 266, 3252–3259.
Chu, N., Kučerka, N., Liu, Y.F., Tristram-Nagle, S., Nagle, J.F., 2005. Anomalous swelling of lipid bilayer stacks is caused by softening of the bending modulus. Phys. Rev. E 71, 041904.
de Almeida, R.F.M., Fedorov, A., Prieto, M., 2003. Sphingomyelin/phosphatidylcholine/cholesterol phase diagram: boundaries and composition of lipid rafts. Biophys. J. 85, 2406–2416.
van Meer, G., Voelker, D.R., Feigenson, G.W., 2008. Membrane lipids: where they are and how they behave. Nat. Rev. Mol. Cell Biol. 9, 112–124.
Epand, R.M., Epand, R.F., 1980. Studies of thermotropic phospholipid phase-transitions using scanning densitometry. Chem. Phys. Lipids 27, 139–150.
Filippov, A., Oradd, G., Lindblom, G., 2006. Sphingomyelin structure influences the lateral diffusion and raft formation in lipid bilayers. Biophys. J . 90, 2086–2092.
Garcia-Arribas, A.B., Axpe, E., Mujika, J.I., Merida, D., Busto, J.V., Sot, J., Alonso, A., Lopez, X., Garcia, J.A., Ugalde, J.M., Plazaola, F., Goni, F.M., 2016. Cholesterol-ceramide interactions in phospholipid and sphingolipid bilayers as observed by positron annihilation lifetime spectroscopy and molecular dynamics simulations. Langmuir: ACS J. Surf. Colloids 32, 5434–5444.
Goni, F.M., Alonso, A., 2006. Biophysics of sphingolipids I. Membrane properties of sphingosine: ceramides and other simple sphingolipids. Biochim. Biophys. Acta 1758, 1902–1921.
Guler, S.D., Ghosh, D.D., Pan, J., Mathai, J.C., Zeidel, M.L., Nagle, J.F., Tristram-Nagle, S., 2009. Effects of ether vs ester linkage on lipid bilayer structure and water permeability. Chem. Phys. Lipids 160, 33–44.
Hentschel, M.P., Rustichelli, F., 1991. Structure of the ripple phase P-beta' in hydrated phosphatidylcholine multimembranes. Phys. Rev. Lett. 66, 903–906.
Jimenez-Rojo, N., Garcia-Arribas, A.B., Sot, J., Alonso, A., Goni, F.M., 2014. Lipid bilayers containing sphingomyelins and ceramides of varying N-acyl lengths: a glimpse into sphingolipid complexity. Biochim. Biophys. Acta 1838, 456–464.
Katsaras, J., Tristram-Nagle, S., Liu, Y., Headrick, R.L., Fontes, E., Mason, P.C., Nagle, J.F., 2000. Clarification of the ripple phase of lecithin bilayers using fully hydrated, aligned samples. Phys. Rev. E 61, 5668–5677.
Kučerka, N., Nagle, J.F., Sachs, J.N., Feller, S.E., Pencer, J., Jackson, A., Katsaras, J., 2008. Lipid bilayer structure determined by the simultaneous analysis of neutron and X-ray scattering data. Biophys. J. 95, 2356–2367.
Kučerka, N., Liu, Y.F., Chu, N.J., Petrache, H.I., Tristram-Nagle, S.T., Nagle, J.F., 2005. Structure of fully hydrated fluid phase DMPC and DLPC lipid bilayers using X-ray scattering from oriented multilamellar arrays and from unilamellar vesicles. Biophys. J . 88, 2626–2637.
Lubensky, T.C., Mackintosh, F.C., 1993. Theory of ripple phases of lipid bilayers. Phys. Rev. Lett. 71, 1565–1568.
Mannock, D.A., McIntosh, T.J., Jiang, X., Covey, D.F., McElhaney, R.N., 2003. Effects of natural and enantiomeric cholesterol on the thermotropic phase behavior and structure of egg sphingomyelin bilayer membranes. Biophys. J . 84, 1038–1046.
Mason, P.C., Gaulin, B.D., Epand, R.M., Wignall, G.D., Lin, J.S., 1999. Small-angle scattering studies of the fully hydrated phospholipid DPPC. Phys. Rev. E 59, 921–928.
Matuoka, S., Kato, S., Hatta, I., 1994. Temperature-change of the ripple structure in fully hydrated dimyristoylphosphatidylcholine cholesterol multibilayers. Biophys. J . 67, 728–736.
Maulik, P.R., Shipley, G.G., 1996. N-palmitoyl sphingomyelin bilayers: structure and interactions with cholesterol and dipalmitoylphosphatidylcholine. Biochemistry-Us 35, 8025–8034.
Mckeone, B.J., Pownall, H.J., Massey, J.B., 1986. Ether phosphatidylcholines – comparison of miscibility with ester phosphatidylcholines and sphingomyelin, vesicle fusion, and association with apolipoprotein-a-I. Biochemistry-Us 25, 7711–7716.
Mehnert, T., Jacob, K., Bittman, R., Beyer, K., 2006. Structure and lipid interaction of N-palmitoylsphingomyelin in bilayer membranes as revealed by H-2-NMR spectroscopy. Biophys. J . 90, 939–946.
Metcalf, R., Pandit, S.A., 2012. Mixing properties of sphingomyelin ceramide bilayers: a simulation study. J. Phys. Chem. B 116, 4500–4509.
Mills, T.T., Toombes, G.E.S., Tristram-Nagle, S., Smilgies, D.M., Feigenson, G.W., Nagle, J.F., 2008. Order parameters and areas in fluid-phase oriented lipid membranes using wide angle x-ray scattering. Biophys. J . 95, 669–681.
Nagle, J.F., Wilkinson, D.A., 1978. Lecithin bilayers: density measurement and molecular interactions. Biophys. J . 23, 159–175.
Nagle, J.F., Akabori, K., Treece, B.W., Tristram-Nagle, S., 2016. Determination of mosaicity in oriented stacks of lipid bilayers. Soft Matter 12, 1884–1891.
Nagle, J.F., 2017. Experimentally determined tilt and bending moduli of single-component lipid bilayers. Chem. Phys. Lipids 205, 18–24.
Niemela, P., Hyvonen, M.T., Vattulainen, I., 2004. Structure and dynamics of sphingomyelin bilayer: insight gained through systematic comparison to phosphatidylcholine. Biophys. J. 87, 2976–2989.
Quinn, P.J., Wolf, C., 2009. Thermotropic and structural evaluation of the interaction of natural sphingomyelins with cholesterol. Biochim. Biophys. Acta 1788, 1877–1889.
Ramstedt, B., Slotte, J.P., 1999. Comparison of the biophysical properties of racemic and d-erythro-N-acyl sphingomyelins. Biophys. J. 77, 1498–1506.
Ramstedt, B., Slotte, J.P., 2002. Membrane properties of sphingomyelins. FEBS Lett. 531, 33–37.

Ramstedt, B., Leppimäki, P., Axberg, M., Slotte, J.P., 1999. Analysis of natural and synthetic sphingomyelins using high-performance thin-layer chromatography. Eur. J. Biochem. 266, 997–1002.
Rappolt, M., Rapp, G., 1996. Structure of the stable and metastable ripple phase of dipalmitoylphosphatidylcholine. Eur. Biophys. J. Biophys. 24, 381–386.
Rujanavech, C., Henderson, P.A., Silbert, D.F., 1986. Influence of sterol structure on phospholipid phase-behavior as detected by parinaric acid fluorescence spectroscopy. J. Biol. Chem. 261, 7204–7214.
Shaw, K.P., Brooks, N.J., Clarke, J.A., Ces, O., Seddon, J.M., Law, R.V., 2012. Pressure-temperature phase behaviour of natural sphingomyelin extracts. Soft Matter 8, 1070–1078.
Slotte, J.P., 2013. Molecular properties of various structurally defined sphingomyelins – correlation of structure with function. Prog. Lipid Res. 52, 206–219.
Slotte, J.P., 2016. The importance of hydrogen bonding in sphingomyelin's membrane interactions with co-lipids. Biochim. Biophys. Acta 1858, 304–310.
Steinbauer, B., Mehnert, T., Beyer, K., 2003. Hydration and lateral organization in phospholipid bilayers containing sphingomyelin: a H-2-NMR study. Biophys. J. 85, 1013–1024.
Sun, W.J., Suter, R.M., Knewtson, M.A., Worthington, C.R., Tristram-Nagle, S., Zhang, R., Nagle, J.F., 1994. Order and disorder in fully hydrated unoriented bilayers of gel phase dppc. Phys. Rev. E. 49, 4665–4676.
Sun, W.J., Tristram-Nagle, S., Suter, R.M., Nagle, J.F., 1996a. Structure of gel phase saturated lecithin bilayers: temperature and chain length dependence. Biophys. J. 71, 885–891.
Sun, W.J., Tristram-Nagle, S., Suter, R.M., Nagle, J.F., 1996b. Structure of the ripple phase in lecithin bilayers. Proc. Natl. Acad. Sci. U. S. A. 93, 7008–7012.
Tristram-Nagle, S., Zhang, R., Suter, R.M., Worthington, C.R., Sun, W.J., Nagle, J.F., 1993. Measurement of chain tilt angle in fully hydrated bilayers of gel phase lecithins. Biophys. J. 64, 1097–1109.
Tristram-Nagle, S., Liu, Y.F., Legleiter, J., Nagle, J.F., 2002. Structure of gel phase DMPC determined by X-ray diffraction. Biophys. J. 83, 3324–3335.
Tristram-Nagle, S., 2007. Preparation of Oriented, Fully Hydrated Lipid Samples for Structure Determination Using X-ray Scattering. Humana Press, Totowa, NJ.
Veiga, M.P., Arrondo, J.L.R., Goñi, F.M., Alonso, A., Marsh, D., 2001. Interaction of cholesterol with sphingomyelin in mixed membranes containing phosphatidylcholine, studied by spin-label ESR and IR spectroscopies. A possible stabilization of gel-phase sphingolipid domains by cholesterol. Biochemistry-Us 40, 2614–2622.
Venable, R.M., Sodt, A.J., Rogaski, B., Rui, H., Hatcher, E., MacKerell, A.D., Pastor, R.W., Klauda, J.B., 2014. CHARMM all-atom additive force field for sphingomyelin: elucidation of hydrogen bonding and of positive curvature. Biophys. J. 107, 134–145.
Wack, D.C., Webb, W.W., 1989. Synchrotron X-ray study of the modulated lamellar phase P-beta' in the lecithin-water system. Phys. Rev. A 40, 2712–2730.
Yao, H., Matuoka, S., Tenchov, B., Hatta, I., 1991. Metastable ripple phase of fully hydrated dipalmitoylphosphatidylcholine as studied by small-angle X-ray-scattering. Biophys. J. 59, 252–255.

ACKNOWLEDGMENTS

ACKNOWLEDGMENTS

The present thesis has been carried out at the Biofisika Institute (UPV/EHU, CSIC), under the supervision of Prof. Félix M. Goñi. The work has been supported by the Basque Government (IT 849-13, IT 838-13) and the Spanish Government (FEDER/MINECO BFU 2015- 66306-P, BFU 2015-66306-P,). The author received a research fellowship from the University of the Basque Country (March 2015-February 2019).

The author is grateful to Prof. Alicia Alonso for her invaluable assistance throughout the thesis, as well as all members of the laboratory, to Dr. S. Tristram Nagle (Carnegie Mellon University, Pittsburgh, USA) for her productive collaboration in the work described in chapter 3, to Dr. I. Artetxe for the fluorescence spectroscopy measurements in chapter 4, to Dr. Frank Lafont and Dr. Lorena Redondo Morata for their training in high-speed atomic force microscopy (Institute Pasteur, Lille, France).